DEPARTAMENTO DE ASTROFÍSICA

Universidad de La Laguna

Simulations of the solar chromosphere in the two-fluid approximation

Memoria que presenta
Beatrice Popescu Braileanu
para optar al grado de
Doctora por la Universidad de La Laguna.

INSTITUTO Đ ASTROFISICA Đ CANARIAS
febrero de 2020

Thesis supervisors: Dr. Elena Khomenko and Dr. Angel de Vicente

Part of the included material has been already published in A&A.
Parte del material incluido en este documento ya ha sido publicado en A&A.

Acknowledgments

I am grateful for the financial support received from the Spanish Ministry of Science through the scholarship I had during the PhD, associated to the project AYA2014-55078-P. I would like to thank to my supervisors, Elena Khomenko and Angel de Vicente, but also to my collaborator Slava Lukin who helped me greatly during these years. I appreciate the help that I received from James Leake and Paul Cally during my short stays. I am very grateful to Stefaan Poedts and Andrew Hillier who accepted the hard task to be the referees of this thesis. I would also like to thank to all the members of the solar group at the IAC who helped me with very useful discussions. I appreciate the help of my family who supported me during the work.

I would like to acknowledge the contribution of Teide High-Performance Computing facilities to the results of this research. TeideHPC facilities are provided by the Instituto Tecnológico y de Energías Renovables (ITER, SA). URL:`http://teidehpc.iter.es` I want to thank to all the employees of the IAC who made my life easy and pleasant during these years at work, especially the IT colleagues.

Resumen

Este trabajo presenta el estudio numérico de la propagación de ondas y la inestabilidad Rayleigh-Taylor en la atmósfera solar usando un modelo de dos fluidos. La atmósfera solar es fuertemente estratificada, y con campos magnéticos complejos, creando capas con regímenes muy diferentes. La fotosfera es la capa más densa con campo magnético mas intenso. La gran densidad hace que el plamsa esté completamente acoplado por colisiones y que la aproximación del modelo magnetohidrodinámico (MHD) sea válida. Debido al gran número de colisiones entre diferentes tipos de partículas: iones, electrones y neutros, el plasma se comporta como un conductor perfecto. En términos matemáticos, esta característica se refleja en que los términos no ideales de la ley generalizada de Ohm son muy pequeños comparados con el término ideal. En un plasma perfectamente conductor las líneas de campo están ligadas al plasma. La corona está totalmente ionizada, e incluso si el campo magnético es más débil que en la fotosfera, la muy baja densidad del plasma hace que la corona sea una capa dominada por el campo magnético. Debido a la disminución de la densidad, las frecuencias de colisión también decrecen desde la fotosfera hacia la corona. En estos casos límite, de la fotosfera completamente acoplada por colisiones y la corona completamente ionizada y sin acoplamiento colisional, las simulaciones que usan modelos MHD dan resultados muy buenos comparados con las observaciones, pero esta situación no es el caso de la cromosfera. La cromosfera es una capa dinámica de la atmósfera solar situada entre la fotosfera y la corona. Es una capa de transición donde la evolución del plasma cambia de estar dominada por la presión del gas a estar dominada por el campo magnético, y donde el acoplamiento colisional decrece y la fracción de ionización crece. El tiempo medio entre las colisiones entre cargas y neutros es del mismo orden que el tiempo característico de evolución de las variables hidrodinámicas. Eso hace que los neutros y las cargas se desacoplen parcialmente y que la aproximación MHD clásica no sea válida en la cromosfera. Una alternativa al modelo MHD es un modelo de dos fluidos que ha sido implementado de forma numérica en este trabajo.

La complejidad de la atmósfera solar hace que sea imposible resolver de forma analítica las ecuaciones, así que los problemás se resuelven de forma numérica mediante simulaciones. Hemos extendido el código MHD no ideal Mancha3D, para implementar el modelo de dos fluidos. El código Mancha3D usa un esquema numérico temporal explícito, que presenta una serie de ventajas en el caso de simulaciones paralelas a gran escala en dominios 3D. Los efectos de ionización parcial se tienen en cuenta en la aproximación MHD a través de la ley de Ohm generalizada. Sin embargo, el modelo de dos fluidos introduce términos de acoplamiento colisional, lo que puede hacer que un código con un esquema numérico explícito se haga numéricamente inestable. Para asegurar la estabilidad cuando los términos colisionales se incluyen en un esquema explícito, el paso temporal necesario para integrar temporalmente las ecuaciones es inversamente proporcional a la frecuencia de colisión. Esta restricción se puede evitar implementando los términos colisionales de manera implícita. En el nuevo código, tratamos dichos términos de forma implícita usando un esquema semi implícito.

Para probar el esquema numérico y determinar el orden de convergencia del esquema, hacemos unos tests de ondas acústicas y Alfvén en un medio uniforme, donde la solución numérica se puede comparar con la solución analítica exacta. Después hacemos simulaciones más realistas de ondas

magnetoacústicas rápidas, usando el modelo de la atmósfera solar VALC. En los dos casos observamos amortiguamiento de las ondas, que es más grande cuando la frecuencia de colisión es parecida a la frecuencia de la onda. Los resultados son consistentes con resultados presentados en la literatura. Cuando la amplitud es suficientemente grande, podemos observar el mecanimso adicional de damping no lineal que no puede ser predicho por una solución analítica, pero se puede apreciar a través de simulaciones numéricas. Hemos hecho una simulacion usando el modelo MHD y una configuración correspondiente a la configuración para el modelo de dos fluidos, donde la interacción entre neutros y cargas se introduce a través del término ambipolar en la ecuación de inducción. Observamos que aunque el damping de la onda es parecido en los dos casos, el aumento en la temperatura es mayor en el modelo con dos fluidos comparado al modelo MHD.

En la última parte presentamos simulaciones de la inestabilidad Rayleigh-Taylor (RTI) en la interfaz entre una protuberancia y la corona solar. Estudiamos la tasa de crecimiento, el desacoplamiento y los modos dominates en un modelo donde la transición entre la prominencia y la corona es continua con una escala característica. Realizamos varias simulaciones donde estudiamos el efecto de las colisiones elásticas e inelásticas, la viscosidad y la conductividad térmica, la compresibilidad, la configuración del campo magnético, el contraste de densidad y la perturbación inicial sobre el desarrollo de la inestabilidad. En estas simulaciones hemos considerado la ley de Ohm ideal (sin difisividad magnética). Observamos que la tasa de crecimento lineal es menor que en el caso MHD (completamente acoplado por colisiones) ideal (sin viscosidad y conductividad térmica), e incompresible. En el modelo MHD ideal sin campo mgnético, la compresibilidad aumenta la tasa de crecimiento lineal para nuestro perfil de densidad.

Summary

This work presents the study of wave propagation and the Rayleigh-Taylor instability in the solar atmosphere using a two-fluid model. The solar atmosphere is strongly stratified and permeated by magnetic fields with a complex configuration, thus creating very different regimes throughout its layers. Of the different layers of the solar atmosphere the photosphere is the one with the highest density and the strongest magnetic field. The high density makes the plasma collisionally coupled and the magnetohydrodynamic (MHD) assumption valid. Because of the high collision frequencies between different constituents: ions, free electrons and neutral particles, the plasma becomes a perfect conductor. In mathematical terms, the non-ideal terms which appear in the generalized Ohm's law are very small compared to the ideal term. In the assumption of a perfectly conducting plasma, the field lines are tied to the plasma. The corona is fully ionized, and even if the magnetic fields are weaker than in the photosphere, the very low density of plasma makes the corona a layer dominated by the magnetic field. Because the density decreases, the collision frequencies also decrease from the photosphere towards the corona. In these two extreme collisional regimes, coupled and uncoupled, MHD simulations give good results compared to the observations, but this is not the case for the chromosphere. The solar chromosphere is a complex and dynamic layer located between the photosphere and the corona. It is a transition layer where the properties of plasma change abruptly from gas pressure dominated to magnetic field dominated, and where the collisional coupling of the plasma decreases and the ionization fraction increases. The collisional timescales between ionized and neutral atomic species become equal or larger than the hydrodynamic timescale causing partial decoupling between charges and neutrals. Therefore, classical MHD approach is not valid in the chromosphere. A suitable alternative for this approach is a two-fluid model, numerically implemented in this work.

The complexity of the solar atmosphere does not allow to solve the equations analytically, and the problems are solved numerically using simulations. We have extended the non-ideal single-fluid code, Mancha3D, to simultaneously treat neutral and ionized plasma components in the two-fluid approach. The Mancha3D code uses an explicit scheme which has a series of advantages in the case of large-scale parallel simulations in 3D domains. The partial ionization effects are taken into account in the single-fluid approach through a generalized Ohm's law. However, the two-fluid approach introduces collisional coupling terms which can lead an explicit code to become numerically unstable. For high collision frequencies the equations become stiff. In order to ensure stability when the collisional terms are included in an explicit scheme, the time step needed to integrate the equations in time numerically is of order of the inverse of the collision frequency. When the collisional frequency is high, the time step imposed is very small. This restriction can be overcome by implementing the collisional terms implicitly. In our newly developed code we treat such terms implicitly in a semi implicit scheme.

We perform tests of acoustic and Alfvén waves in a uniform atmosphere, where we can compare the numerical solutions to exact analytical solutions, for the purpose of the verification of the code and the determination of the order of accuracy of the scheme. Afterwards, we run more realistic simulations of fast magnetoacoustic waves in a stratified atmosphere, where we have used the VALC model. In both cases we observe damping of the waves, more pronounced when the collision frequency

is similar to the wave frequency. These results are consistent with results present in the literature. When the amplitude is large enough, an additional mechanism of damping can be observed, which cannot be predicted by an analytical solution, but it can be shown through numerical simulations. We have performed a simulation using the MHD model, with a setup corresponding to the setup used in the two-fluid approach, where the interaction between neutrals and charges is introduced through the ambipolar term in the induction equation. We observed that, even if the damping of the wave is similar in the two cases, the increase in temperature is several times smaller in the MHD case.

In the last part we study Rayleigh-Taylor instability at the interface between a solar prominence and corona. We analyze the growth rate, the decoupling, the energy spectra in several simulations where we want to study the effect of the elastic and inelastic collisions, viscosity and thermal conductivity, compressibility, density contrast, initial perturbation, and the background magnetic field on the development of the instability in a non uniform medium where the transition between the prominence and the corona is continuous with a characteristic length scale. In these simulations we have considered ideal Ohm's law (no magnetic diffusivity). We observe that the linear growth rate is considerably smaller than in the ideal incompressible MHD case without viscosity and thermal conductivity. We conclude that the ion-neutral collisions, the viscosity and thermal conductivity have a stabilizing effect. The magnetic field also inhibits the instability. For our equilibrium configuration, in the ideal case without magnetic field, the compressibility increases the linear growth rate.

Contents

1

Introduction

The Sun is our closest star and its activity directly affects the life on Earth and the space weather. Disturbances in the solar wind can cause geomagnetic storms, and strong flares can produce emission of dangerous radiation. Predicting these phenomena becomes ever important because of the increasing number of artificial satellites.

By studying the Sun our knowledge of other stars and theoretical models can be improved. The Sun is a large natural plasma laboratory that can be studied in detail. A plasma is a gas where some of the atoms are ionized. The motion of ions and electrons creates electromagnetic forces, that, in return, influence the motion of these charged particles. The study of these complex interactions in a plasma of extreme temperature and density conditions is possible for the Sun because we can spatially resolve its surface in observations.

The Sun is a main sequence star, which burns hydrogen to helium into its core and the energy is transported towards the surface mainly by radiation and convection mechanisms. The Sun is mostly made up of hydrogen (about 92.1% of the number of atoms, 75% of the mass), helium (7.8% of the number of atoms and 25% of the mass), and the other 0.1% consists of heavier elements, such as: carbon, nitrogen, oxygen, neon, magnesium, silicon and iron.

The Sun is a big plasma sphere, denser towards its core, and it is observed that different latitudes rotate at different rates: faster at the equator than at the poles, a fact that can also be observed by looking at the sunspots as they move across the Sun's disk. The differential rotation causes its magnetic field to become twisted and tangled and this can produce very strong localized magnetic fields. The places where these tangled field lines break the surface are the sunspots.

A sketch of the solar interior is presented in Figure 1.1. The core is the innermost part of the Sun, where the nuclear reactions take place, with very high temperatures estimated at 15 millions K and densities of 150 000 kg/m^3. The energy produced in the core is transported in the form of radiation through the radiation zone until it reaches the convection zone. While the temperature drops towards

the exterior, the plasma becomes more opaque, and the trapped radiation makes the temperature gradient even larger. As the radiation is absorbed towards the surface, the radiation mechanism becomes insufficient to transport the energy and the plasma will be unstable to convection motions. The condition for convective instability is expressed by the Schwarzschild criterion,

$$\left|\frac{dT}{dz}\right|_{\rm rad} > \left|\frac{dT}{dz}\right|_{\rm ad} , \tag{1.1}$$

where $|dT/dz|_{\rm rad}$ and $|dT/dz|_{\rm ad}$ are the absolute values of the temperature gradient obtained if all the energy were transported by radiation, and the temperature gradient obtained in an adiabatic process, respectively. This criterion is fulfilled in the convection zone.

Because of small values of the viscosity, the motions of the plasma in the convection zone are turbulent. The tachocline, a thin layer at the base of the convective zone, is the transition between this turbulent layer and the radiative region. In this layer the rotation changes from solid body rotation in the interior to the differential rotation in the convection zone, therefore the rotation speed strongly changes. It is believed that the shear at the tachocline helps the Sun's magnetic field generation by a magnetic dynamo.

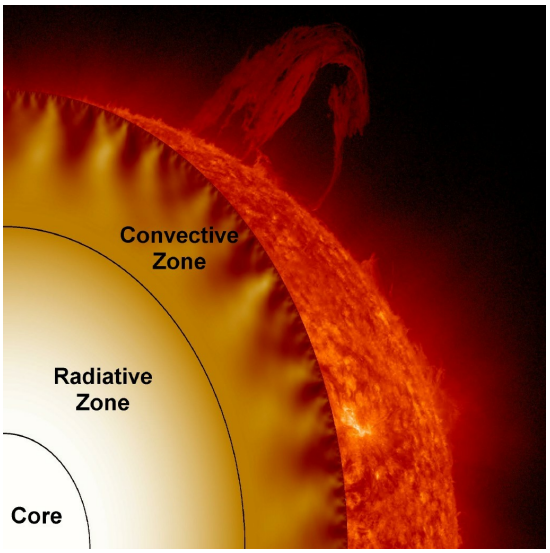

Figure 1.1: Schematic representation of the solar interior. Image taken from `https://solarscience.msfc.nasa.gov/images/cutaway.jpg`.

The interest of this thesis is in the study of the solar chromosphere. Therefore, in the first chapter of this work we describe the general properties of the solar atmosphere, with an emphasis on the

chromosphere and the need for going beyond a classical MHD approach for its modeling. Below, section 1.1 presents an introduction to the Sun's atmosphere, the motivation of this work in given in section 1.2, and the outlook of the thesis are presented in section 1.3.

1.1 The layers of the Sun's atmosphere

The atmosphere is the outer part of the Sun from where radiation escapes into space. It is composed of several layers: the photosphere, the chromosphere, the transition region and the corona. We discuss the properties of each of these layers, and the main structures that can be observed in each of them below.

The photosphere is the deepest layer from where most of the radiation escapes and that we see with naked eye. It is about 500 km thick, and has a temperature around 5800 K. A white light image of the photosphere is presented in Figure 1.2. The location where magnetic flux which rises, enters

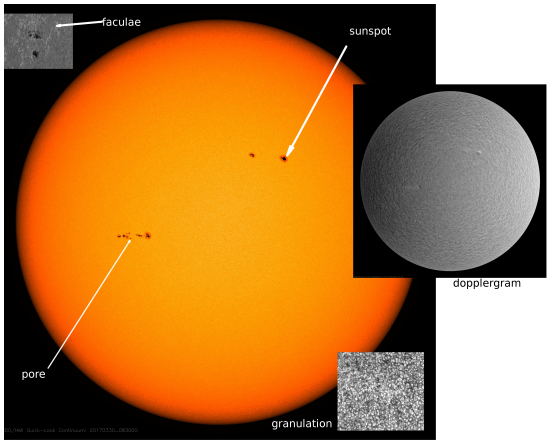

Figure 1.2: White light image of the solar photosphere obtained by the satellite SDO on March 30, 2017 https://sdo.gsfc.nasa.gov/data/. The gray-scale image on the right shows the dopplergram, while the smaller images at the upper and lower corners show high resolution pictures of a facular region and of granulation. The latter are taken from `https://solarscience.msfc.nasa.gov/feature1.shtml#Faculae`.

the solar atmosphere, and the field is mostly vertical, is called a pore. The pores grow in time and become darker (Loughhead & Bray 1961). Some of them transform into sunspots, but not all of them. There are still open questions about the process of pore transformation into sunspots and the formation of the penumbra. The magnetic field inhibits the horizontal flow in the sunspots, thus the temperature is lower than in its surroundings and the sunspots appear darker (Cowling 1953; Borrero & Ichimoto 2011). The interaction between the magnetic flux and the convection flows is responsible for the difference in properties between the umbral and photospheric granules (Loughhead & Bray 1961). The magnitude of the magnetic field is calculated by means of inversion techniques from the information contained in polarization parameters of the spectral lines observed. The magnetic field in

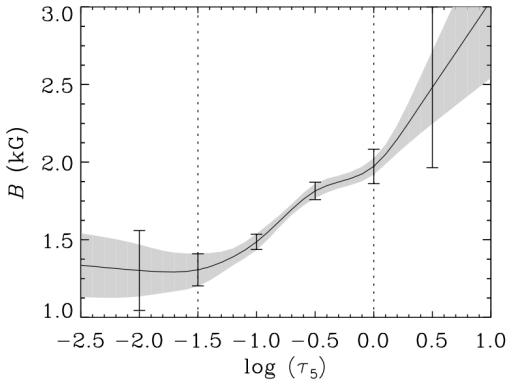

Figure 1.3: The magnitude of magnetic field measured in a sunspot from the inversion of the polarization parameters from two Fe I lines as a function of the optical depth. Taken from Mathew et al. (2003).

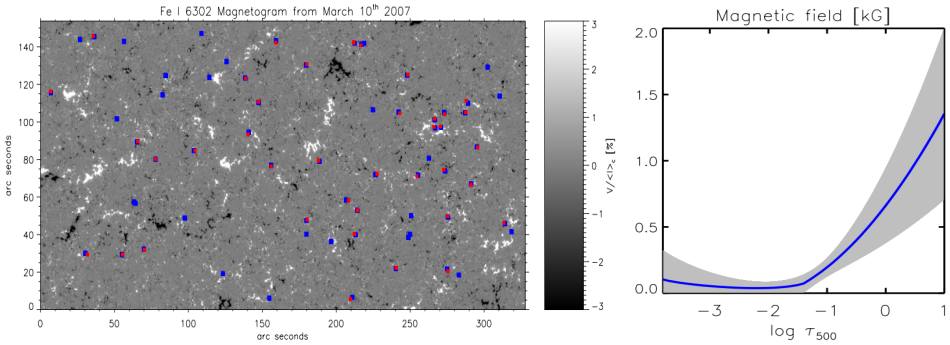

Figure 1.4: Left: Magnetogram of a region of the quiet Sun, where the red points are associated to bright regions located at the granular edges, and the blue points are associated to dark regions located at the intergranular lanes. Right: The magnitude of magnetic field measured at the location of the blue points by inversion of the 6300 Å Fe I line as a function of the optical depth. Images taken from Quintero Noda et al. (2014).

the sunspots is of the order of kilogauss (Borrero & Ichimoto 2011). Mathew et al. (2003) measured the magnetic field in a sunspot by inverting two Fe I lines and observed decreasing magnetic field strength with height all over the sunspot umbra, as presented in Figure 1.3.

The quiet Sun field is more difficult to observe because it evolves much more rapidly and on much

smaller spatial scales than the field in sunspots (Bellot Rubio & Orozco Suárez 2019). The magnetic field in the quiet Sun shows a pattern of intense kilogauss fields which form the magnetic network (Bellot Rubio & Orozco Suárez 2019). Left panel of Figure 1.4, taken from Quintero Noda et al. (2014) shows the magnetogram of a region of a quiet Sun, where the red points are associated to bright regions located at the granular edges, and the blue points are associated to dark regions located at the intergranular lanes. Both blue and red points are related to the magnetic network, and the magnetic field profile inferred for each type of them was very similar. Right panel of of Figure 1.4 shows the magnetic field obtained by inversion of the 6300 Å Fe I line data from the regions indicated by the blue points and we can observe very large magnetic fields, comparable to those measured in sunspots, shown in Figure 1.3. Observational studies of Martínez González et al. (2008) who inverted the 15600 Å and 6300 Å lines have confirmed the large field strength measured at the intergranules locations, and concluded that outside this magnetic network, the field strengths are well below the kilogauss regime. Later measurements of Martínez González et al. (2016) confirmed weak fields in the very quiet Sun, with field strength distribution peak at ≈ 250 G.

At the boundary of the supergranulation cells the horizontal flow turns into downflow. An idealized representation of these concentrations of field at the intergranules locations can be in the form of flux tubes because the magnetic field is mostly in the vertical direction. The walls of these flux tubes expand with height until they merge with adjacent tubes in the chromosphere (Pneuman et al. 1986; Bellot Rubio & Orozco Suárez 2019). A significant fraction of the photospheric magnetic flux resides in the quiet Sun, and these fields are important also for the dynamics and energetics of the solar atmosphere: through processes of emergence and cancellation, they couple the different atmospheric layers and may contribute effectively to the heating of the chromosphere and the corona (Bellot Rubio & Orozco Suárez 2019). The photosphere is dominated by elastic collisions. It has a low temperature,

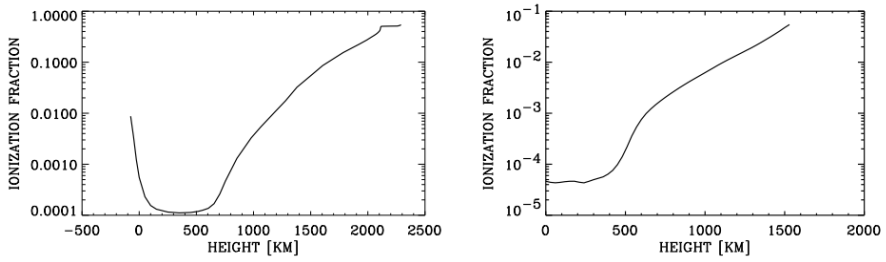

Figure 1.5: Ionization fraction as a function of height in the VALC model(left) and in the sunspot umbra model (right). Figure 4 from Khomenko et al. (2014a).

so that most of the hydrogen is in neutral state. Figure 1.5, taken from Khomenko et al. (2014a) shows an example of the ionization fraction as a function of height in the quiet Sun model, at the left panel,

and a sunspot umbra model at the right panel. Taking into account that the photosphere is defined as being between the heights $z = 0$ and $z = 500$ km, we can observe that in the quiet Sun model (at the left panel) the ionization fraction decreases with height by almost two orders of magnitude, reaching a value $\approx 10^{-4}$, because of the decrease of the temperature in this model. In the sunspot umbra model, the temperature is even lower, but the gradient in the temperature is smaller, for this reason the ionization fraction has an almost uniform value, below $\approx 10^{-4}$.

The density exponentially drops with height in the solar atmosphere. Therefore, the outer layers above the photosphere are not so bright, and cannot be generally observed just "by eye". These layers can only be observed during solar eclipses, or by using a coronagraph or special filters. The chromosphere is located right above the photosphere. This layer is 10^5 less dense than than the photosphere. It can be better observed in Hα emission line of hydrogen (6563 Å). In the chromosphere the temperature starts to rise with height, from 4000 K in its lower part, where the minimum in the whole atmosphere is reached, up to 8000 K in its upper part.

The chromosphere seen in Hα and the structures that can be observed in the chromosphere are illustrated in Figure 1.6. The chromospheric network continues the magnetic network from the photosphere, mentioned above. It is best seen in Hα and the line of calcium (Ca II K, 3933 Å), more clearly in the wings of the former (Pikelner 1963). Bright patches surrounding sunspots, called plages, are also associated with concentrations of magnetic fields found in the active regions and form a network of bright emissions. They are best seen in Hα. Small jet-like eruptions can be seen throughout the chromospheric network. They are called spicules when they are observed at the limb, and fibrils when seen on-disc. Spicules have diameters between 300 to 1500 km, last a few minutes and eject material outward into the hot corona at speeds of 20 to 30 km/s (Sterling 2000). Other structures that can be seen in the chromosphere are the filaments, which are dark thread-like features seen in Hα. These are denser, cooler, clouds of material that are suspended above the solar surface thanks to the magnetic field tension. Their counterpart seen off-limb are called prominences. These structures may persist from a few days to several months. They may undergo large-scale instabilities which may lead to their eruption, often associated with flares and coronal mass ejections (CMEs).

The transition region is a very narrow (100 km) and dynamic layer between the chromosphere and the corona where the temperature rises abruptly from about 8000 K to about 500 000 K. Hydrogen is ionized at these temperatures and is therefore difficult to see using standard Hα filters. Emitted light here comes mainly from ions such as C IV (figure 1.7, left panel), O IV , and Si IV in the ultraviolet region of the solar spectrum that is only accessible from space (`https://solarscience.msfc.nasa.gov/t_region.shtml`). The transition region is successfully observed with the IRIS mission.

The corona is 10^{12} times less dense than the photosphere and it is 10^6 times dimmer. It can be better observed in iron emission lines at very high ionization states, emitting at extremely high temperatures. The origin of the coronal heating and acceleration of the solar wind still represents an open problem in solar physics. The main structures seen in the corona are illustrated at the right panel of Figure 1.7.

In the photosphere the magnetic field is much stronger than in corona, but the plasma density is also much larger and the dynamics is governed by the gas motion. By the contrary, in the corona the

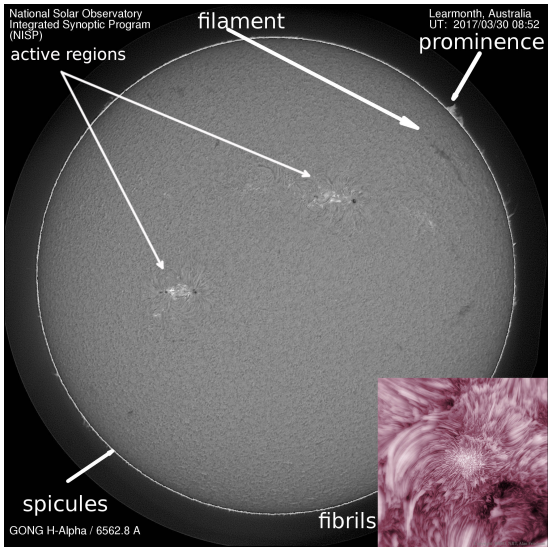

Figure 1.6: Image of the solar chromosphere in Hαfilter taken by NSO on March 30, 2017 (`http://halpha.nso.edu/`). The smaller image at the bottom corner shows a high resolution picture of chromospheric fibrils taken by BBSO (`https://apod.nasa.gov/apod/ap150217.html`).

magnetic fields are not as strong as in the photosphere, but the very low plasma density makes the corona to be dominated by the magnetic field.

1.2 The motivation of a two-fluid approach for modeling the solar chromosphere

As we have seen in the previous section, the chromosphere can be viewed as a transition from the gas pressure dominated photosphere to the magnetic field dominated corona. It is also a transition layer from the almost neutral to the fully ionized plasma. Plasma in the chromosphere is only partially ionized. The collisional frequency between charges and neutrals in the chromosphere may become smaller than the cyclotron frequency of ions. The ratio between these frequencies can be taken as a measure of the collisional coupling of the plasma, i.e. its collective behavior. Figure 1.8 (Khomenko et al. 2014a) shows the collision, cyclotron and Langmuir frequencies calculated for the solar atmosphere as a function of height. We can observe that the collision frequency decreases more than six orders of magnitude, and we expect that the collisional decoupling effects are important in the upper part of the atmosphere. The neutral atoms in plasma do not feel the action of electromagnetic forces directly but through the collisions with charges. When the collisional coupling weakens, neutral and charged plasma components become decoupled giving rise to physical effects that can only be captured by a multi-fluid model. Therefore, the classical MHD approach is not the best approximation to treat the

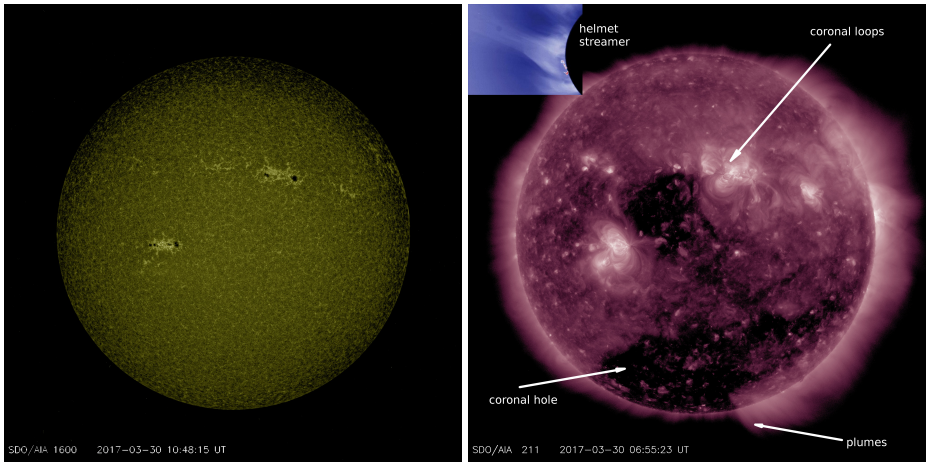

Figure 1.7: Left: Transition region seen in C IV 1600 Å, Right: image of the solar corona in 211 Å. Images taken from SDO on March 30, 2017.

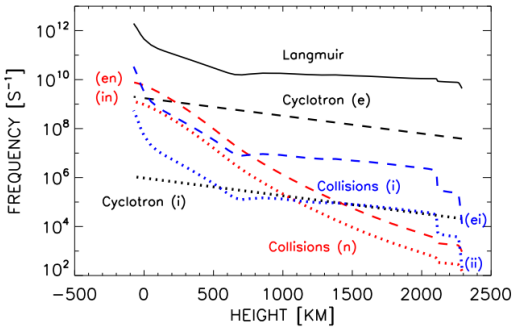

Figure 1.8: Collision, cyclotron and Langmuir frequencies calculated in the Sun atmosphere as a function of height. The species which appear in the plot are: neutrals (n), ions (i), and electrons (e). Part of Figure 1 from Khomenko et al. (2014a).

plasma processes in the chromosphere.

The chromosphere is not in local thermodynamic equilibrium. Athay & House (1962) measured and compared intensities in strong emission lines of H, He I, He II, Ca II, and the deduced ratios of the populations of various levels indicated a significant departure from a Boltzmann distribution of the

Parameter	Quiet Sun	Coronal hole	Active region
Transition layer pressure (dyn cm^{-2})	2×10^{-1}	7×10^{-2}	2
Coronal temperature (K, at $r\approx1.1\,R_\odot$)	1.1 to 1.6×10^{6}	10^{6}	2.5×10^{6}
Coronal energy losses (erg cm^{-2} sec^{-1})			
Conduction flux F_c	2×10^{5}	6×10^{4}	10^{5} to 10^{7}
Radiative flux F_r	10^{5}	10^{4}	5×10^{6}
Solar wind flux F_w	$\lesssim5\times10^{4}$	7×10^{5}	($<10^{5}$)
Total corona loss $F_c+F_r+F_w$	3×10^{5}	8×10^{5}	10^{7}
Chromospheric radiative losses (erg cm^{-2} sec^{-1})[a]			
Low chromosphere	2×10^{6}	2×10^{6}	$\gtrsim10^{7}$
Middle chromosphere	2×10^{6}	2×10^{6}	10^{7}
Upper chromosphere	3×10^{5}	3×10^{5}	2×10^{6}
Total chromospheric loss	4×10^{6}	4×10^{6}	2×10^{7}
Solar wind mass loss (g cm^{-2} sec^{-1})	$\lesssim2\times10^{-11}$	2×10^{-10}	($<4\times10^{-11}$)

Figure 1.9: Energy losses in the chromosphere and corona. Table 1 from Withbroe & Noyes (1977).

levels studied. In the high chromosphere the ratio of neutral atoms to ions exceeds the LTE values by about 10^7-10^8 in the case of He I and by about 10^6-10^7 in the case of hydrogen, and there is evidence that significant departures from LTE extend well into the photospheric layers. The formation of many photospheric lines is well described using LTE when radiation is fully coupled to the local physical conditions. However, in the chromosphere, when collisional rates are lower, the radiation begins to decouple from the local physical conditions, invalidating the LTE assumption.

The chromosphere is a very dynamic layer, whose behavior is governed by magnetic fields, flows, waves and shocks. Even though the chromosphere has a much lower temperature than the solar corona, it has much higher energy density and requires more energy to compensate for the radiative losses (Jess et al. 2015; Withbroe & Noyes 1977; Anderson & Athay 1989). Therefore, mechanisms providing energy to the chromosphere have to be very efficient. Table 1.9, taken from Withbroe & Noyes (1977) shows the energy losses calculated from observations for the chromosphere and corona. We can observe that the energy loss in the chromosphere is more than 10 times larger than in the corona. There are many mechanisms thought to be responsible for the heating of the solar atmosphere, and two of them are thought to have more contribution: magnetic reconnection and waves. These two mechanisms are not independent, since the magnetic reconnection can be a source of waves (Verwichte et al. 2004; Jess et al. 2008; Luna et al. 2008; Li & Zhang 2012; Provornikova et al. 2018), and waves can produce instabilities needed to trigger reconnection processes (Isobe & Tripathi 2006; Lee et al. 2014; McLaughlin et al. 2009).

1.2.1 Waves in the chromosphere

Waves can be observed by measuring fluctuations in the radiation intensity due to fluctuations in density and temperature created by compressible (acoustic and magneto-acoustic) waves, and by measuring the Doppler shift associated with fluctuations in velocity for incompressible waves. Line of sight (LOS) velocity oscillations have been measured for the first time by Leighton et al. (1962) by a technique of Doppler imaging. Waves have been observed at different layers in the solar atmosphere, from the photosphere to the corona, but limited spatial and temporal resolution restricts their de-

tection to low frequency waves, below 10 mHz in most cases. A significant effort has been addressed to measuring waves in the solar corona in the recent years, in the advent of the specially dedicated space missions (Verwichte et al. 2004; Ofman et al. 2008; Gupta 2014). Photospheric and chromospheric oscillations in different magnetic structures have been measured for decades. Interpretation of chromospheric measurements is especially difficult because of the fast evolving structures, supersonic motions and high frequency oscillatory phenomena. Physical processes in the chromosphere happen at characteristic times dictated by the Alfvén speed that can reach several hundreds of $\mathrm{km\,s^{-1}}$. A review of multi-wavelength studies of waves in the chromosphere is provided by Jess et al. (2015).

Waves might also be responsible for the formation of the spicules. The magnetic field has also an important role in the formation of the spicules as the bright emissions in the Ca II K line coincide with the regions of large magnetic field (Babcock & Babcock 1955; Howard 1959; Leighton 1959) and their direction corresponds closely to that of the magnetic field (van de Hulst 1953; Osterbrock 1961). It is shown that the coupling from Alfvén and kink waves into slow modes can generate shocks which can heat the upper chromosphere and drive spicules (Kudoh & Shibata 1999; Brady & Arber 2016).

The maxima of the observed solar wave spectra falls into $3-5$ mHz range, depending on the height in the atmosphere that is being observed. This low-frequency part of the solar wave spectrum has been extensively studied both theoretically and observationally. From the theoretical point of view, a magnetohydrodynamic (MHD) approximation can be safely used for the studies of low-frequency wave phenomena. A review of theoretical studies of wave propagation through photospheric, chromospheric and coronal structures can be found in Khomenko & Santamaria (2013, for quiet Sun); Khomenko & Collados (2015, for sunspots). Waves are sensitive to the horizontal and vertical magnetic structure of the atmosphere. In particular, strong vertical gradients in the acoustic and Alfvén speed lead to phenomena of mode transformation (Cally 2006; Cally & Goossens 2008), or fast magneto-acoustic mode refraction (Bogdan et al. 2003; Khomenko & Collados 2006a), with particularly interesting phenomena happening around singular magnetic field structures such as null points (Lee et al. 2014; Santamaria et al. 2017; Provornikova et al. 2018).

High-frequency waves may play an important role in the energization of the solar chromosphere. From the observational point of view, waves with frequencies above 10-50 mHz are extremely difficult to detect (e.g., see Fossum & Carlsson 2006; Bello González et al. 2009). Musielak et al. (1994) considered wave generation in the solar convection zone and computed the acoustic wave energy flux as a function of frequency. Their theoretical calculations revealed that acoustic flux has a broad maximum in the high frequency region around 100 mHz (periods ≈ 10 s). However, firm detection of the high-frequency part of the solar oscillation spectrum is still uncertain. For example, Bello González et al. (2009, 2010a,b), using high resolution data by GFPI/VTT and IMaX/SUNRISE instruments, revealed a high acoustic flux in the chromosphere for high frequency waves. This result is in contradiction to the earlier work by Fossum & Carlsson (2006) using TRACE data.

Shocks have been observed in the solar atmosphere, formed in the chromosphere (Carlsson & Stein 2002; Centeno et al. 2009). When considering high-frequency waves and shocks, damping or dissipation effects become important. Small-scale disturbances can be easily damped through various non-ideal mechanisms such as viscosity, radiation, thermal conduction, electrical resistivity, or ion-neutral fric-

tion. Other mechanisms related to the atmospheric structure are also at play, e.g., resonant absorption or phase mixing. The importance of these effects depends on the height in the solar atmosphere. For example, damping due to thermal conduction has been studied under coronal conditions (Klimchuk et al. 2004; Gupta 2014; Soler & Terradas 2015), phase mixing and resonant absorption are thought to play a role in damping coronal loop oscillations (Vasquez 2005; Verwichte et al. 2004). High frequency compressible waves are heavily damped by radiative processes at the base of the photosphere, where the energy dissipated by shocks is converted into radiation (Carlsson & Stein 2002). Viscous damping of shock waves has been recently reconsidered by Arber et al. (2016), and resistive dissipation of Alfvén waves, enhanced through ion-neutral interaction, has been considered by Song & Vasyliūnas (2011); Shelyag et al. (2016); Martínez-Sykora et al. (2016).

Under the conditions of the solar chromosphere, the reduction in the collisional coupling with height leads to partial decoupling of the neutral and charged components of the solar plasma, and may produce a series of multi-fluid effects on waves (Ballester et al. 2018). The change in the collision frequency by a few orders of magnitude, as shown in Figure 1.8, can give rise to important decoupling effects. In order to treat these effects, classical MHD modeling may be insufficient and extensions to this approach are needed, such as the use of single-fluid formalism together with the generalized Ohm's law, or a two-fluid (or multi-fluid) formalism.

Wave damping due to ion-neutral collisions

There are a number of theoretical works where two-fluid approximation has been previously applied in the solar physics context. The vast majority of these works are concerned with the propagation of different types of waves and the development of instabilities in chromospheric and prominence plasma conditions. Some research has also been done regarding the overall stability of solar prominences. They will be discussed later in this chapter.

At high collisional frequency, the plasma behaves like a single fluid, but on timescales less than ion-neutral collision time, interaction between ions and neutrals through momentum transfer collisions causes the damping of the waves and alters their oscillation frequency and phase speeds. Damping is most efficient when the wave frequency is of the same order of magnitude as the collisional frequency. Theoretical studies of the damping have been performed by Zaqarashvili et al. (2011b) and Soler et al. (2013a) for Alfvén waves propagation in a uniform medium composed by protons and hydrogen atoms which interact by collisions

The existence of neutral helium atoms, alongside neutral hydrogen, significantly enhances the damping of Alfvén waves at certain intervals of plasma temperature due to ion-neutral collision as compared to the case of neutral hydrogen alone. Zaqarashvili et al. (2011a) analyzed the effects of introducing helium using a three-fluid model where one component is electron-proton-singly ionized helium and the other two components are the neutral hydrogen and neutral helium atoms. Neutral helium causes a few times increase in damping rates in spicules and prominence-corona transition region at the temperature between 10 000 and 40 000 K. Alfvén waves have maximal damping rates at some frequency interval peaking near the ion-neutral collisional frequency. At the same time, the damping

rate is reduced for higher frequencies.

In a gravitationally stratified atmosphere the results are qualitatively similar. In a study about torsional Alfvén waves Zaqarashvili et al. (2013) find that the low-frequency waves are evanescent due to the stratification, while high-frequency waves are damped due to ion neutral collisions.

Similar considerations as for the wave damping due to the ion-neutral interaction applies for propagation in a bounded medium. Soler et al. (2013b) considered magneto-acoustic wave propagation in a magnetic flux tube in a nonuniform atmosphere with a cylindrical symmetry. They find that the wave frequencies only depend on the properties of the ionized fluid when the neutral-ion collisional frequency is much lower than the wave frequency. For high collisional frequencies that realistically represent the solar atmosphere, ions and neutrals behave as a single fluid. The MHD waves are damped by neutral-ion collisions. The damping is most efficient when the wave frequency and the collisional frequency are of the same order of magnitude. For high collisional frequencies slow magneto-acoustic waves are more efficiently damped than transverse kink waves.

Single-fluid approach deals well with slow processes in partially ionized plasmas, but fails for timescales shorter than ion-neutral collision time (Zaqarashvili et al. 2011b). Therefore, the two-fluid approximation should be used for the description of relatively fast processes. Some results of the single-fluid description should be revised in the future, such as the damping of high-frequency Alfvén waves in the solar chromosphere due to ion-neutral collisions. In addition, new wave modes that do not exist in a pure proton-electron plasma can appear, while cut-off wave numbers may appear for other modes.

One particular aspect of the chromospheric physics that has been scarcely studied is the influence of multi-fluid effects on the formation and dissipation of chromospheric shock waves. Recently, Hillier et al. (2016) studied the formation and evolution of slow-mode shocks driven by reconnection in a partially ionized plasma. A complex multi-fluid structure of the shock transition was modeled revealing structures similar to C-shocks or J-shocks in the classification by Draine & McKee (1993). The frictional heating associated with ion-neutral decoupling at the shock front was up to 2% of the available magnetic energy.

1.2.2 Prominences and the Rayleigh-Taylor instability

The transition region between a prominence and the corona is another context susceptible to important multi-fluid effects. As mentioned above, in subsection 1.1, the prominences are formed of cool chromospheric material confined into large magnetic structures in the hot solar corona. A good review of solar prominences is given by Labrosse et al. (2010). The typical temperature of a prominence is of order of 10^4 K, and the electron number density of about 10^{15}-10^{17} m^{-3} (Labrosse et al. 2010). A usual distinction is made between quiescent and eruptive prominences. Quiescent prominences are relatively stable structures outside active regions with large lifetimes up to several solar rotations, contrary to the eruptive prominences which occur in the vicinity of active regions and are usually short-lived. Their formation height is also different: $\approx$ 20 Mm for quiescent prominences, 15 Mm for intermediate and 10 Mm for the plage (active) prominences (Aulanier & Démoulin 2003). Large scale instabilities

lead to eruptions of the prominences. Though active region prominences are more eruptive, quiescent prominences can become eruptive (and geoeffective). These eruptions are often associated with flares and Coronal Mass Ejections (Labrosse et al. 2010). Figure 1.10 shows a quiescent prominence at the left panel and a quiescent and eruptive prominences at the right panel.

The bubbles observed in quiescent prominences (Berger et al. 2010) and their threaded structures are hints of the Rayleigh-Taylor instability (RTI). As the heavier fluid (the prominence) is situated on top of a lighter fluid (the corona), a small perturbation at the interface between these two will grow without bound, developing the RTI. Figure 1.11 shows the RTI developed at the Prominence Corona Transition Region (PCTR), illustrated by the threads which fall from the prominence. When the cold neutrals fall into the hot corona, they get ionized, the falling spikes get surrounded by a thin layer composed of charged material, thus the ionization/recombination processes cannot be neglected at the PCTR. As the density decreases from the prominence towards the corona, the collisional coupling between charges and neutrals also decreases at the PCTR, and the charges decouple from the neutrals, giving rise to additional frictional heating processes.

It can be mentioned that the RTI has been studied by means of numerical simulations in many astrophysical contexts. For example, Porth et al. (2014) studied the RTI developed in the remnant of a supernova explosion and explains that the filaments that are seen during the observation of the Crab Nebula are produced by the instability. Figure 1.12 compares the image resulted from observations in the left panel with a snapshot obtained from numerical simulation in the right panel. The RTI has been also studied by numerical simulations in the Earth's ionosphere (Leake et al. 2014) and at the partially ionized PCTR (Khomenko et al. 2014c; Leake et al. 2014).

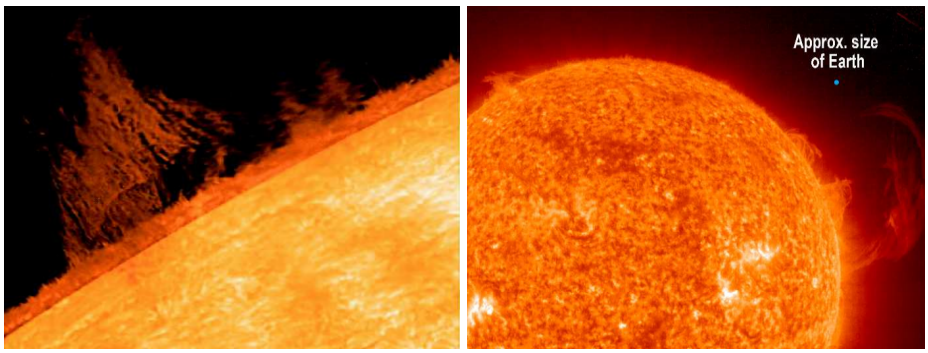

Figure 1.10: Left: A quiescent prominence observed above the limb in Hα with the Hinode/SOT NFI filter. Right: Quiescent (top left) and eruptive (right side) prominences observed by SOHO/EIT on 21 April 2005 in the 304 Å channel. Fig. 1 and 2 from Labrosse et al. (2010).

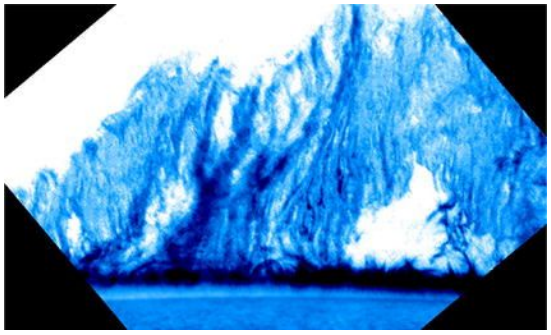

Figure 1.11: A quiescent prominence observed by Hinode SOT using the Ca II H broadband filter on 29 September 2008. Fig. 2 from Hillier (2018).

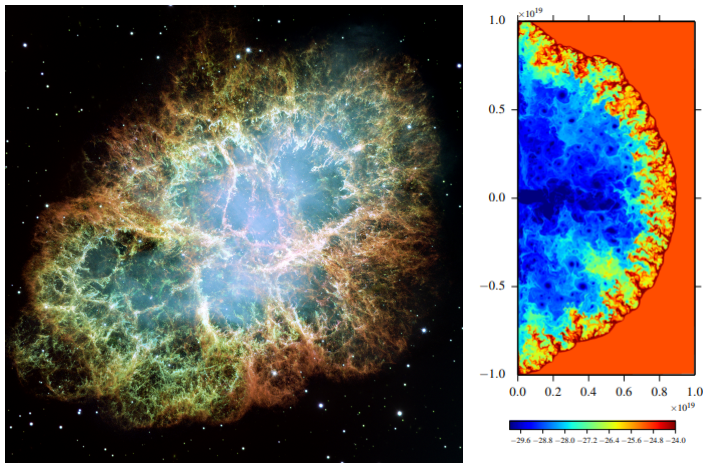

Figure 1.12: Left: Mosaic image, taken by NASA's Hubble Space Telescope of the Crab Nebula, a six-light-year-wide expanding remnant of a star's supernova explosion. Source: `https://en.wikipedia.org/wiki/Crab_Nebula#/media/File:Crab_Nebula.jpg`. Right: Logarithmic densities from a simulation of the Crab Nebula. Part of Fig.2 from Porth et al. (2014).

Cross-field diffusion of neutrals across the magnetic field in solar prominences

Due to incomplete coupling, neutral atoms can diffuse and slip across the field in solar prominences. This slip would produce a net motion of the neutral material across the magnetic field. Depending on the species, the diffusion velocity may differ. Gilbert et al. (2002) propose a model with hori-

zontal magnetic field in the X direction and and no flow along the magnetic field, with five species: H, H^+, He, He^+, e^- and with the geometry shown in the Figure 1.13. They considered only the momentum equation with constant density and temperature throughout the system, and assumed equilibrium momentum balance in the y and z direction for the five species. The model resulted in neutral He velocity across the magnetic field to be around 81 m/s and neutral H velocity around 3.7 m/s. In the assumption that the timescale for diffusion is much shorter than the dynamical timescale, the draining timescales come proportional to the vertical total atom column density. They find a loss time scale of 22 days for hydrogen, much larger than the one for helium (1 day).

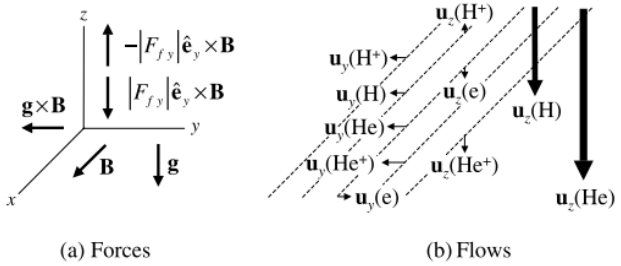

Figure 1.13: Schematic representation of the forces (a), and relative magnitudes of the vertical and horizontal flow (b) in a model of a neutral atoms diffusion in solar prominences, taken from Gilbert et al. (2002)

1.2.3 Observations of multi-fluid effects

Chromospheric observations generally show that neutrals and charges are coupled. The decoupling suggested from theoretical grounds should be happening at small temporal and spatial time scales and it is very difficult to observe. However, there are some observations of such decoupling, described below. These are observations of solar prominences, whose material is colder and denser than the surrounding solar corona.

There are only a few direct observations of the neutral-ion decoupling in solar prominences. One of the reported results comes from Gilbert et al. (2007), who apparently confirm the model of neutral atoms diffusion in prominences by Gilbert et al. (2002). They compared He I (10830 Å) and Hα data observing the drainage across magnetic field with different timescales. They saw that a majority of stable, quiescent filaments showed a relative helium deficit in the upper portions of their structure coupled with a relative helium surplus in the lower regions as seen in Figure 1.14, a consequence of the large loss timescale for neutral hydrogen compared to neutral helium. They called this phenomenon "edge effects".

Another indirect evidence of ion-neutral decoupling was reported by de la Cruz Rodríguez & Socas-

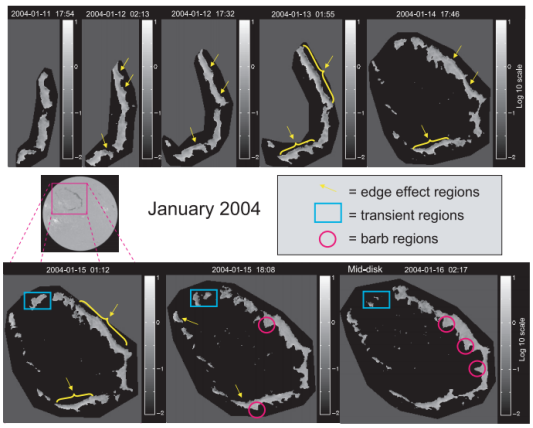

Figure 1.14: Series of images showing absorption ratios, He/H, for a large/stable filament observed in 2004 January by Gilbert et al. (2007). The images are produced such that the color represents the absorption ratio in a logarithmic scale, log(He I$H\alpha$), and a darker pixel correlates to a deficit of absorption in He I as compared to Hα , while a brighter pixel has a relative surplus of helium. The yellow arrows and brackets highlight the regions where edge effects are visible.

Navarro (2011) who deduced misalignment in the visible direction of chromospheric fibrils and the measured magnetic field vector. They observed that most of the fibrils aligned with the magnetic field, although there are a few noteworthy cases where significant misalignments occur, well beyond the observational uncertainty. Such misalignment can, in principle be expected from the theoretical grounds, because neutrals (that do not directly feel the magnetic Lorentz Force) can move cross-field and drag charges with them. This effect results in ambipolar diffusion. Two-dimensional realistic simulations by Martínez-Sykora et al. (2016) have shown that chromospheric material and the magnetic field in spicule-like structure can indeed be misaligned. Martínez-Sykora et al. (2016) found that the conditions for misalignment require large ambipolar diffusion with characteristic time-scale smaller than the hydrodynamic time-scale and strong currents perpendicular to the magnetic field.

A more direct measurement would be to determine the ion and neutral velocities directly from the Doppler shift of emission lines of the corresponding species, simultaneously over the same volume of plasma. This technique requires high spatial and temporal resolution, apart from a careful selection of spectral lines for the analysis. One has to be very careful in interpreting the results of such measurements.

Anan et al. (2017) simultaneously observed spectra of H I 3970 Å, H I 4340 Å, Ca II 3970 Å, and Ca II 8540 Å in an active region prominence, comparing the Doppler velocities, derived from the shift of the peak of the spectral lines presumably emitted from optically-thin plasma. They found instances when the difference in velocities between neutral atoms and ions is significant. However, they also found significant differences between the Doppler velocities of pairs of neutral species (or ionized species) themselves. In fact, the probability density functions of velocity difference of the latter were similar to the former. Anan et al. (2017) concluded that the difference of Doppler velocities is a result of the

motions of different components in the prominence along the line of sight, rather than the decoupling of neutral atoms from plasma.

By measuring the Doppler shift in ion Fe II and neutral Fe I lines, simultaneously over the same volume of plasma, differences between ion and neutral velocities of the Evershed flow have been found in sunspot penumbra as deep as the photosphere by Khomenko et al. (2015). In a similar way, Khomenko et al. (2016) also attempted to measure differences between neutrals and ions velocities in a solar prominence. They measured Doppler shift in Ca II 8542 Å and the He I 10830 Å emission lines. The patches of non-zero drift velocity show coherence on time-distance diagrams as we can see in the figure 1.15. In order to make sure that both spectra originate from the same volume of plasma, Khomenko et al. (2016) only selected areas where the plasma was optically thin and no multi-component events overlapped in the field of view. Khomenko et al. (2016) found evidences to confirm

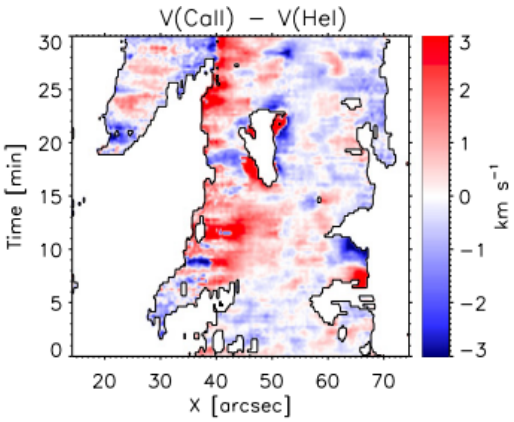

Figure 1.15: Drift velocity w = v(Ca II) - v(He I) as a function of time and distance along the slit from prominence observations by Khomenko et al. (2016). Contours underline the locations retained for the analysis, after removing pixels with multiple components among the line of sight, or locations where the plasma is not optically thin.

that both Ca II 8542 Å and He I 10830 Å lines trace the same plasma at locations satisfying the selection criteria above. The authors claim that the observed differences in Ca and He velocities are due to a physical effect and not an observational issue. It is justified by the correlation between the plasma parameters extracted from information present in the lines of both elements, and the coherence in time and space of the patches found, even if they are short-lived and only occupy small areas. Numerical simulations show that similar amplitudes of the drift velocities are expected in the prominence-corona transition region (Khomenko et al. 2014c).

Khomenko et al. (2016) were able to detect drift velocities thanks to their very high temporal resolution observations. If the signal were integrated over larger intervals, the effect would probably be lost or become much smaller. It is then expected that, if the resolution increases, the amplitudes of the ion-neutral velocity difference would become larger. More observational studies in the future

will be needed to confirm or discard the detection of the decoupling effects.

Wiehr et al. (2019) also find a larger velocity for ions than for neutrals. They analyze LOS velocities from the Doppler shift of two emission lines of ions (Sr II Fe II) and two emission lines of neutrals (Na I He I). Wiehr et al. (2019) find systematic excess of the velocity of ions over the velocity of neutrals, the velocities of Sr II are ≈ 1.22 larger than for Na I and those calculated from the line of Fe II is ≈ 1.11 larger than in the case of He I whereas a comparison between neutrals (H, He) gives a 1:1 relation. They argue that the systematic decoupling observed might be due to the fact that the emission lines of Sr II and Na I are optically thin and narrow, and that they analyzed a quiet prominence. The smaller decoupling found in the case of Fe II and He I might be due to a a different degree of ionization or to a different density in the activated phase of the prominence.

1.2.4 Numerical modeling

Realistic models that incorporate non-ideal effects due to neutrals have only been performed so far using a single-fluid approach. The realism of the multi-fluid simulations is still limited.

Let us enumerate some recent works on the single-fluid and multi-fluid multi-dimensional simulations of different solar phenomena. Most numerical models of partially ionized solar plasma use a single-fluid approach introducing the partial ionization effects through a generalized Ohm's law (Khomenko & Collados 2012; Cheung & Cameron 2012; Martínez-Sykora et al. 2012; Khomenko et al. 2014c; Martínez-Sykora et al. 2016; Shelyag et al. 2016; Khomenko et al. 2017, 2018). One of the advantages of this numerical approach is the simplicity for the study of the wave dissipation and heating due to ion-neutral interactions (Song & Vasyliūnas 2011; Khomenko 2017). The ambipolar diffusion may also be the explanation for the misalignment of chromospheric fibrils and magnetic field (Martínez-Sykora et al. 2016).

Another recent example of realistic 3D simulations of magneto-convection including ambipolar diffusion is the work of Khomenko et al. (2018). These authors have shown how incompressible perturbations (Alfvén waves) can be dissipated thanks to the ambipolar mechanism, assisting chromospheric heating. Realistic models including Hall effect are even more scarce (but see, however Cheung & Cameron 2012). In the photosphere, realistic models based on classical MHD without non-ideal effects due to neutrals provide results that are practically indistinguishable from observations even in strongly magnetized regions (e.g., Rempel et al. 2009). This is so because photospheric observations do not reach scales where ion-neutral effects can be detected directly in plasma dynamics, see e.g. Figure 1.8, taken from Khomenko et al. (2014a). However, this is not the case for the chromosphere (see e.g. the discussion in Leenaarts 2010). In the chromosphere, the ion-neutral interaction scales become larger and may be possible to reach in some dedicated observations, see subsection 1.2.3 above. Indirect ion-neutral decoupling effects, such as heating, are also expected to be more pronounced in the chromosphere.

A suitable alternative to the MHD approach is a two-fluid plasma-neutrals model, numerically implemented in this work. This kind of model is most appropriate for high density plasmas such as in the chromosphere, where kinetic models cannot be efficiently applied. Kinetic models have been success-

fully applied to the corona and the solar wind, where much lower particle density makes the problem more computationally feasible and the kinetic description more necessary and appropriate. Multi-fluid models preserve a number of important physical effects coming from weak collisional coupling, still allowing for an efficient implementation, as any fluid-based description.

Recently, two-fluid fully non-linear modeling of waves in the solar atmosphere has been performed (Maneva et al. 2017). Maneva et al. (2017) modeled magneto-acoustic wave propagation in the solar stratified chromosphere including effects of impact ionization and radiative recombination. They found numerous difficulties in constructing an equilibrium model atmosphere for the wave propagation, and in interpreting the results of their simulations in comparisons to more standard, single fluid models.

Martínez-Gómez et al. (2017) use a five-fluid model with three ionized and two neutral components, which takes into consideration Hall's current and Ohm's diffusion in addition to the friction due to collisions between different species. They apply their model to study the wave propagation in homogeneous plasmas composed of hydrogen and helium, similar to the analytical models described above. The ionization degree was allowed to vary. Martínez-Gómez et al. (2017) confirmed the theoretical result that the inclusion of neutral components in the plasma modifies the oscillation period of the low-frequency Alfvén waves and that collisions produce a damping of the perturbations, this damping being more efficient when the collisional frequency is of the order of the oscillation frequency.

Magnetic reconnection has been studied using a two fluid model by Smith & Sakai (2008); Leake et al. (2012); Leake et al. (2013); Alvarez Laguna et al. (2014); Hillier et al. (2016). Important decoupling between the flows of neutrals and ions where observed in their simulations close to a reconnection site with considerable differences between inflows and outflows. Ni et al. (2018) also found that even in the absence of flow decoupling, dynamics of the ionization and recombination processes can have important consequences for the thermodynamics and observable properties of plasma at chromospheric reconnection sites.

The heating is expressed in the two-fluid approach via the frictional heating term (Leake et al. 2014). This term is dropped in the linear theory, being quadratic in the perturbed quantities. Non-linear simulations allow to fully take into account the effects of wave heating due to neutrals.

From all of the above it is evident that numerical modeling of solar chromospheric plasma including multi-fluid effects is a promising approach, and that a significant effort is required in this direction. Both previous theoretical and observational results suggest the need for such modeling.

1.3 Outlook of the thesis

The purpose of this work is to study two-fluid effects in the solar chromosphere in the propagation of waves and the Rayleigh-Taylor instability at the interface between a prominence and the solar corona. As we have seen, in the chromosphere the MHD assumption might break down when the ion-neutral collision time scale becomes comparable to the hydrodynamic time scale. In most situations, however, the charges and neutrals are well coupled by collisions, the collisional terms which couple the equations of charges and neutrals become large and the equations are stiff. In order to model solar

chromospheric plasma in the two-fluid approach, a numerical code must be capable to simultaneously deal with the regimes of the strong and weak collisional coupling in the single domain. The collisional terms usually imply very strong restrictions on the time step in explicit schemes. In order to overcome these restrictions, we have applied a semi-implicit method in the two-fluid (charges+neutrals) code. The collisional terms are treated implicitly.

The two-fluid code has been built on top of the existing MANCHA3D code (Khomenko & Collados 2006b; Felipe et al. 2010; Khomenko & Collados 2012), which solves the MHD equations including partial ionization effects, and this gave us the possibility to adapt algorithms already implemented there such as hyperdiffusivity, Perfect Matching Layer (PML), and filtering. After testing the code against known analytical solutions, we use the code for more realistic situations, such as wave propagation in stratified atmosphere and the Rayleigh-Taylor instability at the interface of a prominence and the solar corona. The novelty of this study consists in the use of a sheared magnetic field configuration, and it continues the work of Leake et al. (2014).

We now briefly outline the content of the thesis. In this chapter we have seen that MHD modeling including partial ionization effects, gives very good results at the limits of the strong collisional coupling (as in the photosphere). It also gives good results in the limit of very weak collisional coupling, as in the corona. However, we have shown that for intermediate collisional regimes, as in the chromosphere, a two-fluid model should give better results. This thesis implements a two-fluid treatment and performs several numerical simulations either to verify the correctness of the new implementation, or to achieve scientifically new results on propagation of waves and shocks and on the development of RTI instabilities in the chromosphere. We achieve these goals in the following steps,

- **The two-fluid mathematical model.** We investigate the equations that had to be implemented in Chapter 2.
- **The numerical scheme.** The collisional terms are usually large, especially in the deep layers of the solar atmosphere. Because the collisional terms are proportional to the variables that evolve in time, they impose time-steps of the order of the inverse of the collision frequencies in an explicit scheme. We implement the terms in a semi-implicit scheme where the collisional terms are implemented implicitly. For the same reason, that the collisional terms are proportional to the variables that evolve in time, the implicit implementation is straightforward, and no matrix inversion, which is usually required in implicit implementations, is needed. The expression of the updated variables can be obtained analytically. This is exposed in Chapter 3.
- **Verification of the code.** Usually, in order to test the code, the numerical solutions are compared to known analytical solutions, or to other numerical solutions obtained in the literature. Accuracy tests are also performed. We test the code against analytical solutions of waves in uniform atmosphere, and we perform time accuracy tests. We test that the code performs well in a isothermal stratified atmosphere, with almost exact analytical solution, where the collision frequency varies in the atmosphere, so that we check that the code handles properly different collisional regimes in the same simulation. We present these tests in Chapter 4.

- **Study of fast magneto-acoustic waves in a stratified atmosphere** We perform realistic simulations with the two-fluid code under chromospheric conditions of fast magnetoacoustic waves. We study the damping of the waves due to the shocks and the interaction between the neutrals and charges. We compare the results to the results obtained with the single fluid code, where the interaction between charges and neutrals was modeled by the ambipolar term. We compare the damping of the waves and the increase in the background temperature. The study of the fast magneto-acoustic waves is presented in Chapter 5.
- **Study of Rayleigh-Taylor instability (RTI) at the interface between a prominence and the corona** We perform 2D simulations of the RTI with different configurations of the magnetic field: perpendicular to the plane defined by the gravity and the direction of the perturbation or slightly sheared. We study the the effects of the viscosity, thermal conductivity and magnetic field configuration on the growth rate, decoupling and energy spectra in Chapter 6. In Chapter 7 we study the effects of changing parameters that could theoretically be observed: the magnetic field strength, the density contrast, and the importance of the elastic and inelastic collisions on the development of the instability.

2

Theoretical concepts

In this chapter we describe the mathematical model used in this work. The coupling between plasma and magnetic field is described by a set of near-conservation laws, under different levels of approximations. The ideal MHD approach assumes perfect collisional coupling of the plasma and no neutral component. When the neutrals are taken into account, but the plasma is strongly collisionally coupled, the single-fluid, or quasi MHD approach is used, see Khomenko et al. (2014a). When the collisional timescale between charged and neutral particles is similar or larger than the hydrodynamical timescale, either three-fluid or two-fluid equations are used. The latter sets of equations are considered below. Here we summarize the main steps and approximations done in the derivation of the two-fluid equations: Section 2.1 presents how the multi-fluid equations and the collisional terms which couple them, as well as the viscosity and thermal conduction coefficients, are obtained from the kinetic equations, Section 2.2 shows how three-fluid equations are obtained from generic multi-fluid equations, and finally Section 2.3 shows how two-fluid equations are obtained from three-fluid equations.

Notations used in this chapter:

- "·" indicates the scalar product between two vectors, or between a matrix and a vector.
- No operator between two vectors indicates the outer product between these two vectors. The result is a matrix. The following example is the gradient of a vector field: $(\nabla \mathbf{u})_{ij} = \partial u_i / \partial x_j$.
- ":" indicates the contraction between two matrices. The result is a scalar.

2.1 From microscopic to macroscopic scale

The kinetic theory derives the equations which describe the collective behavior of a plasma by applying the methods of statistical mechanics. A multicomponent plasma is completely determined by the

distribution function of each of its species,

$$f_\alpha = f_\alpha(\mathbf{v}, \mathbf{r}, t)\,, \tag{2.1}$$

where f_α is the distribution function and α indicates the type of particles, and $\mathbf{v}$ and $\mathbf{r}$ are vectors indicating individual particle's velocity and coordinate, respectively. The total derivative of the distribution function f_α with respect to time can be written as,

$$\frac{Df_\alpha}{Dt} = \frac{\partial f_\alpha}{\partial t} + \frac{\partial \mathbf{r}}{\partial t}\cdot\frac{\partial f_\alpha}{\partial \mathbf{r}} + \frac{\partial \mathbf{v}}{\partial t}\cdot\frac{\partial f_\alpha}{\partial \mathbf{v}}\,. \tag{2.2}$$

Using the notations $\nabla_\mathbf{r} = \partial f_\alpha/\partial \mathbf{r}$, $\nabla_\mathbf{v} = \partial f_\alpha/\partial \mathbf{v}$, $\mathbf{a} = \partial \mathbf{v}/\partial t$, and taking into account that $\mathbf{v} = \partial \mathbf{r}/\partial t$, the total derivative can be written as,

$$\frac{Df_\alpha}{Dt} = \frac{\partial f_\alpha}{\partial t} + \mathbf{v}\cdot\nabla_\mathbf{r} f_\alpha + \mathbf{a}\cdot\nabla_\mathbf{v} f_\alpha\,. \tag{2.3}$$

$\mathbf{a}$ is the acceleration. It has the following form for each species α,

$$\mathbf{a} = \frac{q_\alpha}{m_\alpha}(\mathbf{v}\times\mathbf{B} + \mathbf{E}) + \mathbf{g}\,, \tag{2.4}$$

where m_α and q_α are particle mass and electric charge, respectively. We have considered the electromagnetic force and the force due to gravity.

2.1.1 Boltzmann equation

The time evolution of the distribution function is described by the Boltzmann equation,

$$\frac{Df_\alpha}{Dt} = \left(\frac{\partial f_\alpha}{\partial t}\right)_{\text{coll}}. \tag{2.5}$$

The term which appears at the right-hand side (RHS) of the above Eq. 2.5 represents the rate of change of the distribution function of particles α due to collisions. The kinetic (microscopic) equations comprise Boltzmann equations and Maxwell's equations described later, in subsection 2.3.5. From the computational point of view, kinetic equations allow to study processes in plasmas with low number density as, for example, the plasma of the solar wind. An example of a process where the kinetic physics becomes important is magnetic reconnection, when the scale of the problem, the current sheet thickness, falls below the ion kinetic scale (Stanier et al. 2019). However, most of the studies involve processes which happen on time scales larger than the periods of Langmuir plasma oscillations, and on space scales larger than the characteristic Debye length, so that some simplifications can be made in order to reduce the computational cost of solving the kinetic equations numerically.

Macroscopic equations, which do no longer contain velocity space details are obtained from expanding the Boltzmann equation in a finite number of moments. Generally, in the multifluid approximation,

the evolution can be described by equations of continuity, momentum and energy of its components which are obtained via momenta (0th, 1st, and 2nd moment) of the Boltzmann equation above, Eq. 2.5. A comprehensive description of the derivation of the multifluid equations is given in Chapter 3 of Goedbloed et al. (2019).

The particle velocity can be decomposed into macroscopic velocity, $\mathbf{u}_\alpha$ and random velocity, $\mathbf{c}_\alpha$:

$$\mathbf{v}_\alpha = \mathbf{u}_\alpha + \mathbf{c}_\alpha \,. \tag{2.6}$$

From the distribution function we can compute the macroscopic variables, which depend only on space and time, by integrating it over the velocity space. The number of particles is defined as the zeroth moment of the distribution function,

$$n_\alpha(\mathbf{r}, t) = \int_V f_\alpha(\mathbf{v}, \mathbf{r}, t) d^3\mathbf{v} \,, \tag{2.7}$$

where $d^3\mathbf{v}$ is the volume element in the velocity space. Other macroscopic variables are defined in a similar way,

$$\overline{\chi}(r, t) = \langle \chi(\mathbf{v}, \mathbf{r}, t) \rangle_\alpha = \frac{\int_V \chi(\mathbf{v}, \mathbf{r}, t) f_\alpha(\mathbf{v}, \mathbf{r}, t) d^3\mathbf{v}}{\int_V f_\alpha(\mathbf{v}, \mathbf{r}, t) d^3\mathbf{v}} = \frac{\int_V \chi(\mathbf{v}, \mathbf{r}, t) f_\alpha(\mathbf{v}, \mathbf{r}, t) d^3\mathbf{v}}{n_\alpha(\mathbf{r}, t)} \,. \tag{2.8}$$

The first moment of the distribution function represents the macroscopic velocity,

$$u_\alpha(\mathbf{r}, t) = \langle v_\alpha \rangle = \frac{\int_V \mathbf{v} f_\alpha(\mathbf{v}, \mathbf{r}, t) d^3\mathbf{v}}{n_\alpha(\mathbf{r}, t)} \,. \tag{2.9}$$

The stress tensor $\hat{\mathbf{p}}_\alpha$ and the heat flux $\mathbf{q}_\alpha$ are related to the second and third momentum, respectively:

$$\begin{aligned} \hat{\mathbf{p}}_\alpha &= n_\alpha m_\alpha \langle \mathbf{c}_\alpha \mathbf{c}_\alpha \rangle \,, \\ \mathbf{q}_\alpha &= \frac{1}{2} n_\alpha m_\alpha \langle c_\alpha^2 \mathbf{c}_\alpha \rangle . \end{aligned} \tag{2.10}$$

The scalar pressure is defined as:

$$p_\alpha = \frac{1}{3} \mathrm{Tr}(\hat{\mathbf{p}}_\alpha) \,, \tag{2.11}$$

where Tr means the trace of the matrix (the sum of the elements on the main diagonal). The pressure stress tensor is decomposed into the diagonal part, the isotropic pressure tensor $\hat{\mathbf{p}}^{\mathrm{iso}}$ and the traceless contribution, $\hat{\mathbf{\Pi}}_\alpha$,

$$\hat{\mathbf{p}}_\alpha^{\mathrm{iso}} = p_\alpha \hat{\mathbb{I}} \,, \tag{2.12}$$

where $\hat{\mathbb{I}}$ is the identity matrix.

$$\hat{\mathbf{p}}_\alpha = \hat{\mathbf{p}}_\alpha^{\mathrm{iso}} + \hat{\mathbf{\Pi}}_\alpha \,. \tag{2.13}$$

The individual elements of the traceless matrix $\hat{\mathbf{\Pi}}_\alpha$ might be non-zero, but their sum is zero. The viscosity tensor is defined,

$$\hat{\tau}_\alpha = -\hat{\mathbf{\Pi}}_\alpha. \tag{2.14}$$

The "-" sign appears because the terms that appear off diagonal in the pressure tensor are with reversed sign to what is usually referred as viscosity, see the definition of this term below, in Eq. 2.53.

The macroscopic temperature is defined as,

$$T_\alpha = \frac{m_\alpha}{3k_\mathrm{B}}\langle c_\alpha^2\rangle\,, \tag{2.15}$$

which states the ideal gas law:

$$p_\alpha = \frac{1}{3}n_\alpha m_\alpha\langle c_\alpha^2\rangle = n_\alpha k_\mathrm{B}T_\alpha\,. \tag{2.16}$$

k_B which appears in the equations above is the Boltzmann constant. An alternative form of the gas law is:

$$T_\alpha = \frac{p_\alpha\mu_\alpha}{\rho_\alpha R}\,, \tag{2.17}$$

where $R = k_\mathrm{B}/m_\mathrm{H}$ is the gas constant and μ_α is the mean molecular weight of particles α in units of g/mole.

Any gas in thermal equilibrium which consists of n_α particles, with temperature T_α and macroscopic velocity u_α is characterized by a Maxwellian distribution function $f_{\alpha 0}$, defined as,

$$f_{\alpha 0}(c_\alpha) = n_\alpha\left(\frac{m_\alpha}{2\pi k_\mathrm{B}T_\alpha}\right)^{\frac{3}{2}}\exp\left(-\frac{m_\alpha(\mathbf{v}_\alpha-\mathbf{u}_\alpha)^2}{2k_\mathrm{B}T_\alpha}\right)\,. \tag{2.18}$$

The Maxwellian distribution function is isotropic (does not depend on the direction of the velocity, but only on its module). It is a Gaussian centered in the macroscopic velocity u_α with standard deviation equal to $v_{\mathrm{th}\alpha}/\sqrt{2}$, where the thermal velocity $v_{\mathrm{th}\alpha} = \sqrt{(2k_\mathrm{B}T_\alpha)/m_\alpha}$.

2.1.2 Multifluid equations

Using the notations:

$$C_\alpha = \left(\frac{\partial f_\alpha}{\partial t}\right)_{\mathrm{coll}}\,, \tag{2.19}$$

$$S_\alpha = m_\alpha\int_V C_\alpha d^3\mathbf{v}\,, \tag{2.20}$$

$$\mathbf{R}_\alpha = m_\alpha\int_V \mathbf{v}C_\alpha d^3\mathbf{v}\,, \tag{2.21}$$

$$M_\alpha = \frac{1}{2}m_\alpha\int_V v^2C_\alpha d^3\mathbf{v}\,, \tag{2.22}$$

the zeroth, the first and the second moment of Boltzmann equation are shown to be, (Goedbloed et al. 2019; Khomenko et al. 2014a):

$$\frac{\partial \rho_\alpha}{\partial t} + \nabla \cdot (\rho_\alpha \mathbf{u}_\alpha) = S_\alpha \,, \tag{2.23}$$

$$\frac{\partial (\rho_\alpha \mathbf{u}_\alpha)}{\partial t} + \nabla \cdot (\rho_\alpha \mathbf{u}_\alpha \mathbf{u}_\alpha + \hat{\mathbf{p}}_\alpha) = q_\alpha n_\alpha (\mathbf{E} + \mathbf{u}_\alpha \times \mathbf{B}) + \rho_\alpha \mathbf{g} + \mathbf{R}_\alpha \,, \tag{2.24}$$

$$\frac{\partial}{\partial t}\left(e_\alpha + \frac{1}{2}\rho_\mathrm{i} u_\alpha^2\right) + \nabla \cdot \left(\mathbf{u}_\alpha (e_\alpha + \frac{1}{2}\rho_\alpha u_\alpha^2) + \hat{\mathbf{p}}_\alpha \cdot \mathbf{u}_\alpha + \mathbf{q}_\alpha\right) = \rho_\alpha \mathbf{u}_\alpha \cdot \mathbf{g} + q_\alpha n_\alpha \mathbf{u}_\alpha \cdot \mathbf{E} + M_\alpha \,, \tag{2.25}$$

where q_α is the electric charge of the particles α (not to be confused with the heat flux $\mathbf{q}_\alpha$). The internal energy,

$$e_\alpha = \frac{1}{\gamma - 1} p_\alpha \,, \tag{2.26}$$

where γ is the adiabatic index. For a monoatomic ideal gas with 3 degrees of freedom the adiabatic index $\gamma = \frac{5}{3}$. The above Eqs. 2.23, 2.24 and 2.25 are also called the continuity, the momentum and the energy equations, respectively.

2.1.3 Collisional terms

Taking into account the collisions with all species β, the collisional terms can be written :

$$C_\alpha = \sum_\beta C_{\alpha,\beta}, \tag{2.27}$$

where $C_{\alpha,\beta}$ is the collisional operator between particles α and β. The collisional operators $C_{\alpha,\beta}$ is usually a function of the distribution functions of the two species α, and β and may have complicated forms. If two fluids α and β had Maxwellian distributions with the same macroscopic velocities and temperatures, the collisional term $C_{\alpha,\beta}$ is zero (Goedbloed et al. 2019).

The collisional terms can be split into an elastic and an inelastic part:

$$C_\alpha = C_\alpha^{\text{inelastic}} + C_\alpha^{\text{elastic}} \tag{2.28}$$

The properties of the elastic collisional operator are given in Braginskii (1965):

$$\begin{aligned}
\int_V C_{\alpha,\beta}^{\text{elastic}} d^3\mathbf{v} &= 0 \\
\int_V m_\alpha \mathbf{v} C_{\alpha,\alpha}^{\text{elastic}} d^3\mathbf{v} &= 0 \\
\int_V \frac{1}{2} m_\alpha v^2 C_{\alpha,\alpha}^{\text{elastic}} d^3\mathbf{v} &= 0 \\
\int_V m_\alpha \mathbf{v} C_{\alpha,\beta}^{\text{elastic}} d^3\mathbf{v} + \int m_\beta \mathbf{v} C_{\beta,\alpha}^{\text{elastic}} d^3\mathbf{v} &= 0 \\
\int_V \frac{1}{2} m_\alpha v^2 C_{\alpha,\beta}^{\text{elastic}} d^3\mathbf{v} + \int \frac{1}{2} m_\beta v^2 C_{\beta,\alpha}^{\text{elastic}} d^3\mathbf{v} &= 0
\end{aligned} \tag{2.29}$$

The first assumption means that elastic collisions do not produce new particles, and the other four are imposed by the momentum and energy conservation.

For the elastic collisions, $C_{\alpha,\beta}^{\text{elastic}}$ the most general operator is the Boltzmann operator:

$$C_{\alpha,\beta}^{\text{elastic}}(\mathbf{v}_\alpha) = \int_V \int_\Omega \Big(f_\alpha(\mathbf{r}, \mathbf{v}_\alpha{}', t) f_\beta(\mathbf{r}, \mathbf{v}_\beta{}', t) - f_\alpha(\mathbf{r}, \mathbf{v}_\alpha, t) f_\beta(\mathbf{r}, \mathbf{v}_\beta, t) \Big) |\mathbf{v}_\beta - \mathbf{v}_\alpha| \sigma(\Omega) d\Omega d^3\mathbf{v}_\beta, \quad (2.30)$$

where $\mathbf{v}_\alpha$ and $\mathbf{v}_\beta$ are the velocities of particles α and β before collision, $\mathbf{v}_\alpha{}'$ and $\mathbf{v}_\beta{}'$ are the velocities after collision, and $\sigma(\Omega)$ is the cross section which depends on the solid angle Ω. $\mathbf{v}_\alpha{}'$ and $\mathbf{v}_\beta{}'$ are not independent variables, and must be calculated from momentum and energy conservation laws:

$$\begin{aligned} m_\alpha \mathbf{v}_\alpha + m_\beta \mathbf{v}_\beta &= m_\alpha \mathbf{v}_\alpha{}' + m_\beta \mathbf{v}_\beta{}' \\ m_\alpha v_\alpha^2 + m_\beta v_\beta^2 &= m_\alpha v_\alpha'^{\,2} + m_\beta v_\beta'^{\,2}. \end{aligned} \quad (2.31)$$

$\sigma(\Omega)d\Omega$ is determined from the geometry of the particular collision considered. In the approximation of small angle deflections the Boltzmann operator is approximated by the Fokker-Planck operator. For charged particles interaction, Braginskii (1965) uses the Landau operator. A simplified form of the collisional operator is described by the Krook operator:

$$C_{\alpha,\beta}^{\text{elastic}}(\mathbf{v}) = -\frac{f_\alpha(\mathbf{v}) - f_{\alpha 0}(\mathbf{v})}{\tau_{\alpha,\beta}}, \quad (2.32)$$

where $\tau_{\alpha,\beta} = \nu_{\alpha,\beta}^{-1}$ is the relaxation time of the distribution function f_α to the equilibrium distribution function, $f_{\alpha 0}$ because of collisions with particles β. Bittencourt (2004) shows that in the case that $m_\beta \gg m_\alpha$, the velocity of the much heavier species can be considered zero, and from energy conservation, the velocity module of the lighter particle is conserved,

$$\begin{aligned} \mathbf{v}_\beta{}' &= \mathbf{v}_\beta = 0\,, \\ v_\alpha{}' &= v_\alpha\,. \end{aligned} \quad (2.33)$$

The Boltzmann collisional operator can be written as a Krook operator, defined in the Eq. 2.32, where $\tau_{\alpha\beta} = \nu_{\alpha\beta}^{-1}$ and the collision frequency $\nu_{\alpha\beta} = n_\beta v_\alpha \sigma(\Omega) d\Omega$. Neglecting the dependency of $\nu_{\alpha\beta}$ on v_α, the momentum collisional term become:

$$\mathbf{R}_{\alpha\beta}^{\text{elastic}} = -\rho_\alpha \nu_{\alpha\beta} \mathbf{u}_\alpha. \quad (2.34)$$

It has been shown by Braginskii (1965), by using the Landau operator and considering that one of the distribution function, f_α, is a Maxwellian function with zero macroscopic velocity, and that the other one, f_β, is a small departure from a Maxwellian distribution function centered in the macroscopic relative velocity, $\mathbf{u}_\beta - \mathbf{u}_\alpha$, that the above formula is valid generally, without any assumption about their masses:

$$\mathbf{R}_{\alpha\beta}^{\text{elastic}} = \rho_\alpha \nu_{\alpha\beta} (\mathbf{u}_\beta - \mathbf{u}_\alpha)\,, \quad (2.35)$$

where the expression of the collisional frequency of α particles with β particles as $\nu_{\alpha\beta}$ is:

$$\nu_{\alpha\beta} = n_\beta \frac{m_\beta}{m_\alpha + m_\beta} \sqrt{\frac{8k_\mathrm{B}T_{\alpha\beta}}{\pi m_{\alpha\beta}}} \sigma_{\alpha\beta}^{\mathrm{elastic}} \,. \tag{2.36}$$

with the term $\sigma(\Omega)d\Omega$ included in the elastic cross section $\sigma_{\alpha\beta}^{\mathrm{elastic}}$.
The collision frequencies defined like this have the property that

$$\rho_\alpha \nu_{\alpha\beta} = \rho_\beta \nu_{\beta\alpha} \,, \tag{2.37}$$

thus fulfilling the fourth property of Eqs. 2.29, and generally $\nu_{\alpha\beta} \neq \nu_{\beta\alpha}$.
The energy elastic collisional term is shown to be (Braginskii 1965):

$$M_{\alpha\beta}^{\mathrm{elastic}} = \mathbf{u}_\alpha \mathbf{R}_\alpha^{\mathrm{elastic}} + \frac{1}{2}\rho_\alpha \nu_{\alpha\beta} \big(\mathbf{u}_\beta - \mathbf{u}_\alpha\big)^2 + \frac{1}{2}\rho_\alpha \nu_{\alpha\beta} \left(\frac{3k_\mathrm{B}T_\beta}{m_\beta} - \frac{3k_\mathrm{B}T_\alpha}{m_\beta} \right) . \tag{2.38}$$

The first term of this expression is the work done by the momentum collisional term, the second is called frictional heating and the third term is known as thermal exchange.

2.1.4 Viscosity and conductivity coefficients

We can observe that in the equation for each moment of the distribution function there are quantities which represent the next moment of the distribution function. These quantities appear as the divergence of a flux term, the flux being: the momentum in the continuity equation, the pressure tensor in the momentum equation, and the heat flux in the energy equation. In order to close the equations after calculating n moments of the Boltzmann equation, the moment n+1 of the distribution function must be prescribed. We show next the derivation of the pressure tensor elements, when we consider the heat flux zero. We consider the Krook operator for the collisional term in Boltzmann equation, (see Braginskii 1965; Hunana et al. 2019):

$$\frac{\partial f_\alpha}{\partial t} + \mathbf{v} \cdot \nabla_\mathbf{r} f_\alpha + \mathbf{a} \cdot \nabla_\mathbf{v} f_\alpha = -\nu \big(f_\alpha - f_{\alpha 0}\big) \,, \tag{2.39}$$

where $\nu = 1/t_r$ is the inverse of the relaxation time t_r of the distribution function f_α to the equilibrium distribution function $f_{\alpha 0}$. For the moment we do not specify how the distribution function relaxes to the equilibrium distribution function. As we will see later, ν is usually considered the collision frequency of particles of the same species, but some authors consider collisions with all particles of all species.

After multiplying the above Eq. 2.39 by $\mathbf{c}_i\mathbf{c}_j$, and integrating in velocity space, we obtain the equation of the evolution of the pressure tensor (Hunana et al. 2019),

$$\frac{\partial \hat{\mathbf{p}}_\alpha}{\partial t} + \nabla \cdot \mathbf{q}_\alpha + (\nabla \cdot \mathbf{u}_\alpha)\hat{\mathbf{p}} + \hat{\mathbf{p}}_\alpha \cdot \nabla \mathbf{u}_\alpha + (\hat{\mathbf{p}}_\alpha \cdot \nabla \mathbf{u}_\alpha)^T + \Omega_\alpha \frac{B}{B_0} \left[\mathbf{b} \times \hat{\mathbf{p}}_\alpha + (\mathbf{b} \times \hat{\mathbf{p}}_\alpha)^T \right] = -\nu \hat{\mathbf{\Pi}}_\alpha \,, \tag{2.40}$$

where $\mathbf{b}$ is the unit vector in the direction of the magnetic field: $\mathbf{b} = \mathbf{B}/B$, and $\mathbf{B_0}$ is the equilibrium magnetic field, assumed to be in the z direction. Ω_α is the cyclotron frequency:

$$\Omega_\alpha = \frac{q_\alpha B_0}{m_\alpha}\,. \tag{2.41}$$

As mentioned above, we are considering a zero heat flux in this approximation, and thus, the related term $\nabla \cdot \mathbf{q}_\alpha$, can be omitted.

We present next the main steps in obtaining the pressure tensor (Hunana et al. 2019). We have:

$$\mathbf{b} \times \hat{\mathbf{p}}_\alpha^{\rm iso} + (\mathbf{b} \times \hat{\mathbf{p}}_\alpha^{\rm iso})^T = \hat{\mathbf{0}}\,, \tag{2.42}$$

where $\hat{\mathbf{0}}$ is the matrix identically zero. Applying Tr to Eq. 2.40, we obtain the scalar pressure equation,

$$\frac{\partial p_\alpha}{\partial t} + \mathbf{u}_\alpha \cdot \nabla p_\alpha + \frac{5}{3} p_\alpha \nabla \cdot \mathbf{u}_\alpha + \frac{2}{3}\hat{\mathbf{\Pi}}_\alpha : \nabla \mathbf{u}_\alpha = 0\,, \tag{2.43}$$

which is the same equation that can be deduced from the energy equation, Eq. 2.25 above. Taking into account Eq. 2.42, and separating the traceless terms, Eq. 2.40 can be written,

$$\frac{B}{B_0}\left[\mathbf{b} \times \hat{\mathbf{\Pi}}_\alpha + (\mathbf{b} \times \hat{\mathbf{\Pi}}_\alpha)^T\right] + \frac{\nu}{\Omega_\alpha}\hat{\mathbf{\Pi}}_\alpha = -\frac{1}{\Omega_\alpha}\left[\frac{\partial \hat{\mathbf{p}}_\alpha}{\partial t} + (\nabla \cdot \mathbf{u}_\alpha)\hat{\mathbf{p}}_\alpha + \hat{\mathbf{p}}_\alpha \cdot \nabla \mathbf{u}_\alpha + (\hat{\mathbf{p}}_\alpha \cdot \nabla \mathbf{u}_\alpha)^T\right]\,. \tag{2.44}$$

In the linear calculation $\mathbf{B} = \mathbf{B_0}$ and the left-hand side (LHS) of Eq. 2.44 becomes:

$$LHS = \begin{pmatrix} -2\Pi_{\alpha xy} & \Pi_{\alpha xx} - \Pi_{\alpha yy} & -\Pi_{\alpha yz} \\ \Pi_{\alpha xx} - \Pi_{\alpha yy} & 2\Pi_{\alpha xy} & \Pi_{\alpha xz} \\ -\Pi_{\alpha yz} & \Pi_{\alpha xz} & 0 \end{pmatrix} + \frac{\nu}{\Omega_\alpha}\begin{pmatrix} \Pi_{\alpha xx} & \Pi_{\alpha xy} & \Pi_{\alpha xz} \\ \Pi_{\alpha xy} & \Pi_{\alpha yy} & \Pi_{\alpha yz} \\ -\Pi_{\alpha xz} & \Pi_{\alpha yz} & \Pi_{\alpha zz} \end{pmatrix}\,. \tag{2.45}$$

We can observe that $\mathrm{Tr}(LHS) = 0$. In order to calculate the off-diagonal terms we consider an expansion of $\hat{\mathbf{p}}_\alpha$ in $\hat{\mathbf{p}}_\alpha^{\rm iso}$ term in the the right-hand side (RHS) of Eq. 2.44. This means that the "first order" terms (off-diagonal terms, in this case) are obtained after removing the contribution form the diagonal terms, by solving:

$$LHS = RHS - \frac{1}{3}\mathrm{Tr}(RHS)\hat{\mathbb{I}}\,. \tag{2.46}$$

It can be shown that for the RHS of Eq. 2.44 we have,

$$\frac{1}{3}\mathrm{Tr}(RHS) = \frac{\partial p_\alpha}{\partial t} + \frac{5}{3} p \nabla \cdot \mathbf{u}_\alpha. \tag{2.47}$$

Then, we can write:

$$RHS - \frac{1}{3}\mathrm{Tr}(RHS)\hat{\mathbb{I}} = -\frac{p_\alpha}{\Omega_\alpha}\hat{\mathbf{W}}\,, \tag{2.48}$$

where

$$\hat{\mathbf{W}} = \begin{pmatrix} 2\frac{\partial u_{\alpha x}}{\partial x} - \frac{2}{3}\nabla\cdot\mathbf{u}_\alpha & \frac{\partial u_{\alpha x}}{\partial y} + \frac{\partial u_{\alpha y}}{\partial x} & \frac{\partial u_{\alpha x}}{\partial z} + \frac{\partial u_{\alpha z}}{\partial x} \\ \frac{\partial u_{\alpha x}}{\partial y} + \frac{\partial u_{\alpha y}}{\partial x} & 2\frac{\partial u_{\alpha y}}{\partial y} - \frac{2}{3}\nabla\cdot\mathbf{u}_\alpha & \frac{\partial u_{\alpha y}}{\partial z} + \frac{\partial u_{\alpha z}}{\partial y} \\ \frac{\partial u_{\alpha x}}{\partial z} + \frac{\partial u_{\alpha z}}{\partial x} & \frac{\partial u_{\alpha y}}{\partial z} + \frac{\partial u_{\alpha z}}{\partial y} & 2\frac{\partial u_{\alpha z}}{\partial z} - \frac{2}{3}\nabla\cdot\mathbf{u}_\alpha \end{pmatrix}. \tag{2.49}$$

$\hat{\mathbf{W}}$ defined above in Eq. 2.49 can be decomposed into an anisotropic and isotropic parts,

$$\hat{\mathbf{W}} = \hat{\mathbf{W}}' - \frac{2}{3}\nabla\cdot\mathbf{u}_\alpha\hat{\mathbb{I}}, \tag{2.50}$$

Replacing 2.45 and 2.48 into Eq. 2.46, we obtain for the element in the pressure tensor, which describes viscosity along the magnetic field ($\Pi_{\alpha zz}$), the following expression:

$$\Pi_{\alpha zz} = -\frac{p_\alpha}{\nu}W_{zz}\,. \tag{2.51}$$

Choosing the element zz, along the magnetic field, means that we do not take into account the contribution of the magnetic field in the pressure tensor. We define the isotropic viscosity by generalizing the above 2.51:

$$\hat{\mathbf{\Pi}}_\alpha = -\frac{p_\alpha}{\nu}\hat{\mathbf{W}}\,. \tag{2.52}$$

The viscosity terms have been defined as, (Leake et al. 2013)

$$\tau_{\alpha ij} = \xi_\alpha\left(\frac{\partial u_{\alpha i}}{\partial x_j} + \frac{\partial u_{\alpha j}}{\partial x_i}\right), \tag{2.53}$$

where ξ_α is the viscosity coefficient,

$$\xi_\alpha = \frac{n_\alpha k_\mathrm{B} T_\alpha}{\nu}\,. \tag{2.54}$$

With the definition of the anisotropic part $\hat{\mathbf{W}}'$ from the above decomposition, Eq. 2.53 can be written,

$$\hat{\tau}_\alpha = \frac{p_\alpha}{\nu}\hat{\mathbf{W}}'\,. \tag{2.55}$$

If we neglect the isotropic part of $\hat{\mathbf{W}}$, i.e. the second term which appears in its decomposition described by Eq. 2.50, and take into account Eq. 2.52, we observe that the definition of the viscosity by Leake et al. (2013), equivalent to the expression of Eq. 2.55, is consistent with the definition in Eq. 2.14.

In order to calculate the heat flux, the next moment of Boltzmann equation has to be considered, the heat flux equation. The heat flux has been calculated by Braginskii (1965) by considering an expansion of the distribution function around the equilibrium distribution function, assumed to be a Maxwellian. From the first order terms, the thermal force in the momentum equation, and the

heat flux in the energy equation, both proportional to the gradient in the temperature are obtained (Braginskii 1965). The heat flux is shown to be:

$$\mathbf{q}_\alpha = -K_\alpha \nabla T_\alpha \,, \tag{2.56}$$

where K_α is the thermal conduction coefficient (Braginskii 1965; Leake et al. 2013),

$$K_\alpha = \frac{4 n_\alpha k_\mathrm{B} T_\alpha}{\nu m_\alpha}. \tag{2.57}$$

Relaxation due to collisions with particles of the same species

In the approximation that the collisions inside the same species are dominant over the collisions with other species, $\nu_{\alpha\alpha} \gg \nu_{\alpha\beta}, \forall \beta \neq \alpha$, ν is taken to be $\nu_{\alpha\alpha}$ (see e.g. the model used by Leake et al. 2013). Replacing for the collisional frequencies defined in Eq. 2.36 in the above Eqs. 2.54 and 2.57 we obtain,

$$\begin{aligned} \xi_\alpha &= \frac{\sqrt{\pi k_\mathrm{B} T_\alpha m_\alpha}}{2\sigma_{\alpha\alpha}^{\mathrm{elastic}}} \,, \\ K_\alpha &= 2\sqrt{\frac{\pi k_\mathrm{B} T_\alpha}{m_\alpha}} \frac{1}{\sigma_{\alpha\alpha}^{\mathrm{elastic}}} \,. \end{aligned} \tag{2.58}$$

As we can see, the dependence on the number density has canceled out, and these coefficients only depend on temperature. In the cases where the number density is low, the viscosity and the thermal conduction coefficient become large compared to the other terms in the momentum and energy equation, respectively, especially when the temperature is high. As we will see later, in Chapter 6, where we simulate the Rayleigh Taylor instability at the interface between a prominence and the surrounding corona, there are very few neutrals in the corona, and the temperature is very high, which results in a very large viscosity. It has been suggested by Hillier (2020), that the mean free path of the neutrals is greatly affected by the collisions with charged particles rather than by collisions with neutral particles, and that the viscosity coefficient, defined in Eq. 2.54 should include also collision frequencies with other species, besides the collision frequency between the particles of the same species.

Relaxation due to collisions with particles of all the species

The idea of having a multi-fluid model with equations for each species, coupled by explicit collisional terms, is that the relaxation time because of collisions of particles inside same species is smaller than the relaxation time because of collisions with other species. However, no assumption about the ordering of these scales has been made in the derivation of these terms. Dorf (2014); Vranjes & Krstic (2013) include collisions with other species in the viscosity coefficient, which can be generally written as,

$$\xi_\alpha = \frac{n_\alpha k_\mathrm{B} T_\alpha}{\sum_\beta \nu_{\alpha\beta}} \,, \tag{2.59}$$

and similarly for the thermal conduction coefficient,

$$K_\alpha = \frac{4 n_\alpha k_\mathrm{B} T_\alpha}{m_\alpha \sum_\beta \nu_{\alpha\beta}}. \tag{2.60}$$

The viscosity ($\hat{\tau_\alpha}$) and thermal conduction ($\mathbf{q}_\alpha$) of a gas with a Maxwellian distribution are zero (Goedbloed et al. 2019). In a more general context, the viscosity term is zero for any isotropic distribution function (Braginskii 1965).

2.2 Three fluids equations

Next, we briefly show the three fluid equations, with $\alpha \in i, e, n$ for a plasma composed by: neutrals(n), ions(i), and electrons(e).

2.2.1 Continuity equations

Replacing α for n, i, and e in Eq. 2.23, we obtain,

$$\begin{aligned}
\frac{\partial \rho_\mathrm{n}}{\partial t} + \nabla \cdot (\rho_\mathrm{n} \mathbf{u}_\mathrm{n}) &= S_\mathrm{n}\,, \\
\frac{\partial \rho_\mathrm{i}}{\partial t} + \nabla \cdot (\rho_\mathrm{i} \mathbf{u}_\mathrm{i}) &= S_\mathrm{i}\,, \\
\frac{\partial \rho_\mathrm{e}}{\partial t} + \nabla \cdot (\rho_\mathrm{e} \mathbf{u}_\mathrm{e}) &= S_\mathrm{e}\,,
\end{aligned} \tag{2.61}$$

where S_n, S_e, S_i are density (inelastic) collisional terms fulfilling $S_\mathrm{n} + S_\mathrm{e} + S_\mathrm{i} = 0$. These terms describe the mass loss/gain due to such processes as ionization or recombination.

2.2.2 Momentum equations

Replacing α for n,i, and e in Eq. 2.24, we obtain,

$$\begin{aligned}
\frac{\partial (\rho_\mathrm{n} \mathbf{u}_\mathrm{n})}{\partial t} + \nabla \cdot (\rho_\mathrm{n} \mathbf{u}_\mathrm{n} \mathbf{u}_\mathrm{n} + \hat{\mathbf{p}}_\mathrm{n}) &= \rho_\mathrm{n} \mathbf{g} + \mathbf{R}_\mathrm{n}\,, \\
\frac{\partial (\rho_\mathrm{i} \mathbf{u}_\mathrm{i})}{\partial t} + \nabla \cdot (\rho_\mathrm{i} \mathbf{u}_\mathrm{i} \mathbf{u}_\mathrm{i} + \hat{\mathbf{p}}_i) &= q_\mathrm{i} n_\mathrm{i} (\mathbf{E} + \mathbf{u}_\mathrm{i} \times \mathbf{B}) + \rho_\mathrm{i} \mathbf{g} + \mathbf{R}_\mathrm{i}\,, \\
\frac{\partial (\rho_\mathrm{e} \mathbf{u}_\mathrm{e})}{\partial t} + \nabla \cdot (\rho_\mathrm{e} \mathbf{u}_\mathrm{e} \mathbf{u}_\mathrm{e} + \hat{\mathbf{p}}_e) &= -e n_\mathrm{e} (\mathbf{E} + \mathbf{u}_\mathrm{e} \times \mathbf{B}) + \rho_\mathrm{e} \mathbf{g} + \mathbf{R}_\mathrm{e}\,,
\end{aligned} \tag{2.62}$$

where $\mathbf{R}_\mathrm{n}$, $\mathbf{R}_\mathrm{i}$, and $\mathbf{R}_\mathrm{e}$ are momentum collisional terms fulfilling $\mathbf{R}_\mathrm{n} + \mathbf{R}_\mathrm{i} + \mathbf{R}_\mathrm{e} = 0$. These collisional terms describe the loss/gain of momenta via both elastic and inelastic collisions.

2.2.3 Energy (kinetic+internal) equations

Replacing α for n,i, and e in Eq. 2.25, we obtain,

$$\begin{aligned}
\frac{\partial}{\partial t}\left(e_{\rm n}+\frac{1}{2}\rho_{\rm n}u_{\rm n}^2\right)+\nabla\cdot\left(\mathbf{u}_{\rm n}(e_{\rm n}+\frac{1}{2}\rho_{\rm n}u_{\rm n}^2)+\hat{\mathbf{p}}_{\rm n}\cdot\mathbf{u}_{\rm n}+\mathbf{q}_n\right)&=\rho_{\rm n}\mathbf{u}_{\rm n}\cdot\mathbf{g}+M_{\rm n}\,,\\
\frac{\partial}{\partial t}\left(e_{\rm i}+\frac{1}{2}\rho_{\rm i}u_{\rm i}^2\right)+\nabla\cdot\left(\mathbf{u}_{\rm i}(e_{\rm i}+\frac{1}{2}\rho_{\rm i}u_{\rm i}^2)+\hat{\mathbf{p}}_{\rm i}\cdot\mathbf{u}_{\rm i}+\mathbf{q}_i\right)&=\rho_{\rm i}\mathbf{u}_{\rm i}\cdot\mathbf{g}+q_{\rm i}n_{\rm i}\mathbf{u}_{\rm i}\cdot\mathbf{E}+M_{\rm i}\,,\\
\frac{\partial}{\partial t}\left(e_{\rm e}+\frac{1}{2}\rho_{\rm e}u_{\rm e}^2\right)+\nabla\cdot\left(\mathbf{u}_{\rm e}(e_{\rm e}+\frac{1}{2}\rho_{\rm e}u_{\rm e}^2)+\hat{\mathbf{p}}_{\rm e}\cdot\mathbf{u}_{\rm e}+\mathbf{q}_e\right)&=\rho_{\rm e}\mathbf{u}_{\rm e}\cdot\mathbf{g}-en_{\rm e}\mathbf{u}_{\rm e}\cdot\mathbf{E}+M_{\rm e}\,,
\end{aligned}\tag{2.63}$$

where $M_{\rm n}$, $M_{\rm i}$, and $M_{\rm e}$ are energy (kinetic+internal) collisional terms fulfilling: $M_{\rm n}+M_{\rm i}+M_{\rm e}=0$. Yet again, these terms describe energy loss/gain in both elastic and inelastic collisions.

2.2.4 Inelastic collisions

For the inelastic collisions of species α we have to consider inelastic collisions that transform particles α' into particles α and those that transform particles α into particles α',

$$C_{\alpha}^{\rm inelastic}=\sum_{\alpha'}(C_{\alpha'\alpha}^{\rm inelastic}-C_{\alpha\alpha'}^{\rm inelastic})\,.\tag{2.64}$$

We can distinguish further the collisions that transform particles α into particles α' by the type of particles with which they are colliding,

$$C_{\alpha\alpha'}^{\rm inelastic}=\sum_{\beta}C_{\alpha\alpha',\beta}^{\rm inelastic}\,.\tag{2.65}$$

Meier (2011); Meier & Shumlak (2012) consider the operator:

$$C_{\alpha,\beta}^{\rm inelastic}=f_{\alpha}\int_V\sigma_{\alpha,\beta}f_{\beta}|\mathbf{v}_{\beta}-\mathbf{v}_{\alpha}|d^3\mathbf{v}_{\beta}\,,\tag{2.66}$$

where $\sigma_{\alpha,\beta}=\sigma_{\alpha,\beta}(c_{\alpha},c_{\beta})$ is the collisional cross section of α and β. In ionized plasma the inelastic collisions are:

- recombination: ions colliding with electrons creating neutrals

$$C^{\rm rec}=C_{\rm in,e}^{\rm inelastic}=f_{\rm i}\int_V\sigma_{in,e}f_{\rm e}|\mathbf{v}_{\rm e}-\mathbf{v}_{\rm i}|d^3\mathbf{v}_{\rm e}\,.\tag{2.67}$$

- ionization: neutrals colliding with electrons creating ions

$$C^{\rm ion}=C_{\rm ni,e}^{\rm inelastic}=f_{\rm n}\int_V\sigma_{ni,e}f_{\rm e}|\mathbf{v}_{\rm e}-\mathbf{v}_{\rm n}|d^3\mathbf{v}_{\rm e}\,.\tag{2.68}$$

It is assumed that the thermal velocity of the electrons is much larger than the macroscopic and thermal velocities of ions and neutrals (Meier 2011), so that $|\mathbf{v}_\mathrm{e} - \mathbf{v}_\mathrm{i}| = |\mathbf{v}_\mathrm{e} - \mathbf{v}_\mathrm{n}| = c_\mathrm{e}$. Then:

$$C_\mathrm{n}^\mathrm{inelastic} = C^\mathrm{rec} - C^\mathrm{ion} = f_\mathrm{i} \int_V \sigma_\mathrm{ion} f_\mathrm{e} c_\mathrm{e} d^3\mathbf{v}_\mathrm{e} - f_\mathrm{n} \int_V \sigma_\mathrm{rec} f_\mathrm{e} c_\mathrm{e} d^3\mathbf{v}_\mathrm{e}\,, \tag{2.69}$$

where $\sigma_\mathrm{ion} = \sigma_\mathrm{in,e}$, and $\sigma_\mathrm{rec} = \sigma_\mathrm{ni,e}$, the ionization and recombination cross sections depend only on c_e. We use the the following notations for the collisional ionization and radiative recombination rates:

$$\begin{aligned} \Gamma^\mathrm{ion} &= n_\mathrm{e} \langle \sigma_\mathrm{ion} c_\mathrm{e} \rangle\,, \\ \Gamma^\mathrm{rec} &= n_\mathrm{e} \langle \sigma_\mathrm{rec} c_\mathrm{e} \rangle\,, \end{aligned} \tag{2.70}$$

where the average is over electrons velocity space, and Eq. 2.69 becomes:

$$C_\mathrm{n}^\mathrm{inelastic} = f_\mathrm{i}\Gamma^\mathrm{ion} - f_\mathrm{n}\Gamma^\mathrm{rec}\,, \tag{2.71}$$

and expressions for Γ^ion and Γ^recas functions of n_e and T_e are given in Voronov (1997) and Smirnov (2003):

$$\Gamma^\mathrm{rec} \approx \frac{n_\mathrm{e}}{\sqrt{T_\mathrm{e}^*}} 2.6 \cdot 10^{-19};\ \ \mathrm{s}^{-1}\,, \tag{2.72}$$

$$\Gamma^\mathrm{ion} \approx n_\mathrm{e} A \frac{1}{X + \phi_\mathrm{ion}/T_\mathrm{e}^*} \left(\frac{\phi_\mathrm{ion}}{T_\mathrm{e}^*}\right)^K e^{-\phi_\mathrm{ion}/T_\mathrm{e}^*};\ \ \mathrm{s}^{-1}\,, \tag{2.73}$$

where $\phi_\mathrm{ion} = 13.6eV$, T_e^* is electron temperature in eV, $A = 2.91 \cdot 10^{-14}$, $K = 0.39$, and $X = 0.232$. The rates have been calculated in a theretical approach. The ionization rate formula has been obtained in more general context, regardless the atom or ion type, by fitting the data obtained by varying the electron temperature in a range of values for each atom or ion. This formula is valid for the electron temperature up to 10 keV. For the hydrogen atom the data has been fit for electron temperatures between 1 eV and 20 eV.

Figure 2.1 shows the above quantities $\langle \sigma_\mathrm{ion} c_\mathrm{e} \rangle$, and $\langle \sigma_\mathrm{rec} c_\mathrm{e} \rangle$ that enter the definition of Γ^rec and Γ^ion, which have been defined as a function of the electron temperature for a range between 4000 K and 2×10^5 K. While the recombination rate per electron decreases slowly with temperature, the ionization rate per electron increases steeply and seems to saturate. They are equal for temperature around 15000 K.

The contributions in the continuity, momentum and energy equations of the inelastic collisional terms are:

$$S_\mathrm{n}^\mathrm{inelastic} = \rho_\mathrm{c}\Gamma^\mathrm{rec} - \rho_\mathrm{n}\Gamma^\mathrm{ion}\,. \tag{2.74}$$

Generally, for $C_{\alpha\alpha',\beta}^\mathrm{inelastic}$ defined in 2.66, we have:

$$\mathbf{R}_{\alpha\alpha',\beta}^\mathrm{inelastic} = m_\alpha \int_V \mathbf{v}_\alpha f_\alpha \int_V \sigma_{\alpha\alpha',\beta}^\mathrm{inelastic} f_\beta \mid \mathbf{v}_\beta - \mathbf{v}_\alpha \mid d^3\mathbf{v}_\beta d^3\mathbf{v}_\alpha = \mathbf{u}_\alpha S_{\alpha\alpha',\beta}^\mathrm{inelastic}\,, \tag{2.75}$$

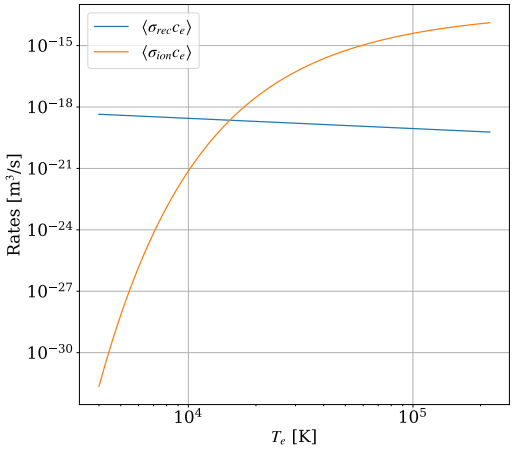

Figure 2.1: Ionization and recombination rates per electron, the quantities $\langle\sigma_{\rm ion}c_{\rm e}\rangle$, and $\langle\sigma_{\rm rec}c_{\rm e}\rangle$ defined by Voronov (1997) and Smirnov (2003) as a function of the electron temperature.

$$M^{\rm inelastic}_{\alpha\alpha',\beta} = \frac{1}{2}m_\alpha \int_V v_\alpha^2 f_\alpha \int_V \sigma^{\rm inelastic}_{\alpha\alpha',\beta} f_\beta \mid \mathbf{v}_\beta - \mathbf{v}_\alpha \mid d^3\mathbf{v}_\beta d^3\mathbf{v}_\alpha = \frac{1}{2}u_\alpha^2 S^{\rm inelastic}_{\alpha\alpha',\beta} + \frac{3k_{\rm B}T_\alpha}{2m_\beta} S^{\rm inelastic}_{\alpha\alpha',\beta}\,, \quad (2.76)$$

where we have used the notation:

$$S^{\rm inelastic}_{\alpha\alpha',\beta} = \int_V C^{\rm inelastic}_{\alpha\alpha',\beta} d^3\mathbf{v}_\alpha\,. \quad (2.77)$$

2.3 Two-fluid equations

When treated numerically by an explicit code, the equation of evolution of electron momentum imposes very small time steps. This is so because electrons have very large velocities. Therefore, treating electrons is numerically problematic. To avoid this problem, we use the fact that electrons have three orders of magnitude less mass compared to ions and neutrals. This allows us to neglect electron inertia. Ion and electron equations will be added together, producing a single set of evolution equations of the charged fluid. In this approach, a generalized Ohm's law has to be supplied to close the system.
In our two-fluid model we assume:

- same temperatures of ions and electrons, $T_{\rm c} = T_{\rm e} = T_{\rm i}$
- center of mass velocity of charges is essentially ion velocity, $\mathbf{u}_{\rm c} = \mathbf{u}_{\rm i}$ (this implies $\mathbf{u}_{\rm e} = \mathbf{u}_{\rm c} - \frac{\mathbf{J}}{en_{\rm e}}$)
- the possibility of neglecting the electrons. In some situations, we do not want to take the electrons into account. As their mass is negligible compared to the mass of the ions, they

effectively contribute only to the pressure. The pressure of charges is defined as:

$$p_{\rm c} = {\rm A} n_{\rm i} k_{\rm B} T_{\rm c} \,. \tag{2.78}$$

where A = 2 when electrons are included in the charged fluid, and A = 1 when the electrons are not included.

- purely hydrogen. This implies a constant mean molecular weight for neutrals: $\mu_{\rm n} = 1$ g/mole.
- singly ionized plasma, and charge neutrality. These two assumptions, purely hydrogen, and singly ionized plasma, imply $n_{\rm i} = n_{\rm e}$ and a constant mean molecular weight, used in the alternative definition of the temperature, Eq. 2.17 for charges: $\mu_{\rm c} = 1/{\rm A}$ g/mole, where A has been defined in the above Eq. 2.78. At the same time, charge-exchange reactions can be introduced via collisional cross section.

The two-fluid model is also described by Meier (2011); Meier & Shumlak (2012); Leake et al. (2012); Leake et al. (2013); Khomenko et al. (2014a).

2.3.1 Continuity equations

$$\begin{aligned} \frac{\partial \rho_{\rm n}}{\partial t} + \nabla \cdot (\rho_{\rm n} \mathbf{u}_{\rm n}) &= S_{\rm n} \,, \\ \frac{\partial \rho_{\rm c}}{\partial t} + \nabla \cdot (\rho_{\rm c} \mathbf{u}_{c}) &= -S_{\rm n} \,, \end{aligned} \tag{2.79}$$

with $S_{\rm n}$ given later in subsection 2.3.4 in Eq. 2.83.

2.3.2 Momentum equations

$$\begin{aligned} \frac{\partial (\rho_{\rm n} \mathbf{u}_{\rm n})}{\partial t} + \nabla \cdot (\rho_{\rm n} \mathbf{u}_{\rm n} \mathbf{u}_{\rm n} + \hat{\mathbf{p}}_{\rm n}) &= \rho_{\rm n} \mathbf{g} + \mathbf{R}_{\rm n} \,, \\ \frac{\partial (\rho_{\rm c} \mathbf{u}_{\rm c})}{\partial t} + \nabla \cdot (\rho_{\rm c} \mathbf{u}_{\rm c} \mathbf{u}_{\rm c} + \hat{\mathbf{p}}_{\rm c}) &= [\mathbf{J} \times \mathbf{B}] + \rho_{\rm c} \mathbf{g} - \mathbf{R}_{\rm n} \,, \end{aligned} \tag{2.80}$$

with $\mathbf{R}_{\rm n}$ given later in subsection 2.3.4 in Eqs. 2.84 and 2.85.
The Lorentz Force term in charges momentum equation will be numerically implemented in conservative form:

$$\mathbf{J} \times \mathbf{B} = -\nabla \cdot \left(\frac{B}{2\mu_0} \hat{\mathbb{I}} - \frac{1}{\mu_0} \mathbf{B}\mathbf{B} \right) \,.$$

2.3.3 Energy (kinetic+internal) equations

$$\frac{\partial}{\partial t}\left(e_\mathrm{n}+\frac{1}{2}\rho_\mathrm{n}u_\mathrm{n}^2\right)+\nabla\cdot\left(\mathbf{u}_\mathrm{n}(e_\mathrm{n}+\frac{1}{2}\rho_\mathrm{n}u_\mathrm{n}^2)+\hat{\mathbf{p}}_\mathrm{n}\cdot\mathbf{u}_\mathrm{n}-K_\mathrm{n}\nabla T_\mathrm{n}\right)=\rho_\mathrm{n}\mathbf{u}_\mathrm{n}\cdot\mathbf{g}+M_\mathrm{n}\,,$$
$$\frac{\partial}{\partial t}\left(e_\mathrm{c}+\frac{1}{2}\rho_\mathrm{c}u_\mathrm{c}^2\right)+\nabla\cdot\left(\mathbf{u}_\mathrm{c}(e_\mathrm{c}+\frac{1}{2}\rho_\mathrm{c}u_\mathrm{c}^2)+\hat{\mathbf{p}}_\mathrm{c}\cdot\mathbf{u}_\mathrm{c}-K_\mathrm{c}\nabla T_\mathrm{c}\right)=\rho_\mathrm{c}\mathbf{u}_\mathrm{c}\cdot\mathbf{g}+\mathbf{J}\cdot\mathbf{E}-M_\mathrm{n}\,, \tag{2.81}$$

with M_n given later in subsection 2.3.4 in Eqs. 2.86 and 2.87. In these equations, e_α is the internal energy:

- Ideal gas for neutrals: $e_\mathrm{n}=p_\mathrm{n}/(\gamma-1)$
- Ionization energy contribution to internal energy of charges: $e_\mathrm{c}=p_\mathrm{c}/(\gamma-1)+n_\mathrm{e}\phi_\mathrm{ion}$. For the moment we did not take into account the contribution of the ionization energy.

2.3.4 Collisional terms

After replacing the assumptions used in the two-fluid model, described above into the expressions for the collisional terms, and also replacing 3/2 by the more general $1/(\gamma-1)$ in the terms containing k_B in the energy equations 2.38 and 2.76 (where three degrees of freedom were assumed), the collisional terms for neutrals become:

$$S_\mathrm{n}^\mathrm{elastic}=0\,, \tag{2.82}$$
$$S_\mathrm{n}^\mathrm{inelastic}=\rho_\mathrm{c}\Gamma^\mathrm{rec}-\rho_\mathrm{n}\Gamma^\mathrm{ion}\,, \tag{2.83}$$
$$\mathbf{R}_\mathrm{n}^\mathrm{inelastic}=(\rho_\mathrm{c}\mathbf{u}_\mathrm{c}-\frac{\rho_\mathrm{e}}{en_\mathrm{e}}\mathbf{J})\Gamma^\mathrm{rec}-\rho_\mathrm{n}\mathbf{u}_\mathrm{n}\Gamma^\mathrm{ion}\,, \tag{2.84}$$

$$\mathbf{R}_\mathrm{n}^\mathrm{elastic}=(\rho_\mathrm{e}\nu_\mathrm{en}+\rho_\mathrm{i}\nu_\mathrm{in})(\mathbf{u}_\mathrm{c}-\mathbf{u}_\mathrm{n})-\frac{\mathbf{J}}{en_\mathrm{e}}\rho_\mathrm{e}\nu_\mathrm{en}\,, \tag{2.85}$$

$$M_\mathrm{n}^\mathrm{inelastic}=\frac{1}{2}\Gamma^\mathrm{rec}\rho_\mathrm{c}u_\mathrm{c}^2-\frac{1}{2}\rho_\mathrm{n}u_\mathrm{n}^2\Gamma^\mathrm{ion}+\frac{1}{\gamma-1}\frac{k_\mathrm{B}}{m_\mathrm{n}}\left(\rho_\mathrm{c}T_\mathrm{c}\Gamma^\mathrm{rec}-\rho_\mathrm{n}T_\mathrm{n}\Gamma^\mathrm{ion}\right)$$
$$+\frac{1}{2}\Gamma^\mathrm{rec}\rho_\mathrm{e}\left(\frac{J^2}{(en_\mathrm{e})^2}-\frac{2}{en_\mathrm{e}}\mathbf{u}_\mathrm{c}\cdot\mathbf{J}\right)\,, \tag{2.86}$$

$$M_\mathrm{n}^\mathrm{elastic}=\frac{1}{2}({u_\mathrm{c}}^2-{u_\mathrm{n}}^2)(\rho_\mathrm{e}\nu_\mathrm{en}+\rho_\mathrm{i}\nu_\mathrm{in})+\frac{1}{\gamma-1}\frac{k_\mathrm{B}}{m_\mathrm{n}}(T_\mathrm{c}-T_\mathrm{n})(\rho_\mathrm{e}\nu_\mathrm{en}+\rho_\mathrm{i}\nu_\mathrm{in})$$
$$+\rho_\mathrm{e}\nu_\mathrm{en}\left(\frac{1}{2}\left(\frac{\mathbf{J}}{en_\mathrm{e}}\right)^2-\frac{\mathbf{J}}{en_\mathrm{e}}\cdot\mathbf{u}_\mathrm{c}\right)\,. \tag{2.87}$$

We will neglect the terms related to the current density **J**, which appear in the equations above. They are small, as they are proportional to the electron density. They appear because of the difference of the velocity between ions and electrons, which are evolved together as the charged fluid.
The elastic collisions between ions and neutrals and between electrons and neutrals can be combined into a single collision frequency between charges and neutrals. By defining the collisional parameter:

$$\alpha = \frac{\rho_{\rm e}\nu_{\rm en} + \rho_{\rm i}\nu_{\rm in}}{\rho_{\rm n}\rho_{\rm c}}, \tag{2.88}$$

the effective collision frequencies between charges and neutrals, and between neutrals and charges become, respectively:

$$\begin{aligned} \nu_{\rm cn} &= \alpha\rho_{\rm n}, \\ \nu_{\rm nc} &= \alpha\rho_{\rm c}\,. \end{aligned} \tag{2.89}$$

Here, $\nu_{\rm en}$ and $\nu_{\rm in}$ are the electron-neutral and ion-neutral collision frequencies, respectively, with expressions given in Eq. 2.36. Using these expressions in Eq. 2.88 gives the expression for α:

$$\alpha = \frac{m_{\rm in}}{{m_{\rm n}}^2}\sqrt{\frac{8k_{\rm B}T_{\rm cn}}{\pi m_{\rm in}}}\sigma_{\rm in}^{\rm elastic} + \frac{m_{\rm en}}{{m_{\rm n}}^2}\sqrt{\frac{8k_{\rm B}T_{\rm cn}}{\pi m_{\rm en}}}\sigma_{\rm en}^{\rm elastic}\,. \tag{2.90}$$

The momentum collisional term $\mathbf{R}_{\rm n}$, with the definition of the collisional parameter α above, and neglecting the contribution due to the current density, **J**, can be written as:

$$\mathbf{R}_{\rm n} = \rho_{\rm c}\mathbf{u}_{\rm c}\Gamma^{\rm rec} - \rho_{\rm n}\mathbf{u}_{\rm n}\Gamma^{\rm ion} + \alpha\rho_{\rm n}\rho_{\rm c}(\mathbf{u}_{\rm c} - \mathbf{u}_{\rm n}). \tag{2.91}$$

If we take into account the charge-exchange reactions, $\alpha_{\rm cx}$, as defined in Eq. (2.92), below (Meier & Shumlak 2012), should be added to the elastic collision parameter α,

$$\alpha_{\rm cx} = \frac{1}{m_{\rm n}}\left(V_0^{\rm cx} + V_{\rm 1n}^{\rm cx} + V_{\rm 1c}^{\rm cx}\right)\sigma_{\rm cx}, \tag{2.92}$$

with:

$$\begin{aligned} V_0^{\rm cx} &= \sqrt{\frac{4}{\pi}{v_{Tn}}^2 + \frac{4}{\pi}{v_{Ti}}^2 + {v_{\rm rel}}^2}\,, \\ V_{\rm 1n}^{\rm cx} &= {v_{Tn}}^2\left(4(\frac{4}{\pi}{v_{Ti}}^2 + {v_{\rm rel}}^2) + \frac{9\pi}{4}{v_{Tn}}^2\right)^{-0.5}\,, \\ V_{\rm 1c}^{\rm cx} &= {v_{Ti}}^2\left(4(\frac{4}{\pi}{v_{Tn}}^2 + {v_{\rm rel}}^2) + \frac{9\pi}{4}{v_{Ti}}^2\right)^{-0.5}\,, \\ \sigma_{\rm cx} &= 1.12\times10^{-18} - 7.15\times10^{-20}\ln(V_0^{cx})\,, \end{aligned} \tag{2.93}$$

where v_{Tn}, v_{Ti}, and $v_{\rm rel}$ are the neutral thermal velocity, the ion thermal velocity, and the absolute value of the relative velocity between neutrals and charges, respectively:

$$v_{Tn} = \sqrt{\frac{2k_{\rm B}T_{\rm n}}{m_{\rm n}}}, \quad v_{Ti} = \sqrt{\frac{2k_{\rm B}T_{\rm c}}{m_{\rm i}}}, \quad v_{\rm rel} = \mid \mathbf{u_n} - \mathbf{u_c} \mid . \tag{2.94}$$

With the above notations, the expressions for the neutral viscosity and thermal conductivity coefficients when the collisions with charges are also taken into account, besides the neutral-neutral collisions, Eqs. 2.59, 2.60 become:

$$\begin{aligned} \xi_{\rm n} &= \frac{n_{\rm n}k_{\rm B}T_{\rm n}}{2n_{\rm n}\sqrt{\frac{k_{\rm B}T_{\rm n}}{\pi m_{\rm n}}}\sigma_{\rm nn}^{\rm elastic} + \alpha\rho_{\rm c}}, \\ K_{\rm n} &= \frac{4n_{\rm n}k_{\rm B}T_{\rm n}}{2n_{\rm n}\sqrt{\frac{m_{\rm n}k_{\rm B}T_{\rm n}}{\pi}}\sigma_{\rm nn}^{\rm elastic} + m_{\rm n}\alpha\rho_{\rm c}}. \end{aligned} \tag{2.95}$$

The elastic collisional cross sections used were (Draine et al. 1983; Leake et al. 2012; Leake et al. 2013; Meier & Shumlak 2012): $\sigma_{\rm nn}^{\rm elastic} = 2.1 \times 10^{-18}{\rm m}^2$, $\sigma_{\rm ei}^{\rm elastic} = \sigma_{\rm ii}^{\rm elastic} = \frac{40\pi}{3}\left(\frac{e^2}{4\pi\epsilon_0 k_{\rm B}T_{\rm c}}\right)^2$, where e is the elementary charge, and ϵ_0 the permitivity of free space, $\sigma_{\rm in}^{\rm elastic} = 1.16 \times 10^{-18}{\rm m}^2$, and $\sigma_{\rm en}^{\rm elastic} = 10^{-19}{\rm m}^2$.
Neglecting the terms related to the current density $\mathbf{J}$, and with the above definition of the effective collisional parameter α, Eq. 2.88, the collisional term M_n becomes,

$$\begin{aligned} M_{\rm n} &= \left(\frac{1}{2}\Gamma^{\rm rec}\rho_{\rm c}u_c^2 - \frac{1}{2}\rho_{\rm n}u_{\rm n}^2\Gamma^{\rm ion}\right) + \frac{1}{\gamma-1}\frac{k_{\rm B}}{m_{\rm n}}\left(\rho_{\rm c}T_{\rm c}\Gamma^{\rm rec} - \rho_{\rm n}T_{\rm n}\Gamma^{\rm ion}\right) \\ &+ \frac{1}{2}({u_c}^2 - {u_{\rm n}}^2)\alpha\rho_{\rm c}\rho_{\rm n} + \frac{1}{\gamma-1}\frac{k_{\rm B}}{m_{\rm n}}(T_{\rm c} - T_{\rm n})\alpha\rho_{\rm c}\rho_{\rm n}. \end{aligned} \tag{2.96}$$

Among the four terms of the expression of M_n, the first two are related to ionization/recombination processes, and the last two terms are related to elastic collisions. Terms containing temperatures, namely the second and the fourth terms, represent the thermal exchange between charges and neutrals due to inelastic and elastic collisions, respectively. Because the energy equations evolve kinetic and internal energy, the M_n terms include kinetic energy gains/losses due to the change in the number of particles, and to the work done by the collisional terms.

2.3.5 Maxwell equations

In the Ampère law:

$$\nabla \times \mathbf{B} = \mu_0\mathbf{J} + \mu_0\varepsilon_0\frac{\partial \mathbf{E}}{\partial t}, \tag{2.97}$$

the second term, related to the displacement current is neglected, a reasonable assumption for non-relativistic flow when this term is shown to be much smaller than the first term in the equation. Thus, the expression for the current density **J** is obtained:

$$\mathbf{J} = \frac{1}{\mu_0}\nabla \times \mathbf{B}\,, \tag{2.98}$$

The time evolution of the magnetic field is obtained from the induction law,

$$\frac{\partial \mathbf{B}}{\partial t} = -\nabla \times \mathbf{E}\,. \tag{2.99}$$

The charge neutrality assumption makes the Poisson's equation, which prescribes the electric field from the charge density, superfluous:

$$\nabla \cdot \mathbf{E} = \frac{\rho_q}{\varepsilon_0}\,, \tag{2.100}$$

where $\rho_q = \sum_\alpha n_\alpha q_\alpha$ is the charge density, because charge neutrality implies $\rho_q = 0$.
The other of the four Maxwell equations:

$$\nabla \cdot \mathbf{B} = 0\,, \tag{2.101}$$

must be ensured.

2.3.6 Ohm's law

Ohm's law closes the two-fluid system of equations, supplying approximate expression for the electric field. For the Ohm's law we sum the momentum equations of ions and electrons (see Khomenko et al. (2014a)) where we assume $q_\mathrm{i} = e$ (singly ionized only):

$$\begin{aligned}\frac{\partial \mathbf{J}}{\partial t} + e\nabla \cdot \left(n_\mathrm{i}\mathbf{u}_\mathrm{i}\mathbf{u}_\mathrm{i} - n_\mathrm{e}\mathbf{u}_\mathrm{e}\mathbf{u}_\mathrm{e}\right) = e^2\left[\frac{n_\mathrm{i}}{m_\mathrm{i}}(\mathbf{E} + \mathbf{u}_\mathrm{i} \times \mathbf{B}) + \frac{n_\mathrm{e}}{m_\mathrm{e}}(\mathbf{E} + \mathbf{u}_\mathrm{e} \times \mathbf{B})\right] + \\ en_\mathrm{i}\mathbf{g} - en_\mathrm{e}\mathbf{g} - e\Big(\frac{1}{m_\mathrm{i}}\nabla p_\mathrm{i} - \frac{1}{m_\mathrm{e}}\nabla p_\mathrm{e}\Big) + e\Big(\frac{1}{m_\mathrm{i}}\mathbf{R}_\mathrm{i} - \frac{1}{m_\mathrm{e}}\mathbf{R}_\mathrm{e}\Big).\end{aligned} \tag{2.102}$$

Because $n_\mathrm{i} = n_\mathrm{e}$, $en_\mathrm{i}\mathbf{g} - en_\mathrm{e}\mathbf{g} = 0$, and neglecting the terms proportional to $\frac{m_\mathrm{e}}{m_\mathrm{i}}$, the equation 2.102 becomes:

$$\frac{e^2 n_\mathrm{e}}{m_\mathrm{e}}(\mathbf{E} + \mathbf{u}_\mathrm{e} \times \mathbf{B}) - \frac{e}{m_\mathrm{e}}\nabla p_\mathrm{e} + e\Big(\frac{1}{m_\mathrm{i}}\mathbf{R}_\mathrm{i} - \frac{1}{m_\mathrm{e}}\mathbf{R}_\mathrm{e}\Big) = \frac{\partial \mathbf{J}}{\partial t} + e\nabla \cdot \left(n_\mathrm{i}\mathbf{u}_\mathrm{i}\mathbf{u}_\mathrm{i} - n_\mathrm{e}\mathbf{u}_\mathrm{e}\mathbf{u}_\mathrm{e}\right). \tag{2.103}$$

We calculate:

$$\begin{aligned}\frac{1}{m_\mathrm{i}}\mathbf{R}_i - \frac{1}{m_\mathrm{e}}\mathbf{R}_e = \frac{1}{m_\mathrm{i}}\big(\rho_\mathrm{i}(\mathbf{u}_n - \mathbf{u}_i)\nu_\mathrm{in} + \rho_\mathrm{e}(\mathbf{u}_e - \mathbf{u}_i)\nu_\mathrm{ei} + \frac{m_\mathrm{i}}{m_\mathrm{n}}\rho_\mathrm{n}\Gamma^{ion}\mathbf{u}_n - \rho_\mathrm{i}\Gamma^{rec}\mathbf{u}_i\big) \\ -\frac{1}{m_\mathrm{e}}(\rho_\mathrm{e}(\mathbf{u}_n - \mathbf{u}_e)\nu_\mathrm{en} + \rho_\mathrm{e}(\mathbf{u}_i - \mathbf{u}_e)\nu_\mathrm{ei} + \frac{m_\mathrm{e}}{m_\mathrm{n}}\rho_\mathrm{n}\Gamma^{ion}\mathbf{u}_n - \rho_\mathrm{e}\Gamma^{rec}\mathbf{u}_e) = \\ n_\mathrm{i}(\mathbf{u}_n - \mathbf{u}_\mathrm{i})\nu_\mathrm{in} + \frac{\rho_\mathrm{e}}{m_\mathrm{i}}(\mathbf{u}_e - \mathbf{u}_\mathrm{i})\nu_\mathrm{ei} - \frac{1}{m_\mathrm{e}}\Big(\rho_\mathrm{e}(\mathbf{u}_n - \mathbf{u}_e)\nu_\mathrm{en} + \rho_\mathrm{e}(\mathbf{u}_\mathrm{i} - \mathbf{u}_e)\nu_\mathrm{ei}\Big)\,,\end{aligned}$$

and Eq. 2.103 becomes:

$$\mathbf{E} = -\mathbf{u}_\mathrm{e}\times\mathbf{B} - \frac{1}{en_\mathrm{e}}\nabla p_\mathrm{e} - \frac{\rho_\mathrm{e}}{en_\mathrm{e}}(\mathbf{u}_n - \mathbf{u}_\mathrm{i})\nu_\mathrm{in} - \frac{m_\mathrm{e}^2}{em_\mathrm{i}}(\mathbf{u}_\mathrm{e} - \mathbf{u}_\mathrm{i})\nu_\mathrm{ei} + \frac{1}{en_\mathrm{e}}\big(\rho_\mathrm{e}(\mathbf{u}_n - \mathbf{u}_\mathrm{e})\nu_\mathrm{en} + \rho_\mathrm{e}(\mathbf{u}_\mathrm{i} - \mathbf{u}_\mathrm{e})\nu_\mathrm{ei}\big) + \frac{m_\mathrm{e}}{e^2 n_\mathrm{e}}\frac{\partial \mathbf{J}}{\partial t} + \frac{m_\mathrm{e}}{en_\mathrm{e}}\nabla\cdot\big(n_\mathrm{i}\mathbf{u}_\mathrm{i}\mathbf{u}_\mathrm{i} - n_\mathrm{e}\mathbf{u}_\mathrm{e}\mathbf{u}_\mathrm{e}\big). \tag{2.104}$$

We neglect second order terms and assume stationary currents (Khomenko et al. 2014b), thus, the terms from the second line disappear, and Eq. 2.104 becomes:

$$\mathbf{E} = -\mathbf{u}_c\times\mathbf{B} + \frac{1}{en_\mathrm{e}}\mathbf{J}\times\mathbf{B} - \frac{1}{en_\mathrm{e}}\nabla p_\mathrm{e} + \frac{\rho_\mathrm{e}}{en_\mathrm{e}}\Big(-(\mathbf{u}_\mathrm{n} - \mathbf{u}_c)\nu_\mathrm{in} + (\mathbf{u}_\mathrm{n} - \mathbf{u}_c + \frac{1}{en_\mathrm{e}}\mathbf{J})\nu_\mathrm{en} + \frac{1}{en_\mathrm{e}}\mathbf{J}\nu_\mathrm{ei}\Big).$$

This results in the **Ohm's law** for 2 fluids:

$$\mathbf{E} + \mathbf{u}_c\times\mathbf{B} = \eta_H\mathbf{J}\times\mathbf{B} - \eta_H\nabla p_e + \eta\mathbf{J} - \eta_D(\mathbf{u}_c - \mathbf{u}_n), \tag{2.105}$$

where:

$$\begin{aligned}\eta_H &= \frac{1}{en_\mathrm{e}},\\ \eta &= \frac{\rho_\mathrm{e}\,(\nu_\mathrm{en} + \nu_\mathrm{ei})}{(en_\mathrm{e})^2},\\ \eta_D &= \frac{\rho_\mathrm{e}(\nu_\mathrm{en} - \nu_\mathrm{in})}{en_\mathrm{e}}\,.\end{aligned} \tag{2.106}$$

Note that the different coefficients η_H, η and η_D have different units.

2.3.7 Manipulation of energy equation

The energy equation can be expressed in different forms. We can evolve the kinetic+internal energy (as seen before) or we can also consider the two following cases:

Evolution of internal energy

Taking into account that:

$$\frac{\partial(\frac{1}{2}\rho u^2)}{\partial t} = \mathbf{u}\cdot\frac{\partial(\rho\mathbf{u})}{\partial t} - \frac{1}{2}u^2\frac{\partial\rho}{\partial t}\,,$$

for both neutrals and charges, we obtain the internal energy equations:

$$\frac{\partial e_\mathrm{n}}{\partial t} + \nabla\cdot(\mathbf{u}_\mathrm{n} e_\mathrm{n} - K_\mathrm{n}\nabla T_\mathrm{n}) = -p_\mathrm{n}\nabla\cdot\mathbf{u}_\mathrm{n} + \hat{\tau}_\mathrm{n} : \nabla\mathbf{u}_\mathrm{n} + M'_\mathrm{n}\,,$$
$$\frac{\partial e_\mathrm{c}}{\partial t} + \nabla\cdot(\mathbf{u}_\mathrm{c} e_\mathrm{c} - K_\mathrm{c}\nabla T_\mathrm{c}) = -p_\mathrm{c}\nabla\cdot\mathbf{u}_\mathrm{c} + \mathbf{J}\cdot\mathbf{E}_\mathrm{diff} + \hat{\tau}_\mathrm{c} : \nabla\mathbf{u}_\mathrm{c} + M'_\mathrm{c}\,, \tag{2.107}$$

where $\mathbf{E}$ is split into ideal and diffusive contributions,

$$\mathbf{E} = \mathbf{E}_\mathrm{ideal} + \mathbf{E}_\mathrm{diff}\,,$$

with $\mathbf{E}_\mathrm{ideal} = -\mathbf{u}_\mathrm{c}\times\mathbf{B}$, and $\mathbf{E}_\mathrm{diff}$, the non-ideal contribution to the electric field, the terms at the right hand side of Eq. 2.105. It has been written like this in order to subtract from the charges energy equation in Eqs. 2.81 the work done by the Lorentz force $\mathbf{u}_c\cdot(\mathbf{J}\times\mathbf{B}) = \mathbf{J}\cdot\mathbf{E}_\mathrm{ideal}$.
The viscous dissipation terms, $\hat{\tau}_\mathrm{n} : \nabla\mathbf{u}_\mathrm{n}$ and $\hat{\tau}_\mathrm{c} : \nabla\mathbf{u}_\mathrm{c}$, which represent the kinetic energy transformed into heat by viscosity, taking into account the expression of the viscosity term τ_α shown in Eq. 2.53, have the following form:

$$\hat{\tau_\alpha} : \nabla\mathbf{u}_\alpha = \xi_\alpha \sum_{i<j}\left(\frac{\partial u_{\alpha i}}{\partial x_j} + \frac{\partial u_{\alpha j}}{\partial x_i}\right)^2. \tag{2.108}$$

The internal energy collisional terms are calculated as:

$$M'_\alpha = M_\alpha - \mathbf{u}_\alpha\cdot\mathbf{R}_\alpha + \frac{1}{2}u_\alpha^2 S_\alpha.$$

After doing the calculation we obtain:

$$M'_\mathrm{n} = \frac{1}{2}\Gamma^\mathrm{rec}\rho_\mathrm{c}(\mathbf{u}_\mathrm{c}-\mathbf{u}_\mathrm{n})^2 + \frac{1}{\gamma-1}\frac{k_\mathrm{B}}{m_\mathrm{n}}(\rho_\mathrm{c}T_\mathrm{c}\Gamma^\mathrm{rec} - \rho_\mathrm{n}T_\mathrm{n}\Gamma^\mathrm{ion}) + \frac{1}{2}(\mathbf{u}_\mathrm{c}-\mathbf{u}_\mathrm{n})^2\alpha\rho_\mathrm{n}\rho_\mathrm{c} +$$
$$\frac{1}{\gamma-1}\frac{k_\mathrm{B}}{m_\mathrm{n}}(T_\mathrm{c}-T_\mathrm{n})\alpha\rho_\mathrm{n}\rho_\mathrm{c} + \rho_\mathrm{e}(\nu_\mathrm{en}+\Gamma^\mathrm{rec})\left(\frac{1}{2}\left(\frac{\mathbf{J}}{en_\mathrm{e}}\right)^2 - \frac{1}{en_\mathrm{e}}\mathbf{J}\cdot(\mathbf{u}_\mathrm{c}-\mathbf{u}_\mathrm{n})\right), \tag{2.109}$$

$$M'_\mathrm{c} = \frac{1}{2}\Gamma^\mathrm{ion}\rho_\mathrm{n}(\mathbf{u}_\mathrm{c}-\mathbf{u}_\mathrm{n})^2 + \frac{1}{\gamma-1}\frac{k_\mathrm{B}}{m_\mathrm{n}}(\rho_\mathrm{n}T_\mathrm{n}\Gamma^\mathrm{ion} - \rho_\mathrm{c}T_\mathrm{c}\Gamma^\mathrm{rec}) + \frac{1}{2}(\mathbf{u}_\mathrm{c}-\mathbf{u}_\mathrm{n})^2\alpha\rho_\mathrm{n}\rho_\mathrm{c} +$$
$$\frac{1}{\gamma-1}\frac{k_\mathrm{B}}{m_\mathrm{n}}\Big(T_\mathrm{n}-T_\mathrm{c}\Big)\alpha\rho_\mathrm{n}\rho_\mathrm{c} - \frac{1}{2}\rho_\mathrm{e}\Big(\nu_\mathrm{en}+\Gamma^\mathrm{rec}\Big)\left(\frac{\mathbf{J}}{en_\mathrm{e}}\right)^2. \tag{2.110}$$

We observe that the second and the fourth terms, related to the thermal exchange are the same as in Eq. 2.96. However, the first and the third terms are different; they become non-negative quantities and thus contribute to dissipative heating. The neutrals and charges are heated because of recombination and ionization processes, respectively (the first term), and both species are heated at the same rate by elastic collisions (the third term, equal for neutrals and charges, also called "frictional heating"). The last term, related to $\mathbf{J}$ can be neglected, being proportional to electron density (as already mentioned for Eq. 2.96).

Evolution of total (internal+kinetic+magnetic) energy

In order to include magnetic energy into charges energy equation taking into account that:

$$\frac{\partial(\frac{B^2}{2\mu_0})}{\partial t} = -\frac{1}{\mu_0}\nabla\cdot(\mathbf{E}\times\mathbf{B}) - \mathbf{E}\cdot\mathbf{J}\,,$$

where we have neglected the term related to electric field in the electromagnetic energy: $\frac{\epsilon_0}{2}E^2$, consistent with neglecting the displacement current in Eq. 2.98, and we obtain the equation of total energy for charges:

$$\frac{\partial}{\partial t}\left(e_\mathrm{c} + \frac{1}{2}\rho_\mathrm{c}u_\mathrm{c}^2 + \frac{B^2}{2\mu_0}\right) + \nabla\cdot\left(\mathbf{u}_\mathrm{c}(e_\mathrm{c} + \frac{1}{2}\rho_\mathrm{c}u_\mathrm{c}^2) + \hat{\mathbf{p}}_\mathrm{c}\cdot\mathbf{u}_\mathrm{c} - K_\mathrm{c}\nabla T_\mathrm{c} + \frac{1}{\mu_0}\mathbf{E}\times\mathbf{B}\right) = \rho_\mathrm{c}\mathbf{u}_\mathrm{c}\cdot\mathbf{g} - M_\mathrm{n}.$$

The ideal part of Poynting flux is implemented like:

$$\frac{1}{\mu_0}\mathbf{E}_\mathrm{ideal}\times\mathbf{B} = 2\mathbf{u}_\mathrm{c}\frac{B^2}{2\mu_0} - \frac{1}{\mu_0}\mathbf{B}(\mathbf{u}_\mathrm{c}\cdot\mathbf{B}).$$

2.4 Summary

In this chapter we have described the equations implemented by our model. We have shown briefly how the multifluid equations are derived from Boltzmann equation and how they couple to the Maxwell's equations in order to obtain the two-fluid equations used in this work. When we consider processes on time scales larger than the periods of Langmuir plasma oscillations, and on space scales larger than the characteristic Debye length, charge neutrality is assumed. Boltzmann equation can be integrated in the velocity space, and the equation for each moment introduces a variable which represents the next moment of the Boltzmann equation. This serie has to be truncated, usually after calculating two moments, as in our case, and the higher moments, as the heat flux, should be approximated by other methods (Braginskii 1965; Hunana et al. 2019). Three fluid equations are obtained from Boltzmann equation, by taking the zeroth, the first and the second moment. Afterwards, two-fluid equations are obtained by combining the equations of ions and electrons, neglecting the electron inertia because of their much lower mass compared to the mass of the ions.

For the same reason that the electron mass is much smaller than ion mass, the velocity of the charged fluid is considered to be the velocity of the ions, and the velocity of the electrons is calculated from the definition of the current density **J**. This difference in the velocity of ions and electrons introduces some terms in the momentum and energy collisional terms, which contain the current density **J**, can be neglected as they are proportional to the electron density.

In order to obtain the two fluid model, used in this work, we have assumed pure hydrogen plasma (which also implies singly ionized), and that the temperatures of ions and electrons are equal. The current density **J**, and the equation for the evolution of the magnetic field are obtained from Maxwell's

equations. The electric field is calculated from the generalized Ohm's law, by assuming that the mass ratio for electrons and ions is very small, the currents are stationary, and neglecting second order terms. The difference from the single-fluid Ohm's law is that the ideal electric field is now calculated with the velocity of charges, and the ambipolar term disappears.

However, the main difference from the single-fluid equations is that, now, we have two continuity, momentum and energy equations, one of each for the two species, coupled by the collisional terms. The collisional terms are of the form νu, where u is the variable that evolve in time (density, momentum, energy), and we know from the stability analysis that, in order to solve $du/dt = \nu u$ numerically in an explicit implementation, the time-step should be at most $1/\nu$.

In the next chapter we present details of the numerical implementation.

3

Numerical implementation

This chapter presents the details of the numerical implementation of the newly developed two-fluid code, Mancha3D 2F. In this work we use as a base for our numerical developments the Mancha3D code, a single-fluid code, where the effects of partial ionization had been implemented through a generalized Ohm's law including Ohmic, ambipolar, Hall and Biermann battery terms. We have extended the code, so that it can solve the two-fluid equations in approximation of purely hydrogen plasma, where ions and electrons are evolved together through the same continuity, momentum and energy equations, and neutrals are evolved separately. The neutral and charges equations are coupled by collisions. We first describe some of the algorithms already existing in Mancha3D, that have been extended in Mancha3D 2F in section 3.1. Then, we present the semi-implicit implementation for the numerical treatment of the collisional terms.

3.1 Extensions in Mancha3D 2F of algorithms already existent in Mancha3D

The original Mancha3D code is described elsewhere (Khomenko & Collados 2006b; Felipe et al. 2010; Khomenko & Collados 2012; González-Morales et al. 2018). The code is fully 3D, written in Fortran 90, and parallelized with MPI; the output files are in HDF5 format. The units used in the equations are SI units. The variables are split into background and perturbation variables, keeping all non-linear terms. The code has the option to solve linear or non-linear equations, so that non-linear effects can be directly observed. The spatial discretization scheme is fourth-order accurate. The original temporal discretization scheme was a fourth-order explicit Runge-Kutta modified in the latest version of the code due to implementation of STS and HDS schemes (González-Morales et al. 2018). The Super Time Stepping (STS) technique overcomes the small CFL (Courant et al. 1967) time-step imposed on parabolic terms, such as the ambipolar term in the induction equation. However, when the Hall term dominates in the induction equation, it cannot be implemented using the same technique, because it is unstable. It has been implemented using the Hall Diffusion Scheme (HDS). Both schemes

can be combined using the Strang operator splitting. The two-fluid implementation required further modification of the explicit Runge-Kutta integration. We present now the equations solved in the two approximations in subsection 3.1.1, and existing numerical techniques already implemented in Mancha3D that have been extended in Mancha3D 2F: hyperdiffusivity in subsection 3.1.2, filtering in subsection 3.1.3, and Perfect Mathching Layer (PML) in subsection 3.1.4.

3.1.1 Equations solved in Mancha3D and Mancha3D 2F

We present below the equations that are solved in Mancha3D and Mancha3D 2F, including the hyperdiffusive terms, written explicitly, which appear with the superscript "hyp".

Single-fluid equations

$$\begin{aligned}
&\frac{\partial \rho}{\partial t} + \nabla \cdot \left(\rho \mathbf{u} + \mathbf{m}^{\mathrm{hyp}}\right) = 0,\\
&\frac{\partial (\rho \mathbf{u})}{\partial t} + \nabla \cdot (\rho \mathbf{u}\mathbf{u} + p\mathbb{I} - \hat{\tau}^{\mathrm{hyp}}) = [\mathbf{J} \times \mathbf{B}] + \rho \mathbf{g},\\
&\frac{\partial}{\partial t}\left(e + \frac{1}{2}\rho u^2\right) + \nabla \cdot \left(\mathbf{u}(e + \frac{1}{2}\rho u^2) + (p\mathbb{I} - \hat{\tau}^{\mathrm{hyp}}) \cdot \mathbf{u} + \mathbf{q}_c{}^{\mathrm{hyp}}\right) = \rho \mathbf{u} \cdot \mathbf{g} + \mathbf{J} \cdot (\mathbf{E} + \mathbf{E}^{\mathrm{hyp}}),\\
&\frac{\partial \mathbf{B}}{\partial t} = -\nabla \times (\mathbf{E} + \mathbf{E}^{\mathrm{hyp}})\,.
\end{aligned} \tag{3.1}$$

The current density $\mathbf{J}$ is calculated from the Maxwell equation:

$$\mathbf{J} = \frac{1}{\mu_0} \nabla \times \mathbf{B}\,. \tag{3.2}$$

The electric field $\mathbf{E}$ is calculated from Ohm's law which contains the terms of partial ionization:

$$\begin{aligned}
\mathbf{E} + \mathbf{u} \times \mathbf{B} &= \eta_H \mathbf{J} \times \mathbf{B} - \eta_H \nabla p_{\mathrm{e}} + \eta \mathbf{J} - \eta_A \frac{[(\mathbf{J} \times \mathbf{B}) \times \mathbf{B}]}{|B|^2},\\
\eta_A = \frac{\xi_{\mathrm{n}}^2 |B|^2}{\rho_{\mathrm{n}} (\nu_{\mathrm{ni}} + \nu_{\mathrm{ne}})}, &\quad \eta_H = \frac{1}{e n_{\mathrm{e}}}, \quad \eta = \frac{\rho_{\mathrm{e}} (\nu_{\mathrm{en}} + \nu_{\mathrm{ei}})}{(e n_{\mathrm{e}})^2},
\end{aligned} \tag{3.3}$$

where ξ_n is the ionization fraction. Note that the coefficients η_A, η_H and η which appear in the above Eq. 3.3 have different units. The four terms that appear at the right hand side of the above equation correspond to physical terms and they are called from left to right: Hall term, Biermann battery term, Ohmic term, and ambipolar term. We can observe that the ambipolar term is proportional to $\mathbf{J}_\perp$, the component of $\mathbf{J}$ perpendicular to the magnetic field. The current perpendicular to the magnetic field from the Ohmic term and the ambipolar terms can be combined as (Leake & Arber 2006; Khomenko et al. 2014b):

$$\eta \mathbf{J} - \eta_A \frac{[(\mathbf{J} \times \mathbf{B}) \times \mathbf{B}]}{|B|^2} = \eta \mathbf{J}_\parallel + \eta_C \mathbf{J}_\perp\,, \tag{3.4}$$

where $\mathbf{J}_\parallel$ is the component of $\mathbf{J}$ parallel to the magnetic field, and η_C is called Cowling diffusivity. The number of electrons, ions and neutrals are calculated from precomputed tables which also contain the information needed to compute the equation of state (Vitas & Khomenko 2015).

Two-fluid equations

The equations implemented in MANCHA3D 2F, presented in Chapter 2, are summarized below:

$$
\begin{aligned}
&\frac{\partial \rho_\mathrm{n}}{\partial t} + \nabla \cdot \left(\rho_\mathrm{n} \mathbf{u}_\mathrm{n} + \mathbf{m}_\mathrm{n}^\mathrm{hyp} \right) = S_\mathrm{n}, \\
&\frac{\partial \rho_\mathrm{c}}{\partial t} + \nabla \cdot \left(\rho_\mathrm{c} \mathbf{u}_\mathrm{c} + \mathbf{m}_\mathrm{c}^\mathrm{hyp} \right) = -S_\mathrm{n}, \\
&\frac{\partial (\rho_\mathrm{n} \mathbf{u}_\mathrm{n})}{\partial t} + \nabla \cdot (\rho_\mathrm{n} \mathbf{u}_\mathrm{n} \mathbf{u}_\mathrm{n} + p_\mathrm{n} \mathbb{I} - \hat{\tau}_\mathrm{n} - \hat{\tau}_\mathrm{n}^\mathrm{hyp}) = \rho_\mathrm{n} \mathbf{g} + \mathbf{R}_\mathrm{n}, \\
&\frac{\partial (\rho_\mathrm{c} \mathbf{u}_\mathrm{c})}{\partial t} + \nabla \cdot (\rho_\mathrm{c} \mathbf{u}_\mathrm{c} \mathbf{u}_\mathrm{c} + p_\mathrm{c} \mathbb{I} - \hat{\tau}_\mathrm{c} - \hat{\tau}_\mathrm{c}^\mathrm{hyp}) = [\mathbf{J} \times \mathbf{B}] + \rho_\mathrm{c} \mathbf{g} - \mathbf{R}_\mathrm{n}, \\
&\frac{\partial}{\partial t} \left(e_\mathrm{n} + \frac{1}{2} \rho_\mathrm{n} u_\mathrm{n}^2 \right) + \nabla \cdot \left(\mathbf{u}_\mathrm{n} (e_\mathrm{n} + \frac{1}{2} \rho_\mathrm{n} u_\mathrm{n}^2) + (p_\mathrm{n} \mathbb{I} - \hat{\tau}_\mathrm{n} - \hat{\tau}_\mathrm{n}^\mathrm{hyp}) \cdot \mathbf{u}_\mathrm{n} + \mathbf{q}_\mathrm{n} + \mathbf{q}_\mathrm{n}{}^\mathrm{hyp} \right) = \rho_\mathrm{n} \mathbf{u}_\mathrm{n} \cdot \mathbf{g} + M_\mathrm{n}, \\
&\frac{\partial}{\partial t} \left(e_\mathrm{c} + \frac{1}{2} \rho_\mathrm{c} u_\mathrm{c}^2 \right) + \nabla \cdot \left(\mathbf{u}_\mathrm{c} (e_\mathrm{c} + \frac{1}{2} \rho_\mathrm{c} u_\mathrm{c}^2) + (p_\mathrm{c} \mathbb{I} - \hat{\tau}_\mathrm{c} - \hat{\tau}_\mathrm{c}^\mathrm{hyp}) \cdot \mathbf{u}_\mathrm{c} + \mathbf{q}_\mathrm{c} + \mathbf{q}_\mathrm{c}{}^\mathrm{hyp} \right) = \rho_\mathrm{c} \mathbf{u}_\mathrm{c} \cdot \mathbf{g} + \mathbf{J} \cdot (\mathbf{E} + \mathbf{E}^\mathrm{hyp}) - M_\mathrm{n}, \\
&\frac{\partial \mathbf{B}}{\partial t} = -\nabla \times (\mathbf{E} + \mathbf{E}^\mathrm{hyp}),
\end{aligned}
\tag{3.5}
$$

with the collisional terms:

$$
\begin{aligned}
&S_\mathrm{n} = \rho_\mathrm{c} \Gamma^\mathrm{rec} - \rho_\mathrm{n} \Gamma^\mathrm{ion}, \\
&\mathbf{R}_\mathrm{n} = \rho_\mathrm{c} \mathbf{u}_\mathrm{c} \Gamma^\mathrm{rec} - \rho_\mathrm{n} \mathbf{u}_\mathrm{n} \Gamma^\mathrm{ion} + \alpha \rho_\mathrm{n} \rho_\mathrm{c} (\mathbf{u}_\mathrm{c} - \mathbf{u}_\mathrm{n}), \\
&M_\mathrm{n} = \frac{1}{2} \Gamma^\mathrm{rec} \rho_\mathrm{c} u_\mathrm{c}^2 - \frac{1}{2} \rho_\mathrm{n} u_\mathrm{n}^2 \Gamma^\mathrm{ion} + \frac{1}{2} \alpha \rho_\mathrm{n} \rho_\mathrm{c} ({u_\mathrm{c}}^2 - {u_\mathrm{n}}^2) + \frac{1}{\gamma - 1} \frac{k_\mathrm{B}}{m_\mathrm{n}} \left[\left(\rho_\mathrm{c} T_\mathrm{c} \Gamma^\mathrm{rec} - \rho_\mathrm{n} T_\mathrm{n} \Gamma^\mathrm{ion} \right) + \alpha \rho_\mathrm{n} \rho_\mathrm{c} (T_\mathrm{c} - T_\mathrm{n}) \right].
\end{aligned}
\tag{3.6}
$$

Generally, for the species α, the physical viscosity and thermal conduction are defined as

$$
\tau_{\alpha ij} = \xi_\alpha \left(\frac{\partial u_{\alpha i}}{\partial x_j} + \frac{\partial u_{\alpha j}}{\partial x_i} \right), \quad \xi_\alpha = \frac{n_\alpha k_\mathrm{B} T_\alpha}{\nu_{\alpha\alpha}} \forall i, j \in \{1, 2, 3\}, \tag{3.7}
$$

$$
\mathbf{q}_\alpha = -K_\alpha \nabla T_\alpha, \quad K_\alpha = \frac{4 n_\alpha k_\mathrm{B} T_\alpha}{m_\alpha \nu_{\alpha\alpha}}, \tag{3.8}
$$

when we have considered collisions inside same species for the viscosity and thermal conductivity coefficients, see discussion from previous chapter in subsection 2.1.4.

The collisional parameter α has been defined in Eq. 2.88. The current density is calculated as in the single-fluid version, Eq. 3.2 above, and the Ohm's law for two-fluid becomes:

$$\mathbf{E}+\mathbf{u}_\mathrm{c}\times\mathbf{B}=\eta_H\mathbf{J}\times\mathbf{B}-\eta_H\nabla p_\mathrm{e}+\eta\mathbf{J}-\eta_D(\mathbf{u}_\mathrm{c}-\mathbf{u}_n),$$
$$\eta_D=\frac{\rho_\mathrm{e}(\nu_\mathrm{en}-\nu_\mathrm{in})}{en_\mathrm{e}}\,. \tag{3.9}$$

η_H, and η are calculated as in the singe-fluid assumption, Eq. 3.3. Note that the coefficients η_A, η_H, η and η_D which appear in the above Eq. 3.9 have different units. The fourth term at the right-hand side of the above equation, also exists in the single-fluid approximation (see last term of Eq. 128 from Khomenko et al. 2014b), where it is neglected. However, it is kept in the two-fluid assumption.

In Mancha3D and Mancha3D 2F we have the possibility to evolve the equation of internal energy only, internal+kinetic energy or total (internal+kinetic+magnetic) energy. As the collisional terms are different when we evolve only internal energy, we summarize below the internal energy equations and the collisional terms.

$$\frac{\partial e_\mathrm{n}}{\partial t}+\nabla\cdot(\mathbf{u}_\mathrm{n}e_\mathrm{n}+\mathbf{q}_\mathrm{n}+\mathbf{q}_\mathrm{n}{}^\mathrm{hyp})=-p_\mathrm{n}\nabla\cdot\mathbf{u}_\mathrm{n}+\hat{\tau}_\mathrm{n}:\nabla\mathbf{u}_\mathrm{n}+\hat{\tau}_\mathrm{n}^\mathrm{hyp}:\nabla\mathbf{u}_\mathrm{n}+M_\mathrm{n}'\,,$$
$$\frac{\partial e_\mathrm{c}}{\partial t}+\nabla\cdot(\mathbf{u}_\mathrm{c}e_\mathrm{c}+\mathbf{q}_\mathrm{c}+\mathbf{q}_\mathrm{c}{}^\mathrm{hyp})=-p_\mathrm{c}\nabla\cdot\mathbf{u}_\mathrm{c}+\mathbf{J}\cdot(\mathbf{E}_\mathrm{diff}+\mathbf{E}^\mathrm{hyp})+\hat{\tau}_\mathrm{c}:\nabla\mathbf{u}_\mathrm{c}+\hat{\tau}_\mathrm{c}^\mathrm{hyp}:\nabla\mathbf{u}_\mathrm{c}+M_\mathrm{c}'\,, \tag{3.10}$$

where:

$$\mathbf{E}_\mathrm{diff}=\mathbf{E}+\mathbf{u}_\mathrm{c}\times\mathbf{B}\,. \tag{3.11}$$

The collisional terms are:

$$M_\mathrm{n}'=\frac{1}{2}\Gamma^\mathrm{rec}\rho_\mathrm{c}(\mathbf{u}_\mathrm{c}-\mathbf{u}_\mathrm{n})^2+\frac{1}{2}(\mathbf{u}_\mathrm{c}-\mathbf{u}_\mathrm{n})^2\alpha\rho_\mathrm{n}\rho_\mathrm{c}+\frac{1}{\gamma-1}\frac{k_\mathrm{B}}{m_\mathrm{n}}\left[(T_\mathrm{c}-T_\mathrm{n})\,\alpha\rho_\mathrm{n}\rho_\mathrm{c}+\left(\rho_\mathrm{c}T_\mathrm{c}\Gamma^\mathrm{rec}-\rho_\mathrm{n}T_\mathrm{n}\Gamma^\mathrm{ion}\right)\right]\,,$$
$$M_\mathrm{c}'=\frac{1}{2}\Gamma^\mathrm{ion}\rho_\mathrm{n}(\mathbf{u}_\mathrm{c}-\mathbf{u}_\mathrm{n})^2+\frac{1}{2}(\mathbf{u}_\mathrm{c}-\mathbf{u}_\mathrm{n})^2\alpha\rho_\mathrm{n}\rho_\mathrm{c}+\frac{1}{\gamma-1}\frac{k_\mathrm{B}}{m_\mathrm{n}}\left[(T_\mathrm{n}-T_\mathrm{c})\,\alpha\rho_\mathrm{n}\rho_\mathrm{c}+\left(\rho_\mathrm{n}T_\mathrm{n}\Gamma^\mathrm{ion}-\rho_\mathrm{c}T_\mathrm{c}\Gamma^\mathrm{rec}\right)\right]\,. \tag{3.12}$$

We describe next some numerical algorithms implemented in Mancha3D, that have been extended to Mancha3D 2F.

3.1.2 Hyperdiffusivity

The viscous forces and the Ohmic dissipation tend to eliminate high-frequency oscillations. However, collisional viscosity ($\xi_\mathrm{c,n}$; Eq. 3.7) and Ohmic (η; Eqs. 3.3, 3.9) coefficients for the parameters of the solar atmosphere are too small to effectively damp non-resolved variations of different parameters at the grid cell size. Therefore, for numerical stability, these coefficients have corresponding numerical analogs referred to as hyperdiffusive coefficients. They appeared with the superscript "hyp" in the above equations Eqs. 3.1, 3.5.

The implementation already existent in MANCHA3D code has been extended for MANCHA3D 2F, the latter being described next. The hyperdiffusive terms can be defined generally, in a multi-fluid approach, for species α. In particular, for the two-fluid model α represents neutral or charged species. The hyperdiffusive viscosity resembles the physical viscosity term defined in Eq. 3.7,

$$\tau_{\alpha_{ij}}^{\text{hyp}} = \frac{1}{2}\rho_\alpha \left(\nu_{x_j}(u_{\alpha i}) \frac{\partial u_{\alpha i}}{\partial \mathrm{x_j}} + \nu_{x_i}(u_{\alpha j}) \frac{\partial u_{\alpha j}}{\partial x_i} \right) \forall i,j \in \{1,2,3\}\,. \tag{3.13}$$

The hyperdiffusive term in the energy equation has the form of the physical heat conduction term, defined in Eq. 3.8,

$$q_{\alpha_i}^{\text{hyp}} = -\rho_\alpha \nu_{x_i}(e_\alpha) \frac{\partial T_\alpha}{\partial x_i}, \forall i \in \{1,2,3\}\,. \tag{3.14}$$

The magnetic hyperdiffusivity defined below,

$$\begin{aligned} E_x^{\text{hyp}} &= \nu_y(B_z)\frac{\partial B_z}{\partial y} - \nu_z(B_y)\frac{\partial B_y}{\partial z}\,, \\ E_y^{\text{hyp}} &= \nu_z(B_x)\frac{\partial B_x}{\partial z} - \nu_x(B_z)\frac{\partial B_z}{\partial x}\,, \\ E_z^{\text{hyp}} &= \nu_x(B_y)\frac{\partial B_y}{\partial x} - \nu_y(B_x)\frac{\partial B_x}{\partial y}\,, \end{aligned} \tag{3.15}$$

is similar to physical Ohmic conductivity term ($\eta\mathbf{J}$), as in the Ohm law in the single-fluid assumption 3.3 and the two-fluid assumption 3.9.
The following term, the hyperdiffusivity of the density does not have a physical corresponding term,

$$m_{\alpha_i}^{\text{hyp}} = -\nu_{x_i}(\rho_\alpha) \frac{\partial \rho_\alpha}{\partial x_i}, \forall i \in \{1,2,3\}\,. \tag{3.16}$$

$i \in \{1,2,3\}$ are for the three spatial dimensions, and α indicates the species (charge or neutral in the two-fluid model).

Calculation of hyperdiffusive coefficients

The amplitude of the hyperdiffusive coefficients is a complex function of space coordinates and of gradients of the corresponding variables (for details see Vögler et al. (2005); Felipe et al. (2010)). The method of calculation of these anisotropic coefficients is summarized below.

They contain three terms: a shock capturing term, indicated in the following equations by the subindex "$_{\text{sh}}$", a hyperdiffusive term indicated by the subindex "$_{\text{var}}$", and a constant diffusivity term, indicated by "$_{\text{ct}}$":

$$\begin{aligned} \nu_{x_i}(r) = c_{\text{sh}}\nu_{\text{sh}}(r)\mathrm{dx}_i^2 + c_{\text{var}}(r)v_{\text{var}}(r)\mathrm{dx}_i\mathrm{h}_{x_i}(r) + c_{\text{ct}}(r)v_{\text{ct}}(r)\mathrm{dx}_i\mathbf{C}, \\ \forall i \in \{1,2,3\}, r \in \{\rho_n, \rho_c, u_{nx_i}, u_{cx_i}, e_n, e_c, B_{x_i}\}\,, \end{aligned} \tag{3.17}$$

where $c_{\rm sh}$, $c_{\rm var}(r)$, and $c_{\rm ct}(r)$ are coefficients with values chosen between 0 and 1, and dx_i is the grid cell size in the x_i direction, $\mathbf{C}$ is an input matrix with the dimensions of the physical domain with values that should be between 0 and 1, representing the spatial distribution of the artificial constant diffusivity. Below Eqs. 3.18, 3.21, and 3.22 show how the quantities $\nu_{\rm sh}(r)$, $v_{\rm var}(r)$, and $v_{\rm ct}(r)$, respectively, are defined in MANCHA3D 2F, $\forall i \in \{1,2,3\}$:

$$\begin{aligned}\nu_{\rm sh}(\rho_n) = \nu_{\rm sh}(u_{nx_i}) = \nu_{\rm sh}(e_n) = \mathrm{conv}(\mathbf{u}_n),\\ \nu_{\rm sh}(\rho_c) = \nu_{\rm sh}(u_{cx_i}) = \nu_{\rm sh}(e_c) = \mathrm{conv}(\mathbf{u}_c),\\ \nu_{\rm sh}(B_{x_i}) = \mathrm{conv}(\mathbf{u}_{c_{\perp\mathbf{B}}})\,,\end{aligned} \tag{3.18}$$

where $\mathbf{u}_{c_{\perp\mathbf{B}}}$ is the component of $\mathbf{u_c}$ perpendicular to $\mathbf{B}$:

$$\mathbf{u_{c\perp B}} = \mathbf{u_c} - (\mathbf{u_c}\cdot\mathbf{B})\mathbf{B}\,, \tag{3.19}$$

and,

$$\mathrm{conv}(\mathbf{u}) = \begin{cases} -\nabla\cdot\mathbf{u}, & \text{if } \nabla\cdot\mathbf{u} < 0\\ 0, & \text{otherwise}\,.\end{cases} \tag{3.20}$$

$$\begin{aligned}v_{\rm var}(\rho_{\rm n}) = v_{\rm var}(u_{{\rm n}x_i}) = v_{\rm var}(e_{\rm n}) = \mid \mathbf{u}_{\rm n} \mid + c_{\rm n},\\ v_{\rm var}(\rho_{\rm c}) = v_{\rm var}(u_{{\rm c}x_i}) = v_{\rm var}(e_{\rm c}) = v_{\rm var}(B_{x_i}) = \mid \mathbf{u}_{\rm c} \mid + c_{\rm c} + v_{\rm A},\end{aligned} \tag{3.21}$$

$$\begin{aligned}v_{\rm ct}(\rho_{\rm n}) = v_{\rm ct}(u_{{\rm n}x_i}) = v_{\rm ct}(e_{\rm n}) = c_{\rm n},\\ v_{\rm ct}(\rho_{\rm c}) = v_{\rm ct}(u_{{\rm c}x_i}) = v_{\rm ct}(e_{\rm c}) = v_{\rm ct}(B_{x_i}) = c_{\rm c} + v_{\rm A}\,.\end{aligned} \tag{3.22}$$

$c_{\rm n}$, $c_{\rm c}$, and $v_{\rm A}$ are the neutral and charge sound speed, and the Alfvén velocity, respectively. We can see that $\mathrm{conv}(\mathbf{u})$ is always positive. Its values are limited in the upper part by a value defined in the code. The coefficients $\nu_{\rm sh}(r)$ are averaged in the three directions over five points.
The function $\mathrm{h}_{x_i}(r)$ at the point n in the direction x_i is calculated as:

$$\mathrm{h}_{x_i}(r)(n) = \frac{\max\limits_{k=n-1,n,n+1} \mid 3(r(k+1)-r(k)) - (r(k+2)-r(k-1)) \mid}{\max\limits_{k=n-1,n,n+1} \mid r(k+1)-r(k) \mid} \tag{3.23}$$

$\mathrm{h}_{x_i}(r)$ is limited to values between 0 and 1. Finally, it is averaged in the direction x_i over five points.

3.1.3 Filtering

Since high numerical diffusion is not always desirable, an additional filtering of small wavelengths following Parchevsky & Kosovichev (2007) is implemented in MANCHA3D . This is a low pass filtering

method which attenuates high frequencies in the Fourier space. Having $u(x)$ one of the quantities that evolve in time, as a function of one of the spatial directions x before the filtering, and $u'(x)$ the quantity after the filtering, and using the $\mathscr{F}$ and $\mathscr{F}^{-1}$ operators in order to indicate the direct and inverse Fourier transforms, respectively, we have:

$$\mathscr{F}[u'](k) = \mathscr{F}[u](k) - \mathscr{F}[u](k) \cdot h(k)\,, \tag{3.24}$$

where $h(k)$ is a filter function, chosen to reduce high frequencies. In order to obtain the filtered quantity $u'(x)$, applying $\mathscr{F}^{-1}$ to Eq. 3.24 we have,

$$u'(x) = u(x) - u(x) * \mathscr{F}^{-1}[h](x)\,, \tag{3.25}$$

where "$*$" indicates the convolution of the functions. The coefficients of the direct and inverse Fourier transform used are defined below[1]:

$$\begin{aligned} \mathscr{F}[u](k) &= \int_{-\infty}^{\infty} u(x)\exp(ikx)dx \\ \mathscr{F}^{-1}[h](x) &= \sqrt{\frac{1}{(2\pi)^2}} \int_{-\infty}^{\infty} h(k)\exp(-ikx)dk\,. \end{aligned} \tag{3.26}$$

The filtering function used by Parchevsky & Kosovichev (2007) is:

$$h(k) = \sin^6\Big(k\frac{\Delta x}{2}\Big)\,, \tag{3.27}$$

which has the following inverse Fourier transform:

$$\begin{aligned} \mathscr{F}^{-1}[h](x) = &-\frac{1}{64}\delta(x+3\Delta x) + \frac{3}{32}\delta(x+2\Delta x) - \frac{15}{64}\delta(x+\Delta x) + \frac{5}{16}\delta(x) \\ &-\frac{15}{64}\delta(x-\Delta x) + \frac{3}{32}\delta(x-2\Delta x) - \frac{1}{64}\delta(x-3\Delta x) \end{aligned} \tag{3.28}$$

where δ is the Dirac delta function. The filtering is applied for the three space directions successively.

3.1.4 PML

In order to avoid reflections at the boundaries, Mancha3D uses the PML technique (Felipe et al. 2010). For each dimension, a layer of a defined width can be added at each of the boundaries, in which the variables are damped, separately for each dimension. This is done, by solving the split 3D equations for each dimension. For example, the following equation which evolves the variable u:

$$\frac{\partial u}{\partial t} + \nabla \cdot \mathbf{F}(u) = S(u)\,, \tag{3.29}$$

[1]Generally, the coefficients of the Fourier transform and the inverse Fourier transform can be defined using two arbitrary parameters (see references at `http://mathworld.wolfram.com/FourierTransform.html`; related to FourierParameters in Mathematica software).

is solved in the code:

$$\frac{\partial u_x}{\partial t} + \frac{\partial F_x}{\partial x} = S_x(u) - \sigma_x u_x \,,$$
$$\frac{\partial u_y}{\partial t} + \frac{\partial F_y}{\partial y} = S_y(u) - \sigma_y u_y \,,$$
$$\frac{\partial u_z}{\partial t} + \frac{\partial F_z}{\partial z} = S_z(u) - \sigma_z u_z \,, \tag{3.30}$$

with $S_x + S_y + S_z = S$. σ_x, σ_y, and σ_z are zero in the physical domain and non-zero in PML layers. However, σ_x, σ_y, and σ_z are non-zero only for PML layers which are defined for the dimension x, y, and z, respectively. σ_x, σ_y, and σ_z are related to the damping of the variables and depend only on the dimension for which they are defined, with values increasing towards the boundaries. Initially, u_x, u_y, and u_z in the PML are obtained from the value of the whole variable, u at that point divided by the number of all the PML layers that point belongs to. At each time-step the solution is obtained by the sum of the solutions obtained for each dimension:

$$u = u_x + u_y + u_z \,. \tag{3.31}$$

3.2 Implementation of the collisional terms

Since the solar atmosphere is strongly gravitationally stratified, the collisional frequencies change by orders of magnitude from the photosphere to the chromosphere. In the deep layers, collisional terms are typically very large and dominate over the hydrodynamical timescales. In the chromosphere this situation may change, since collisional frequencies become significantly smaller. Therefore, the numerical scheme of our two-fluid numerical code has to be able to handle large variations in collision frequencies. In the case of dominant collisional terms the equations become stiff and therefore an explicit integration scheme is unstable. This is because the collisional terms that appear in the equations of continuity, momentum, and energy are proportional to the variables that evolve in time, and the time step should be at most the inverse of the collision frequency in order to ensure stability in an explicit scheme. This imposes very small time steps when the collisions are dominant. A suitable alternative is to use semi-implicit schemes similar to that described by Tóth et al. (2012) as a point implicit scheme.

Our system of equations, Eqs. 3.5 can be schematically written as follows.

$$\frac{\partial \mathbf{U}}{\partial t} = \mathbf{R}(\mathbf{U}) \,, \tag{3.32}$$

where $\mathbf{U}$ is the vector of variables,

$$\mathbf{U} = \{\rho_n, \rho_c, \rho_n \mathbf{u}_n, \rho_c \mathbf{u}_c, e_n + \frac{1}{2}\rho_n u_n^2, e_c + \frac{1}{2}\rho_c u_c^2, \mathbf{B}\}, \tag{3.33}$$

and $\mathbf{R}(\mathbf{U})$ is the sum of fluxes and collisional terms.

In order to evolve this system of equations in time: we split $\mathbf{R}$ into an explicit operator $\mathbf{E}$ and an implicit operator $\mathbf{P}$,

$$\mathbf{R}(\mathbf{U}) = \mathbf{E}(\mathbf{U}) + \mathbf{P}(\mathbf{U})\,. \tag{3.34}$$

The explicit operator $\mathbf{E}(\mathbf{U})$ contains fluxes, while the implicit operator contains the collisional terms, Eqs. 3.6. The code solves three pairs of coupled equations during the implicit update, with $\mathbf{U}$ being in the three cases a vector with two components, as defined above by Eq. 3.33, $\mathbf{U} = \{\{\rho_n, \rho_c\}, \{\rho_n \mathbf{u}_n, \rho_c \mathbf{u}_c\}, \{e_n + \frac{1}{2}\rho_n u_n^2, e_c + \frac{1}{2}\rho_c u_c^2\}\}$, meaning that all of the collisional terms, namely S_n, $\mathbf{R}_n$, and M_n defined in Eqs. 3.6, can be treated in the same way. We note however that depending on the magnitude of the collisional terms S_n in the continuity equations, it might not be worth treating them implicitly. In such cases we add these terms into the explicit operator $\mathbf{E}(\mathbf{U})$.

With $\mathbf{U}^*$ being the solution after applying the explicit update,

$$\mathbf{U}^* = \mathbf{U}^n + \Delta t \mathbf{E}, \tag{3.35}$$

we apply the implicit update using the following discretization.

$$\mathbf{U}^{n+1} = \mathbf{U}^* + (1-\beta)\Delta t \mathbf{P}(\mathbf{U}^*) + \beta \Delta t \mathbf{P}(\mathbf{U}^{n+1})\,, \tag{3.36}$$

which is a generalization of Crank-Nicolson method for arbitrary $\beta \in [0,1]$. Linearizing $\mathbf{P}(\mathbf{U}^{n+1})$ around "*", it can be written as:

$$\mathbf{P}(\mathbf{U}^{n+1}) = \mathbf{P}(\mathbf{U}^*) + \frac{\partial \mathbf{P}}{\partial \mathbf{U}}(\mathbf{U}^*) \cdot \left(\mathbf{U}^{n+1} - \mathbf{U}^*\right)\,, \tag{3.37}$$

and Eq. 3.36 becomes:

$$\mathbf{U}^{n+1} = \mathbf{U}^* + (1-\beta)\Delta t \mathbf{P}^* + \beta \Delta t \left[\mathbf{P}^* + \hat{\mathbf{J}}^* \cdot \left(\mathbf{U}^{n+1} - \mathbf{U}^*\right)\right]\,, \tag{3.38}$$

where we have used the notation of the jacobian:

$$\hat{\mathbf{J}} = \frac{\partial \mathbf{P}}{\partial \mathbf{U}}\,, \tag{3.39}$$

and $\mathbf{P}^* = \mathbf{P}(\mathbf{U}^*)$.
One of the assumptions of the linearization of the implicit term is that the jacobian vary on timescales much larger than the variables and is assumed constant during the whole update. For this reason we will omit the superscript "*" for the jacobian $\hat{\mathbf{J}}$.
Equation 3.38 can be further simplified to:

$$\mathbf{U}^{n+1} = \mathbf{U}^* + \Delta t \mathbf{P}^* + \beta \Delta t \hat{\mathbf{J}} \cdot \left(\mathbf{U}^{n+1} - \mathbf{U}^*\right)\,, \tag{3.40}$$

and has the following formal solution:

$$\mathbf{U}^{n+1} = \mathbf{U}^* + \Delta t \left(\mathbb{I} - \beta \Delta t \hat{\mathbf{J}}\right)^{-1} \cdot \mathbf{P}^*\,. \tag{3.41}$$

In our case, $\mathbf{U}$ and $\mathbf{P}$ are vectors with 2 elements, the jacobian $\hat{\mathbf{J}}$ is a 2×2 matrix, and the elements of the second row of the jacobian are the elements of the first row with reversed sign ($J_{21} = -J_{11}, J_{22} = -J_{12}$), so the inversion can be calculated analytically. The formal solution Eq. 3.41 can be written explicitly as:

$$\mathbf{U}^{n+1} = \mathbf{U}^* + \Delta t \frac{(1-\beta)\mathbf{P}^n + \beta \mathbf{P}^*}{1 + \beta \Delta t (J_{12} - J_{11})} \,. \tag{3.42}$$

The explicit expressions of the jacobian for the equations considered are described later, in the section 5.1. The influence of the value of β which varies between 0 (fully explicit) and 1 (fully implicit), on the final solution will be discussed in Chapter 4. We show next that this scheme with two sub-steps and using $\beta = 1$ in the first sub-step and $\beta = 1/2$ in the second sub-step is almost equivalent to Toth's original formulation.

3.3 Toth's original formulation

Tóth et al. (2012) describes a two-steps Runge Kutta explicit scheme, where the implicit part is added in each sub-step linearizing around "n" and using $\beta = 1$ in the first sub-step and $\beta = \frac{1}{2}$ in the second. The two sub-steps can be summarized like:

$$\begin{aligned} \mathbf{U}^{n+\frac{1}{2}} &= \mathbf{U}^n + \frac{\Delta t}{2}\mathbf{E}^n + \frac{\Delta t}{2}\mathbf{P}^n + \frac{\Delta t}{2}\frac{\partial \mathbf{P}^n}{\partial \mathbf{U}} \cdot \left(\mathbf{U}^{n+\frac{1}{2}} - \mathbf{U}^n\right) \,, \\ \mathbf{U}^{n+1} &= \mathbf{U}^n + \Delta t \mathbf{E}^{n+\frac{1}{2}} + \Delta t \mathbf{P}^n + \frac{\Delta t}{2}\frac{\partial \mathbf{P}^n}{\partial \mathbf{U}} \left(\mathbf{U}^{n+1} - \mathbf{U}^n\right) \,. \end{aligned} \tag{3.43}$$

This scheme is second order accurate. The explanation is presented below.
The term which appears in the second sub-step, $\mathbf{E}^{n+\frac{1}{2}}$, can be written:

$$\mathbf{E}^{n+\frac{1}{2}} = \mathbf{E}(\mathbf{U}^{n+\frac{1}{2}}) = \mathbf{E}\left(\mathbf{U}^n + \frac{\Delta t}{2}\mathbf{R}^n + \frac{\Delta t}{2}\frac{\partial \mathbf{P}^n}{\partial \mathbf{U}} \cdot \left(\mathbf{U}^{n+\frac{1}{2}} - \mathbf{U}^n\right)\right) \,. \tag{3.44}$$

We write the above expression as Taylor expansion and we retain only the first term, and taking into account that $\mathbf{U}^{n+\frac{1}{2}}$ can also be written in Taylor expansion,

$$\mathbf{U}^{n+\frac{1}{2}} = \mathbf{U}^n + \frac{\Delta t}{2}\frac{\partial \mathbf{U}^n}{\partial t} + \mathcal{O}(\Delta t^2) \,,$$

the expression for $\mathbf{E}^{n+\frac{1}{2}}$, Eq. 3.44 becomes:

$$\mathbf{E}^{n+\frac{1}{2}} = \mathbf{E}(\mathbf{U}^n) + \frac{\Delta t}{2}\frac{\partial \mathbf{E}^n}{\partial \mathbf{U}}\frac{\partial \mathbf{U}^n}{\partial t} + \frac{\Delta t}{2}\frac{\partial \mathbf{P}^n}{\partial \mathbf{U}} \cdot \left(\frac{\Delta t}{2}\frac{\partial \mathbf{U}^n}{\partial t} + \mathcal{O}(\Delta t^2)\right) + \mathcal{O}(\Delta t^2) \,.$$

Finally,

$$\mathbf{E}^{n+\frac{1}{2}} = \mathbf{E}^n + \frac{\Delta t}{2}\frac{\partial \mathbf{E}^n}{\partial t} + \mathcal{O}(\Delta t^2) \,. \tag{3.45}$$

We write $\mathbf{U}^{n+1}$ in Taylor expansion, retaining the first term,

$$\mathbf{U}^{n+1} = \mathbf{U}^n + \Delta t \frac{\partial \mathbf{U}^n}{\partial t} + \mathcal{O}(\Delta t^2)\,, \tag{3.46}$$

and the following term can be written as,

$$\frac{\partial \mathbf{P}^n}{\partial \mathbf{U}} \left(\mathbf{U}^{n+1} - \mathbf{U}^n\right) = \Delta t \frac{\partial \mathbf{P}^n}{\partial \mathbf{U}} \frac{\partial \mathbf{U}^n}{\partial t} + \mathcal{O}(\Delta t^2) = \Delta t \frac{\partial \mathbf{P}^n}{\partial t} + \mathcal{O}(\Delta t^2)\,. \tag{3.47}$$

Replacing 3.47 and 3.45 into the second equation of 3.43, we obtain,

$$\mathbf{U}^{n+1} = \mathbf{U}^n + \Delta t \left(\mathbf{E}^n + \frac{\Delta t}{2}\frac{\partial \mathbf{E}^n}{\partial t} + \mathcal{O}(\Delta t^2) + \mathbf{P}^n + \frac{\Delta t}{2}\frac{\partial \mathbf{P}^n}{\partial t} + \mathcal{O}(\Delta t^2)\right)\,,$$

which can be rewritten as,

$$\mathbf{U}^{n+1} = \mathbf{U}^n + \Delta t \frac{\partial \mathbf{U}^n}{\partial t} + \frac{\Delta t^2}{2}\frac{\partial^2 \mathbf{U}^n}{\partial t^2} + \mathcal{O}(\Delta t^3)\,.$$

This shows that the scheme is second order accurate.

The above Eqs. 3.43 can be written in the compact form as:

$$\mathbf{U}^{n+\frac{1}{k}} = \mathbf{U}^n + \Delta t \mathbf{E} + \Delta t \mathbf{P} + \beta \Delta t \frac{\partial \mathbf{P}}{\partial \mathbf{U}} \cdot \left(\mathbf{U}^{n+\frac{1}{k}} - \mathbf{U}^n\right)\,, \tag{3.48}$$

where we take into account that $\mathbf{P}$ is calculated using variables at step "n" ($\mathbf{P} = \mathbf{P}^n$). Δt, $\mathbf{E}$ and β, which appear in the above expression, are specific for each sub step k,

- $\Delta t_{\frac{1}{k}} = \frac{1}{k}\Delta t$;
- The explicit term $\mathbf{E}$ is always calculated using the values of the variables from the previous substep: $\mathbf{E}_{\frac{1}{2}} = \mathbf{E}(\mathbf{U}^n)$, $\mathbf{E}_1 = \mathbf{E}(\mathbf{U}^{n+\frac{1}{2}})$;
- $\beta_{\frac{1}{2}} = 1$, $\beta_1 = \frac{1}{2}$,

where k = 2, 1 for the 2 sub-steps. For simplicity of notation, we will further omit the sub-step subscripts "$\frac{1}{k}$" for β, Δt and $\mathbf{E}$ as well as step superscript "n" for $\mathbf{P}$.

In our case, the vector $\mathbf{U}$ has two components, and each system is composed by two equations, therefore, the jacobian is a 2×2 matrix. Because of conservation of mass, momentum and energy, the elements of the second row are equal to the elements of the first row with reversed sign for the jacobian matrix. This way, the solution for sub-step $\frac{1}{k}$ can be written by components as:

$$\begin{aligned} U_1^{n+\frac{1}{k}} &= U_1^n + \Delta t \frac{E_1 + \beta \Delta t (E_1 + E_2) J_{12} + P_1}{1 + \beta \Delta t (J_{12} - J_{11})}\,, \\ U_2^{n+\frac{1}{k}} &= U_2^n + \Delta t \frac{E_2 - \beta \Delta t (E_1 + E_2) J_{11} + P_2}{1 + \beta \Delta t (J_{12} - J_{11})}\,. \end{aligned} \tag{3.49}$$

Plugging the solution obtained after the explicit update, $\mathbf{U}^*$ defined in Eq. 3.35, for each component, Eq. 3.49 becomes:

$$\begin{aligned} U_1^{n+\frac{1}{k}} &= U_1^* + \Delta t \frac{(1-\beta)P_1 + \beta(P_1 + \Delta t(J_{11}E_1 + J_{12}E_2))}{1 + \beta\Delta t(J_{12} - J_{11})}\,, \\ U_2^{n+\frac{1}{k}} &= U_2^* + \Delta t \frac{(1-\beta)P_2 + \beta(P_2 - \Delta t(J_{11}E_1 + J_{12}E_2))}{1 + \beta\Delta t(J_{12} - J_{11})}\,. \end{aligned} \tag{3.50}$$

In the vector notation, the above equation can be written as:

$$\mathbf{U}^{n+\frac{1}{k}} = \mathbf{U}^* + \frac{\Delta t}{1 + \beta\Delta t(J_{12} - J_{11})}\left[(1-\beta)\mathbf{P} + \beta\left(\mathbf{P} + \Delta t\hat{\mathbf{J}}\cdot\mathbf{E}\right)\right]\,. \tag{3.51}$$

Because $\mathbf{P}$ is assumed linear in $\mathbf{U}$:

$$\mathbf{P}^* = \mathbf{P}(\mathbf{U}^*) = \mathbf{P} + \Delta t\hat{\mathbf{J}}\cdot\mathbf{E}\,, \tag{3.52}$$

and replacing in 3.65, this becomes:

$$\mathbf{U}^{n+\frac{1}{k}} = \mathbf{U}^* + \frac{\Delta t}{1 + \beta\Delta t(J_{12} - J_{11})}\left[(1-\beta)\mathbf{P} + \beta\mathbf{P}^*\right]\,. \tag{3.53}$$

The above equation is exactly Eq. 3.42.

3.4 Semi-implicit scheme implemented in Mancha3D 2F

3.4.1 Continuity equations

In some conditions, when the plasma is far from thermodynamic equilibrium, the processes of ionization/recombination are very fast and the terms in continuity equations should also be implemented implicitly. We consider the linear dependence on ρ_c and ρ_n of the continuity collisional term,

$$S_n = \rho_c\Gamma^{\text{rec}} - \rho_n\Gamma^{\text{ion}}\,. \tag{3.54}$$

Thus we have neglected the dependence of Γ^{ion} and Γ^{rec} on the number of electrons. The elements of the jacobian are:

$$\begin{aligned} J_{11} &= -\Gamma^{\text{ion}}\,, \\ J_{12} &= \Gamma^{\text{rec}}\,. \end{aligned} \tag{3.55}$$

3.4.2 Momentum equations

The collision terms which enter the momentum equations are:

$$\mathbf{R}_n = \rho_c \mathbf{u}_c \Gamma^{\rm rec} - \rho_n \mathbf{u}_n \Gamma^{\rm ion} + \alpha \rho_n \rho_c (\mathbf{u}_c - \mathbf{u}_n)\,; \quad \mathbf{R}_c = -\mathbf{R}_n\,. \tag{3.56}$$

Using the $\mathbf{U}$ and $\mathbf{P}$ notation, we have,

$$\begin{aligned} U_1 &= \rho_n \mathbf{u}_n\,, \\ U_2 &= \rho_c \mathbf{u}_c\,, \\ P_1 &= \Gamma^{\rm rec} U_2 - \Gamma^{\rm ion} U_1 + \alpha(\rho_n U_2 - \rho_c U_1)\,, \\ P_2 &= -P_1\,. \end{aligned} \tag{3.57}$$

We observe that the jacobian has an analytical expression,

$$\begin{aligned} J_{11} &= -\Gamma^{\rm ion} - \alpha \rho_c\,, \\ J_{12} &= \Gamma^{\rm rec} + \alpha \rho_n\,. \end{aligned} \tag{3.58}$$

3.4.3 Energy equations

The collisional terms are different if the energy variable which is evolved is only the internal energy, or if it includes the kinetic energy, see Eqs. 3.12 and 3.6. We split the collisional terms $\mathbf{P}$ into terms related to the kinetic energy $\mathbf{P}_m$, and terms related to the internal energy $\mathbf{P}_T$, so that $\mathbf{P} = \mathbf{P}_m + \mathbf{P}_T$. For clarity, we use the same notation, $\mathbf{U}_T$ for the internal energy, and $\mathbf{U}_m$ for the kinetic energy.

$$\begin{aligned} U_{T_1} &= \frac{1}{\gamma - 1}\frac{k_{\rm B}}{m_{\rm n}} \rho_{\rm n} T_{\rm n}\,, \\ U_{T_2} &= \frac{\rm A}{\gamma - 1}\frac{k_{\rm B}}{m_{\rm n}} \rho_{\rm c} T_{\rm c}\,, \\ U_{m_1} &= \frac{1}{2}\rho_{\rm n} u_{\rm n}^2\,, \\ U_{m_2} &= \frac{1}{2}\rho_{\rm c} u_{\rm c}^2\,, \\ P_{T_1} &= \frac{1}{\gamma - 1}\frac{k_{\rm B}}{m_{\rm n}} \left[\left(\rho_{\rm c} T_{\rm c} \Gamma^{\rm rec} - \rho_{\rm n} T_{\rm n} \Gamma^{\rm ion} \right) + \alpha \rho_{\rm n} \rho_{\rm c} (T_{\rm c} - T_{\rm n}) \right]\,, \\ P_{T_2} &= -P_{T_1}\,, \end{aligned} \tag{3.59}$$

kinetic + internal energy equation:

$$\begin{aligned} P_{m_1} &= \frac{1}{2}\Gamma^{\rm rec}\rho_{\rm c}u_{\rm c}^2 - \frac{1}{2}\rho_{\rm n}u_{\rm n}^2\Gamma^{\rm ion} \\ &+\frac{1}{2}\alpha\rho_{\rm c}\rho_{\rm n}\left({u_{\rm c}}^2 - {u_{\rm n}}^2\right), \\ P_{m_2} &= -P_{m_1}\,. \end{aligned} \tag{3.60}$$

internal energy equation:

$$\begin{aligned} P_{m_1} &= \frac{1}{2}\Gamma^{\rm rec}\rho_{\rm c}(\mathbf{u}_{\rm c}-\mathbf{u}_{\rm n})^2 \\ &+\frac{1}{2}(\mathbf{u}_{\rm c}-\mathbf{u}_{\rm n})^2\rho_{\rm n}\rho_{\rm c}\alpha\,, \\ P_{m_2} &= \frac{1}{2}\Gamma^{\rm ion}\rho_{\rm n}(\mathbf{u}_{\rm c}-\mathbf{u}_{\rm n})^2 \\ &+\frac{1}{2}(\mathbf{u}_{\rm c}-\mathbf{u}_{\rm n})^2\rho_{\rm n}\rho_{\rm c}\alpha\,. \end{aligned} \tag{3.61}$$

The parameter A which appears in the above Eq. 3.59 comes from the possibility of excluding the electrons when we calculate the charges pressure (see definition of the pressure of charges in Eq. 2.78 and the explanation from the previous chapter). A = 1 if we consider that charges are only ions, and A = 2 when we consider that charges = ions + electrons. We consider only changes in the internal energy when we calculate the jacobian: $\hat{\mathbf{J}} = \partial\mathbf{P}/\partial\mathbf{U}_T = \partial\mathbf{P}_T/\partial\mathbf{U}_T$.

$$\begin{aligned} J_{11} &= -\Gamma^{\rm ion} - \alpha\rho_{\rm c}\,, \\ J_{12} &= \frac{1}{\rm A}\left(\Gamma^{\rm rec} + \alpha\rho_{\rm n}\right). \end{aligned} \tag{3.62}$$

We observe that when A = 1, the jacobian is the same jacobian as for the momentum equations.

The linearization of the collisional term in the energy equation is not exact. In this case, the collisional term $\mathbf{P}$ can be written as,

$$\mathbf{P} = \hat{\mathbf{J}}\mathbf{U} + \hat{\mathbf{K}}\mathbf{U}_{\mathbf{m}}\,. \tag{3.63}$$

Eq. 3.48 becomes:

$$\mathbf{U}^{n+\frac{1}{k}} = \mathbf{U}^n + \Delta t\mathbf{E} + \Delta t\mathbf{P} + \beta\Delta t\left[\hat{\mathbf{J}}\cdot\left(\mathbf{U}^{n+\frac{1}{k}} - \mathbf{U}^n\right) + \hat{\mathbf{K}}\cdot\left({\mathbf{U}_{\mathbf{m}}}^{n+\frac{1}{k}} - {\mathbf{U}_{\mathbf{m}}}^n\right)\right], \tag{3.64}$$

which translates into the solution as:

$$\mathbf{U}^{n+\frac{1}{k}} = \mathbf{U}^* + \frac{\Delta t}{1+\beta\Delta t(J_{12}-J_{11})}\left\{(1-\beta)\mathbf{P} + \beta\left[\mathbf{P} + \hat{\mathbf{K}}\cdot\left({\mathbf{U}_{\mathbf{m}}}^{n+\frac{1}{k}} - {\mathbf{U}_{\mathbf{m}}}^n\right) + \Delta t\hat{\mathbf{J}}\cdot\mathbf{E}\right]\right\}. \tag{3.65}$$

We observe that,

$$\mathbf{P} + \hat{\mathbf{K}}\cdot\left({\mathbf{U}_{\mathbf{m}}}^{n+\frac{1}{k}} - {\mathbf{U}_{\mathbf{m}}}^n\right) + \Delta t\hat{\mathbf{J}}\cdot\mathbf{E} = \hat{\mathbf{J}}\mathbf{U}^* + \hat{\mathbf{K}}{\mathbf{U}_{\mathbf{m}}}^{n+\frac{1}{k}}\,, \tag{3.66}$$

and represents the value of $\mathbf{P}$ calculated using values of the variables $\mathbf{U}$ after the implicit update of the momentum, when the kinetic energy, $\mathbf{U}_{\mathbf{m}}$ already have the final value calculated in the substep $n+\frac{1}{k}$.

In conclusion each RK sub-step should be divided in three parts:

- explicit update

- implicit update of momentum equations
- implicit update of energy equations, using for the calculation of the implicit term the values of the kinetic energy obtained after the momentum implicit update

3.5 Summary

In this chapter we have presented the implementation of the two-fluid code used in this work. The code is based on MANCHA3D, a code that solves MHD equations including partial ionization effects through a generalized Ohm's law. The original MANCHA3D has a Runge-Kutta (RK) explicit scheme. Several features of our numerical code, such as shock resolving, have previously been thoroughly tested (Khomenko & Collados 2006b; Felipe et al. 2010; Khomenko & Collados 2012; González-Morales et al. 2018).

We have described how we implemented a semi-implicit scheme in order to overcome a very small timestep imposed by stability in an explicit scheme. Classical explicit schemes would be limited by the explicit time step dictated by the CFL condition due to collisional terms, making it very small and significantly slowing the numerical code. A suitable alternative suggested by Tóth et al. (2012) is a semi-implicit implementation. This implementation allowed us to keep the advantages of an explicit code (efficient parallelization and lower memory requirements), but at the same time to overcome the restrictions imposed by small collisional times. We based our implementation on the already existing numerical code, MANCHA3D , and were therefore able to keep all its already implemented functionalities such as hyper-diffusivities, noise-filtering modules, PML boundary condition, and parallelization. The original Toth's scheme is second order accurate with the choice of $\beta = 1$ in the first substep, and $\beta = 1/2$ in the second substep. We showed that, our implementation, is equivalent to Toth's formulation, and in the case when the linearization of the implicit term is not exact, and depends on variables that have been updated previously, this formulation suggests an easier implementation. The update of the energy, when some of the collisional terms depend on the kinetic energy should be calculated using the values of the kinetic energy after the implicit update of the velocity.

Written in this form, it is also easier to implement in any Runge-Kutta method. Even if formally second-order accurate, it is known that the Crank-Nicolson scheme, used for the implementation of the collisional terms in the second RK sub-step, suffers from oscillations (Østerby 2003). For this reason, as we will see in the next chapter, even if the dependency of the error on the time-step is linear, the error might be smaller if we use $\beta = 1$ in the second sub-step.

Most of the existing multi-fluid codes (Lukin et al. 2016; Maneva et al. 2017; Alvarez Laguna et al. 2017) have a fully implicit implementation, which is computationally more expensive. Usually, an implicit implementation requires the calculation of matrix inversions, which has to be done by iterations for an easier parallelization.

Smith & Sakai (2008) implement a semi-implict scheme similar to Toth's scheme, with the parameter β equal to 1. These authors considered ionization/recombination terms in continuity and momentum equations, elastic collisions in momentum equations, and the work done by the collisional terms in the

energy equations. However, unlike our implementation, they did not consider the inelastic collision terms, the thermal exchange, or the frictional heating in the energy equations.

In the particular case of the collisional terms in a two-fluid model, the inversion of the matrix can be done analytically, and thus decreases the computational time. However, because of this particularity, the scheme cannot be easily extended in order to include more fluids (such as for example having separate temperature for ions and electrons, evolved independently) and the design should be reconsidered in this case. The improvement of the scheme, the trade-off between accuracy and stability in the case of introducing more implicit operators, such as for physical diffusivity, is part of future work.

As a future work, the implementation of a method that ensures that the divergence of the magnetic field remain zero has to be considered.

Next we describe some tests with purpose of verification of the code, and determination of the accuracy of the scheme.

4

Verification of the code Mancha3D 2F

The code developed in this work solves the two-fluid equations of conservation of mass, momentum, and energy, together with the induction equation for the case of the purely hydrogen plasma with collisional coupling between the charged and neutral fluid components. The equations solved by Mancha3D 2F, Eqs. 3.5 were shown in the previous chapter, 3. The implementation of a semi-implicit algorithm allows us to overcome the numerical stability constraints due to the stiff collisional terms. In this chapter, we describe the tests of the code against analytical solutions of acoustic and Alfvén wave propagation in uniform medium in several regimes of the collisional coupling. By the end of this chapter we demonstrate that the results of our simulations are consistent with the analytical results, and with other results described in the literature. We check the accuracy of the newly implemented semi-implicit temporal scheme. Finally, we model a test of a fast wave in a gravitationally stratified isothermal atmosphere, where the collisional coupling also varies, and test the numerical solution against the almost exact analytical solution in this case.

This chapter is based on Popescu Braileanu et al. (2019a).

4.1 Introduction

In order to verify a code's performance, it has to be tested against known analytical solutions when available, or against other numerical solutions obtained with other codes. An example of the standard tests performed to a code is the work of Felipe et al. (2010) for the Mancha3D code. In order to test the convergence and the accuracy of the numerical scheme, they performed simulations of 1D acoustic and Alfvén waves in a stratified medium. They tested the way the code resolves the shocks in the hydrodynamic case: the 1D Riemann shock tube test, that has analytical solution and Brio and Wu shock tube test, or magnetohydrodynamic (MHD) shocks in a 2D geometry: the Orszag-Tang test. The latter two, the Brio and Wu shock tube and the Orszag-Tang problems do not have an analytical solution and the results of the tests had to be compared to the results obtained by other

codes. Moreover, simulations obtained with Mancha3D show results comparable to observations, when realistic simulations of magneto-convection are considered (Khomenko et al. 2018).

Usually, accuracy tests are performed in order to study the space and time convergence of the solution (Meier et al. 2010; Lukin et al. 2016). When an Adaptive Mesh Refinement (AMR) is used, its implementation is tested against analytical solutions and the results from simulations using AMR are compared to the results obtained in a static grid with the finest refinement (Keppens et al. 2003). MPI parallelization and performance are tested by measuring the scalability with the number of processes (van der Holst et al. 2011). Usually, the analytical solutions are available for idealized cases and 1D geometry. Therefore, more complex configurations can only be compared to the results obtained with other codes. The results of the simulations of reconnection performed with COOLFluiD (Lani et al. 2014) have been compared to the results of Leake et al. (2012); Leake et al. (2013) (Alvarez Laguna et al. 2017). Maneva et al. (2017) compared the solutions of propagation of magnetosonic waves in the chromosphere with the results obtained with other codes.

Mancha3D 2F code solves the two-fluid equations presented in the previous chapter. The main difference in the implementation, from the single-fluid version consists of the modification of the temporal explicit Runge-Kutta scheme to a semi-implicit scheme, as described in Section 5.1 from Chapter 3. Even if some of the single-fluid standard tests have been redone: as the 1D Riemann problem, the Orszag-Tang, these are not presented here. The effort has been concentrated to test the aspects related to the two-fluid effects.

Hillier et al. (2016) noticed that since collisional terms introduce a very different timescale, the solution of the two-fluid equations can be obtained semi-analytically. In their approach, the equations with only collisional terms are solved analytically and then the rest of the terms are evolved numerically using an explicit scheme. Such an approach has a drawback since the splitting error is large especially in the weak coupling limit.

Similarly to our method, Smith & Sakai (2008) implemented the collisional terms following a semi-implicit approach. Smith & Sakai (2008) used a two-fluid code, where they considered the plasma composed by ions and neutrals, and they implemented most of the collisional terms in a scheme similar to that of Tóth et al. (2012) with a β parameter equal to 1.

Yet another widely used code for multi-fluid simulations is the HiFi code by Lukin et al. (2016), which uses an implicit temporal discretization and spectral element spatial decomposition. This code has been extensively used for simulations of reconnection in partially ionized plasma (Leake et al. 2012; Leake et al. 2013; Ni et al. 2018).

It must be noted that despite the advantage of the stability, implicit schemes are more computationally expensive because generally the matrix inversions needed in the implicit part are implemented by iterations, increasing the computational time. However, if one only deals with the collisional terms such as $S_{\rm n}$, $\mathbf{R}_{\rm n}$ and $M_{\rm n}$ in Eqs. 3.5, there is an important advantage since these terms are linear with respect to the main set of variables and do not contain derivatives. Therefore, the matrix inversion can be done fully analytically, improving the precision and the computational capabilities of the implicit code. Such an analytical approach is not possible when dealing with physical effects such as thermal conduction or viscosity. In general, semi-implicit implementations such as the one presented here are

less computationally expensive, but are also less accurate than fully implicit ones.

In this chapter we compare the numerical simulations of propagation of waves in a uniform atmosphere and compare the results with analytical solutions. The collisional forces in the upper layers of the solar atmosphere have values similar to the rest of the forces in the momentum equation. In the lower layers (photosphere) their values significantly dominate over the rest of the terms. However, coupling between these layers plays an important role in the energy and momentum transfer from the solar interior to the corona, and therefore it is necessary to create numerical tools that would be able to treat both extreme situations in a single simulation domain. In order to test this aspect, we present in the last part of the chapter a simulation in an isothermal stratified atmosphere, where the collisional frequency strongly varies with height.

4.2 Analytical model of waves in a uniform plasma

In order to check the scheme implemented in Mancha3D 2F, we performed simulations of wave propagation in a uniform plasma. We used two simple analytical cases. In the first case we consider purely acoustic waves propagating in an atmosphere where the background equilibrium temperature of charges and neutrals is different. In this case the difference in behavior between charges and neutrals is created by the different sound speeds of the background atmosphere. In the second case we consider the propagation of Alfvén waves. Here the difference in the behavior of charges and neutrals is produced additionally due to the presence of the magnetic field. In this simple setup the problems have analytical solutions that can be obtained by linearizing the two fluid equations and looking for solutions in the form of monochromatic waves. The sections below describe the analytical solution and results for both sets of simulations, together with the tests of numerical convergence of the scheme.

4.2.1 Acoustic waves

Acoustic waves are longitudinal waves, therefore their velocity vector and direction of propagation are parallel, that is, $\mathbf{u}_\mathrm{n} \parallel \mathbf{k}$ and $\mathbf{u}_\mathrm{c} \parallel \mathbf{k}$. The subscripts "$_\mathrm{n}$" and "$_\mathrm{c}$" refer to neutral and charged species, respectively. We choose the direction of propagation along z direction. We neglect the effects of ionization, recombination, thermal exchange, thermal conduction, and radiation. Therefore, we only consider the momentum exchange due to elastic collisions. In this simple situation the linearized

continuity, momentum, and adiabatic energy equations, described by Eqs. 3.5 become:

$$\begin{aligned}
\frac{\partial \rho_{\rm n1}}{\partial t} + \rho_{\rm n0}\frac{\partial u_{\rm nz}}{\partial z} &= 0,\\
\frac{\partial \rho_{\rm c1}}{\partial t} + \rho_{\rm c0}\frac{\partial u_{\rm cz}}{\partial z} &= 0,\\
\rho_{\rm n0}\frac{\partial u_{\rm nz}}{\partial t} + \frac{\partial p_{\rm n1}}{\partial z} &= \alpha\rho_{\rm n0}\rho_{\rm c0}(u_{\rm cz}-u_{\rm nz}),\\
\rho_{\rm c0}\frac{\partial u_{\rm cz}}{\partial t} + \frac{\partial p_{\rm c1}}{\partial z} &= -\alpha\rho_{\rm n0}\rho_{\rm c0}(u_{\rm cz}-u_{\rm nz}),\\
\frac{\partial p_{\rm n1}}{\partial t} - {c_{\rm n0}}^2\frac{\partial \rho_{\rm n1}}{\partial t} &= 0,\\
\frac{\partial p_{\rm c1}}{\partial t} - {c_{\rm c0}}^2\frac{\partial \rho_{\rm c1}}{\partial t} &= 0,
\end{aligned} \tag{4.1}$$

where $u_{\rm nz}$ and $u_{\rm cz}$ are the velocity projections along z direction, and $c_{\rm n0}$ and $c_{\rm c0}$ are sound speeds of neutrals and charges. Variables with subscript "0" refer to the background unperturbed atmosphere, and variables with subscript "1" refer to the perturbation. The collisional parameter α defined by Eq. (2.88) uses the values of the unperturbed mass densities of electrons, ions, neutrals, and charges. Since for the simple model assumed here the value of α only depends on the homogeneous background variables in the linear approximation, it is kept constant in time and space.

We search for solutions of form,

$$\{u_{\rm nz}, u_{\rm cz}, \rho_{\rm n1}, \rho_{\rm c1}, p_{\rm n1}, p_{\rm c1}\} = \{U_n, U_c, R_n, R_c, P_n, P_c\}{\rm e}^{i(\omega t - kz)}, \tag{4.2}$$

where $\{U_{\rm n}, U_{\rm c}, R_{\rm n}, R_{\rm c}, P_{\rm n}, P_{\rm c}\}$ are, in general, complex amplitudes for all the perturbed variables. These amplitudes are related through the so-called polarization relation, so one needs to set one of the amplitudes to obtain the rest of them through the following relations:

$$U_{\rm c} = \frac{\omega R_{\rm c}}{k\rho_{\rm c0}};\ U_{\rm n} = \frac{\omega R_{\rm n}}{k\rho_{\rm n0}}, \tag{4.3}$$

$$\frac{R_{\rm c}}{R_{\rm n}} = \frac{i\omega^2 - ik^2 c_{\rm n0}^2 + \alpha\rho_{\rm c0}\omega}{\alpha\rho_{\rm n0}\omega},$$

$$P_{\rm c} = c_{\rm c0}^2 R_{\rm c};\ P_{\rm n} = c_{\rm n0}^2 R_{\rm n}. \tag{4.4}$$

The resulting dispersion relation, which relates the frequency and the wave number, has the following form:

$$i\omega^4 + \alpha\omega^3(\rho_{\rm c0}+\rho_{\rm n0}) - i\omega^2k^2(c_{\rm n0}^2+c_{\rm c0}^2) - \omega k^2\alpha(\rho_{\rm c0}c_{\rm c0}^2+\rho_{\rm n0}c_{\rm n0}^2) + ik^4c_{\rm n0}^2c_{\rm c0}^2 = 0. \tag{4.5}$$

Once the background values are specified, the value of the collisional parameter α is determined. It is then convenient to operate in terms of the following parameters: $\omega/(kc_{\rm tot})$, and $\alpha\rho_{\rm tot}/(kc_{\rm tot})$. Here

$\rho_{\rm tot} = \rho_{\rm n0} + \rho_{\rm c0}$ and $c_{\rm tot} = \sqrt{\gamma(p_{n_0} + p_{\rm c0})/(\rho_{\rm n0} + \rho_{\rm c0})}$ are the total density and the sound speed of the whole fluid. The analysis below will be done in terms of the nondimensional variables:

$$E = \frac{\omega}{k c_{\rm tot}}; \;\; F = \frac{\alpha \rho_{\rm tot}}{k c_{\rm tot}}. \tag{4.6}$$

The latter ratio, F, is an effective measure of the collisional strength. These variables are similar to those used in Soler et al. (2013a). Using nondimensional variables, the polarization relations and the dispersion relation become:

$$\frac{U_{\rm c}}{R_{\rm c}} = E\frac{c_{\rm tot}}{\rho_{\rm c0}}; \;\; \frac{R_{\rm n}}{R_{\rm c}} = \frac{EF\rho_{\rm n0}/\rho_{\rm tot}}{iE^2 - ic_{\rm n0}^2/c_{\rm tot}^2 + EF\rho_{\rm c0}/\rho_{\rm tot}}, \tag{4.7}$$

$$iE^4 + FE^3 - iE^2 a_2 - EF + ia_0 = 0, \tag{4.8}$$

where:

$$a_2 = \frac{c_{\rm n0}^2 + c_{\rm c0}^2}{c_{\rm tot}^2}; \;\; a_0 = \frac{c_{\rm n0}^2 c_{\rm c0}^2}{c_{\rm tot}^4}. \tag{4.9}$$

4.2.2 Alfvén waves

Alfvén waves are transverse incompressible waves, polarized perpendicularly to the direction of the background magnetic field. The analytical solution for the Alfvén wave propagation in partially ionized plasma used in our work is similar to those developed previously by Soler et al. (2013a). We consider here a simple case of Alfvén waves with propagation only along the background magnetic field. These are frequently called pure Alfvén waves. In our case, $\mathbf{k} \parallel \mathbf{B_0}, \mathbf{u}_n \parallel \mathbf{B_1}, \mathbf{u}_c \parallel \mathbf{B_1}, \mathbf{B_1} \perp \mathbf{B_0}$. We choose the equilibrium magnetic field along z direction and perturbation of magnetic field and velocities along x direction.

$$\begin{aligned} \mathbf{B}_0 &= (0,0,B_0), \;\; \mathbf{k} = (0,0,k), \;\; \mathbf{B}_1 = (B_{1\rm x},0,0), \\ \mathbf{u}_{\rm c} &= (u_{\rm cx},0,0), \;\; \mathbf{u}_{\rm n} = (u_{\rm nx},0,0). \end{aligned}$$

Otherwise the assumptions of the equations are similar to the acoustic wave case. The linearized momentum and induction equations take the following form.

$$\begin{aligned} \rho_{\rm n0}\frac{\partial u_{\rm nx}}{\partial t} &= \alpha\rho_{\rm n0}\rho_{\rm n0}(u_{\rm cx} - u_{\rm nx}), \\ \rho_{\rm c0}\frac{\partial u_{\rm cx}}{\partial t} &= \frac{B_0}{\mu_0}\frac{\partial B_{1\rm x}}{\partial z} - \alpha\rho_{\rm c0}\rho_{\rm n0}(u_{\rm cx} - u_{\rm nx}), \\ \frac{\partial B_{1\rm x}}{\partial t} &= B_0\frac{\partial u_{\rm cx}}{\partial z}. \end{aligned} \tag{4.10}$$

The equations of continuity and energy conservation are not needed in this case because the Alfvén waves are purely incompressible. Similar to acoustic waves we use the solutions of the form

$$\{u_{\rm nx}, u_{\rm cx}, B_{1\rm x}\} = \{U_n, U_c, B\}{\rm e}^{i(\omega t - kz)}, \tag{4.11}$$

where the amplitudes can be complex in general. Plugging this ansatz into Eqs. 4.10, we obtain the following polarization relations.

$$\begin{aligned} B &= -\frac{kU_{\rm c}B_0}{\omega}, \\ \frac{U_{\rm c}}{U_{\rm n}} &= \frac{i\rho_{\rm n0}\omega + \alpha\rho_{\rm n0}\rho_{\rm c0}}{\alpha\rho_{\rm n0}\rho_{\rm c0}}\,. \end{aligned} \tag{4.12}$$

and the dispersion relation in the following form.

$$-\mu_0\rho_{\rm c0}\omega^3 + i\mu_0\alpha\rho_{\rm c0}(\rho_{\rm c0}+\rho_{\rm n0})\omega^2 + {B_0}^2k^2\omega - i\alpha\rho_{\rm c0}{B_0}^2k^2 = 0. \tag{4.13}$$

Using the nondimensional variables:

$$C = \frac{\omega}{kv_{A0}};\;\; D = \frac{\alpha\rho_{\rm tot}}{kv_{A0}}, \tag{4.14}$$

the dispersion relation, and the polarization relations are

$$-C^3 + iDC^2 + C - iD\frac{\rho_{\rm c0}}{\rho_{\rm tot}} = 0, \tag{4.15}$$

$$\frac{B}{U_c} = -\frac{B_0}{Cv_{A0}},\;\; \frac{U_c}{U_n} = 1 + i\frac{C}{D}\frac{\rho_{\rm tot}}{\rho_{\rm c0}}. \tag{4.16}$$

Similarly to the variable F in the case of acoustic waves, the variable D is a measure of the collisional coupling.

4.2.3 Background atmosphere

The values of the uniform background atmosphere used in this study are given in Table 4.1. For the Alfvén wave tests, a z-directed magnetic field $B_0 = 5\cdot10^{-3}T$ is also added. The corresponding Alfvén speed calculated using the density of charges is $v_{A0} = B_0/\sqrt{\mu_0\rho_{\rm c0}} = 6.32\cdot10^4$ m/s. The collisional parameter α defined in Eq. (2.88) calculated for the background has the value 7.324×10^{12} m^3/kg/s. In this test the temperature of electrons is assumed to be zero, they do not contribute to the pressure of charges, and the effective neutral-charge and charge-neutral collision frequencies defined in Eq. (2.89) become the neutral-ion and ion-neutral collision frequencies, with values $\nu_{\rm ni} \approx 3.65\times10^4$ s^{-1}, and $\nu_{\rm in} \approx 7.3\times10^4$ s^{-1}, respectively.

4.2.4 Parameters of the perturbation

We have to supply several free parameters to calculate the solution. We have chosen the real wave number k, and obtain the complex ω from the dispersion relations, Eqs. (4.5) and (4.13). This means that we consider wave damping in time. Additionally, since the perturbations in all the magnitudes

Table 4.1: Values of the background atmosphere parameters used in the tests of the wave propagation in the uniform medium for neutrals (left) and charges (right).

Neutrals	Charges
$n_{\mathrm{n0}} = 6 \cdot 10^{18} m^{-3}$	$n_{\mathrm{c0}} = \frac{1}{2} n_{\mathrm{n0}} = 3 \cdot 10^{18} m^{-3}$
$\rho_{\mathrm{n0}} = 9.96 \cdot 10^{-9} kg/m^3$	$\rho_{\mathrm{c0}} = \frac{1}{2} \rho_{\mathrm{n0}} = 4.98 \cdot 10^{-9} kg/m^3$
$p_{\mathrm{n0}} = 0.35$ Pa	$p_{\mathrm{c0}} = 2 p_{\mathrm{n0}} = 0.7$ Pa
$c_{\mathrm{n0}} = 7.65 \cdot 10^3$ m/s	$c_{\mathrm{c0}} = 2\ c_{\mathrm{n0}} = 1.53 \cdot 10^4$ m/s
$T_{\mathrm{n0}} = 4227$ K	$T_{\mathrm{c0}} = 4 T_{\mathrm{n0}} = 16908$ K

are related, we need to supply the amplitude of one of them in order to calculate the others. Generally, since the polarization relations are complex, there will be a phase shift between oscillations of different quantities.

We have selected the wave number to be $k = 2\pi m / L_z$ m^{-1}, with m being an integer number. We vary the wave number k by varying the domain length L_z in order to have m = 11 (a random choice) for all the simulations.

For the acoustic waves we choose the amplitude of the perturbation in density of charges, $R_{\mathrm{c}} = 10^{-3} \rho_{\mathrm{c0}}$, and for the Alfvén waves we choose the amplitude of the perturbation in velocity of charges, $U_{\mathrm{c}} = 10^{-5} v_{\mathrm{A0}}$. We calculate the other amplitudes from Eqs. (4.3) for the acoustic waves and Eqs. (4.10) for the Alfvén waves. In all cases, for the numerical solution we used periodic boundary conditions. For the initial condition of the perturbation we used the analytical solution at t = 0 s in the whole domain.

We run all simulations for a total time t_F so that we have L_z / t_F equal to 7447.273 m/s for all the simulations of acoustic waves and equal to 32125.49 m/s for the Alfvén wave simulations. These values are of the order of the characteristic speeds: the sound speed and the Alfvén speed.

4.2.5 Solution of the dispersion relation for acoustic waves

The acoustic wave dispersion relation Eq. 4.8 is a fourth-order equation in the non-dimensional variable E. If the neutrals and charges have the same background temperature, the dispersion relation has four solutions, with simple expressions as shown in Eq. (4.18). In our case $T_{c0}/T_{n0} = 4$, and the values of the coefficients in Eq. (4.8) are $a_2 = 5/2$ and $a_0 = 1$, and the expressions for the solutions[1] in this

[1] obtained using Mathematica software

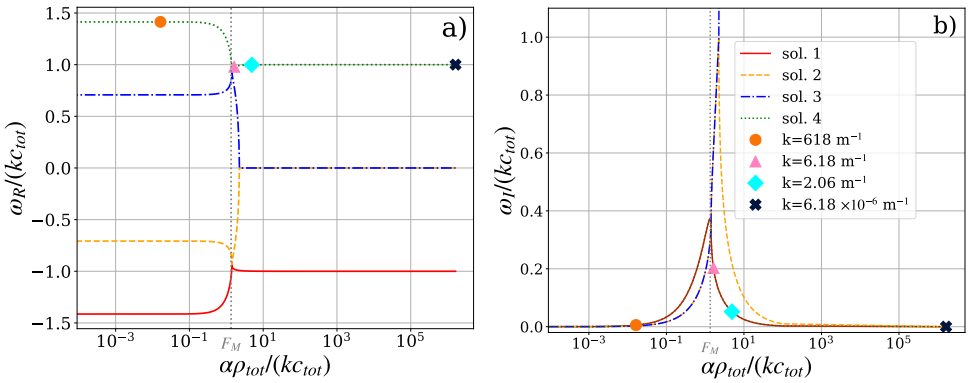

Figure 4.1: Solutions of the dispersion relation, Eq. 4.5, for the acoustic wave case. Left (a) and right (b) panels present the real and imaginary parts of the dimensionless wave frequency ω, respectively, as functions of the dimensionless wave number k. The axes are scaled in nondimensional units E and F, defined in Eq. (4.6) for better visualization. Four solutions are marked with different colors and line styles: solid red for solution 1, orange dashed for solution 2, blue dot-dashed for solution 3, and green dotted for solution 4. We note that solutions 1 and 4 have the same imaginary parts and are superposed in the right-hand panel. Solutions 2 and 3 have the same real part equal to zero for large F (strong collisional coupling) and are also superimposed on top of one another. The values of k for which we compare the analytical and numerical solution using the values of ω, corresponding to solution 4 (green dots), are marked in the panels: orange circle ($k = 618$ m^{-1}), pink triangle ($k = 6.18$ m^{-1}), cyan diamond ($k = 2.06$ m^{-1}), and black "X" ($k = 6.18 \times 10^{-6}$ m^{-1}). F_M is the location on the x-axis of the maximum value of C for the solutions 2 and 3.

case are as follows:

$$E_{4,1} = \frac{1}{4}\left(iF - \sqrt{2-F^2} \pm \sqrt{18 - 2F^2 - 2iF\sqrt{2-F^2}}\right),$$
$$E_{3,2} = \frac{1}{4}\left(iF + \sqrt{2-F^2} \pm \sqrt{18 - 2F^2 + 2iF\sqrt{2-F^2}}\right). \quad (4.17)$$

We keep in mind that F is inversely proportional to the wave number k with the multiplicative factors fixed (by "varying the collisional strength F" we understand this to be equivalent to varying the wave number k, since the value of α is fixed). We compute the complex frequency, ω, for the values of k between 6180 and 6.18×10^{-6} m^{-1}, for each of the four expressions of the mathematical solutions shown in Eq. (4.17), and marked as solutions 1, 2, 3, and 4 in Figure 4.1. The real and imaginary parts of the four solutions are shown in the normalized units, $E = f(F)$, defined in Eq. (4.6), that is, $\omega_{\{I,R\}}/(kc_{\rm tot})$ as a function of $\alpha\rho_{\rm tot}/(kc_{\rm tot})$ for better visualization. The solutions with positive ω_R travel in the positive direction of the z axis, and those with negative ω_R travel in the negative direction.

Waves corresponding to solutions 1 and 4 (red and green colors) propagate with a speed ($v_{ph} = \omega_R/k$) equal to the sound speed of the charges ($c_{c0}/c_{tot} = \sqrt{2} \approx 1.414$) for small values of F (weak collisional coupling), in the negative and positive direction of the z axis, respectively. For the large values of F (strong collisional coupling), their propagation speed becomes that of the whole fluid, c_{tot}. The imaginary part of the frequency ω_I is positive meaning wave damping. The imaginary part would be zero if the charges and neutrals had the same background temperature, since in that case the solutions of the dispersion relation, Eq. 4.8, would simplify to

$$E_{4,1} = \pm 1, \tag{4.18}$$

with zero imaginary part for solutions 1 and 4. As the only difference between neutrals and charges in this particular model is in their sound speed, it is not surprising that by making the sound speed the same the damping disappears, since both fluids would oscillate with exactly the same velocity and therefore the frictional damping term would become strictly zero.

The value of damping is the same for solutions 1 and 4. For either very low or very high values of F, the damping E_I is small and approaching zero. The value of E_I is maximum at a point located on the x-axis at $F_M = \alpha\rho_{tot}/(k_M c_{tot}) = \sqrt{2}$, and corresponds to $k_M \approx 7.5\ \mathrm{m}^{-1}$. $E(F = F_M) = 1/4(\sqrt{14}+i\sqrt{2})$; this gives the value of $\omega_R(F = F_M)/(\alpha\rho_{n0}) = 3\sqrt{7}/8 \approx 1$, which means that the real part of the wave frequency is approximately equal to the ion-neutral collision frequency at the point where the damping, E_I, is maximum (F_M).

Waves corresponding to solutions 2 and 3 (orange and blue colors) propagate with a speed equal to the sound speed of neutrals ($c_{n0}/c_{tot} = \sqrt{2}/2 \approx 0.707$) for small values of F (weak collisional coupling). For large F, these solutions have zero propagation speed (zero ω_R). The ratio E_I is again small for weak or strong collisional coupling (small or large F), and has the maximum located on the x axis at a point very close to F_M.

These results are easy to interpret. For small collisional frequencies compared to the real part of the wave frequency, i.e., weak collisional coupling, the propagation of the waves mostly depends on the properties of either of the fluids. Since the neutrals and the charges have different sound speeds, in the case of weak collisional coupling the waves propagate either at the sound speed of neutrals or of charges. Correspondingly, if one perturbs charges with a certain amplitude, the weak drag forces will translate some of this perturbation to neutrals, but the amplitude of this perturbation will be very small, as indeed follows from the polarization relations in Eq. 4.3. The opposite is also true.

For large collision frequencies compared to the real part of the wave frequency, that is, strong collisional coupling, the charges and the neutrals become coupled and the wave propagates at the sound speed of the whole fluid. Subsequently, the amplitudes of the velocities of neutrals and charges are equal.

For the numerical tests, we only show the results corresponding to solution 4 (the green lines in Figure 4.1), that is, the solution for waves which propagate at the sound speed of the charges for small F. The results in other cases are similar. We have selected one wave number so that F is less than F_M, and three values of k, for which this quantity is larger than F_M. These frequencies are marked with symbols in Figure 4.1. In order to relate the results to observations, Table 4.2 provides

the period, $P = 2\pi/\omega_R$, and the damping time, $T_D = 2\pi/\omega_I$ for the waves used in the simulations (the wave numbers k marked in Figure 4.1), and for the wave corresponding to the maximum damping relative to the wave number (with wave number k_M) in physical units. We can see that the waves have extremely short periods and wavelengths and do not correspond to the waves observed in the chromosphere, which have typical frequencies of 3-5 mHz. This is due primarily to our use of a uniform, unstratified background atmosphere which does not correspond to the chromosphere. The temperatures of charges and neutrals differ by a factor of four, and this situation is also unrealistic. For these reasons, the value of the collisional parameter α corresponding to the background atmosphere may be unphysical for the chromosphere. Moreover, for the purposes of code verification we wanted to test both uncoupled and strongly coupled cases, and the values of k that we have chosen cover the full range, even if the waves corresponding to the largest values of k have small temporal and spatial scales that cannot be observed.

4.2.6 Solution of the dispersion relation for Alfvén waves

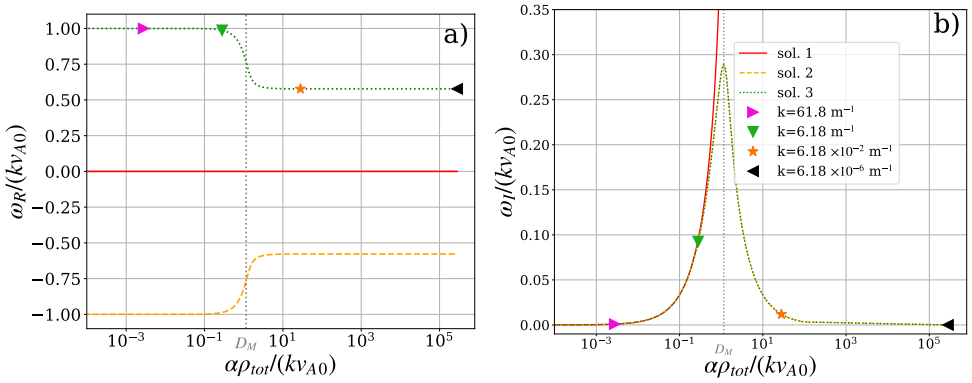

Figure 4.2: Solutions of the dispersion relation, Eq. 4.13, for the Alfvén wave case. Left (a) and right (b) panels present the real and imaginary parts of the wave frequency ω, respectively, as a function of the wave number k. The axes are scaled in the nondimensional units: C and D, defined in Eq. (4.14) for better visualization. Three solutions are marked with different colors and line styles: red solid for solution 1, orange dashed for solution 2, and green dotted for solution 3. The values of k for which we compare the analytical and numerical solutions using the values of ω, corresponding to solution 3 (green dots), are marked in the panels: pink triangle ($k = 61.8$ m^{-1}), green triangle ($k = 6.18$ m^{-1}), orange star ($k = 6.18 \times 10^{-2}$ m^{-1}), and black triangle ($k = 6.18 \times 10^{-6}$ m^{-1}). D_M is the location on the x-axis of the maximum value of C for the solutions 2 and 3.

For the same reason as for the acoustic waves, we vary the collision strength by varying the wave number k parameter to study its influence on the propagation properties of the waves. As in the case

of the acoustic waves, we solve the dispersion relation for values of k between 6180 and 6.18×10^{-6} m^{-1}, and we plot the real and imaginary parts of the wave frequency in Figure 4.2, as a function of the wave number in nondimensional units, $C = f(D)$, defined in Eq. (4.14), i.e., $\omega_{\{I,R\}}/(kv_{A0})$ as function of $\alpha\rho_{\mathrm{tot}}/(kv_{A0})$. The dispersion relation is a third-order equation in ω and there are three solutions. In our case, $\rho_{\mathrm{c0}}/\rho_{\mathrm{tot}} = 1/3$, and the solutions [2] are:

$$\begin{aligned} C_1 &= \frac{i}{3}\left(D + \frac{D^2-3}{G} + G\right), \\ C_{3,2} &= \frac{i}{3}\left(D + L^0_{3,2} i^{-4/3}\frac{D^2-3}{G} - L^1_{3,2} i^{-2/3} G\right), \end{aligned} \tag{4.19}$$

with

$$\begin{aligned} G &= \left(D^3 + 3\sqrt{3 - 3D^2 + D^4}\right)^{1/3}, \\ L^0_3 &= -i\sqrt{3}/2 - 1/2;\ \ L^0_2 = 1, \\ L^1_3 &= i\sqrt{3}/2 - 1/2;\ \ L^1_2 = 1\,. \end{aligned} \tag{4.20}$$

These represent one wave which does not propagate ($\omega_R = 0$, red color), one wave traveling in the positive direction of z axis (green color), and a similar wave traveling in the negative direction (orange color).

For small values of the collisional frequency compared to the real part of the wave frequency, the propagation speed ($v_{ph} = \omega_R/k$) is the Alfvén speed considering only the density of charges (v_{A0}). For the large values of D (strong collisional coupling), the value of v_{ph} is the Alfvén speed of the whole plasma considering both neutrals and charges, v_{Atot}. We note that $v_{Atot}/v_{A0} = \sqrt{\rho_{\mathrm{c0}}/\rho_{\mathrm{tot}}} = 1/\sqrt{3} \approx 0.577$. With no collisions between charges and neutrals, the imaginary part of solutions 2 and 3 vanishes,

$$C_{3,2} = \pm 1, \tag{4.21}$$

meaning that the damping is related to the presence of neutrals. In our case, the imaginary part is positive, and the maximum damping, C_I, is located at a point $D_M = \alpha\rho_{\mathrm{tot}}/(k^A_M v_{\mathrm{A0}}) = 2/\sqrt{3}$ on the x axis, corresponding to a value of $k^A_M \approx 8.8$ m^{-1}. This gives the value of $\omega_R(D = D_M)/(\alpha\rho_{\mathrm{n0}}) \approx 1$. As in the case of the acoustic waves, the real part of the wave frequency is almost equal to the ion-neutral collision frequency at the point where C_I is maximum. Otherwise, C_I is very small.

For the numerical tests below we use the solution traveling in the positive direction of the z axis (green color in Fig. 4.2) and for values of the wave numbers, k, indicated in the legend of Fig. 4.2. The period and the damping time for the waves used in the simulations (corresponding to the values of k marked in Fig. 4.2), and for the wave corresponding to the maximum damping relative to the wave number (with wave number k^A_M) are given in Table 4.3. For the same reasons as the acoustic wave tests, the frequencies and the wave numbers of the Alfvén waves do not correspond to typically observed waves in the chromosphere.

[2] obtained using Mathematica software

4.3 Results of numerical calculations

We ran simulations of acoustic and Alfvén waves using the equilibrium atmosphere and perturbation described in Sects. 4.2.3 and 4.2.4 as initial conditions. We used several values of the wave number k marked in the corresponding panels described in the above section. In order to observe the damping in time we choose a point located in the center of the domain and plot the evolution of the variables at the same point as function of time. The numerical solution is then compared to the analytical solution.

4.3.1 Temporal damping of acoustic waves

Figure 4.3 shows the numerical and analytical solutions for the acoustic waves with wave number values of $k = 618$, 6.18, 2.06, and 6.18×10^{-6} m^{-1}.

We can observe that for different values of k the amplitude damping and propagation velocity vary in agreement with what is expected from Fig. 4.1. For the large value of $k = 618$ m^{-1} (panel *a* of Figure 4.3) there is a phase shift between the oscillating fluid velocities of neutrals and charges, and both are slightly damped. We highlight the fact that the amplitude of oscillations of velocity of charges is significantly larger than that of the neutrals. For the intermediate values of $k = 6.18$ and 2.06 m^{-1} (panels *b* and it c of Figure 4.3), we observe significant damping of both velocity oscillations but similar amplitudes and a smaller phase shift. For the small k case, that is, $k = 6.18 \times 10^{-6}$ m^{-1} (panel *d*), the velocities of charges and neutrals are the same, and the wave propagation velocity is the sound speed of the plasma as a whole. This is expected since charges and neutrals are collisionally coupled.

We observe from Fig. 4.3 that numerical and analytical solutions are in very good agreement; in all panels, we plotted the difference between the numerical and the analytical solution, labeled Δ right below the plots for $u_{\rm nz}$. The error can be seen to accumulate over time, but this is nevertheless very small.

The values from Table 4.2 are consistent with the values deduced from the numerical simulations.

Table 4.2: Values of the period, and damping time for the waves used in the simulations and the wave with the maximum damping relative to the wave number for the case of the acoustic waves

Acoustic waves

k [m^{-1}]	$P = 2\pi/\omega_R$ [s]	$T_D = 2\pi/\omega_I$ [s]
618	6.65×10^{-7}	1.72×10^{-4}
7.5 (k_M)	7.36×10^{-5}	2.07×10^{-4}
6.18	9.6×10^{-5}	4.63×10^{-4}
2.06	2.82×10^{-4}	5.43×10^{-4}
6.18×10^{-6}	94.5	6.15×10^{8}

The amplitude of a wave will decrease to a fraction $f = \exp(-2\pi P/T_D)$ in a period. For example, in the case of the wave with wave number $k = 6.18$ m^{-1}, $f \approx \exp(-9.6/7.37) \approx 0.27$, which is consistent with the value observed in panel (b) of Fig. 4.3.

4.3.2 Temporal damping of Alfvén waves

Figure 4.4 shows the numerical and analytical solutions for the Alfvén waves with the wave number k set to the following values, $k = 61.8$, 6.18, 6.18×10^{-2}, and 6.18×10^{-6} m^{-1}. These values of k are marked in Fig. 4.2.

We observe that numerical and analytical solutions are in very good agreement and the amplitude damping and wave propagation speed vary with the variable D as expected from Fig. 4.2.

For small D, the wave propagates at the Alfvén speed of the charges and the velocity of neutrals is almost zero (panel *a* of Figure 4.4). For large D (strong coupling), the wave propagates at the Alfvén speed of the whole fluid and the velocities of neutrals and charges are equal (panel *d*). Yet again, for intermediate values of D, the damping of all perturbations is observed (panels *b* and *c*).

For all the panels in Fig. 4, we show the difference between the numerical and the analytical solution of $u_{\rm cx}$, labeled Δ, right below the plots for $u_{\rm cx}$. The error, similarly to the case of the acoustic waves, accumulates over time and is small. For the Alfvén waves, the values from Table 4.3 are also consistent with the values obtained from the numerical simulations. For example, the wave with wave number k = 6.18 m^{-1} should decrease the amplitude to a fraction $f \approx \exp(-1.63/2.76) \approx 0.55$ in a period, and this value can also be deduced from panel (b) of Fig. 4.4.

4.3.3 Time convergence test

In order to quantify the degree of agreement between the analytical and numerical solutions, we performed a time-step convergence test. We study the normalized error, $\varepsilon(f, g)$, between analytical and numerical solutions as a function of the normalized integration time step, i.e. the ratio between the time step of the simulations, Δt, and the time step imposed by the single-fluid CFL condition,

Table 4.3: Values of the period, and damping time for the waves used in the simulations and the wave with the maximum damping relative to the wave number for the case of the Alfvén waves

Alfvén waves

k [m^{-1}]	$P = 2\pi/\omega_R$ [s]	$T_D = 2\pi/\omega_I$ [s]
61.8	1.6×10^{-7}	1.72×10^{-4}
6.18	1.63×10^{-5}	1.73×10^{-4}
8.8 (k_M^A)	8.67×10^{-5}	2.3×10^{-4}
6.18×10^{-2}	2.79×10^{-3}	0.135
6.18×10^{-6}	27.89	1.35×10^{7}

Δt_{CFL}. The normalized error is defined as

$$\varepsilon(f,g) = \sqrt{\frac{\sum_i (f(x_i) - g(x_i))^2}{\sum_i (g(x_i))^2}}. \tag{4.22}$$

In this expression, f and g are numerical and analytical solutions, respectively, computed at grid points x_i with i = 1,..N. The analytical solution, g, is independent of Δt. The normalized error defined this way was computed independently for all perturbed variables of the simulations. These are $u_{\rm cz}, u_{\rm nz}, \rho_{\rm c1}, \rho_{\rm n1}, p_{\rm c1}$, and $p_{\rm n1}$ for the acoustic waves, and $u_{\rm nx}$, $u_{\rm cx}$, and $B_{\rm 1x}$ for the Alfvén waves. The results for different variables came to be very similar, therefore we only show the error for the velocity of charges, $u_{\rm cz}$ (acoustic waves) and $u_{\rm cx}$ (Alfvén waves). Computations for different wave number k also lead to very similar results. In the tests below we used $k = 6.18$ m^{-1} for acoustic waves and $k = 6.18 \times 10^{-2}$ m^{-1} for Alfvén waves.

Figure 4.5 shows the results of the convergence tests for both types of waves. The errors are global errors computed after running simulations of acoustic and Alfvén waves until $t = t_F$, and the total time t_F corresponds to 15.96 periods for the acoustic waves and to 12.55 periods for the Alfvén waves. The maximum time step, Δt, used for the convergence test is close to the time step imposed by the single-fluid CFL condition. The numerical solutions were computed using time steps with a ratio of $\Delta t/\Delta t_{CFL} = 0.812$, 0.406, 0.203, 0.102, 0.051, and 0.025 for the acoustic waves and $\Delta t/\Delta t_{CFL} = 0.84$, 0.42, 0.21, 0.105, 0.053, and 0.026 for the Alfvén waves. The convergence tests were carried out for three values of the scheme parameter β (see Section 3.2) of 0.5, 0.6 and 1. This parameter, defined in Eq. 3.36 determines the fraction of the implicit contribution to the numerical solution.

Figure 4.5 shows that, as expected, the error between the analytical and the numerical solutions increases with the increase of the integration time step. However, this increase is different for different values of the parameter β. For $\beta = 1$ the scheme is expected to be first-order accurate in time, and for $\beta = 0.5$ it is expected to be second-order accurate. In order to test if this is the case in our implementation, we performed a polynomial fit to the error function using the expression $\varepsilon = a(\Delta t/\Delta t_{CFL})^2 + b(\Delta t/\Delta t_{CFL}) + c$, with the constraint a≥0. The coefficients resulting from the fit are given in Table 4.4 for the acoustic waves and in Table 4.5 for the Alfvén waves. The results confirm that the polynomial fit to the numerical values is dominantly second order for $\beta \approx 0.5$ and first order for $\beta = 1$. We also observe that while higher-order convergence of numerical schemes is generally desirable, the absolute value of the error for the $\beta = 1$ tests at a practical time step is of similar magnitude (acoustic waves) or smaller (Alfvén waves) than for the $\beta \approx 0.5$ tests. This might be related, as already mentioned in the previous chapter, to the fact that the Alfvén wave convergence test has been performed in a more collisonally coupled regime than the acoustic wave convergence test, which makes the value of the collisional terms larger in that case. The collisional terms are implemented implicitly, and $\beta = 0.5$ corresponds to the Crank-Nicolson method, which is known to suffer from oscillations (Østerby 2003).

It must be noted that the numerical solution here uses Δt up to the value dictated by the explicit single-fluid CFL condition. Therefore, we conclude that our implementation allows us to efficiently

overcome the small time-step limitations implied by the stiff collisional terms in the two-fluid model.

4.4 Waves in a gravitationally stratified atmosphere

In this section we test the capabilities of the code to model waves in a strongly gravitationally stratified solar chromosphere. We assume a model atmosphere with all hydrodynamical parameters and purely horizontal magnetic field, $B_{\rm x0}$, stratified in the vertical direction, z. The temperature is considered uniform (height-independent), and different for charges and neutrals. If we neglect viscosity, and consider only elastic collisions, adiabatic equation of energy, and ideal Ohm's law, the linearized equations can be written as follows.

$$\begin{aligned}
\frac{\partial \rho_{\rm c1}}{\partial t} &+ u_{\rm cz}\frac{d\rho_{\rm c0}}{dz} + \rho_{\rm c0}\frac{\partial u_{\rm cz}}{\partial z} = 0,\\
\frac{\partial \rho_{\rm n1}}{\partial t} &+ u_{\rm nz}\frac{d\rho_{\rm n0}}{dz} + \rho_{\rm n0}\frac{\partial u_{\rm nz}}{\partial z} = 0,\\
\rho_{\rm c0}\frac{\partial u_{\rm cz}}{\partial t} &+ \rho_{\rm c1}g + \frac{\partial p_{\rm c1}}{\partial z} + \frac{1}{\mu_0}\left(\frac{\partial B_{\rm x1}}{\partial z}B_{\rm x0} + \frac{dB_{\rm x0}}{dz}B_{\rm x1}\right)\\
&= \alpha\rho_{\rm n0}\rho_{\rm c0}(u_{\rm nz} - u_{\rm cz}),\\
\rho_{\rm n0}\frac{\partial u_{\rm nz}}{\partial t} &+ \rho_{\rm n1}g + \frac{\partial p_{\rm n1}}{\partial z} = \alpha\rho_{\rm n0}\rho_{\rm c0}(u_{\rm cz} - u_{\rm nz}),\\
\frac{\partial p_{\rm c1}}{\partial t} &- c_{\rm c0}^2\frac{\partial \rho_{\rm c1}}{\partial t} - c_{\rm c0}^2 u_{\rm cz}\frac{d\rho_{\rm c0}}{dz} + u_{\rm cz}\frac{dp_{\rm c0}}{dz} = 0,\\
\frac{\partial p_{\rm n1}}{\partial t} &- c_{\rm n0}^2\frac{\partial \rho_{\rm n1}}{\partial t} - c_{\rm n0}^2 u_{\rm nz}\frac{d\rho_{\rm n0}}{dz} + u_{\rm nz}\frac{dp_{\rm n0}}{dz} = 0,\\
\frac{\partial B_{\rm x1}}{\partial t} &+ B_{\rm x0}\frac{\partial u_{\rm cz}}{\partial z} + u_{\rm cz}\frac{dB_{\rm x0}}{dz} = 0.
\end{aligned} \tag{4.23}$$

We separate the time dependence, assumed to be of the form $\exp(i\omega t)$ with constant ω, and combine the system into the equation of the vertical velocity for the charges: $u_{\rm cz}(z,t) = \tilde{u}_{\rm cz}(z)\exp(i\omega t)$, obtaining

Table 4.4: Values of the coefficients for the acoustic waves together with their standard deviations obtained after the polynomial fit $\varepsilon = a(\Delta t/\Delta t_{CFL})^2 + b(\Delta t/\Delta t_{CFL}) + c$ to the numerically obtained errors ε, for the convergence curves in panel (a) of Fig. 4.5.

Acoustic waves

β	a/10^{-1}	b/10^{-2}	c/10^{-3}
0.5	2.06 ± 0.11	-2.83 ± 0.92	3.27 ± 1.19
0.6	1.82 ± 0.12	3.71 ± 1.02	-0.91 ± 1.31
1	0 ± 0.16	21.7 ± 1.39	-1.31 ± 1.79

Table 4.5: Values of the coefficients for Alfvén waves together with their standard deviations obtained after the polynomial fit $\varepsilon = a(\Delta t/\Delta t_{CFL})^2 + b(\Delta t/\Delta t_{CFL}) + c$ to the numerically obtained errors ε, for the convergence curves in panel (b) of Fig. 4.5.

Alfvén waves

β	$a/10^{-1}$	$b/10^{-3}$	$c/10^{-3}$
0.5	1.16 ± 0.10	-7.85 ± 9.02	3.27 ± 1.19
0.6	1.08 ± 0.12	5.38 ± 10.9	0.59 ± 1.45
1	0 ± 0.08	33.4 ± 7.26	-0.18 ± 0.97

a fourth-order ODE:

$$\begin{aligned} \frac{\mathrm{d}^4\tilde{u}_{\mathrm{cz}}}{\mathrm{d}z^4}a_c a_n + \frac{\mathrm{d}^3\tilde{u}_{\mathrm{cz}}}{\mathrm{d}z^3}\left(a_n b_c + a_c b_n\right) + \\ \frac{\mathrm{d}^2\tilde{u_{cz}}}{\mathrm{d}z^2}\left[b_c b_n + \omega^2\left(a_c + a_n\right) - i\alpha\omega(a_c\rho_{\mathrm{c0}} + a_n\rho_{\mathrm{n0}})\right] + \\ \frac{\mathrm{d}\tilde{u}_{\mathrm{cz}}}{\mathrm{d}z}\omega\left[\omega\left(b_c + b_n\right) - i\alpha\left(b_c\rho_{\mathrm{c0}} + b_n\rho_{\mathrm{n0}}\right)\right] + \\ u_{\mathrm{cz}}\omega^3\left[\omega - i\alpha\left(\rho_{\mathrm{c0}} + \rho_{\mathrm{n0}}\right)\right] = 0\,. \end{aligned} \tag{4.24}$$

where:

$$\begin{aligned} a_c(z) = {c_{\mathrm{c0}}}^2 + {v_{A0}}^2, a_n(z) = c_{\mathrm{n0}}^2, b_{c,n}(z) = \frac{1}{\rho_{\mathrm{c,n0}}}\frac{\partial\left(\rho_{\mathrm{c,n0}}a_{c,n}\right)}{\partial z}, \\ c_{\mathrm{c,n0}}^2 = \gamma\frac{p_{\mathrm{c,n0}}}{\rho_{\mathrm{c,n0}}}, \quad \text{and} \quad {v_{A0}}^2 = \frac{{B_{\mathrm{x0}}}^2}{\mu_0\rho_{\mathrm{c0}}}. \end{aligned} \tag{4.25}$$

The equilibrium variables for neutrals and for charges must fulfill the equations of state: Eq. (2.16) and the hydrostatic (HS) and magneto-hydrostatic (MHS) equilibrium conditions, respectively:

$$\begin{aligned} \frac{dp_{\mathrm{n0}}}{dz} + \rho_{\mathrm{n0}}g = 0, \\ \frac{d}{dz}\left(p_{\mathrm{c0}} + {B_{\mathrm{x0}}}^2/(2\mu_0)\right) + \rho_{\mathrm{c0}}g = 0. \end{aligned}$$

Since the temperature is assumed uniform, the pressure for neutrals has an exponential profile with a uniform scale height, and the sound speed of neutrals is constant. If we consider that the magnetic pressure has the same scale height as the pressure on the charges, after solving HS/MHS equations we

obtain

$$\begin{aligned} p_{\rm n0}(z) &= p_{\rm n0}(z_0)\exp\left(-\frac{z}{H_{\rm n}}\right), \\ p_{\rm c0}(z) &= p_{\rm c0}(z_0)\exp\left(-\frac{z}{H_{\rm c}}\right), \\ B_{\rm x0}(z) &= B_{\rm x0}(z_0)\exp\left(-\frac{z}{2H_{\rm c}}\right), \end{aligned} \tag{4.26}$$

with uniform scale heights:

$$\begin{aligned} H_{\rm n} &= \frac{k_{\rm B}T_{n0}}{m_{\rm n}g}, \\ H_{\rm c} &= \frac{2k_{\rm B}T_{c0}}{m_{\rm n}g}\frac{p_{\rm c0}(z_0)+B_{\rm x0}(z_0)^2/(2\mu_0)}{p_{\rm c0}(z_0)}. \end{aligned} \tag{4.27}$$

The densities obtained from the ideal gas laws for neutrals and charges (Eq. 2.16) also have an exponential profile. In these conditions, the quantities defined in Eq. 5.23, namely $a_{c,n}$, $b_{c,n} = -a_{c,n}/H_{\rm c,n}$n and α, are uniform; however, there are coefficients that explicitly contain density. We assumed that the scale of the height variation of the nonuniform coefficients in Eq. 4.24 is large compared to the oscillation wavelength, and therefore we can search for the solution in terms of plane waves, as

$$\tilde{u}_{\rm cz}(z) = V_c\exp\left(-ikz\right),$$

with V_c being the uniform real amplitude, and k the uniform complex wave number. The other variables are also in the form of plane waves (including the time dependence):

$$\begin{aligned} \left\{u_{\rm nz}, \frac{\rho_{\rm c1}}{\rho_{\rm c0}}, \frac{\rho_{\rm n1}}{\rho_{\rm n0}}, \frac{p_{\rm c1}}{p_{\rm c0}}, \frac{p_{\rm n1}}{p_{\rm n0}}, \frac{B_{\rm x1}}{B_{\rm x0}}\right\} =& \{V_{\rm n}, \tilde{R}_{\rm c}, \tilde{R}_{\rm n}, \tilde{P}_{\rm c}, \tilde{P}_{\rm n}, \tilde{B}\}\times \\ & \exp\left(i(\omega t - kz)\right), \end{aligned} \tag{4.28}$$

where $V_{\rm n}, \tilde{R}_{\rm c}, \tilde{R}_{\rm n}, \tilde{P}_{\rm c}, \tilde{P}_{\rm n}$, and $\tilde{B}$ are uniform complex amplitudes. The following relations are obtained,

$$\begin{aligned} V_{\rm n} &= V_{\rm c}\left(1+\frac{i(\omega^2 - ikb_{\rm c} - k^2a_{\rm c})}{\alpha\omega\rho_{\rm n0}}\right), \\ \tilde{R}_{\rm c,n} &= \frac{V_{\rm c,n}}{\omega}\left(k - i\frac{1}{H_{\rm c,n}}\right), \\ \tilde{P}_{\rm c,n} &= \frac{V_{\rm c,n}}{\omega}\left(k\gamma - i\frac{1}{H_{\rm c,n}}\right), \\ \tilde{B} &= \frac{V_{\rm c}}{\omega}\left(k - i\frac{1}{2H_{\rm c}}\right). \end{aligned} \tag{4.29}$$

The dispersion relation is a fourth-order equation in ω:

$$(-\omega^2 + k^2 a_c + ikb_c + i\omega\alpha\rho_{\rm n0})(-\omega^2 + k^2 a_n + ikb_n + i\omega\alpha\rho_{\rm c0}) + \omega^2\alpha^2\rho_{\rm n0}\rho_{\rm c0} = 0. \tag{4.30}$$

In our particular case, the wave number k obtained from this space-dependent dispersion relation turns out to be almost uniform, and therefore we consider the plane wave solution to be a fair approximation.

4.4.1 Initial conditions

Equilibrium atmosphere

We choose the temperature for neutrals to be $T_{\rm n0} = 6000$ K. Further, for the number density of the neutrals and charges we use the values taken from the VALC (Vernazza et al. 1981) model at $z_0 \approx 500$ km: $n_{\rm c0}(z_0) = 5 \times 10^{17}$ m^{-3}, and $n_{n0}(z_0) = 2.1 \times 10^{21}$ m^{-3}. In this test we take the temperature of the electrons into account; unlike the tests in the uniform atmosphere, they contribute to the pressure of charges and to collisions. We choose the value of $B_{\rm x0}(z_0) = 10^{-4}$ T. In order to have the same scale height for neutrals and charges, we use the following temperature for the charges.

$$T_{\rm c0} = \frac{n_{\rm c0}(z_0)k_{\rm B}T_{\rm n0} - B_{\rm x0}(z_0)^2/(2\mu_0)}{2n_{\rm c0}(z_0)k_{\rm B}}. \tag{4.31}$$

This gives the value of $T_{\rm c0} \approx 2422.47$ K and $H_{\rm n} = H_{\rm c} \approx 1.8 \times 10^5$ m. Subsequently, the pressures of charges and neutrals at z_0, $p_{\rm c0}(z_0)$ and $p_{\rm n0}(z_0)$ are obtained from the ideal gas law (Eq. 2.16). In these conditions, the wave number k obtained from the dispersion relation Eq. (4.30) is almost uniform, and has a value of $k \approx 1.383 \times 10^{-4} + 2.767 \times 10^{-6} i$ m^{-1}. Therefore, the wavelength is about four times shorter than the density scale height. The densities are calculated afterwards from the ideal gas laws for neutrals and charges (Eq. 2.16), taking $\rho_{\rm n0} = n_{\rm n} m_{\rm n}$, $\rho_{\rm c0} = n_{\rm e} m_{\rm n}$. We cover the domain $L_z = 1.6$ Mm with 32000 grid points.

Perturbation

We choose the period of the wave to be P=5 s, and calculate the frequency ($\omega = 2\pi/P$) and the wave number (k) from the dispersion relation, Eq. (4.30). We choose the amplitude of the perturbation of the velocity of charges as a fraction of the background sound speed, $V_{\rm c} = 10^{-3} c_0$, where

$$c_0 = \sqrt{\gamma(p_{\rm n0} + p_{\rm c0})/(\rho_{\rm n0} + \rho_{\rm c0})} \tag{4.32}$$

is the sound speed of the whole fluid, and its value is $c_0 \approx 9.1$ km/s. We calculate the amplitudes of the other perturbations from the polarization relations, Eq. (4.29). The perturbation is generated by a driver at each time step in the ghosts points at the bottom of the atmosphere, which makes it the lower boundary condition. The perfectly matched layer (PML) is used as the upper boundary condition and is specially designed to absorb waves without reflections. It was first introduced for the first time for electromagnetic waves in the Maxwell equation by Berenger (1994), applied to Euler equations by Hu

(1996), and to acoustic waves in a strongly stratified solar convection zone by Parchevsky & Kosovichev (2007). The description of the implementation of the PML in MANCHA3D and MANCHA3D 2F can be found in Felipe et al. (2010) and in Chapter 3. In this test we have used the value of the scheme parameter β=1.

4.4.2 Results

We run the code in two regimes. In the first case, we solved the fully nonlinear equations for the perturbations, and in the second case we evolved the linearized equations where only the first-order terms were kept. The latter was done for comparison purposes, since the analytical solution assumes a linear regime. We compare the numerical solutions at time $t = 215.115$ s with the analytical solution. At this time, simulations reached the stationary state, since the wave has reached the upper boundary and several periods of the wave have passed through the boundary. The results are shown in Figs. 4.6 and 4.7.

Figure 4.6 shows the analytical solution (green, solid line) superposed on the linear numerical solution (red, dashed line) for the vertical velocity of charges ($u_{\rm zc}$) in the first panel, the vertical velocity of neutrals ($u_{\rm zn}$) in the second panel, and for the perturbation in the x component of the magnetic field ($B_{\rm x1}$) in the third panel. Below the panel of $u_{\rm zc}$ we show the difference (Δ) between the linear numerical and the analytical solution of $u_{\rm zc}$. We observe that the numerical linear solution is in very good agreement with the analytical solution for the three quantities considered, and that the spatially localized error is small (below 2%).

The first panel of Fig. 4.7 shows the nonlinear effects by superposing the nonlinear numerical solution (blue, dotted line) of $u_{\rm zc}$ along with the analytical solution (green solid line) and the linear numerical solution (red dashed line), for the same snapshot taken at $t = 215.115$ s. In the second and third panels we show the decoupling in the vertical velocity ($u_{\rm nz} - u_{\rm cz}$) for the analytical and linear solutions superposed, and the nonlinear solution, respectively.

We observe that the wave profile steepens at the end of the domain when the amplitude becomes large and nonlinear effects are visible in the case of the nonlinear solution. As a consequence, the amplitude of the wave is smaller than in the linear case (see e.g., Landau & Lifshitz 1987). Wave amplitude grows with height in a gravitationally stratified atmosphere because of the density decrease. In the case considered here, the damping is not large enough to overcome this growth, and therefore the wave evolves into a shock. The amplitude growth is nevertheless below the growth in the MHD limit.

We also observe that the decoupling predicted analytically from the relation between $\tilde{V}_n$ and V_c in Eq. (4.29) agrees with the decoupling obtained from the linear numerical simulation. In order to intuitively understand the reason for the linear decoupling, we show in Fig. 4.8 the relevant frequencies corresponding to this problem. Even though the collisional parameter α is uniform because of the uniform background temperature of neutrals and charges, and has the value $\approx 4.1 \times 10^{11}$ m^3/kg/s, the collision frequency also depends on density (Eq. 2.89), and has an exponential profile. While for the charges the collision frequency $\nu_{\rm cn}$ is larger than both the ion-cyclotron frequency ($\omega_{\rm ci}$) and the wave frequency (which determine the hydrodynamical timescale), for the neutrals the neutral-

charges collision frequency goes from being greater than the wave frequency to being less than the wave frequency at a point located at $z \approx 1.4$ Mm in the atmosphere. This is the point after which we observe the decoupling for the linear numerical solution and the analytical solution. The code efficiently captures the transition from a coupled to a partially decoupled regime. In the nonlinear case, the hydrodynamical timescale is smaller than in the linear case. The shock front width, which determines the hydrodynamical space scale in the nonlinear case, is smaller than the wavelength. The nonlinear decoupling appears spatially at the shock front, and is almost five times larger than the linear decoupling.

4.5 Discussion and conclusions

Strong vertical and horizontal stratification in solar atmospheric plasma parameters makes theoretical modeling of the solar chromosphere particularly complicated, where it is expected that the collisional timescales between charged and neutral plasma components may become similar or longer than MHD timescales, leading to a breakdown of the single-fluid MHD approximation. In such conditions, neutrals start to decouple from charges, behaving as two independent fluids. This chapter describes our effort to verify the performance of the semi-implicit fluid-coupling algorithm. To this end we compared the numerical solution with the known analytical solutions for propagation of acoustic and Alfvén waves in a homogeneous plasma with a different degree of collisional coupling.

Our analytical results are similar to those obtained by Zaqarashvili et al. (2011b) and Soler et al. (2013a). When the temperatures of charges and neutrals are initially different, if the ratio $F = \alpha\rho_{\rm tot}/(kc_{\rm tot})$, which describes the collisional coupling for the acosutic waves case, is small, the acoustic waves in each of the fluids propagate nearly independently of each other with their respective sound speeds. The Alfvén waves propagate with the Alfvén speed of the charged fluid if the collisional coupling is weak, i.e. the value of the variable $D = \alpha\rho_{\rm tot}/(kv_{\rm A0})$ is small. In the opposite limit, when F or D are large, the two fluids become coupled. The acoustic waves propagate with the sound speed of the whole fluid, and the Alfvén waves propagate with the Alfvén speed calculated using the total atom mass density. In this case, the velocities of neutrals and charges are of equal amplitude and are in phase. At these two extremes, when the quantities F and D are either low or high, the waves have little damping relative to wave number, but when the collisional frequency is of the order of the wave frequency the damping relative to wave number is maximum.

Our numerical solution reproduces the analytical solution for the full range of the values of the wave number k. The temporal convergence tests have shown that, as expected, the newly implemented scheme is first-order accurate when the scheme parameter $\beta = 1$, and is second-order accurate when $\beta \approx 0.5$. However, we note that even if the scheme converges linearly with Δt for the scheme parameter $\beta = 1$, the overall behavior of the scheme is more stable, and the errors are in fact smaller.

Our current study must be viewed in the context of other similar developments by other groups of authors. There have been several approaches proposed to overcome the limitations introduced by large collisional terms. Martínez-Gómez et al. (2017) use a five-fluid model with three ionized and two neutral components and the implementation is fully explicit. As already mentioned, this requires very

small time-steps when the collision frequencies are high. The fully implicit implementations (Lukin et al. 2016; Maneva et al. 2017; Alvarez Laguna et al. 2017) are also very computationally expensive, because of the matrix inversions needed in the implementation. The analytical implementation of the terms only in the strongly coupled regime (Hillier et al. 2016) requires a criterion to distinguish between the collisionally coupled and uncoupled regimes. We have seen that our scheme handles both of them well and in the same way.

All in all, the above implementations have their advantages and disadvantages. In our case, we have chosen a semi-implicit approach because the collisional terms that need to be implemented implicitly, are linear in the variables that evolve in time, and the implicit solution can be obtained analytically. The tests we carried out in order to verify the code showed satisfactory results.

Convergence tests were carried out for the coupled regime, and the errors were shown to be larger. The neutrals and charges are more coupled at larger values of the variables F and D. We have seen from the convergence test that the scheme behaves better in the strongly coupled regime for the values of the scheme parameter β closer to 1 than to 0.5, and this is the reason for choosing this value for the last test. The last test, the simulation in the gravitationally stratified atmosphere, deals with the situation where the waves pass from a collisionally coupled regime to a decoupled regime, and the numerical results are satisfactory.

While the present chapter only presents calculations in cases where analytical solutions exist and can be compared to the numerical solution, in the next chapter we show results where we demonstrate that the algorithm implemented in Mancha3D 2F is able to efficiently deal with chromospheric gravitational stratification and can be used for modeling of propagation of chromospheric shock waves under the two-fluid framework.

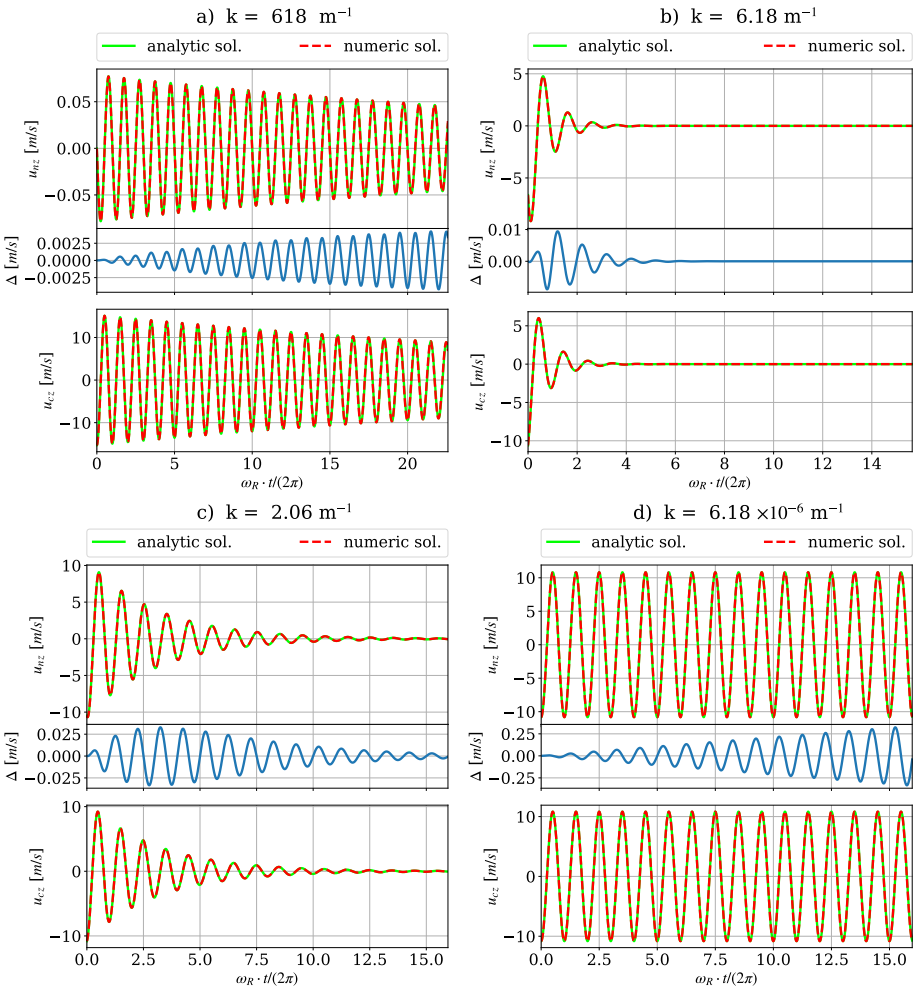

Figure 4.3: Comparison between the numerical (red dashed line) and analytical (green solid line) solutions of the velocity of neutrals as a function of time for acoustic wave propagation in a homogeneous plasma. Below the panels showing the velocity of neutrals, the difference (Δ) between the numerical solution and the analytical solution for u_{nz} is given. Time is measured in units of the wave period, $2\pi/\omega_R$. Panels from left to right and from top to bottom show simulations for different values of the wave number k, as indicated in the legend of Fig. 4.1.

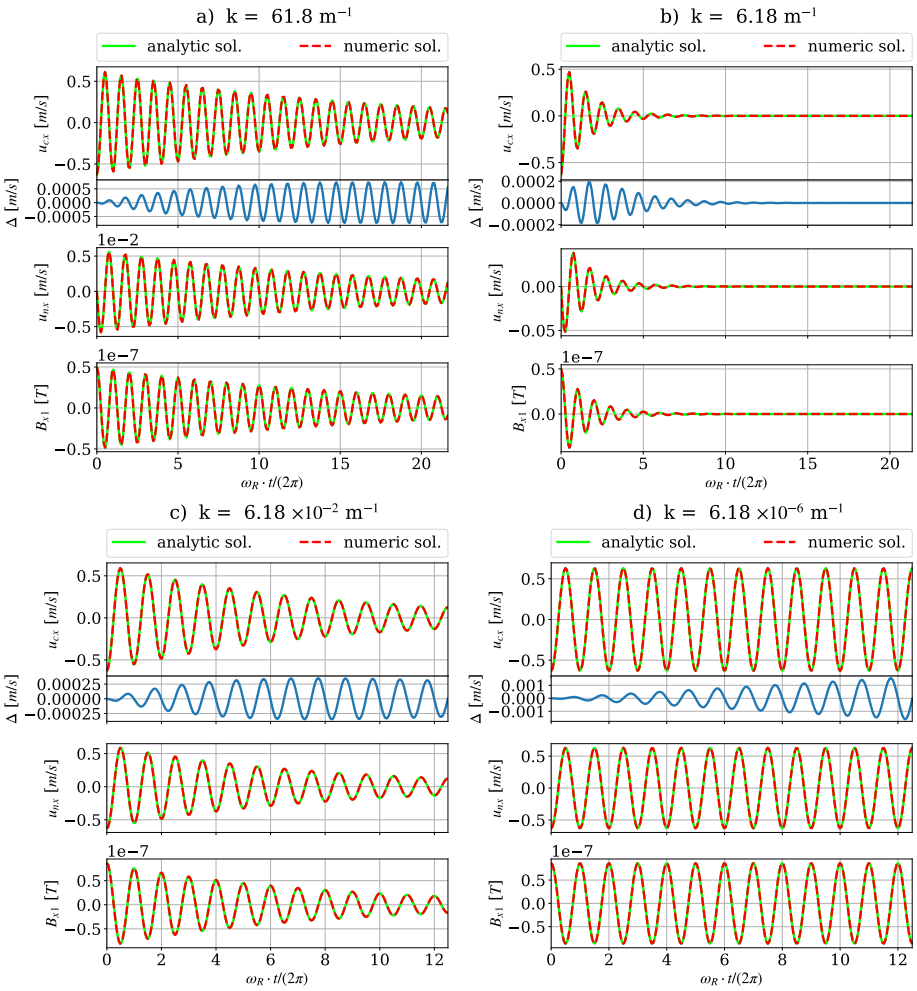

Figure 4.4: Comparison between the numerical (red dashed line) and analytical (green solid line) solutions of the velocity of neutrals as a function of time for Alfvén wave propagation in a homogeneous plasma. Below the panels showing the velocity of charges, the difference (Δ) between the numerical solution and the analytical solution for u_{cx} is plotted. Time is measured in units of the wave period, $2\pi/\omega_R$. Panels from left to right and from top to bottom show simulations for different values of the wave number k, as indicated in the legend of Fig. 4.2.

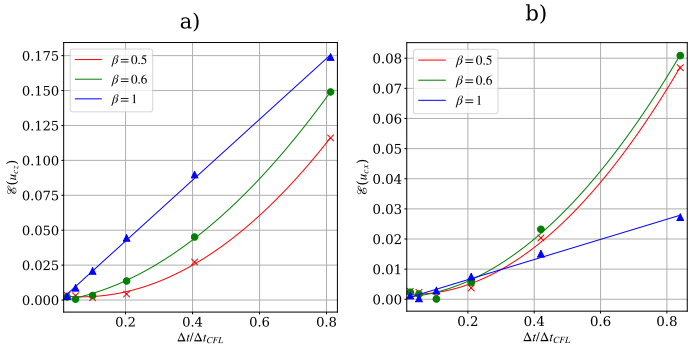

Figure 4.5: Normalized errors, ε, defined by Eq. 4.22, in the velocity of charges as a function of the ratio between the integration time step Δt and Δt_{CFL}, accumulated after running the simulation until $t = t_F$. Panel (a) corresponds to simulations of acoustic waves, and panel (b) to simulations of Alfvén waves. Blue triangles show results for $\beta = 1$ (defined in Eq. 3.36); green circles are for $\beta = 0.6$, and red crosses are for $\beta = 0.5$. Solid lines show the results of quadratic polynomial fit $\varepsilon = a(\Delta t/\Delta t_{CFL})^2 + b(\Delta t/\Delta t_{CFL}) + c$, with coefficients given in Tables 4.4 and 4.5.

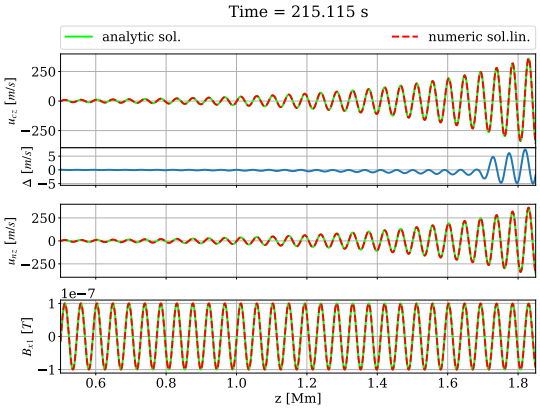

Figure 4.6: Analytical solution (green solid line) and numerical linear solution (red dashed line) for the vertical velocity of charges (u_{cz}) and neutrals (u_{nz}), and for the perturbation in the x component of the magnetic field (B_{x1}) for a snapshot taken in stationary state at $t = 215.115$ s. Below the panel showing the solutions for u_{cz}, the difference between the numerical linear solution and the analytical solution for u_{cz} is plotted.

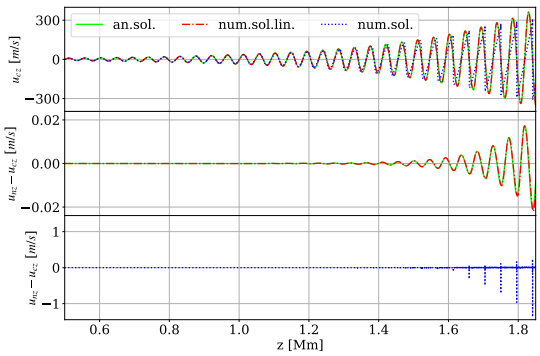

Figure 4.7: First panel: Analytical solution (green solid line) and numerical solutions: linear (red dashed line) and nonlinear (blue dotted line) for u_{zc} for a snapshot taken in stationary state at $t = 215.115$ s. Second and third panels: Decoupling ($u_{nz} - u_{cz}$) for the analytical and linear numerical solutions, and for the nonlinear numerical solutions, respectively.

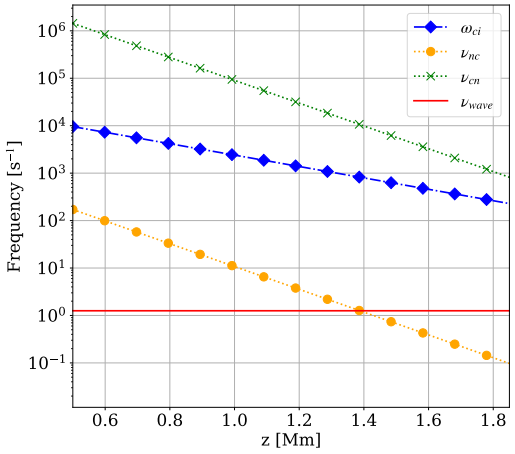

Figure 4.8: Relevant frequencies: ion-cyclotron frequency: ω_{ci} (blue dashed line marked with diamonds), wave frequency: $\nu_{wave} = 2\pi/P_{wave}$ (red solid line), neutral-charge collision frequency: ν_{nc} (orange dotted line marked with circles), and charge-neutral collision frequency: ν_{cn} (green dotted line marked with "X")

5

Fast magneto-acoustic waves in a stratified atmosphere

In this chapter we consider fast magneto-acoustic shock wave formation and propagation in a stratified medium permeated by a horizontal magnetic field, with properties similar to that of the solar chromosphere. Waves and shocks traveling through the solar chromospheric plasma are influenced by its partial ionization and weak collisional coupling, and may become susceptible to multi-fluid effects, similar to interstellar shock waves. The evolution of plasma and neutrals is modeled using our newly deveoped two-fluid code, MANCHA3D 2F, which evolves a set of coupled equations for two separate fluids. In the last section we compare the results with the results obtained in the MHD approximation, modeling the interaction between charges and neutrals with the ambipolar term.

This chapter is based on Popescu Braileanu et al. (2019b).

5.1 Introduction

The aim of the present chapter is to deepen our understanding of the multi-fluid nature of chromospheric shocks and their contribution to the chromospheric heating. Waves in the solar atmosphere were measured for the first time by Leighton et al. (1962). The waves are thought as the principal mechanism of transport of the energy from the deep layers of the atmosphere, and their dissipation in the upper layers may contribute significantly to the heating (Klimchuk et al. 2004; Gupta 2014; Soler & Terradas 2015; Carlsson & Stein 2002; Arber et al. 2016; Brady & Arber 2016). Due to the limits in current spatial and temporal resolutions, observations have been done mainly for low frequency waves. However, theoretical calculations showed that the maximum of the acoustic flux is localized in the high frequency range around 100 mHz (Musielak et al. 1994). In order to understand how higher frequency waves propagate, in more complex configurations than can be studied analytically, numerical simulations have to be performed.

Waves and shocks have been studied in the MHD assumption in many works (Cally 2006; Cally & Goossens 2008; Bogdan et al. 2003; Khomenko & Collados 2006a; Lee et al. 2014; Santamaria et al. 2017; Provornikova et al. 2018). The partial ionization effects have been considered in MHD models through a generalized Ohm's law (Shelyag et al. 2016), converting them in the so-called single-fluid approximation. The single-fluid approach is suitable for dealing with slow processes in partially ionized plasmas, which happen on time scales longer than the collisional time scale. The single-fluid approximation fails for time scales comparable to or shorter than the characteristic time scales for interaction between the charged and neutral particle populations.

The vast majority of properly multi-fluid studies of ion-neutral effects in solar plasmas address propagation of different types of waves and the development of instabilities in chromospheric and prominence plasma conditions, using rather simplified assumptions. Zaqarashvili et al. (2011b) and Soler et al. (2013a) studied theoretically the propagation of Alfvén waves in a uniform medium composed by protons and hydrogen atoms which interact by collisions. Refinements of this theory were introduced by Zaqarashvili et al. (2011a) by adding helium atoms, by Zaqarashvili et al. (2013) by considering a nonuniform gravitationally stratifed atmosphere, and by Soler et al. (2013b) by applying a flux tube model. It was found that in situations when the neutral-ion collisional frequency is much lower than the wave frequency, the propagation properties of the waves only depend on the properties of the ionized fluid. These properties change with height due to stratification, and the Alfvén wave may become evanescent in some regions of the solar atmosphere. The waves can be damped by neutral-ion collisions, and the existence of neutral helium atoms, alongside with neutral hydrogen, significantly enhances the damping. The damping is most efficient when the wave frequency and the collisional frequency are of the same order of magnitude.

Realistic problems cannot be solved analytically in multi-fluid approach, and must be modeled by numerical simulations. Lately the waves have been studied in multi-fluid models numerically by (Leake et al. 2012; Maneva et al. 2017; Martínez-Gómez et al. 2017; Soler et al. 2013b).

One particular aspect of the chromospheric physics that has been scarcely studied is the influence of multi-fluid effects on the formation and dissipation of chromospheric shock waves. Hillier et al. (2016) study the formation and evolution of slow-mode shocks driven by reconnection in a partially ionized plasma. A complex multi-fluid structure of the shock transition was modeled revealing structures similar to C-shocks or J-shocks in the classification by Draine & McKee (1993). The frictional heating associated with ion-neutral decoupling at the shock front was up to 2% of the available magnetic energy.

Here we perform two-fluid modeling of propagation of fast magneto-acoustic waves generated at the base of the chromosphere for a particular case of horizontal magnetic field. Depending on the conditions, these waves steepen into shocks at the middle-to-upper chromosphere, leading to decoupling between ion and neutral fluid velocities. We fully take into account non-linear effects. We have seen in Figure 1.8 that the collision frequency between ion and neutrals drops with height several orders of magnitude because of the decrease of the densities. We then expect that the waves are damped by either of nonlinear effects mentioned above, but also because of the decrease of the collision frequency with height, which also appears in the linear approximation. The simulations are performed using

our newly extended MANCHA3D 2F code (Popescu Braileanu et al. 2019a). We study the effects of the wave frequency and amplitude, as well as dependence of the background magnetic field strength on the height where ions and neutrals become decoupled. The results of the numerical simulations are compared to analytical solutions within the two-fluid and single-fluid descriptions, thus allowing to separate the non-linear, linear and two-fluid effects on the wave damping and dissipation. The equations solved by MANCHA3D 2F are those in Eqs. 3.5, in Chapter 3.

The collisional timescales can be significantly smaller than the hydrodynamical timescale, making the numerical discretization of the equations stiff. The implicit implementation of the collisional terms overcomes a very small time step limitation imposed by the collisional time scale, making it possible to use the time step determined by the ideal MHD CFL condition, and thus advancing in time about 75 times faster as compared to a fully explicit implementation, see section , in Chapter 3.

5.1.1 Equilibrium atmosphere

We assume a model atmosphere with all hydrodynamic variables and a purely horizontal magnetic field, B_{x0}, stratified in the vertical, z, direction (where the subindex "0" in this and in the ensuing terms refers to equilibrium variables). For our 1D numerical calculation we cover the domain of $L_z = 1.6$ Mm with 32000 equally spaced grid points. MANCHA3D 2F requires variables for the equilibrium atmosphere to be set separately for the neutral and charged components. In practice, any set of equilibrium variables can be used as long as they fulfill the conditions of purely hydrostatic (HS) equilibrium for neutrals, and magneto-hydrostatic (MHS) equilibrium for charges.

In equilibrium, we take the charges and neutrals to have the same background temperature and we use the temperature profile from the VALC (Vernazza et al. 1981) model, starting from heights, z, above $z_0 \approx 500$ km, and ending just below the transition region at a temperature of 9000 K, at $z_f \approx 2.1$ Mm. Apart from the temperature structure, no other stratification from the VALC model can be used directly because Eqs. 3.5 are only valid for hydrogenate plasma. Therefore, we have recalculated the stratification of pressure and density of both neutrals and charges assuming pure hydrogen in order to satisfy the requirements of the HS/MHS equilibrium explained above.

Apart from temperature, the only other parameter taken from VALC is the number density of charges and neutrals at the reference base level, $z_0 \approx 500$ km, with $n_{c0}(z_0) = 5 \times 10^{17}$ m^{-3}, and $n_{n0}(z_0) = 2.1 \times 10^{21}$ m^{-3}. Then, the pressures of charges and neutrals at z_0, $p_{c0}(z_0)$ and $p_{n0}(z_0)$, are obtained from the ideal gas law, Eq. 2.16. As discussed above, we only consider the height range $z = \{z_0, z_f\}$ because the hydrogen plasma model does not provide correct electron number densities in the deeper layers as most available electrons come from metals. Taking into account Eq. 2.16, the equations of HS/MHS balance for neutrals and charges are as follows,

$$\frac{dp_{n0}}{dz} = -\frac{m_n g}{k_B T} p_{n0}, \tag{5.1}$$

$$\frac{d(p_{c0} + p_{m0})}{dz} = -\frac{m_n g}{2k_B T} p_{c0}, \tag{5.2}$$

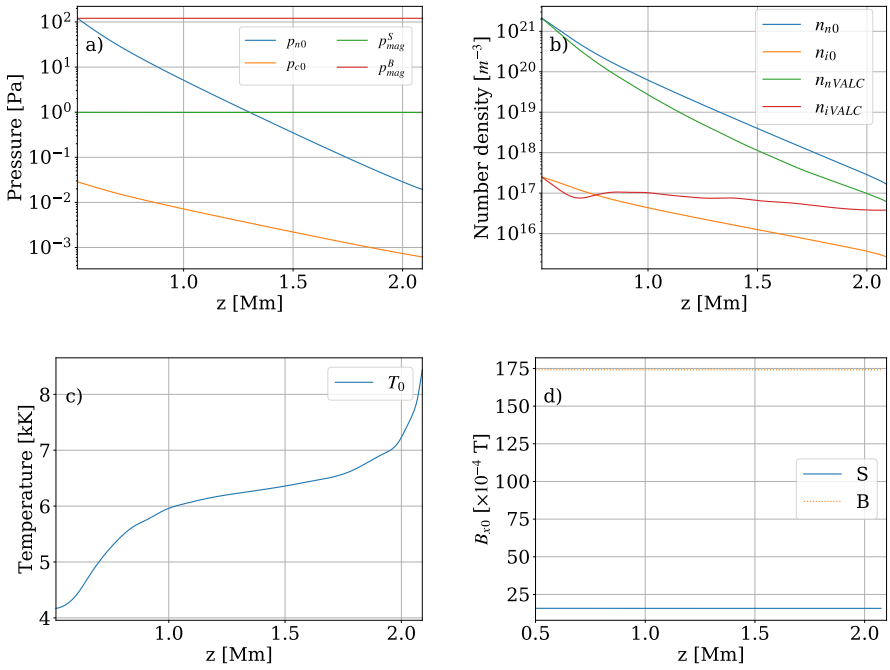

Figure 5.1: Parameters of the background model atmosphere as a function of height. Panel (a): gas pressure of neutrals (blue), charges (orange), and magnetic pressures corresponding to the S magnetic field profile (green) and B profile (red). Panel (b): number density of neutrals (blue), and charges (orange). For comparison, corresponding number densities from VALC model atmosphere are plotted in green and red. Panel (c): temperature. Panel (d): horizontal magnetic field, B_{x0}, of the two background profiles, S and B. Here and below, zero of z axis is taken to be the same as in VALC atmosphere.

where p_{m0} is the magnetic pressure, being the only contribution from the Lorentz force produced by the horizontal magnetic field. The HS equation for neutrals is readily integrated, leading to:

$$p_{n0}(z) = p_{n0}(z_0)\exp\left(-\frac{m_n g}{k_{\rm B}}\int_{z_0}^{z}\frac{1}{T(z')}dz'\right). \tag{5.3}$$

In order to be able to integrate the MHS equation for charges, we assume that the charges pressure

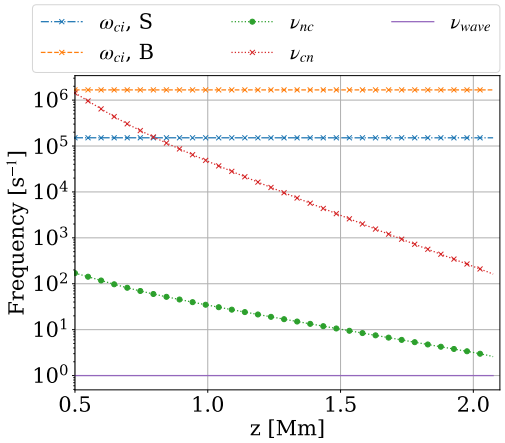

Figure 5.2: Height dependence of the characteristic frequencies calculated for the background atmospheric model: blue and orange lines are ion-cyclotron frequencies corresponding to the S and B magnetic field profiles, red and green lines are ion-neutral and neutral-ion collision frequencies, and violet is the highest wave frequency used is our work, corresponding to the wave period of 1 s.

and the magnetic pressure have the same exponential dependence on height,

$$p_{c0}(z) = p_{c0}(z_0)\exp\left(-2F(z)\right) , \tag{5.4}$$

$$p_{m0}(z) = \frac{B_{x0}(z)^2}{2\mu_0} = \frac{B_{x0}(z_0)^2}{2\mu_0}\exp\left(-2F(z)\right) + C , \tag{5.5}$$

where F should satisfy $F(z) \geq 0$ and $F(z_0) = 0$, and C is a constant. Introducing these expressions into Eq. 5.2, the following expression for $F(z)$ is obtained,

$$F(z) = \frac{m_n g}{4k_{\rm B}} \frac{p_{c0}(z_0)}{p_{c0}(z_0) + B_{x0}(z_0)^2/2\mu_0} \int_{z_0}^{z} \frac{1}{T(z')} dz' . \tag{5.6}$$

By setting the value of $B_{x0}(z_0) = 10^{-4}$ T, a pressure profile of the charged component similar to that of the VALC model is obtained. Given the temperature and pressure profiles with height, the densities are calculated afterwards from the ideal gas laws for neutrals and charges, Eqs. 2.16, taking $\rho_{n0} = n_n m_n$, $\rho_{c0} = n_e m_n$.

The integration constant C in Eq. 5.5 allows flexibility in selecting the strength of the resulting magnetic field. We set,

$$C = p_{n0}\Big|_{z=z_0+jL_z} - \frac{B_{x0}(z_0)^2}{2\mu_0}\exp\left(-2F\Big|_{z=z_0+jL_z}\right) , \tag{5.7}$$

and $B_{x0}(z)$ is then recovered from Eq. 5.5. In this equation, $j \in [0,1]$ is a fraction of the total vertical domain length, $L_z = 1.6$ Mm. By selecting j inside the domain we make sure that neutral pressure and magnetic pressure are equal to each other at $z = z_0 + jL_z$, thus creating two zones in the atmosphere with either neutral gas pressure or magnetic pressure dominating. In the following, we will use two magnetic field profiles, S-profile with $j = 1/2$ and B-profile with $j = 0$. In the case of the S profile, the average field strength is smaller, about 1.5×10^{-3} T, while for the B-profile, it reaches 1.74×10^{-2} T. We note that the integration constant dominates over the space varying term, having the value of 0.988 Pa for the S profile, and 120.73 Pa for the B profile, making the magnetic field profiles almost flat. The difference between the maximum value of the magnetic field, obtained at the base of the atmosphere and the minimum value of the magnetic field, obtained at the top of the atmosphere is maximum for the minimum magnetic field profile that fulfills MHS. This happens when the integration constant is chosen as

$$C = -\frac{B_{x0}(z_0)^2}{2\mu_0}\exp\left(-2F\Big|_{z=z_0+L_z}\right). \tag{5.8}$$

In this case, the magnetic field is zero at the top of the atmosphere and has a value of less than 1G at the base of the atmosphere.

The resulting stratification of pressures, number densities, temperature and magnetic field are displayed in Figure 5.1. It can be observed in panel a that the neutral and magnetic pressures become equal in the middle of the domain for the S profile, and at the bottom of the domain for the B profile, while the thermal pressure of charges always remains below the magnetic pressure. The number densities (panel b) are different compared to those of VALC due to the reasons explained above. However, given all the simplifications of our model, these differences can be considered acceptable.

As will be shown, in order to understand the results of the simulations presented below, it is essential to know the characteristic frequencies associated with the background model atmosphere, such as the ion-cyclotron frequencies and the collision frequencies. The collision frequencies are calculated from Eq. 2.89. These frequencies are given in Figure 5.2 as a function of height. It is observed that for the S magnetic field profile, the ion-neutral collision frequency and the cyclotron frequency become equal in the lower part of the domain at $z \approx 0.8$ Mm, while for the B magnetic field profile the ion-cyclotron frequency is higher than the collision frequency throughout the domain. The highest wave frequency considered in our models corresponds to the period of 1 s (see below). This frequency is at all heights lower than any of the characteristic frequencies.

5.1.2 Perturbation

The perturbation is generated by a driver at the base of the atmosphere. It consists in an oscillatory perturbation in the vertical fluid velocity, and the corresponding perturbations in thermodynamic variables and magnetic field, obtained from an analytical solution. Since the driver is located in the deep and dense layers, we assume strong collisional coupling. The values we choose for the wave frequencies are much smaller than the collisional frequencies (see Figure 5.2). Therefore, in order to

generate the initial solution, we use single-fluid equations, described in Eqs . 3.1, together with the generalized induction equation keeping only the leading effect due to ion-neutral interaction in the solar atmosphere, i.e. the ambipolar diffusion,

$$\begin{aligned}
\frac{\partial \rho}{\partial t} + \nabla \cdot (\rho \mathbf{u}) &= 0, \\
\frac{\partial (\rho \mathbf{u})}{\partial t} + \nabla \cdot (\rho \mathbf{u}\mathbf{u} + p) &= \mathbf{J} \times \mathbf{B} + \rho \mathbf{g}, \\
\frac{\partial}{\partial t}\left(e + \frac{1}{2}\rho u^2\right) + \nabla \cdot \left(\mathbf{u}\,(e + \frac{1}{2}\rho u^2) + p\mathbf{u}\right) &= \mathbf{J} \cdot \mathbf{E} + \rho \mathbf{u} \cdot \mathbf{g}, \\
\frac{\partial \mathbf{B}}{\partial t} - \nabla \times (\mathbf{u} \times \mathbf{B}) - \nabla \times \left[\eta_A \frac{[(\mathbf{J} \times \mathbf{B}) \times \mathbf{B}]}{|B|^2}\right] &= 0,
\end{aligned} \tag{5.9}$$

where the ambipolar diffusivity coefficient is defined as

$$\eta_A = \frac{\xi_n^2 |B|^2}{\alpha \rho_n \rho_c}, \tag{5.10}$$

being $\xi_n = \rho_n/\rho$ the neutral fraction, and the collisional parameter α as defined in Equation (2.88).

These equations can be linearized, taking into account that the magnetic field is purely horizontal and its variation with height is very small compared to the rest of background variables, so that the gradients in B_{x0} can be neglected. We also take into account that both the stratification and the perturbations are only functions of one vertical coordinate, z, and that another independent horizontal direction is x,

$$\begin{aligned}
\frac{\partial \rho_1}{\partial t} &= -u_z \frac{d\rho_0}{dz} - \rho_0 \frac{\partial u_z}{\partial z}, \\
\rho_0 \frac{\partial u_z}{\partial t} &= -\rho_1 g - \frac{\partial p_1}{\partial z} - \frac{1}{\mu_0}\left(\frac{\partial B_{x1}}{\partial z} B_{x0}\right), \\
\frac{\partial p_1}{\partial t} &= c_s^2 \frac{\partial \rho_1}{\partial t} + c_s^2 u_z \frac{d\rho_0}{dz} - u_z \frac{dp_0}{dz}, \\
\frac{\partial B_{x1}}{\partial t} &= -B_{x0} \frac{\partial u_z}{\partial z} + \frac{\eta_A}{\mu_0} \frac{\partial^2 B_{x1}}{\partial z^2} + \frac{1}{\mu_0} \frac{d\eta_A}{dz} \frac{\partial B_{x1}}{\partial z},
\end{aligned} \tag{5.11}$$

where $c_s = \sqrt{\gamma p_0/\rho_0}$ is the sound speed.

Analytical solution of these equations is still complicated and several simplifications need to be made. Since we need to generate the analytical solution in only a few of the bottom grid points (the ghost points), we assume that the temperature is locally uniform, i.e. c_s is also locally uniform, and then the background pressure and density have the same vertical scale height H, i.e.

$$\{p_0, \rho_0\} = \{p_0(z_0), \rho_0(z_0)\} \times \exp(-z/H). \tag{5.12}$$

We further assume that the ambipolar diffusion is negligible at the bottom layer. After these simplifications, the Eqs. 5.11 can be combined into a single wave equation, similar to Eq. 10 provided by Nye & Thomas (1976) for the particular case of $k_x = k_y = 0$,

$$\frac{\partial^2 u_z}{\partial t^2} = \frac{\partial^2 u_z}{\partial z^2}\left(c_s^2 + {v_A}^2\right) - \frac{c_s^2}{H}\frac{\partial u_z}{\partial z}. \tag{5.13}$$

For calculating the solution in the few grid points at the bottom boundary we assume that the quantity $v_A \approx B_{x0}/\sqrt{\mu_0 \rho_0}$ is uniform. Then, the dispersion relation is obtained as usual, assuming the solution of the form, $u_z = V \exp\left(i(\omega t - kz)\right)$,

$$\omega^2 = k^2(c_s^2 + {v_A}^2) - \frac{ik}{H}c_s^2. \tag{5.14}$$

The polarization relations for the amplitudes of the rest of the variables can be derived from Eq. 5.11 by substituting,

$$\left\{\frac{\rho_1}{\rho_0}, \frac{p_1}{p_0}, \frac{B_{x1}}{B_{x0}}\right\} = \{\tilde{R}, \tilde{P}, \tilde{B}\} \exp\left(i(\omega t - kz)\right), \tag{5.15}$$

where $\{\tilde{R}, \tilde{P}, \tilde{B}\}$ are generally complex amplitudes. The following relations are obtained,

$$\begin{aligned} \tilde{R} &= \frac{V}{i\omega}\left(ik + \frac{1}{H}\right), \\ \tilde{P} &= \frac{\gamma V}{i\omega}\left(ik + \frac{1}{\gamma H}\right), \\ \tilde{B} &= \frac{Vk}{\omega}. \end{aligned} \tag{5.16}$$

The wave period $P = 2\pi/\omega$ and the velocity amplitude V at the base of the atmosphere are free parameters of the simulations. Given ω, we obtain k from the dispersion relation, Eq. 5.14. We choose the velocity amplitude at the base of the atmosphere as a fraction of the background sound speed: $V(z_0) = A \cdot 10^{-3} \cdot c_s(z_0)$, where the factor A will be varied from 1 to 100. The wave periods $P = 1, 5, 7.5$ and 20 s are used.

The initial condition for oscillations of neutrals and charges are set in the following way,

$$\begin{aligned} V_n = V \quad &; \quad V_c = V \\ \tilde{R}_n = \frac{\rho_{n0}}{\rho_0}\tilde{R} \quad &; \quad \tilde{R}_c = \frac{\rho_{c0}}{\rho_0}\tilde{R}; \\ \tilde{P}_n = \frac{\rho_{n0}}{\rho_0}\tilde{P} \quad &; \quad \tilde{P}_c = \frac{\rho_{c0}}{\rho_0}\tilde{P}. \end{aligned} \tag{5.17}$$

The analytical wave solution is generated at each time step in the ghost points, as the lower boundary condition. A Perfectly Matched Layer (PML; see Berenger 1994; Felipe et al. 2010) is used as the upper boundary condition. It was described in Section 3.1 of Chapter 3.

5.2 Non-linear wave propagation in stratified plasma

The results of the numerical solution are given in Figures 5.3 and 5.4. Throughout the simulations, we have varied three parameters: the background magnetic field profile, the period, and the amplitude of the wave. The change in the background magnetic field and in the period of the wave can be studied in the linear approximation, while the change in the amplitude is related to the nonlinear effects. These figures show variations with height of the charges and neutral velocities, their temperatures, and the magnetic field, after reaching the stationary state. Figure 5.3 gives the results for two different initial wave amplitudes (factor $A = 1$ and 100), and two different periods ($P = 20$ and 7.5 s) for the background model with S magnetic field profile. Figure 5.4 shows oscillations for two magnetic field profiles (B and S) and two wave periods ($P = 1$ and 5 s), for the same wave amplitude factor $A = 1$.

The first impression from Fig. 5.3 is that the oscillation curves for neutrals and charges are nearly the same. The temperatures of both species are completely collisionally coupled via the thermal exchange process, and therefore oscillations in both temperatures are the same. Nevertheless, one can observe some decoupling in the charges and neutral velocities at the upper part of the atmosphere, at heights above approximately 1.6 Mm. At these heights the collision frequency decreases because of the very low background densities. This strong drop of densities compensates the increase in the background temperature and, consequently, in the value of the collisional parameter α. This decoupling is present independently of the wave amplitude factor, and for both wave periods shown in the figure. It can be observed that velocity oscillations in neutrals slightly lag behind the oscillations in charges. The decoupling is visible not only at the shock wave fronts, but over the entire oscillation curve.

Note that the fast waves considered in this numerical experiment have their vertical wavelength dependent on the Alfvén speed. The increase of the Alfvén speed with height produces oscillations with significantly larger wavelength in the upper part of the atmosphere. This longer wavelength affects the formation of non-linearities (panels c and d). Oscillations have strongly non-linear nature already at the bottom part of the domain for the case $A = 100$. Nevertheless, the shock fronts become smoother at bigger heights.

In general, velocity oscillations in Fig. 5.3 increase their amplitude with height. However, by comparing the panels (a) and (c) it can also be seen that the amplitude increase with height is significantly lower (or even absent) in the case of strong perturbation. Perturbations in the temperature and magnetic field behave differently, and their amplitude starts decreasing after roughly the height where the charges-neutral velocity decoupling becomes visible.

When further decreasing the wave period for the S magnetic field profile, a new effect becomes visible, namely oscillation damping, see Figure 5.4, two upper panels. As a result of this damping, the velocity amplitude decreases after about 1.4 Mm for the wave with $P = 5$ s, and above 1 Mm for the wave with $P = 1$ s. The damping is also apparently sensitive to the magnetic field profile. For the stronger field B (two bottom panels), the $P = 1$ s oscillation becomes damped from the very beginning, and the wave completely disappears after 0.8 Mm. For the $P = 5$ s, oscillations in temperature and magnetic field also become visibly damped, while the velocity amplitude increase is still present. In the case of the wave with $P = 5$ s we can also see significantly larger wavelength of oscillations than

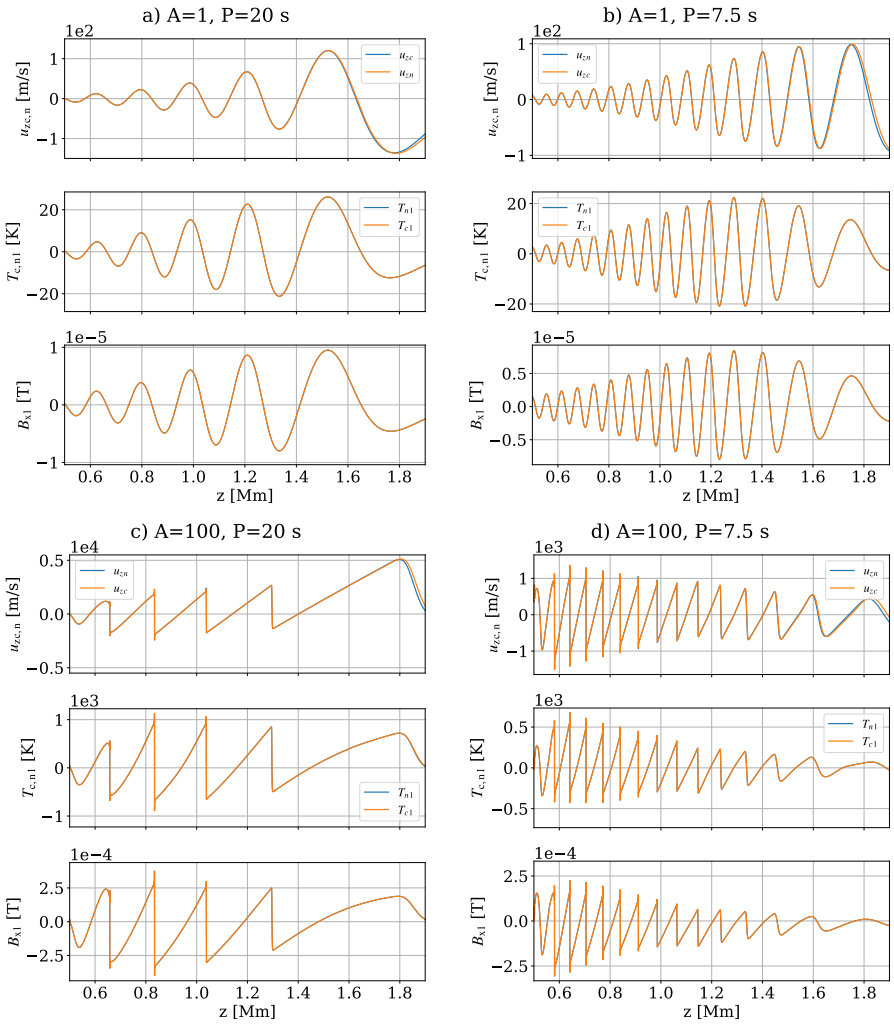

Figure 5.3: Height dependence of the oscillations in velocity and temperature of charges and neutrals, and in the magnetic field after reaching the stationary state, obtained from the numerical solution of the two fluid equations for the magnetic field profile S. Panel (a) and (b) are for the initial wave amplitude factor $A = 1$; panels (c) and (d) are for $A = 100$. The wave period is $P = 20$ s for panels (a) and (c), and $P = 7.5$ s for panels (b) and (d). Orange lines are for the parameters corresponding to charges, and blue lines are those for neutrals. Note that shock overshooting observed in panels c) and d) are numerical artifacts since we run the simulation without any shock capturing algorithm in this case.

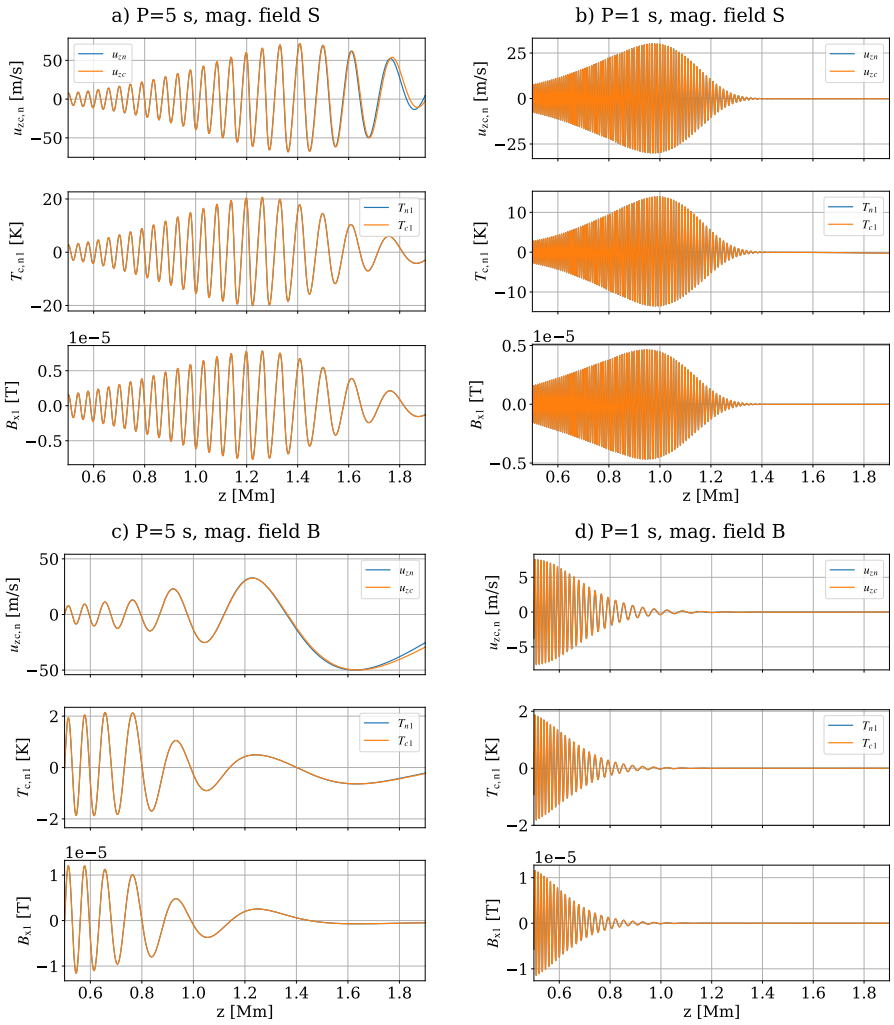

Figure 5.4: Height dependence of the oscillations in velocity and temperature of charges and neutrals, and in the magnetic field after reaching a stationary state, for initial wave amplitude factor $A = 1$. The format of the figure is the same as Fig. 5.3. Panels (a) and (b) are for the S magnetic field profile; panels (c) and (d) are for the B profile. The wave period is $P = 5$ s for panels (a) and (c), and $P = 1$ s for panels (b) and (d).

for the wave with $P = 1$ s, which makes them less affected by collisions. The effect on the damping is discussed in section 5.5.1.

In summary, two main effects on waves are apparent from our simulations: decoupling in charges-neutral velocity, and wave damping. These two effects are not independent from each other. The charges-neutral velocity decoupling can produce wave damping. However the damping can also be produced by more mechanisms. As will be demonstrated later in the chapter, for the case considered here, the wave damping is a consequence of the charges-neutral decoupling and, to a smaller extent, of the nonlinear effects.

5.3 Decoupling

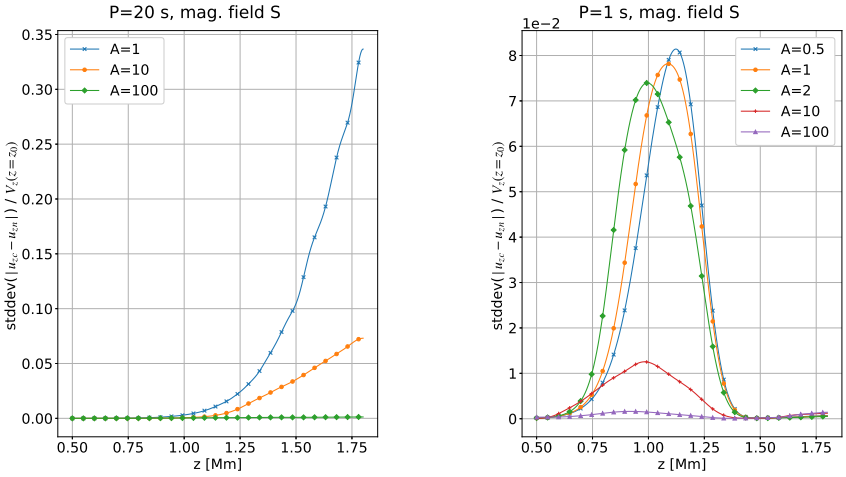

Figure 5.5: Decoupling between charges and neutral velocity as a function of height for the magnetic field profile S. Left panel: wave period 20 s, amplitude factors $A = 1$ (blue), $A = 10$ (orange), $A = 100$ (green). Right panel: wave period 1 s, amplitude factors $A = 0.5$ (blue), $A = 1$ (orange), $A = 2$ (green).

The dependence of the degree of decoupling on the wave period and non-linearities is difficult to evaluate from Figs. 5.3 and 5.4 just "by eye". In order to quantify the effects we have adopted a measure of decoupling by computing the standard deviation in time of $|u_{zc} - u_{zn}|$ in a stationary regime of the simulations (when the waves reached the upper boundary and several periods have passed

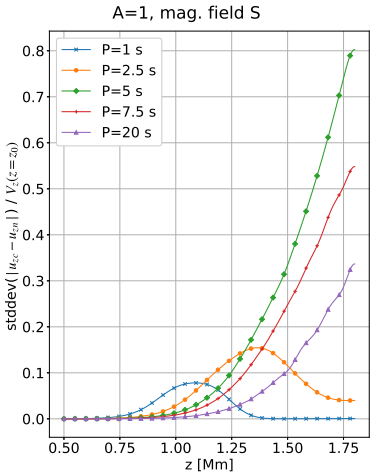

Figure 5.6: Decoupling between charges and neutral velocity as a function of height for the magnetic field profile S and wave amplitude factor $A = 1$, wave periods $P = 20$ s (violet), $P = 7.5$ s (red), $P = 5$ s (green), $P = 2.5$ s (orange) and $P = 1$ s (blue).

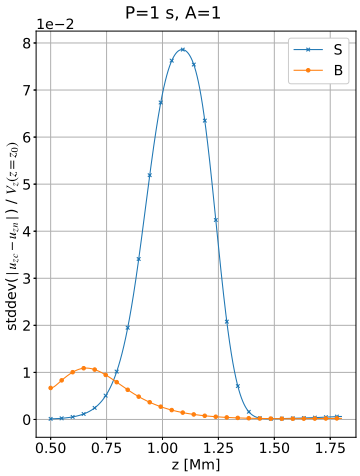

Figure 5.7: Decoupling between charges and neutral velocity as a function of height for the amplitude factor $A = 1$ and wave period $P = 1$ s. The dependence on the magnetic field profiles is shown with different curves: S (blue) and B (orange).

through it), relative to the initial amplitude of the waves at the bottom level z_0 [1]. Such normalization gives us the possibility to better visualize the influence of the non-linear effects. Figures 5.5, 5.6, and 5.7 compare the amount of decoupling as a function of several parameters. In all the cases discussed below, the amount of decoupling normalized to $u_{zc}(z_0)$ varies from a few percent of the initial wave amplitude at the lower layers, to a significant fraction at the upper layers due to the growth of the wave amplitude with height.

Figure 5.5 reveals that the decoupling is a sensitive function of the wave amplitude. For the wave period of 20 s, when oscillation velocities are not visibly damped, see Figure 5.3, the decoupling smoothly grows with height for all the wave amplitudes considered. For progressively more non-linear cases (increasing A) the decoupling starts at lower heights, and increases up to about 1.2 Mm. Above this height, non-linear effects play an important role. Comparing the $A = 1$, $A = 10$ and $A = 100$

[1] Another measure of the decoupling could be simply the value of $u_{zc} - u_{zn}$, with sign. However, $u_{zc} - u_{zn}$ is a quantity which oscillates in time. The standard deviation of $|u_{zc} - u_{zn}|$ (a measure of the decoupling we adopt here) is simply twice smaller than the standard deviation of $|u_{zc} - u_{zn}|$, i.e. stddev $(|u_{zc} - u_{zn}|) = 1/2$ stddev $(u_{zc} - u_{zn})$, thus both measures of decoupling are equivalent.

cases, the decoupling measured relative to the initial wave amplitude is smaller in the later cases.

The action of non-linear effects increases the relative difference between the velocity of charges and neutrals due to the formation of discontinuities associated with shocks. Nevertheless, further increase of A reverses this tendency. The shock waves in the $A = 100$ case become strongly collisionally damped. Because of that, the amplitude of both $u_{\rm zc}$ and $u_{\rm zn}$, and of their difference, decreases compared to the $A = 10$ case. The values of the decoupling measured with respect to the initial wave amplitude become lower at heights where strong shock damping takes place. However, the absolute value of the decoupling (without normalization) will still be larger in the strongly non-linear case $A = 100$.

The right panel of Figure 5.5 shows the case of $P = 1$ s, where strong wave damping was observed. In this case, the decoupling has a broad maximum between 0.8 and 1.2 Mm, and is zero above approximately 1.4 Mm since no wave exists at higher heights. Similar to the previous case, the amount of decoupling depends on the wave amplitude. We observe that the peak becomes slightly lower and it is progressively shifted to lower heights with increasing A, due to non-linear effects.

The amount of decoupling also depends on the wave period. As follows from Figure 5.6, the values of the decoupling smoothly decrease with the period for $P = 5 - 20$ s, showing the same height dependence. The decoupling is maximum for the strongly damped case, $P = 1$ s, at intermediate heights, however it disappears completely above certain height for the reasons explained above. The increase of the magnetic field causes lower decoupling, as shown in Fig. 5.7, and shifts the peak to lower heights.

To better understand the role of the non-linear effects and collisions for the decoupling we have run the simulation with $P = 1$ s again, this time only evolving linear equations with either original collisional parameter α (Eq. 2.88) corresponding to the atmospheric model, or artificially increasing the collisions by a factor 10^4. The results of this experiment are given in Figure 5.8, together with the original non-linear case. It can be seen that the decoupling is larger and its maximum is shifted to higher heights in the linear case (orange line), showing the same tendency as in Fig. 5.5 (right panel). In the case when the collisional parameter α is artificially increased, the decoupling completely disappears (green line).

Therefore, the overall conclusion from the above analysis is that the decoupling increases with decreasing the wave period due to the relative increase of the importance of the collisional time scales compared to the wave scales. Similarly, the absolute value of the decoupling increases with the wave amplitude since non-linearities bring shorter scales to the problem due to the formation of shock waves. However, the value of the decoupling relative to the initial wave amplitude is lower in the strongly non-linear cases due to the collisional damping of the shock waves and the subsequent decrease of the oscillation amplitude of neutrals and charges.

5.4 Evolution of background variables

The difference in the velocity of charges and neutrals leads to frictional dissipation of the kinetic energy of both fluids, and therefore can produce net variations in the atmospheric parameters, such as the temperature. To check the amount of these net variations, we have computed the time averages of the

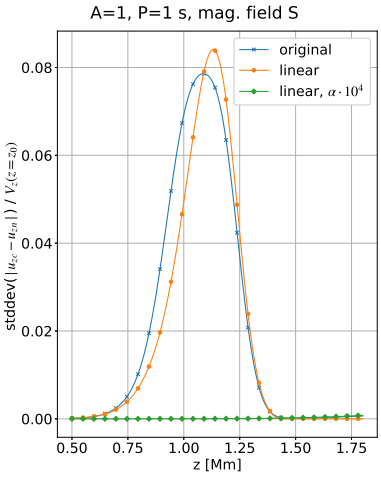

Figure 5.8: Decoupling between charges and neutral velocity as a function of height for the S magnetic field profile and amplitude factor $A = 1$. Blue line: non-linear simulation; orange line: linear simulation; green line: linear simulation with artificially increased collisional parameter α.

perturbed variables as a function of height. The results are given in Figure 5.9 for the case of $P = 1$ s, where the maximum damping was observed for the S magnetic field profile.

Figure 5.9 shows that the temperature has, on average, increased at heights between 0.8 and 1.2 Mm, which coincides with the height range where the decoupling was maximum for this case (Fig. 5.5, right panel). The amount of the temperature increase is about 0.5 K in this case, however it must be compared to the amplitude of the temperature oscillations (about 10 K, see Fig 5.4 b). Therefore, the temperature increase is not negligible. The average temperature increase is accompanied by the decrease of the magnetic field strength, and variations of density and net velocity of the charges and neutrals. As the temperature increases with time, the pressure increases as well producing gas expansion, and a corresponding decrease in the densities. The plasma tied to the magnetic field expands and compresses the field lines. Therefore, the increase in temperature is accompanied by the decrease in the magnetic field. The existence of the non-zero net flow in neutrals and charges (bottom panel) confirms this picture.

A better understanding of the above result is gained through considering the equations of evolution of the internal energy, obtained after removing the kinetic energy part from the corresponding equations of the two-fluid system (Eqs. 2.107, in subsection 2.3.7, Chapter 2), where the viscosity and the

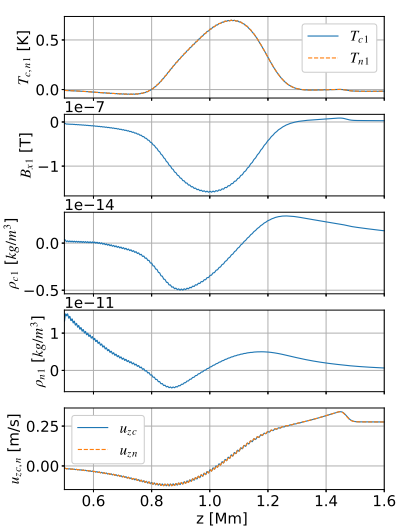

Figure 5.9: Time average of the perturbed variables as a function of height for the simulation with S magnetic field profile, wave period $P = 1$ s and the amplitude factor $A = 2$. From top to bottom: temperatures of neutrals (orange) and charges (blue), magnetic field, density of charges, density of neutrals, velocity of neutrals (orange) and charges (blue).

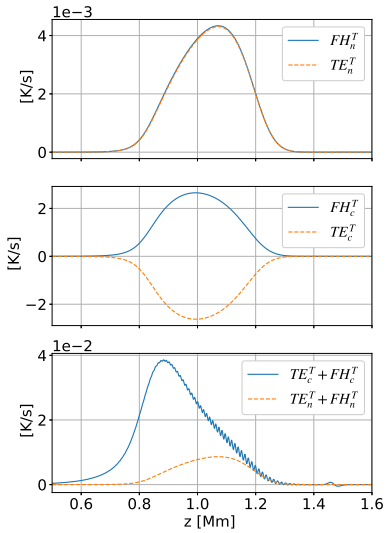

Figure 5.10: Dissipative terms in the temperature equations (Eqs. 5.20) as a function of height for the simulation with S magnetic field profile, wave period $P = 1$ s and the amplitude factor $A = 2$. Top panel: thermal exchange term (TE, orange line) and frictional heating term (FH, blue line) for neutrals. Middle panel: same for charges. Bottom panel: total energy exchange terms for charges (blue), neutrals (orange). Note that apparent oscillations in the bottom panel are numerical artifacts due to averaging the signal with relatively low temporal resolution.

thermal conduction are neglected,

$$\frac{\partial e_{\rm n}}{\partial t} + \nabla \cdot (\mathbf{u}_{\rm n} e_{\rm n}) + p_{\rm n} \nabla \cdot \mathbf{u}_{\rm n} = Q_{\rm n},$$
$$\frac{\partial e_{\rm c}}{\partial t} + \nabla \cdot (\mathbf{u}_{\rm c} e_{\rm c}) + p_{\rm c} \nabla \cdot \mathbf{u}_{\rm c} = \mathbf{J} \cdot \mathbf{E}^* + Q_{\rm c}, \tag{5.18}$$

where $\mathbf{E}^* = \mathbf{E}_{\rm diff} = [\mathbf{E} + \mathbf{u}_{\rm c} \times \mathbf{B}]$. The expressions for collisional terms, Q_n and $Q_{\rm c}$ have the following form,

$$Q_{\rm n} = \frac{1}{2}\alpha\rho_{\rm n}\rho_{\rm c}(\mathbf{u}_{\rm c}-\mathbf{u}_{\rm n})^2 + \frac{1}{\gamma-1}\frac{k_{\rm B}}{m_{\rm n}}\alpha\rho_{\rm n}\rho_{\rm c}(T_{\rm c}-T_{\rm n}),$$
$$Q_{\rm c} = \frac{1}{2}\alpha\rho_{\rm n}\rho_{\rm c}(\mathbf{u}_{\rm c}-\mathbf{u}_{\rm n})^2 - \frac{1}{\gamma-1}\frac{k_{\rm B}}{m_{\rm n}}\alpha\rho_{\rm n}\rho_{\rm c}(T_{\rm c}-T_{\rm n}). \quad (5.19)$$

These collisional terms can be compared with M_n in the total energy equation. The Q_n and Q_c terms do not strictly compensate each other as it happened in the case of M_n. There are contributions proportional to the square of the velocity difference, $(\mathbf{u}_c - \mathbf{u}_n)^2$ that are positive and are added to both charges and neutral energy equations (frictional heating, FH). The second term, i.e. the thermal exchange (TE), is maintained the same compared to M_n. In order to translate the contribution

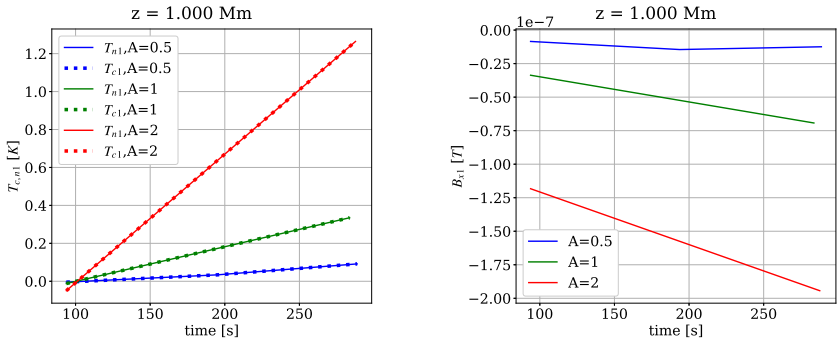

Figure 5.11: Running average of the perturbed temperature (left) and magnetic field (right) as a function of time, for a fixed height $z = 1$ Mm for the simulation with S magnetic field profile, wave period $P = 1$ s. The averaging is taken over three consecutive wave periods. The amplitude factor is $A = 0.5$ (blue), $A = 1$ (green), and $A = 2$ (red). Temperature of neutrals and charges closely match together.

of Q-terms into the temperature increase, one can rewrite the internal energy equation in terms of temperature by substituting $e_n = n_{\rm n}k_{\rm B}T/(\gamma-1)$ and $e_c = 2n_e k_{\rm B}T/(\gamma-1) = n_{\rm c}k_{\rm B}T/(\gamma-1)$. By operating the energy equation using the continuity equations, the temperature evolution equations are

obtained,

$$\frac{\partial T_{\rm n}}{\partial t} + \nabla \cdot (\mathbf{u}_{\rm n} T_{\rm n}) + (\gamma - 1) T_{\rm n} \nabla \cdot \mathbf{u}_{\rm n} = Q_{\rm n} \frac{\gamma - 1}{k_{\rm B} n_{\rm n}},$$
$$\frac{\partial T_{\rm c}}{\partial t} + \nabla \cdot (\mathbf{u}_{\rm c} T_{\rm c}) + (\gamma - 1) T_{\rm c} \nabla \cdot \mathbf{u}_{\rm c} = (\mathbf{J} \cdot \mathbf{E}^* + Q_{\rm c}) \frac{\gamma - 1}{k_{\rm B} n_{\rm c}}. \quad (5.20)$$

The contributions to the terms $Q_{n,c}(\gamma-1)/k_{\rm B}n_{n,c}$ are computed from the same simulation as above. These terms appear to be constant in time. Figure 5.10 shows the height dependence of the frictional heating and thermal exchange terms from Eq. 5.20, for neutrals (upper panel) and charges (middle panel), together with their joint contribution (bottom panel). As expected, the thermal exchange is a positive quantity for the neutrals and a negative quantity for the charges. The negative sign means that the energy would be transferred from charges to neutrals. Due to significantly lower number density of charges, the absolute values of both FH and TE terms in the temperature equation for charges are three orders of magnitude larger than for neutrals. Therefore, the collisions lead to efficient frictional heating of charges, and then this energy is transferred to neutrals via the thermal exchange. With the charges and neutrals thermally coupled, the evolution of the temperature of the fluid as a whole is dominated by the evolution of the neutral temperature.

The constant action of the frictional heating terms leads to an uninterrupted energy supply and an increase of temperature in time. Figure 5.11 shows the time evolution of temperature (left panel) and the magnetic field (right panel) at a fixed point $z = 1$ Mm for the case $P = 1$ s, S magnetic field profile, and varying the amplitude of the perturbation, A. The curves are obtained through calculating the running average over three consecutive wave periods. It can be observed that the increase in temperature is a time cumulative effect, proportional to the square velocity amplitude difference, and that the temperature grows linearly in time. The growth is linear while the modification of the background is of the same order or smaller than the perturbation amplitude. This linear growth is consistent with the value of $Q_{\rm n}(\gamma-1)/k_{\rm B}n_{\rm n} \approx 8 \times 10^{-3}$ K/s, see the bottom panel of Figure 5.10 at the location $z = 1$ Mm. The corresponding drop of the magnetic field strength is also linear with time. The gas is heated and it expands, expelling the field lines, consistent with the picture from Fig. 5.9.

5.5 Reasons for wave damping

One of the interesting results obtained above is the wave damping, i.e. the decrease of the wave amplitude (or even a complete disappearance of the wave) after a certain height. This effect is especially pronounced for the high-frequency perturbations.

There can be several reasons for this damping. One of them can be ion-neutral collisions, well investigated in the linear theory (Ballester et al. 2018). Yet another reason can be wave reflection due to the gradient of the Alfvén speed with height. It is well known that fast magneto-acoustic waves refract and reflect in the solar atmosphere due to this reason (Cally 2006; Khomenko & Collados 2006a), a phenomenon that is actually thought to be responsible for the formation of high frequency acoustic halos in observations (Khomenko & Collados 2009; Rijs et al. 2016).

In order to check if the waves are reflected in our experiment, we have computed the acoustic wave energy fluxes, as $p_{\rm c1}u_{\rm zc}$ for charges, and as $p_{\rm n1}u_{\rm zn}$ for neutrals. It turned out that both fluxes are positive at all heights, meaning vertical wave propagation, and no apparent reflection. The energy fluxes vanish after a certain height above 1.2 Mm, which means that the waves have turned to be non-propagating. The reasons of this behavior are better highlighted with the help of the analytical solution, developed below, in section 5.5.1.

5.5.1 Comparison between analytical and numerical results

In order to distinguish between the damping produced by the decoupling of the neutral and charged fluids in the linear regime, and the damping caused by the decoupling at the shock fronts or the steepening in the wave profile in the non-linear regime, we have compared the numerical solution of the linear and non-linear two-fluid equations, with the analytical solution.

The analytical solution is obtained by solving the linearized two fluid equations with nonuniform background, for each species. We introduced the coupling term in the momentum equations, and assumed the collisional parameter α to be constant in time, equal to the value corresponding to the equilibrium atmosphere, consistent with the linear approximation. The linearized equations take the following form,

$$\begin{aligned}
\frac{\partial \rho_{\rm c1}}{\partial t} + u_{\rm zc}\frac{d\rho_{\rm c0}}{dz} + \rho_{\rm c0}\frac{\partial u_{\rm zc}}{\partial z} &= 0,\\
\frac{\partial \rho_{\rm n1}}{\partial t} + u_{\rm zn}\frac{d\rho_{\rm n0}}{dz} + \rho_{\rm n0}\frac{\partial u_{\rm zn}}{\partial z} &= 0,\\
\rho_{\rm c0}\frac{\partial u_{\rm zc}}{\partial t} = -\rho_{\rm c1}g - \frac{\partial p_{\rm c1}}{\partial z} - \frac{1}{\mu_0}\left(\frac{\partial B_{\rm x1}}{\partial z}B_{\rm x0} + \frac{dB_{\rm x0}}{dz}B_{\rm x1}\right) &+ \alpha\rho_{\rm n0}\rho_{\rm c0}(u_{\rm zn} - u_{\rm zc}),\\
\rho_{\rm n0}\frac{\partial u_{\rm zn}}{\partial t} = -\rho_{\rm n1}g - \frac{\partial p_{\rm n1}}{\partial z} &+ \alpha\rho_{\rm n0}\rho_{\rm c0}(u_{\rm zc} - u_{\rm zn}),\\
\frac{\partial p_{\rm c1}}{\partial t} = c_{\rm c0}^2\frac{\partial \rho_{\rm c1}}{\partial t} + c_{\rm c0}^2 u_{\rm zc}\frac{d\rho_{\rm c0}}{dz} - u_{\rm zc}\frac{dp_{\rm c0}}{dz},&\\
\frac{\partial p_{\rm n1}}{\partial t} = c_{\rm n0}^2\frac{\partial \rho_{\rm n1}}{\partial t} + c_{\rm n0}^2 u_{\rm zn}\frac{d\rho_{\rm n0}}{dz} - u_{\rm zn}\frac{dp_{\rm n0}}{dz},&\\
\frac{\partial B_{\rm x1}}{\partial t} = -B_{\rm x0}\frac{\partial u_{\rm zc}}{\partial z} - u_{\rm zc}\frac{dB_{\rm x0}}{dz}.&
\end{aligned} \tag{5.21}$$

These equations are combined into two coupled partial differential equations for the vertical velocity of each species, coupled by the collisional terms.

$$\begin{aligned}
\frac{\partial^2 u_{\rm zc}}{\partial t^2} &= a_c(z)\frac{\partial^2 u_{\rm zc}}{\partial z^2} + b_c(z)\frac{\partial u_{\rm zc}}{\partial z} + \alpha\rho_{\rm n0}\left(\frac{\partial u_{\rm zn}}{\partial t} - \frac{\partial u_{\rm zc}}{\partial t}\right),\\
\frac{\partial^2 u_{\rm zn}}{\partial t^2} &= a_n(z)\frac{\partial^2 u_{\rm zn}}{\partial z^2} + b_n(z)\frac{\partial u_{\rm zn}}{\partial z} + \alpha\rho_{\rm c0}\left(\frac{\partial u_{\rm zc}}{\partial t} - \frac{\partial u_{\rm zn}}{\partial t}\right),
\end{aligned} \tag{5.22}$$

where

$$a_c(z) = c_{\rm c0}^2 + v_{A0}^2, \quad a_n(z) = c_{\rm n0}^2,$$
$$b_{c,n}(z) = \frac{1}{\rho_{c,n_0}} \frac{d\left(\rho_{c,n_0} a_{c,n}\right)}{dz},$$
$$c_{c,n_0}^2 = \gamma \frac{p_{c,n_0}}{\rho_{c,n_0}}, \quad v_{A0}^2 = \frac{B_{x0}^2}{\mu_0 \rho_{c0}}. \tag{5.23}$$

Assuming the functional dependence on space and time of the vertical velocity of the form $\{u_{\rm zc}(z,t)$, $u_{\rm zn}(z,t)\} = \{\tilde{u}_{\rm zc}(z), \tilde{u}_{\rm zn}(z)\} \times \exp(i\omega t)$, where the frequency ω is fixed, the above coupled system can be rewritten as,

$$-\omega^2 \tilde{u}_{\rm zc} = a_c(z) \frac{d^2 \tilde{u}_{\rm zc}}{dz^2} + b_c(z) \frac{d\tilde{u}_{\rm zc}}{dz} + i\omega\alpha\rho_{\rm n0} \left(\tilde{u}_{\rm zn} - \tilde{u}_{\rm zc}\right),$$
$$-\omega^2 \tilde{u}_{\rm zn} = a_n(z) \frac{d^2 \tilde{u}_{\rm zn}}{dz^2} + b_n(z) \frac{d\tilde{u}_{\rm zn}}{dz} + i\omega\alpha\rho_{\rm c0} \left(\tilde{u}_{\rm zc} - \tilde{u}_{\rm zn}\right). \tag{5.24}$$

Combining these two equations we obtain:

$$\frac{d^4 \tilde{u}_{\rm zc}}{dz^4} a_c a_n + \frac{d^3 \tilde{u}_{\rm zc}}{dz^3} \left(a_n b_c + a_c b_n\right) + \frac{d^2 \tilde{u}_{\rm zc}}{dz^2} \left(b_c b_n + \omega^2 (a_c + a_n) - i\alpha\omega(a_c\rho_{c0} + a_n\rho_{n0})\right) +$$
$$\frac{d\tilde{u}_{\rm zc}}{dz} \omega \left(\omega(b_c + b_n) - i\alpha(b_c\rho_{c0} + b_n\rho_{n0})\right) + \tilde{u}_{\rm zc}\omega^3 \left(\omega - i\alpha(\rho_{c0} + \rho_{n0})\right) = 0. \tag{5.25}$$

The coefficients of the spatial derivatives that appear in Eq. (5.25) are not uniform and there is no apparent exact analytical solution to Eq. (5.25). The waves we consider in this study are short-period waves with wavelengths short relative to the equilibrium gradient scales. Thus, we use the WKB approximation to seek solutions of Eq. (5.25) of the form

$$\{\tilde{u}_{\rm zn}, \tilde{u}_{\rm zc}\} = \{V_n(z), V_c(z)\} \cdot \exp\left[i\phi(z)\right], \tag{5.26}$$

where V_n, and V_c are space dependent complex amplitudes, and

$$\phi(z) = -\int_0^z k(z')dz'. \tag{5.27}$$

In the spirit of the WKB approximation, we assume that the velocity amplitude and the wave number gradients are small and of the same order,

$$\frac{d\phi}{dz} = -k = -k_0 - \epsilon k_1(z),$$
$$V_{c,n}(z) = V_{c,n0} + \epsilon V_{c,n1}(z), \tag{5.28}$$

with ϵ being a small parameter and the second derivatives of $k_1(z)$ and $V_{c,n1}$ being zero. It is then straightforward to calculate,

$$\begin{aligned}
\frac{d\tilde{u}_{zc}}{dz} &= \left(\epsilon\frac{dV_{c1}}{dz} - ikV_{c1}\right)\cdot\exp(i\phi),\\
\frac{d^2\tilde{u}_{zc}}{dz^2} &= \left(-2i\epsilon k\frac{dV_{c1}}{dz} + i\epsilon V_{c1}\frac{dk_1}{dz} - k^2V_{c1}\right)\cdot\exp(i\phi),\\
\frac{d^3\tilde{u}_{zc}}{dz^3} &= \left(-3\epsilon k\frac{dV_{c1}}{dz} - 3\epsilon V_{c1}\frac{dk_1}{dz} + ik^2V_{c1}\right)\cdot k\cdot\exp(i\phi),\\
\frac{d^4\tilde{u}_{zc}}{dz^4} &= \left(4i\epsilon k\frac{dV_{c1}}{dz} + 6i\epsilon V_{c1}\frac{dk_1}{dz} + k^2V_{c1}\right)\cdot k^2\cdot\exp(i\phi).
\end{aligned} \tag{5.29}$$

Substituting these expressions into Eq. 5.25, and keeping only 0th-order terms, the dispersion relation for k is obtained,

$$(\omega^2 - k^2a_c - ikb_c)(\omega^2 - k^2a_n - ikb_n) + i\omega\alpha\rho_0(-\omega^2 + k^2a + ikb) = 0\,, \tag{5.30}$$

where the remaining coefficients have been defined as,

$$b = (\rho_{n0}b_n + \rho_{c0}b_c)/\rho_0; \quad a = (\rho_{n0}a_n + \rho_{c0}a_c)/\rho_0\,, \tag{5.31}$$

with $\rho_0 = \rho_{c0} + \rho_{n0}$.

Next, the relations (5.29) are replaced into equations (5.24). Separating the 0th-order terms, from the 1st-order terms, the expressions for the velocity amplitudes are obtained,

$$V_{c,n}(z) = V_{c,n}|_{z=0}\cdot\exp\left(\int_0^z \frac{dk}{dz}\frac{ia_{c,n}}{b_{c,n} - 2ika_{c,n}}dz'\right). \tag{5.32}$$

In the limit of $\alpha\rho_0 \gg \omega$, Eq. (5.30) reduces to the single-fluid dispersion relation.

$$-\omega^2 + k^2a + ikb = 0. \tag{5.33}$$

In the opposite limit, when $\alpha\rho_0 \ll \omega$ we recover the dispersion relations of either neutrals or charges. Otherwise, if $\frac{\alpha\rho_0}{\omega} \approx 1$, both terms in the equation are equally important.

It is interesting to analyze the effect of collisional damping separately from the effect of the stratification. The effect of the stratification is independent of the wave frequency for high-frequency waves considered here. By neglecting the stratification, the dispersion relation, Eq. (5.30) becomes the dispersion relation in a uniform atmosphere,

$$(\omega^2 - k^2a_c)(\omega^2 - k^2a_n) + i\omega\alpha\rho_0(-\omega^2 + k^2a) = 0. \tag{5.34}$$

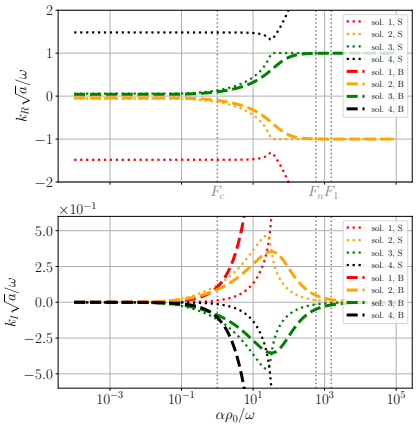

Figure 5.12: Solutions of the non-dimensional dispersion relation without stratification, Eq. (5.36). The upper and lower panels show the real and imaginary part of k, scaled with $\sqrt{a}/\omega$ as a function of the ratio between the collisional and wave frequencies, scaled with ρ_0. Solutions labeled as "S" (dashed lines) are for S magnetic field; solutions labeled "B" (solid lines) are for B magnetic field. The vertical dotted lines mark values of $\omega = \nu_{in}$ (F_c), $\omega = \nu_{ni}$ (F_n), and $\omega = 2\pi/1$ (F_1) for the 1 s period wave.

We consider the solutions of this equation as a function of the wave period. Using the non-dimensional variables,

$$F = \alpha\rho_0/\omega; \qquad E = k\sqrt{a}/\omega, \tag{5.35}$$

the dispersion relation Eq. (5.34) becomes

$$(1 - E^2 a_c/a)(1 - E^2 a_n/a) - iF(1 - E^2) = 0. \tag{5.36}$$

Figure 5.12 shows the real and imaginary part of the four solutions, E, of the fourth order dispersion relation, Eq. (5.36), as a function of the non-dimensional variable F, which is the ratio between the collisional and the wave frequencies, scaled with ρ_0. This dispersion relation has been solved using the values for a_n, a_c, and a corresponding to a point located at the middle of the atmosphere for S and B magnetic field profiles. The values on the horizontal axis cover a large range, from the uncoupled case, when $F = 10^{-4}$ to the strongly coupled case, for $F = 10^5$. We have marked the values of F corresponding to the cases of $\omega = \nu_{in}$ (ion-neutral collision frequency), $\omega = \nu_{ni}$ (neutral-ion collision frequency), and $\omega = 2\pi/1$ (frequency corresponding to the period of a 1 s wave) by F_c, F_n, and F_1, respectively. The values of the frequencies are calculated for the height corresponding to the middle of the domain.

We can observe that for small F, corresponding to high frequencies ω (uncoupled case), the waves propagate with the characteristic speed of either charges ($\sqrt{a_c}$, downward solution #1, and upward solution #4) or with the characteristic speed of neutrals ($\sqrt{a_n}$, downward solution #2, and upward

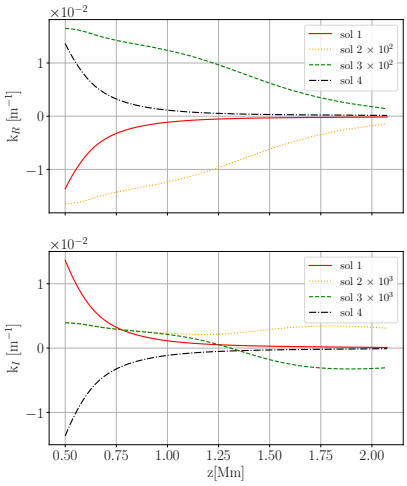

Figure 5.13: Solutions of the dispersion relation (5.30) for the two-fluid linearized equations. The upper and lower panels show the real and imaginary part of k as a function of height, calculated for the magnetic field profile S and 5 s period.

solution #3). The imaginary part of k in the uncoupled case is zero, meaning no damping. This result is similar to that reported in Popescu Braileanu et al. (2019a).

For the large values of F, corresponding to low frequencies ω (strongly coupled case), there are two solutions, which propagate with the characteristic speed in the fluid as a whole, $\sqrt{a}$, both upwards (#2) and downwards (#3). Another two solutions, #1 and #4 have very large real and imaginary part of k. These are waves with very large phase speed but also extremely large damping, and we consider them unphysical.

Solutions #2 and #3 (yellow and green lines) have maximum damping, k_I, for waves in the frequency range between $\nu_{\rm ni}$ and $\nu_{\rm in}$. This is true for both magnetic field profiles B and S. For the larger magnetic field B, the maximum damping shifts to higher frequencies. We have checked that for even higher magnetic fields the dispersion curves remain practically equal to the case B. For the 1 s period wave, the value of damping is decreased from its maximum, but it is still non-zero, which explains the damping we observe in our simulations.

The full dispersion relation which includes stratification, (Eq. 5.30) is also 4th order in k and has four different roots. Examples of these four different solutions as function of the height in the atmosphere are illustrated in Fig. 5.13, calculated for the S magnetic field profile and the wave period of 5 s. According to Figure 5.12, from the point of view of the collisions, this is the coupled case. It can be seen that the solutions #1 and #4 have both very large imaginary and real parts. These modes

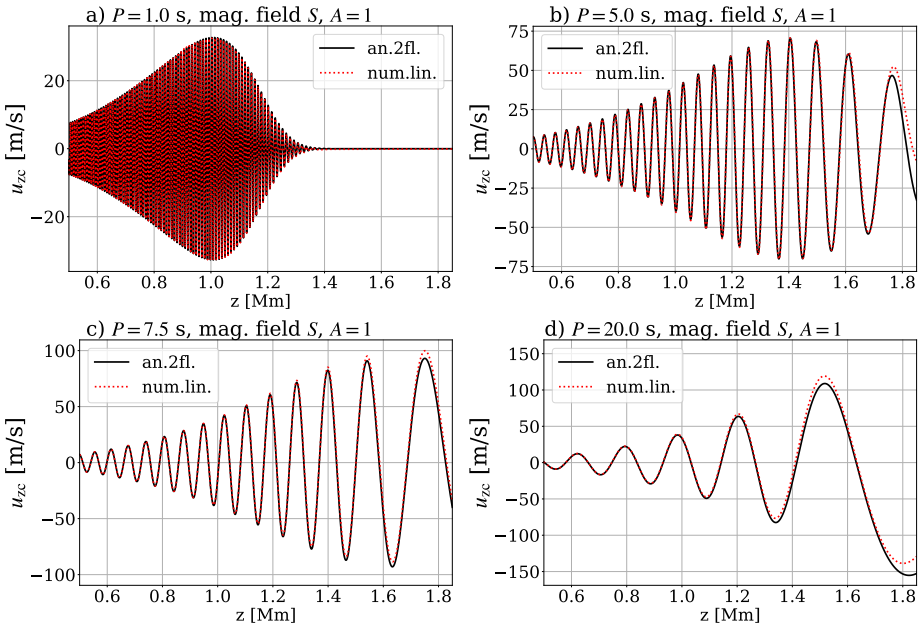

Figure 5.14: Comparison between the numerical solution in the linear regime (black lines) and the analytical solution of the two-fluid equations (red dotted line). Individual panels show snapshots of the velocity of charges as a function of height at fixed time moments in the stationary regime of the simulations. Panels from left to right, from top to bottom are for wave periods of 1, 5, 7.5 and 20 s, and S magnetic field profile. Note that the analytical solution slightly overshoots the numerical solution, the effect being more pronounced towards the upper part of the domain. This is due to the fact that the analytical solution is an approximate solution.

have therefore very low propagation speeds and very high damping, similarly to the case without stratification. We do not consider these solutions further. The other two solutions (marked #2 and #3) represent waves that propagate either up (solution #3) or down (solution #2) and their damping is moderate. It can be seen that k_I of both solutions matches for the first 0.5 Mm from the bottom, and has positive values, corresponding to the wave amplification. At these heights the charges-neutral decoupling is not strong enough to damp the waves and the growth of the wave amplitude with height is caused simply by the gravitational stratification of the atmosphere. Higher up, k_I turns negative for the solution #3, meaning wave damping. The same amount of damping is also present in the solution #2, however k_I is positive because the wave propagates downwards (negative k_R). For the comparison

below we use the solution #3.

Figure 5.14 compares the numerical solutions of the linearized equations with the analytical solution for different wave periods and the magnetic field profile S. One can observe that both solutions match rather well and small differences are only observed in the upper layers. The analytical solution in the WKB approximation is able to describe rather precisely the damping of waves due to collisions in the linear regime. Therefore, we can conclude that the wave damping observed in these simulations is determined mainly by the linear decoupling.

Figure 5.15 illustrates further the effects of the linear decoupling on the wave amplitudes. It shows the imaginary part of the wave vector k_I for the solution #3, as a function of the wave period (left) and of the magnetic field strength (right). The value and sign of k_I is directly related to the modification of the wave amplitude with height. It can be seen that in all cases, k_I changes sign at some height in the atmosphere. At the bottom part of the atmosphere, k_I is positive, meaning the growth of the wave amplitude with height due to gravitational stratification, as explained above. Once the collision frequency decreases with height, the effects of the linear wave damping become progressively more important and k_I changes sign. The damping starts at lower heights for shorter period waves. This happens because the wave frequency approaches the neutral-ion collisional frequency (ν_{ni}) and the collisions alter the wave propagation, consistently with Figure 5.12, where we did not take into account the stratification. The damping also starts at lower height for stronger magnetic fields, consistent with the results of the simulations shown in the previous sections. However, the absolute value of damping is higher for lower B (so the damping length is shorter). Decreasing the value of the magnetic field for a fixed wave frequency results in a decrease of the wavelength, which facilitates the effects of collisions on the wave damping.

Considering the propagation for different magnetic field strengths, we observe two effects, one due to the stratification which increases the amplitude of the wave, and the other due to the collisions which damps the wave. The amplification effects are stronger in the lower part of the atmosphere because of the lower temperatures and, consequently, the pressure scale height. The damping effects is stronger in the upper part of the atmosphere. The interplay between two effects can be observed in Fig. 5.13, by analyzing the imaginary part of the solutions #2 and #3. In the lower part of the atmosphere the values are positive (meaning increase of the amplitude) because of the stratification, and are identical for #3 and #2 because the effects of collisional damping are negligible. When the collisional damping become important in the upper part of the atmosphere, the two curves split and become symmetric with respect to the $k_I = 0$ line, meaning that the stratification does not play a major role in amplifying the wave amplitude anymore. The absolute values of both, amplification and damping, are smaller for larger magnetic fields. The height when the damping effects overcome those of the stratification is lower for smaller magnetic fields.

Approaching the limit of the absence of the magnetic field ($B \approx 0$), since the temperature of charges and neutrals are the same, the propagation speeds of both species will also become very close to each other. In this case, there will be very little damping for the periods considered here, as we can see in Figure 5.15, panel b.

The non-linear effects on the wave damping are shown in Figures 5.16 and 5.17. These figure compare

the numerical solutions done with the same initial amplitudes A=10, and A=100, respectively, but in the linear and non-linear regimes. The non-linear effects significantly increase the wave damping for all considered wave frequencies. At lower heights, when the non-linear steepening of the wave profile is not yet pronounced, the linear and non-linear solutions match, both showing an increase of the wave amplitude with height due to the gravitational stratification. However, at higher heights the amplitudes of the linear and non-linear solutions become very different. The waves are significantly more damped in the non-linear regime, and the effect strongly depends on the wave period. The effective shortening of the scale at the wave fronts facilitates the collisional damping. The non-linear fronts form at lower heights for shorter period waves and therefore, non-linear effects for such waves are significantly more pronounced. One can compare the effective decrease of the amplitude between the non-linear and linear cases in Figures 5.16 and 5.17, showing how the progressively larger periods are less affected by the non-linear effects. For larger amplitudes in Figure 5.17 the damping of the wave due to non-linear effects are more pronounced. We conclude that non-linear steepening of the wave fronts increases dramatically the collisional damping of waves in the chromosphere.

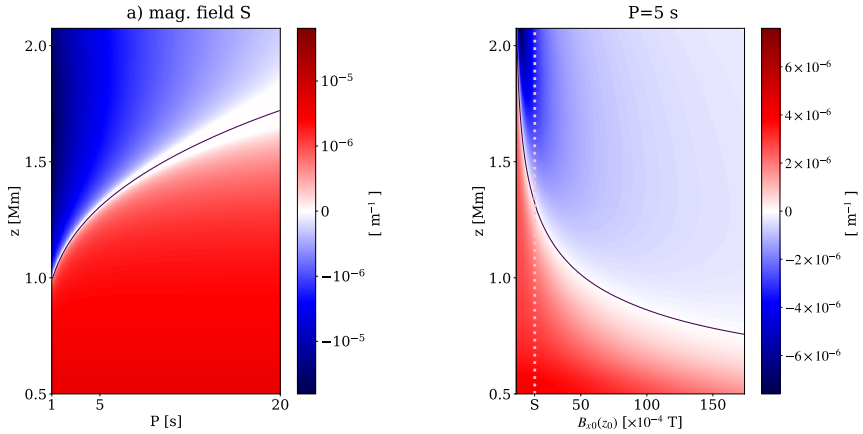

Figure 5.15: Left panel: imaginary part of k as function of the wave period (horizontal axis) and height (vertical axis) obtained after solving the dispersion relation for the two-fluid equations (Eq. 5.30) for S magnetic field profile. Solution #3 from Figure 5.13 is used. The period varies between 1 s and 20 s (the minimum and maximum values used in the simulations). The solid, black line represents the contour of $k_I = 0$. Right panel: imaginary part of k as function of the background magnetic field at the base of the atmosphere (horizontal axis) and height (vertical axis). The wave period is fixed to 5 s.

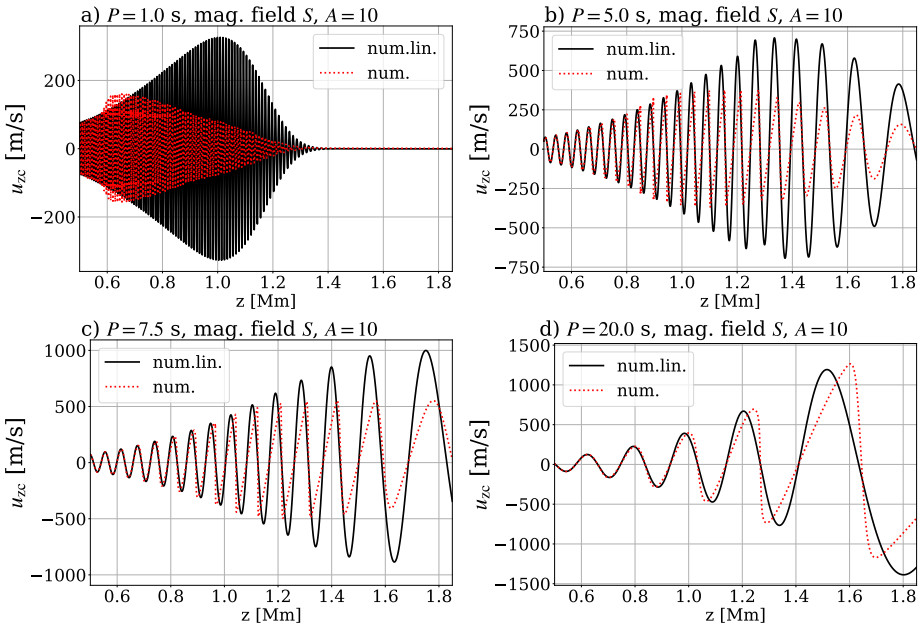

Figure 5.16: Comparison between the numerical solution in the linear regime (black lines) and the non-linear regime with A=10 (red dotted line). Individual panels show snapshots of the velocity of charges as a function of height at fixed time moments in the stationary regime of the simulations. Panels from left to right, from top to bottom are for wave periods of 1, 5, 7.5 and 20 s, and S magnetic field profile.

5.6 Comparison with single fluid model with ambipolar diffusion

Single-fluid approximation incorporates partial ionization effects by including additional terms in the induction equation. The interaction of neutrals with electrons and ions is modeled through the ambipolar term. In order to compare the two models, we have evolved numerically the two fluid equations and the single fluid equations with the ambipolar term, Eqs. 5.9, under the same conditions. The single fluid simulation has been run with the same code. The two-fluid simulation is run with ideal Ohm's law, while for the single-fluid simulation we add the ambipolar term in the Ohm's law. The ambipolar coefficient used in the single-fluid simulation has been calculated from parameters of the two-fluid atmosphere, as defined in Eq. 5.10, but divided by μ_0, and its value as a function of height is plotted in Figure 5.18 in units of m^2/s. We ran both simulations with 10 times lower resolution (3200

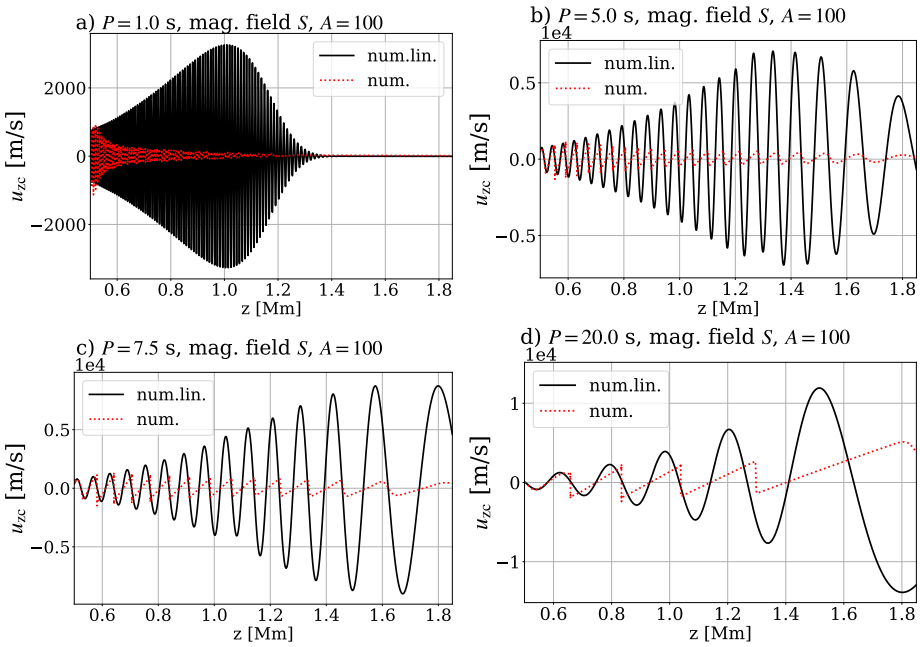

Figure 5.17: Comparison between the numerical solution in the linear regime (black lines) and the non-linear regime with A=100 (red dotted line). Individual panels show snapshots of the velocity of charges as a function of height at fixed time moments in the stationary regime of the simulations. Panels from left to right, from top to bottom are for wave periods of 1, 5, 7.5 and 20 s, and S magnetic field profile.

points in the z direction) than described above. This is so, because the ambipolar term is hyperbolic and requires very small time steps in an explicit implementation. This limitation has been overcome in newer versions of the single fluid MANCHA3D code (see González-Morales et al. 2018), but we did not use this version.

We compare the snapshots of the perturbed variables taken in the stationary regime, as a function of height in Figure 5.19. In the single-fluid case we plot the vertical velocity, and the perturbations in the temperature and the horizontal component of the magnetic field as functions of height. For the two-fluid simulation, the quantity plotted is the vertical velocity of the center of mass of the two fluids, $(\rho_c u_{zc} + \rho_n u_{zn})/(\rho_c + \rho_n)$. Similarly, for the perturbation of the temperature, for the two fluid simulation we plot: $(\rho_c T_{c1} + \rho_n T_{n1})/(\rho_c + \rho_n)$. The full densities, including the equilibrium densities

of neutrals and charges have been used in the above definitions.

We can observe in the three panels of Figure 5.19 that the three quantities plotted match very well at the bottom of the atmosphere, while we can see some differences in the upper part of the domain. Above the height of 1.2 Mm in the atmosphere, the charges start to decouple from the neutrals. This is the main reason for the damping of the wave that can be seen above this height. The ambipolar coefficient varies several orders of magnitude through the atmosphere. The principal reason for this increase is the decrease of the density, and therefore the drop of the collision frequency. The fact that the two solutions match so well in the lower part of the atmosphere, where the charges and neutrals are very well collisionally coupled, is another argument for the correctness of numerics in Mancha3D 2F. The single-fluid solution shows more damping than the two-fluid solution in the upper part of the atmosphere above 1.3 Mm height.

Figure 5.20 compares the time average of the perturbed variables as a function of height calculated from the results of the two simulations. For the two-fluid simulation, the plot shows the sum of the density of neutrals and charges, the center of mass vertical velocity and the mass-weighted temperatures of the two fluids, as before. The average has been done in time, for all the snapshots of the simulation, thus reflecting changes in the background variables. It is shown as a function of height. We can observe that the increase in the background temperature in the two-fluid case, is 5-10 larger than in the single-fluid case, the difference is the largest in the upper part of the atmosphere, above 1.3 Mm, where the two-fluid and single fluid approximations diverge, as follows from Figure 5.19 above. There are also small differences in the average velocity and magnetic field in the upper part of the domain and in the densities in the bottom part of the domain.

As discussed above, in the two-fluid simulation the gas is heated and it expands. This large difference in densities in the deep layers seen in the figure gives a false impression. The density is stratified exponentially, therefore smaller relative differences in density in the deep layers are seen as large absolute differences in our plot, because the values have not been normalized. The small differences in the average velocity and magnetic field between the two models can be consequences of the fact that the plasma is heated more in the two-fluid case. The increase in temperature is due to the frictional heating, i.e. kinetic energy is converted into thermal energy. In the single-fluid approximation, the magnetic field decreases because it is dissipated through the ambipolar term. In this case, the increase in temperature is due to the conversion of magnetic energy into thermal energy through the ambipolar term.

The large differences in the increase in temperature between the two models show that the ambipolar term does not capture in the same way as in the two-fluid assumption the heating due to the collisions.

5.7 Discussion and conclusions

In this work we have performed simulations of fast magneto-acoustic waves in the solar chromosphere using a two-fluid approach. We used stratified temperature distribution and number densities for charges and neutrals consistent with VALC solar model, and considered two magnetic field profiles with an order of magnitude different field strengths. We observe that waves in neutrals and plasma,

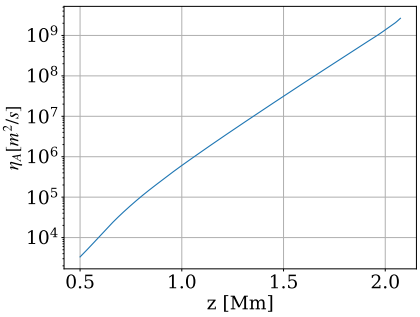

Figure 5.18: The ambipolar diffusivity coefficient as a function of height.

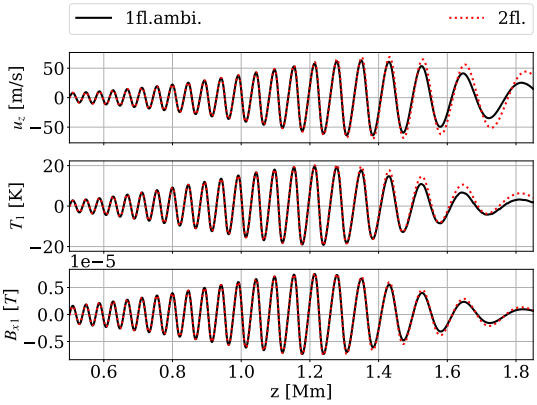

Figure 5.19: Comparison between the numerical solution in the two fluid approximation (black lines) and the single fluid approximation with ambipolar term (red dotted lines) with the following parameters: S magnetic field profile, wave period $P = 5$ s and the amplitude factor $A = 1$. The panels show snapshots of the velocity, and perturbations of the temperature of charges and the magnetic field as a function of height at a fixed time moment in the stationary regime of the simulations. For the two fluid simulation, the quantities plotted for the vertical velocity and the temperature are the center of mass velocity and perturbation of temperature, $(\rho_c u_{zc} + \rho_n u_{zn})/(\rho_c + \rho_n)$, and $(\rho_c T_{c1} + \rho_n T_{n1})/(\rho_c + \rho_n)$, respectively. Notice that these two quantities have been calculated with full densities, $\rho_c = \rho_{c0} + \rho_{c1}$, and $\rho_n = \rho_{n0} + \rho_{n1}$.

initially coupled at the upper photosphere, become uncoupled at higher heights in the chromosphere. This decoupling can be a consequence of either the characteristic spatial scale at the shock front becoming similar to the collisional scale, or the change of the relation between the wave frequency, ion cyclotron frequency, and the collisional frequency with height. The decoupling height is a sensitive function of the wave frequency, wave amplitude, and the magnetic field strength. We observe that the decoupling causes damping of waves and increase of the background temperature due to the frictional heating. The comparison between analytical and numerical results allows us to separate the role of the non-linear effects from the linear ones on the decoupling and damping of waves. Our main findings

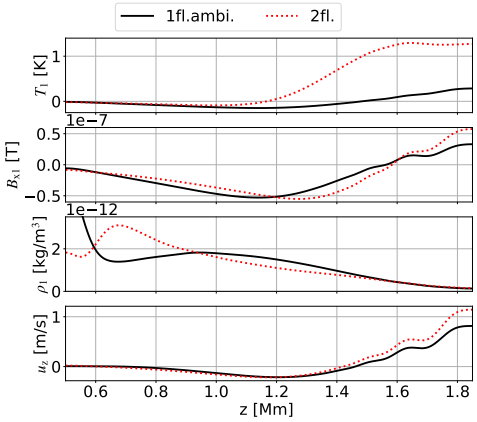

Figure 5.20: Time average of the perturbed variables as a function of height for the for the two fluid simulation (red dotted line) and for the single fluid approximation with ambipolar term (black solid line) run with the following parameters: S magnetic field profile, wave period $P = 5$ s and the amplitude factor $A = 1$. For the two fluid simulation the quantity plotted as density is the sum of the perturbation of the density of charges and neutrals, $\rho_{c1} + \rho_{n1}$, and the quantities plotted for the vertical velocity and the temperature are the center of mass velocity and perturbation of temperature, $(\rho_c u_{zc} + \rho_n u_{zn})/(\rho_c + \rho_n)$, and $(\rho_c T_{c1} + \rho_n T_{n1})/(\rho_c + \rho_n)$, respectively. Notice that these two quantities have been calculated with full densities, $\rho_c = \rho_{c0} + \rho_{c1}$, and $\rho_n = \rho_{n0} + \rho_{n1}$.

can be summarized as follows,

- Waves in neutrals and charges, initially coupled in the photosphere, become decoupled at some height in the chromosphere, meaning that velocities of co-located fluid elements for neutrals and charges become different. In our simulations, the decoupling happens above 0.7 - 1 Mm height. The difference in the charges-neutral velocity can reach up to 30-50% of the initial wave amplitude at the bottom of the domain (about 0.5 Mm in our model).

- The temperatures of neutrals and charges are effectively coupled by the thermal exchange and oscillate with the same amplitude and phase.

- The decoupling in the wave velocity is a function of the wave period, its amplitude and the background magnetic field strength. In general, waves with smaller periods show greater decoupling at the same height. Decoupling happens at lower heights for stronger magnetic fields.

- Charge-neutral collisions cause significant wave damping. We observe significant damping of the shorter period waves, 1 and 5 seconds in our simulations. In such cases, the absolute value of the decoupling is smaller compared to the less damped case, because the velocity amplitude strongly decreases after some height in the chromosphere and, in some cases, the perturbation associated with the waves completely disappears. Waves are damped at lower heights when the magnetic field is larger, but the damping length is shorter in the case of the smaller magnetic field.

- The damping obtained in the simulations in the linear regime can be rather precisely described by the analytic theory solving linear two-fluid equations using the WKB approach. This level of

agreement suggests that the damping observed in such simulations is determined by the linear effects due to decoupling.

- Non-linear wave propagation effects and steepening of wave fronts largely enhance the effects of the linear collisional damping. Non-linear effects for the damping are more pronounced for the shorter period waves, because the shock formation happens at lower heights.

- Collisional damping produces an effective frictional heating and local background temperature increase. The rate of the temperature increase is constant in time and is proportional to the square of the velocity amplitude.

- The damping in the two-fluid approach is similar to the damping in the single-fluid approach, where the interaction between charges and neutrals has been introduced through the ambipolar diffusion term. However, the increase in the background temperature is several times larger due to the frictional heating in the two-fluid approach, than the heat produced by the dissipation of the perpendicular currents in the single-fluid approach.

The charges-neutral velocity decoupling and wave damping are two related multi-fluid effects. The decoupling appears when the collisional time scales become similar or longer than the hydrodynamic time scales. The decoupling determines damping of the waves. The kinetic energy lost in the work done by the collisional terms is converted into internal energy through the frictional heating term which is a positive quantity added in the same amount to the energy equation of both species. The damping of several types of waves by collisions has been suggested in several previous studies (e.g., Zaqarashvili et al. 2011b; Soler et al. 2013a; Zaqarashvili et al. 2013; Soler et al. 2013b).

In our case, the hydrodynamic time scales for the charges are determined by the ion cyclotron frequency and by the wave frequency. The wave frequencies considered here are much smaller than the ion cyclotron frequency at all heights. The collision time scales are determined by the ion-neutral and neutral-ion collision frequencies for the charges and neutrals, respectively. The relative importance of collisional terms, which couple the evolution of charges and neutrals, varies strongly with height due to the gravitational density stratification, as shown in Figure 5.2. For the small background magnetic field (S profile) the ion-neutral collision frequency becomes smaller than the cyclotron frequency at $z \approx 0.8$ Mm in the atmosphere, and we expect the ions to decouple from the neutrals above this point, leading to wave damping. With the same argument, for the larger magnetic field (B profile), we expect the waves to be damped at even lower heights than for the S profile because the ion cyclotron frequency increases, and equals the collision frequency at the bottom of the atmosphere. Our numerical simulations show that it is indeed the case. However, there is an additional effect caused by the gravitational stratification of the atmosphere, which can produce strong variation of the perturbation wavelength with height, depending on the magnetic field strength. The perturbation wavelength is larger for larger fields. Consequently, since the perturbation gradient spatial scale is larger, the absolute value of the damping in the strong-field case is smaller (or, in other words, the

damping length is larger). Both numerical simulations and the analytical WKB solution show similar values of the damping.

In the case of the stratified atmosphere, the effect of the damping competes with the effect of the wave amplitude increase due to the gravitational stratification. The exponential decrease of the background density with height results in the increase of the wave amplitude at lower heights. This effect is well reproduced in the analytical WKB solution.

The non-linear effects result in the steepening of the wave fronts and in the formation of shocks. The effective spatial scale at shock fronts decreases and, depending on the wave period and amplitude, it can reduce to the collision mean free path between neutrals and charges, which is larger in the upper part of the atmosphere, and attains the value of 2 km at the height of 1.5 Mm. But even if the shock width is several orders of magnitude larger than the mean free path, as in the case of Hillier et al. (2016), its size is much smaller than the wavelengths, which greatly enhances the damping of waves. This effect is observed in the simulations when comparing the numerical solutions in the linear and non-linear regimes in Figures 5.16, 5.17.

If the decrease in amplitude of the shock due to collisional damping is large enough, the discontinuity at the shock front smoothes. This smoothing can be observed in Figure 5.16 (upper right and bottom left panels). The wave fronts have a marked saw-tooth profile at intermediate heights, but are smooth at the upper part of the atmosphere. These smoothed shock profiles resemble a C-type shock. Shock waves in a weakly collisional interstellar medium have been extensively studied by Mullan (1971), Draine (1980), and Draine et al. (1983). It was found that, when the Alfvén speed is larger than the shock speed, these shocks are preceded by a "magnetic precursor" which heats and compresses the medium ahead of the front where the neutral gas undergoes a discontinuous change of state. If the magnetic field is strong enough, the shock will be a C-type shock (when all the variables are continuous across the shock), otherwise the neutral gas variables are discontinuous (J-type shock). A substantial fraction of the energy would be dissipated in this magnetic precursor because of the ion-neutral streaming. The solar atmosphere differs from the interstellar medium due to significantly higher density and temperature, therefore the decoupling is less pronounced. Nevertheless, Hillier et al. (2016) found the existence of two both C-type and J-type shocks in their study of the reconnection-driven, slow-mode shocks in the solar chromosphere. Hillier et al. (2016) observed a continuous transition from C-type shocks for subsonic velocity upstream of the shock to J-type shocks (for all the variables) in the case of supersonic upstream velocity. A further study by Snow & Hillier (2019), who have used a magnetic field inclined with respect to the direction of propagation, revealed long-lived intermediate (Alfvén) shocks within the slow-mode shock, with a shock transition from above to below the Alfvén speed and a reversal of the magnetic field across the shock front. Studying the structure of the shocks requires very good spatial resolution and will be the subject of our future investigations.

In the last part we compared the two-fluid model with the single-fluid model, where the interaction between charges and neutrals has been introduced through the ambipolar term in the induction equation. The damping produced by the interaction between charges and neutrals is larger in the upper part of the atmosphere for the single-fluid model compared to the two-fluid model, as we can see from Figure 5.19.

In an analytical study, Zaqarashvili et al. (2011b) compared the single-fluid model with ambipolar term to the two-fluid model with respect to wave propagation. By defining the non-dimensional parameter which compares the wave frequency to the collisional frequency, $a = kv_A/\nu_{\rm in}$, Zaqarashvili et al. (2011b) find the same damping rate for all the types of waves considered, including the fast waves, when $a < 2$, i.e. the ions and neutrals are collisionally coupled. For larger values of a, they find smaller damping rates in the two-fluid approach compared to the single-fluid approximation for the fast waves. The difference between the damping rate calculated in the two models increases with increasing a. In our case, the value of a varies with height, having larger values in the upper part of the atmosphere because the collision frequency decreases with height. However, the value of a is small, of order of 10^{-3}. This is the reason why, in our case, the damping rate is smaller in the two-fluid approach compared to the single-fluid approach. We expect this difference in damping increases more for larger wave frequencies, according to Zaqarashvili et al. (2011b). The increase in the background temperature, that can be seen in Figure 5.20 is several times larger in the two-fluid approximation than in the single-fluid approximation. That means, that even in the cases with relatively low wave frequencies, when the damping rates obtained with the two models are not so different, the big difference in the amount of heating between the two models suggests the need to use a two-fluid model. The mechanism of heating is different in the two models, in the two-fluid approach the heating is caused by the friction between the neutral and charged particles, when the kinetic energy is directly transformed into internal energy. In the single-fluid approach, the heating is caused by the dissipation of the electric currents perpendicular to the magnetic field, meaning that the magnetic energy is dissipated into internal energy. We do not yet fully understand why the mismatch between the two results is so big, and is subject of future research.

6

Rayleigh-Taylor instability

This chapter presents the study of the Rayleigh-Taylor instability at the interface between a solar prominence and the corona. The atmosphere is smoothly non-uniform in the vertical direction, and we use different configurations for the background magnetic field. We use a two-fluid model where we include the terms related to viscosity, thermal conductivity, collisions between neutrals and charges: ionization/recombination, energy and momentum transfer, and frictional heating. We run 2D simulations with the magnetic field originally perpendicular to the direction defined by direction of the gravity (the negative vertical direction z) and the direction of the perturbation (the horizontal direction x), with a setup similar to that used by Leake et al. (2014). We then slightly shear the magnetic field and vary the distance in which the field is rotated. We study how different scales evolve, the linear growth rate of the instability, the decoupling between charges and neutrals, and the power spectra in the non-linear stage. We observe that, while large scales grow exponentially in the linear phase, for intermediate and small scales, affected by viscosity, thermal conduction, and the interaction between neutrals and charges, the linear and the nonlinear phases are superposed. There are several studies which estimate the linear growth rates or predict the the evolution of the scales in the non-linear regime, however, the restrictive assumptions used in these models did not give a clear answer to the problem, and this motivates our investigation through numerical simulations.

6.1 Introduction

There are several models which explain how the dense material in the solar prominences is sustained against gravity. A good review of the magnetic Rayleigh Taylor instability (RTI) and the prominence models that can be practically used in the studies of RTI is given by Hillier (2018). The prominence is supported by the magnetic tension component of the Lorentz force in the Kippenhahn-Schlüter (KS) model (Kippenhahn & Schlüter 1957). In the Kuperus-Raadu model (KR) (Kuperus & Raadu 1974), the prominence is sustained indirectly by the photosphere through the constant magnetic flux

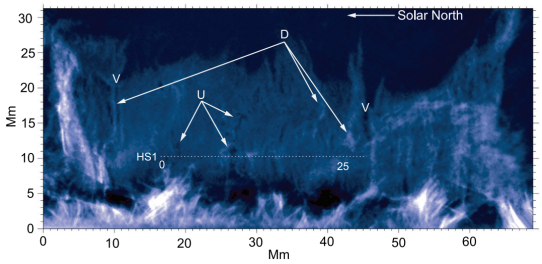

Figure 6.1: Large quiescent prominence observed in the Ca II H-line 3968 Å spectral line on 2006 November 30. Disk position N50, W90. "D" indicates examples of a bright downflow streams. "U" shows several dark inclusions in the sheet that are regions of turbulent upflow. "V" indicates dark "voids" that are not upflows. Image taken from Berger et al. (2008).

boundary condition. The current running through the prominence body creates a field that cannot enter the photosphere, and therefore results in an upward Lorentz force on the prominence body (Schutgens 1997). The two models, KS and KR will give rise to two different field topologies: the Normal Polarity (NP) and the Inverse Polarity (IP), respectively. Usually, as the plasma β is very low in the corona, force-free magnetic field configurations are used in the prominence models. These models are in general used to explain the global stability of the prominences, or the time evolution of the magnetic field. The tearing instability is studied for a KS model (Nishikawa & Sakai 1982; Sakai & Nishikawa 1983; Hillier et al. 2010). The stability of the prominences to vertical and horizontal oscillations is studied in potential magnetic field configurations, taking into account the finite time of propagation of the oscillation for the two topologies (van den Oord et al. 1998), in linear force-free configurations with a NP field topology (Terradas et al. 2015), extrapolated from linear force-free photospheric magnetic field (Aulanier & Demoulin 1998), or adding mass to nonlinear force-free models with a IP configuration (Hillier & van Ballegooijen 2013).

As the prominence sits above the lighter corona, a small perturbation at the interface between the corona and the prominence (PCTR) may grow without bound giving rise to the RTI. Figure 6.1 shows dark upflows and bright downflows, seen during the observation of a quiet prominence in the Ca II 3968 Å line, believed to be due to the RTI. Because the initial perturbation is small compared to the background variables, the evolution is linear, and different modes grow independently without interaction. Comprehensive recent reviews of RTI are given in Zhou (2017a,b).

6.1.1 Discontinuous density at the interface

In the absence of the magnetic field, (the hydrodynamic case), when a system composed by heavier fluid of density, ρ_2, initially on top of a lighter fluid of density, ρ_1, is perturbed, an instability develops for all the wavelengths of the initial perturbation (see Chandrasekhar 1961). With homogeneous densities, in the incompressible and inviscid assumption, and when the transition between the two fluids has negligible width, the growth rate is a monotonically increasing function of the wave number k:

$$-\omega^2 = Agk\,, \tag{6.1}$$

where,

$$A = (\rho_2 - \rho_1)/(\rho_2 + \rho_1)\,, \tag{6.2}$$

is the Atwood number (Chandrasekhar 1961). The assumption of negligible width of the transition means that there is a discontinuity in density at the interface between the upper and the lower fluid, having $\rho_2 > \rho_1$, where ρ_2 and ρ_1 are the homogeneous densities. In our case the lighter fluid, ρ_1, is corona, and the heavier one, ρ_2, is the prominence.

With the same assumptions, a component of the magnetic field in the perturbation direction, considered to be the x direction (see Figure 6.4 later in this chapter, which illustrates the setup used in our simulations and uses the same conventions), stabilizes some of the perturbations. In this case, the growth rate becomes (see Chandrasekhar 1961),

$$-\omega^2 = Agk - \frac{2B_{\mathrm{x0}}^2}{\mu_0\Big(\rho_2 + \rho_1\Big)}\,. \tag{6.3}$$

The condition for stability $-\omega^2 < 0$ gives the expression for the critical wavelength λ_c, so that the scales with wavelength $\lambda < \lambda_c$ do not grow,

$$\lambda_c = \frac{4\pi B_{\mathrm{x0}}^2}{\mu_0 g\Big(\rho_2 - \rho_1\Big)}\,. \tag{6.4}$$

When the equilibrium magnetic field is vertical, i.e., transverse to the discontinuity, Chandrasekhar (1961) finds that the growth rate is increasing with the wave number, with no cutoff. However, the growth is bounded for the limit $k \to \infty$, unlike the hydrodynamic case.

6.1.2 Continuous density profile

Early studies of (Brunt 1927; Vaisala 1925) showed that in an equilibrium atmosphere, accelerated in the vertical direction by the gravity, a small element displaced adiabatically in the vertical direction can have different evolutions determined by the value of:

$$N^2 = g\left(\frac{1}{\gamma p_0}\frac{\mathrm{d}p_0}{\mathrm{d}z} - \frac{1}{\rho_0}\frac{\mathrm{d}\rho_0}{\mathrm{d}z}\right)\,, \tag{6.5}$$

where N is called Brunt-Väisälä frequency. The two possible cases are:

1. Stable case ($N^2 > 0$): the element is restored in its original position by buoyancy forces, and it has a subsequent oscillatory motion with the time frequency N around its equilibrium position.

2. Unstable case ($N^2 < 0$): the element continues to move in the direction in which it was displaced and the displacement grows exponentially in time with the rate $\sqrt{-N^2}$.

[1] In the incompressible case, the evolution of the element displaced in the vertical direction is unstable if the density gradient is positive.

It can be shown that the $N^2 < 0$ condition is equivalent to the Schwarzchild criterion of convective instability. For an ideal gas, i.e.,

$$p = \rho \frac{k_{\rm B}}{m_H \mu_{\rm gas}} T \,, \tag{6.6}$$

where $\mu_{\rm gas}$ is the mean molecular weight of the gas in units of g/mole, in an adiabatic process, the change in temperature for a change in pressure can be written as:

$$\frac{dT}{dp} = \frac{\gamma - 1}{\gamma} \frac{T}{p} \,. \tag{6.7}$$

The temperature gradient of an adiabatic process, can be written as,

$$\left(\frac{dT}{dz}\right)_{\rm ad} = \frac{\gamma - 1}{\gamma} \frac{T}{p} \frac{dp}{dz} \,, \tag{6.8}$$

where γ is the adiabatic index. From the ideal gas law 6.6,

$$\frac{dT}{dz} = \frac{m_H \mu_{\rm gas}}{k_{\rm B}} \left(\frac{1}{\rho} \frac{dp}{dz} - \frac{1}{\rho^2} \frac{d\rho}{dz} \right) \,. \tag{6.9}$$

If we assume $dp/dz < 0$, as it happens in a gravitationally stratified atmosphere, the Schwarzchild criterion becomes:

$$\frac{dT}{dz} < \left(\frac{dT}{dz}\right)_{\rm ad} \,. \tag{6.10}$$

Replacing the expressions from Eqs. 6.8, 6.9 into Eq. 6.10, the Schwarzchild criterion becomes equivalent to $N^2 < 0$.

In a 2D geometry, when the atmosphere is homogeneous in the horizontal direction, the evolution also depends on the horizontal scale and the unstable case is called Rayleigh-Taylor instability. The general case of RTI with arbitrary non-uniform equilibrium profile (in the z direction) does not have a known analytical solution. However, in the absence of the magnetic field, and an exponential density profile $\propto \exp(\beta z)$ with uniform β, in the incompressible case, Chandrasekhar (1961) finds the following expression for the growth rate:

$$-\omega^2 = \frac{g\beta k^2 d^2}{k^2 d^2 + \frac{1}{4}\beta^2 d^2 + m^2 \pi^2} \,, \tag{6.11}$$

[1] Mathematically, for the case $N^2 < 0$ there is another mode damped in time exponentially with the rate $\sqrt{-N^2}$, but the dominant mode is the growing one. For the case $N^2 > 0$ there are two indistinguishable modes which oscillate with frequency N and -N, respectively. The case $N^2 = 0$ is not considered, because the evolution does not depend on the atmosphere properties, but only on the initial conditions.

where it is assumed that the fluid is confined between the heights $z = 0$ and $z = d$ and m is an arbitrary integer associated with the structure of the vertical eigenfunction. The stratification is unstable when $\beta > 0$. The maximum growth rate occurs for $m = 1$. The growth rate obtained above is a monotonically increasing function of the wave number bounded by the value $g\beta$.

Bhatia (1974) extends the analytic calculation in the non-uniform atmosphere with exponential density profile $\propto \exp(\beta z)$, and uniform β, with the assumption that $\beta d \ll 1$, by adding a uniform vertical magnetic field and considering compressibility and viscosity with uniform viscosity coefficient. An additional assumption is that the sound speed varies as $\propto \exp\left[-(\beta/2)z\right]$. Bhatia (1974) finds that the large scales are stabilized by the presence of the magnetic field and the compressibility, without any dependence on the viscosity. The scales with $k < k_c$ are stable, where,

$$k_c = \frac{\pi^4 m^4 v_{\mathrm{A}0}^2 c_0^2}{d^2\left[gd^2\left(g + \beta c_0^2\right) - \pi^2 m^2 v_{\mathrm{A}0}^2 c_0^2\right]}\,. \tag{6.12}$$

c_0 and $v_{\mathrm{A}0}$ are the sound speed and the Alfvén speed calculated at the height $z = 0$. We can observe that the situation is always unstable without magnetic field. The critical number k_c increases when the sound speed is larger (less compressible), and Bhatia (1974) concludes that the compressibility has a destabilizing effect. However, the drawback of this calculation is that no gravitationally stratified magneto-hydrostatic (MHS) equilibrium can be constructed with uniform pressure and uniform magnetic field. The assumption that the square of the sound speed varies exponentially with the same uniform scale height, but opposite sign as the density, implies a uniform pressure.

6.1.3 The effect of viscosity

In the case of a discontinuous density profile at the interface, when the viscosity is taken into account, the mode with fastest growth is not anymore the mode corresponding to the smallest scale as from Eq. 6.1. Chandrasekhar (1961) calculates the growth rate, taking into account the viscosity, and he finds that all the perturbations are unstable regardless the wave number k. Chandrasekhar (1961) obtains that in the limit of $k \to 0$, the growth rate γ is independent of viscosity because, as he points out, the viscosity does not affect the very large scales. The growth rate $\gamma \to 0$ in this case. In the other limit, $k \to \infty$, the growth rate also vanishes. Thus, the wave number of the fastest growing mode has a strictly positive and finite value. Figure 6.2, taken from Chandrasekhar (1961) shows the growth rates for several values of the Atwood number, calculated considering the same value for the viscosity coefficient in units of m^2/s above and below the interface.

The result also holds for an exponentially stratified density profile (Livescu 2004). Right panel of Figure 6.3, taken from Livescu (2004) shows the growth rate as function of the wave number in nondimensional units. The result is very similar to the results obtained by Chandrasekhar (1961) (Figures 106 and 107).

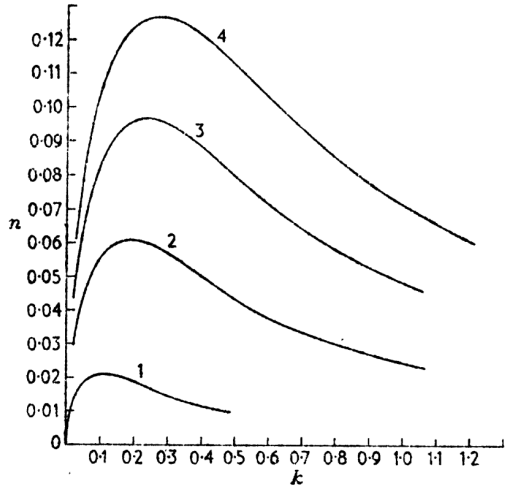

Figure 6.2: Growth rate measured in $(g^2/\nu)^{\frac{1}{3}}$ as a function of the wave number k measured in $(g/\nu^2)^{\frac{1}{3}}$ units in the case with viscosity. The axes are in nondimensional units. ν is the viscosity coefficient in units of m^2/s. Different curves labeled 1, 2, 3, 4 are for different Atwood numbers: 0.01, 0.05, 0.10, and 0.15, respectively. Fig. 106 from Chandrasekhar (1961).

6.1.4 The effect of compressibility

The effect of compressibility on the growth of RTI is a subject very disputed in the literature. Díaz et al. (2014) find an increased growth rate for the incompressible fluid. Left hand-side panel of Figure 6.3 shows the growth rate as a function of the wave number k, obtained in the case of two compressible fluids with uniform physical properties, situated one on top of the other, and separated by a discontinuous interface, with a uniform magnetic field contained in the horizontal plane with a non-zero component along the direction of the perturbation. The incompressible limit, as from Chandrasekhar (1961) is plotted for comparison. They varied the neutral fraction in the upper part of the domain and the plasma β, and we can observe that the growth rate is always smaller when compressibility is taken into account. The stabilizing effect of the compressibility has been concluded also in other studies (Blake 1972; Sharp 1984; Li 1993).

Unlike the above studies, some authors find that compressibility has an unstabilizing effect (Vandervoort 1961; Bhatia 1974; Newcomb 1983). Livescu (2004) tries to explain the disconcordance between the results by arguing that the incompressible flow limit can be achieved in two ways, one giving a higher growth rate, and the other a lower growth rate than the growth rate obtained in the incompressible case. The analytical study of Livescu (2004) considers a single-fluid model which includes the effects of compressibility, besides the effect of the viscosity and thermal conductivity in an exponentially stratified atmosphere. The initial equilibrium consists of two regions with fluid with different mean molecular weights (μ_m), one situated on top of the other, separated by an interface situated at

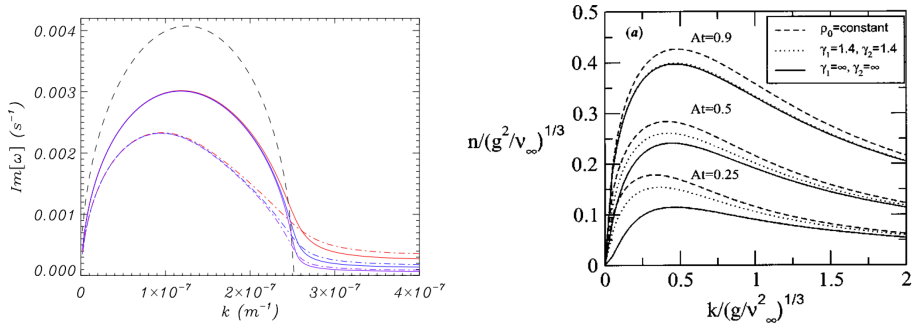

Figure 6.3: **Left**: Growth rate as a function of the wave number k. The equilibrium atmosphere density is assumed discontinuous at the interface with $\rho_2/\rho_1 = 100$, the magnetic field is uniform, contained in the horizontal plane having an angle $\theta = 40°$ with the direction of the perturbation, with a strength so that the reduced Alfvén speed: $\sqrt{B_0^2/[\mu_0(\rho_1+\rho_2)]} = 30$ m/s. The neutral fraction in the lower part of the domain is kept fixed: $\xi_{n1} = \rho_{n1}/\rho_1 = 10^{-6}$. Dot-hashed lines indicate plasma $\beta = 0.5$, and solid lines are for $\beta = 0.1$ The colors indicate different neutral fractions in the upper domain: $\xi_{n2} = 0.1$ (purple), $\xi_{n2} = 0.5$ (blue), and $\xi_{n2} = 0.9$ (red). The incompressible case is indicated by black dashed lines. Fig. 4 from Díaz et al. (2014). **Right**: Growth rate measured in $(g^2/\nu_\infty)^{\frac{1}{3}}$ as a function of the wave number k measured in $(g/\nu_\infty^2)^{\frac{1}{3}}$ units in the case with viscosity, compressible and in the two limits of incompressibility. The axes are in nondimensional units. ν_∞ is the viscosity coefficient calculated at the interface in units of m^2/s. Different curves are for different Atwood numbers specified above. Part of Figure 4 from Livescu (2004).

$z = 0$, which in equilibrium have a vertical exponentially stratified density and pressure profiles:

$$p_{0\mathrm{m}} = p_\infty \exp\left(-\frac{g m_\mathrm{H}\mu_\mathrm{m}}{k_\mathrm{B}T_0} z\right); \quad \rho_{0\mathrm{m}} = p_{0\mathrm{m}} m_\mathrm{H}\mu_m/(k_\mathrm{B}T_0), \text{for m} \in \{1,2\}, \tag{6.13}$$

where p_∞ is the equilibrium pressure at the interface, and T_0 is uniform in adiabatic assumption because of the thermal conductivity. Right panel of Figure 6.3, taken from Livescu (2004) shows the growth rate as a function of the wave number in nondimensional units. The incompressible flow limit ($c_0 \to \infty$) can be obtained by either making $p_\infty \to \infty$ or $\gamma \to \infty$, where γ is the adiabatic index. In the first case, the equilibrium temperature also goes to infinity, and the equilibrium density is uniform at each side of the interface, this case is indicated in the plot with the label "ρ_0=constant" and a dashed line. The second case is shown with a solid line and labeled "$\gamma_1 = \infty, \gamma_2 = \infty$", and allows the exponential profile at each side of the interface. The growth rate for the compressible fluid is shown to be between these limits. We can observe that the difference between the compressible growth rate and the incompressible growth rate is larger for smaller Atwood numbers in the two cases of incompressibility considered.

Ribeyre et al. (2005) consider that the compressible and incompressible cases should be compared for the same density profiles. They consider an isothermal atmosphere, exponentially stratified similarly

to Livescu (2004) and find that the growth rate is enhanced in the compressible case, compared to the incompressible case, both calculated for the stratified atmospheres. They also find that the effect is larger for smaller Atwood numbers. Xue & Ye (2010) agree that the density profile contributes to the evolution of the RTI in the incompressible case, and that the comparison between compressible and incompressible cases should be done by keeping a fixed density profile. When compressibility is taken into account, both the pressure at the interface (p_∞ in the above study of Livescu (2004)) and the value of the adiabatic index contribute to the growth rate. Keeping the density fixed in the incompressible and compressible calculations, Xue & Ye (2010) find that the compressibility always has a destabilizing effect.

6.2 Nonlinear phase

It is considered that linear stage is followed by a nonlinear transition stage to the turbulent mixing regime, when the evolution is believed to be self similar (Abarzhi 2010) and the size (the vertical extent) of the structures scales as t^2. However, in many RTI simulations, even in late stages, the evolution is not completely turbulent and it still depends on the initial conditions.

Many approaches have been considered to study the RTI, but despite many efforts done, there are still open questions, such as the self similarity of the flow in the nonlinear phase, or the influence of the mixing and initial conditions on the growth rate.

Some studies based on turbulence calculate nonlinear growth rates, but the restrictive hypothesis used in this analysis may lead to incorrect results. Cho & Lazarian (2003) explain why isotropic Kolmogorov turbulence model cannot be applied in a magnetized gas. According to Kolmogorov theory, the kinetic energy diminishes as the scale reduces, but the magnetic energy does not. However, it seems that mixing of the fluid in the direction perpendicular to the magnetic field is efficient for magnetic fields of up to the equipartition value.

Later evolution of the instability shows the secondary Kelvin Helmholtz instability (KHI) developed as a result of the bubbles moving up and down. The linear phase is very short, and the structures develop mainly in the nonlinear phase, when smaller scales merge into larger scales, which then break up because of secondary instabilities. The model of Fermi & Von Neumann (1955), based on self similar analysis of the nonlinear phase, improved by Ristorcelli & Clark (2004) reveals three growing regimes. Large scales grow (the vertical extent of the perturbation) as t^2, intermediate scales grow as $t^{1/2}$, and smaller scales (dissipation scales, created by the viscosity) decrease as $t^{-1/4}$. In the self-similar analysis, the self-similar solutions are considered of the form:

$$F(z,t) = F_0(t) f(z/h(t)) \,, \tag{6.14}$$

where F_0 is a temporal scaling function of the solution, f is the spatial similarity function of the solution, and h is the mixing layer half-width. In the hydrodynamic, incompressible case, this solution is replaced into the Navier-Stokes equation where the variables are split into average quantities and fluctuations (Reynolds decomposition), and from dimensional analysis, the growth regimes mentioned above are obtained.

It has been shown by Naveh et al. (2019), that the growth rate depends on the vertical domain length. They apply the group theory analysis and show that in a finite-sized domain the flow is slower compared to the spatially extended case, both in the linear and in the nonlinear phase. The result is similar to the result of the study of Livescu (2004), who finds a decrease of the growth rate as the vertical size of the domain decreases, in all the cases considered, compressible and incompressible.

Analytical work has been done for two limiting time regimes. In the early phase, the instability develops in a linear regime, the modes of the perturbation do not interact and grow exponentially. At very large time it is assumed that the solution is stationary, and a family of solutions is obtained, where the fastest solution is the physically significant. However, the multiplicity of the solutions in the nonlinear regime is determined by the discontinuity at the interface which has significant importance in the development of the instability. The tangential component of the velocity will give rise to the Kelvin-Helmholtz secondary instabilities. Naveh et al. (2019) show that the shear is larger for increasing contrast between the densities and for a smaller domain size. In the cases when the perturbation contains multiple harmonics, Naveh et al. (2019) find that the lowest order harmonic is dominant during the evolution for all Atwood numbers. The memory of the initial conditions is lost for asymptotically large times in the non linear regime.

6.2.1 Bubbles and spikes

Cherniavski & Shtemler (2013) use the integral version of the method of matched asymptotic expansion to obtain the solution to the RTI problem over long intervals of time. In a setup where a uniform heavier fluid is situated on top of a uniform lighter fluid, both inviscible and incompressible, separated by an interface located at $z = 0$, and considering that at late times the flow is symmetric with respect to $z = 0$, Cherniavski & Shtemler (2013), find that the bubbles (the lighter fluid which rises into the heavier fluid) rise with constant velocity, while the spikes (the heavier fluid which fall into the lighter fluid) are in free fall. It has been shown that the result depends on the initial conditions, the limiting upward velocity depends on the initial energy of the perturbation.

Unlike the above work, Cook & Dimotakis (2001) have shown using the ansatz of the self similar solution in the nonlinear regime, that the spikes and bubbles grow in the same way (see e.g. Cook & Dimotakis 2001).The onset of the nonlinear growth is not predicted by available linear-stability theory. In the nonlinear stage, growth rates are found to depend on the initial perturbations, up to the end of their simulations. Mixing is found to be even more sensitive to the initial conditions than the growth rates.

It is shown by Mikaelian (2014) that in the linear regime the amplitudes of the spikes and the bubbles of the same size (corresponding to the same wave number k) are equal. Even if analytical studies based on self similar solutions done by Cook & Dimotakis (2001) show that bubbles and spikes grow in the same way also in the nonlinear phase, Mikaelian (2014) shows by performing numerical simulations that, in the nonlinear regime, the bubbles and the spikes behave differently. The height of the turbulent mixing layer $h^{b,s} = \alpha^{b,s} Agt^2$, where A is the Atwood number, scales as $\propto t^2$, for both bubbles and spikes, but the proportionality constant is different. It has been shown that α^b is

constant between 0.03 and 0.07, but α^s depends on A. For low A, $\alpha^s \approx \alpha^b$, but for large values of A, $\alpha^s/\alpha^b \in [4, 5]$.

Carlyle & Hillier (2017) measures the nonlinear growth of the RTI by means of numerical simulations in a 3D setup and they find asymmetry between upward growth of the bubbles and the downward growth of the spikes. The spikes grow more than the bubbles, and the asymmetry is larger for stronger magnetic fields. Carlyle & Hillier (2017) find that the growth rate decreases with increasing magnetic field, and they consider it to be due to higher magnetic tension requiring greater energy for the frozen-in plasma to move.

6.2.2 Partial ionization effects

There are only a few studies of the RTI in partially ionized solar plasmas in the single-fluid approach. These studies use a 2D geometry and include the interaction between neutrals and charges through the ambipolar term. In their analytical study, Díaz et al. (2014) find that the presence of the neutrals removes the stabilizing effect of the magnetic field for the small scales. Left panel of Figure 6.3 shows that the cutoff imposed by component of the magnetic field parallel to the direction of the perturbation is removed when the ambipolar diffusion is included, and that the growth rate is larger for a higher number of neutrals. The result has been confirmed by numerical simulations of (Khomenko et al. 2014c). On the hand, Díaz et al. (2012) in a study using a two-fluid model, find that the growth rate is reduced in the presence of the neutrals. However, the configuration is always unstable.

6.2.3 3D geometry

In an analytical study of the RTI in a 3D geometry, with two uniform regions separated by an interface and a uniform magnetic field everywhere, Díaz et al. (2012) find that the configuration is always unstable, regardless of the magnetic field, having the same growth as in the hydrodynamic case. In the 3D setup, with uniform magnetic field, the fastest growing mode can be always chosen as the interchange mode.

There are many studies of RTI based on 3D simulations (Anuchina et al. 2004; Stone & Gardiner 2007; Carlyle & Hillier 2017). In a sheared[2] configuration of the magnetic field, the linear growth rate is the same as in the hydrodynamic case only for the small scales, when the wavelength is much smaller than the scale on which the magnetic field changes the direction. For these small scales, the field is seen as uniform, and the shear on much larger scales cannot inhibit the interchange mode (Stone & Gardiner 2007). During the late nonlinear phase, when the motion becomes turbulent, the presence of the magnetic field, enhances the growth because the field reduces the mix between light and heavy fluids, resulting in fingers and bubbles which rise much more quickly (Stone & Gardiner 2007).

[2]By sheared we understand that the magnetic field is smoothly rotated with respect to the plane where the interface between the fluids is contained. We will use the sheared configuration later our in our study in this chapter.

6.2.4 Motivation of the study

The purpose of this chapter is to deepen our understanding of the effects of the partial ionization on the development of RTI using non linear two-fluid numerical simulations. The cold prominences contain a large fraction of neutral particles, that get ionized when they enter the hotter corona during the development of the RTI. Some observational studies show hints for the decoupling in the velocity of ions and neutrals in the prominences (Gilbert et al. 2007; Khomenko et al. 2016; Anan et al. 2017; Wiehr et al. 2019). It is not yet fully clear which role the neutrals play in the development of RTI in prominences, and only few theoretical studies have been performed so far. The interface between the prominence and corona, the so called Prominence-Corona Transition Region (PCTR), must also be susceptible to partial ionization effects because of the drop of collisional frequency towards the corona.

The analytical studies about the linear growth rate were done mainly in the single-fluid approximation, using particular configurations where the heavier uniform fluid is located on top of the lighter uniform fluid, separated by an interface that can be seen as a discontinuity, used more restrictive hypothesis such as incompressibility. The analytical calculation of the linear growth rate of the RTI in the two-fluid approach has been done by Díaz et al. (2012) using the configuration of the two uniform regions separated by a discontinuity in a 3D geometry.

The solution in the nonlinear phase cannot be obtained analytically in the general case. There are analytical approaches which give qualitative results about the nonlinear (and linear) phase of the RTI in a 3D geometry (Hillier 2016), and statistical results obtained in the late nonlinear (turbulent) phase using the self-similar ansatz as described before. However, the work of Hillier (2016) does not consider partial ionization effects at all. But even in MHD case, the hypothesis used in these analytical derivations are restrictive. Moreover, the exact evolution of the RTI can only be obtained by means of numerical simulations in the general case. The numerical studies of the RTI developed at the PCTR in a two-fluid approach are scarce (Leake et al. 2014). In the only work of Leake et al. (2014) only one case was studied, and only initial evolution of the instability was considered, with no profound analysis of the results. Recently, Hillier (2019) studies Kelvin-Helmholtz instability numerically in the two-fluid approach, but this idealized study so far cannot be applied to the prominence conditions and the type of the instability studied by Hillier (2019) is different. Most of the studies, analytical and numerical do not include the effects of the viscosity and thermal conductivity.

In order to capture the two-fluid effects, we have to resolve scales comparable to the mean free path between the collisions between ions and neutrals. These very small scales may be below the gradient scale length, therefore, the density profile cannot be approximated as discontinuous in the analytical calculations. The study presented in this chapter continues the work of Leake et al. (2014). We use a two-fluid model where we include elastic and inelastic collisions, viscosity and thermal conductivity, and use different configurations of the magnetic field, perpendicular to the direction of the perturbation or slightly sheared.

6.3 Setup

For the study of the RTI at the prominence corona interface (PCTR), the equilibrium models used are usually much simpler than the models used for the study of the prominence oscillations, and usually consist of a heavier fluid with prominence physical properties which sits on top of a lighter fluid with coronal characteristics. The gravitational force is balanced by the pressure gradient only (Khomenko et al. 2014c), or additionally by the electromagnetic forces, in particular by the the gradient of the magnetic pressure (Leake et al. 2014) or magnetic tension (Hillier et al. 2010).

The setup used in this study is based on the setup of Leake et al. (2014). The configuration is summarized in Figure 6.4. The gravity, **g** indicated by a green arrow line, is oriented in the negative direction of the z-axis. For the 2D simulations, presented in this chapter, **k** has only one component in the x direction, and is shown with blue arrow. The equilibrium magnetic field, shown by red lines, is located in the XOY plane, with no z-component. The configuration shown in the figure is the sheared field configuration, where the largest component is in the y direction, and it is slowly rotated by an angle, which depends on the height. The magnetic field has the component $B_x = 0$ at the height $z = 0$, and is slightly sheared symmetrically, in different directions, above and below $z = 0$. The maximum angle, indicated by θ_0, is obtained at the top and the bottom of the domain. This configuration is described below, by Eqs. 6.23. The other configuration used for the simulations presented in this chapter is the magnetic field which has only the component along the y-axis (B_y). For this configuration, $\theta_0 = 0°$ in the sketch from Figure 6.4.

We define the characteristic length $L_0 = 1$ Mm, and we choose the domain size is $L_{\rm x} = 2L_0$, $L_{\rm z} = 8L_0$. The resolution is 512×2048 points, this gives the values of the grid cell sizes: $d_{\rm x} = d_{\rm z} = 3.9$ km. We choose the point (0,0) in the middle of the plane XOZ, so that x varies from $-L_0$ to L_0 , and z varies from $-4L_0$ to $4L_0$.

The equilibrium atmosphere is uniform in the x direction. The equations which describe the number density of the ions and neutrals, the background temperature, the magnitude of the magnetic field, and the pressures in equilibrium configurations are (Leake et al. 2014),

$$n_{\rm i0} = n_0 \exp\Big(-\frac{z}{H_c}\Big), \tag{6.15}$$

$$n_{\rm n0} = n_{\rm n00}\mathrm{sech}^2\Big(2\frac{z}{L_0} - 1\Big) + n_{\rm nb}, \tag{6.16}$$

$$T_0 = T_b f(z), \tag{6.17}$$

$$B_0 = B_{00}\left\{1 + \beta\left[\frac{n_{\rm i0}}{n_0}\left(1 - f(z)\right) - \frac{1}{2}\frac{n_{\rm n0}}{n_0}f(z) - \frac{1}{H_c n_0}\left(\frac{1}{2}L_0 n_{\rm n00}\tanh\Big(2\frac{z}{L_0} - 1\Big) + n_{\rm nb}z\right)\right]\right\}^{0.5}, \tag{6.18}$$

$$p_{\rm n0} = n_{\rm n0}k_{\rm B}T_0\,,$$
$$p_{\rm c0} = 2n_{\rm i0}k_{\rm B}T_0\,, \tag{6.19}$$

where the ion number density at $z = 0$, $n_0 = 10^{15}$ m^{-3}, the peak neutral number density, reached at

$z = L_0/2$, is $n_{\rm n00} = 10^{16}$ m^{-3}, the background temperature of the corona, $T_b = 2.02 \times 10^5$ K, the neutral number density corresponding to the corona temperature (T_b), $n_{\rm nb} = 3.5 \times 10^9$ m^{-3}, $B_{00} = 10^{-3}$ T, the charges gravitational scale height, $H_{\rm c} = 2k_{\rm B}T_b/(m_{\rm H}g)$. The plasma $\beta = 4n_0k_{\rm B}T_b\mu_0/B_{00}^2$ is calculated at $z = 0$ using B_{00} as the value of the magnetic field, and has the value $\beta \approx 1.4 \times 10^{-2}$. The function f is defined as follows,

$$f(z) = \frac{\cosh^2\Big(\frac{z}{L_0} - 0.5\Big)}{\Big(\frac{z}{L_0} - 0.5\Big)^2 + L_{\rm t}}\,. \tag{6.20}$$

The temperature profile, described by Eq. 6.17, depends on the definition of the function f. For this reason, the value of $L_{\rm t} = 20$ has been chosen, so that the ionization fraction $\xi_{\rm i} = \rho_{\rm c}/(\rho_{\rm c} + \rho_{\rm n}) = 0.091$, closest to the values observed in the Sun. Figure 6.5 shows the background profiles for the density, pressure, temperature and the module of the magnetic field. The neutrals and charges have the same temperature profile, and are assumed coupled enough by collisions, so that the prominence, composed essentially by neutrals, is supported by the gradient in the magnetic pressure. The equilibrium for the density of neutrals represents a density enhancement at $z = L_0/2$, where it attains the maximum, $n_{\rm n00}$, as from Eq. 6.16. The minimum of the temperature is also attained at $z = L_0/2$, and the maximum temperature is considered to be the coronal temperature (T_b).

The equilibrium density of the charges is gravitationally stratified in an isothermal atmosphere with coronal temperature (T_b). Using these density and temperature profiles, the pressure profiles are obtained from the ideal gas law, Eq. 6.19. The magnetic field profile is obtained from solving the magneto-hydrostatic equation where the total density and pressure are used. Being a differential equation, the integration constants permits the scaling of the magnetic field around some chosen value, B_{00} in Eq. 6.18 shown above.

The momentum and energy equations are coupled by collisional terms which model both elastic and inelastic collisions. We do not use artificial (hyperdiffusive) terms, instead, in some of the simulations we include physical viscosities and neutral thermal conductivity, as mentioned below. We use the ideal Ohm's law. We include the charge-exchange collisions α_{cx} in the collisional parameter α, i.e. the effective value of α used is the sum between α defined in Eq. 2.90, and $\alpha_{\rm cx}$ defined in 2.92, as shown in Chapter 2.

The initial perturbation is a perturbation in the density of neutrals, concentrated at the height $z = 0$,

$$\frac{\rho_{\rm n1}}{\rho_{\rm n0}} = \delta \times r_{\rm x} \times \exp\left(-4\Big(\frac{z}{L_0}\Big)^2\right), \tag{6.21}$$

where $\delta = 10^{-2}$, and $r_{\rm x}$ is a random perturbation, which depends on the x coordinate. The equilibrium atmosphere is homogeneous in the x direction, and the dependence of the perturbation on the x coordinate gives rise to the choice of the ansatz of separable solutions $\propto f(z)\exp(i\omega t)\exp(-ik_{\rm x}x)$. Thus, the perturbation propagates in the x direction, indicated by the vector $\mathbf{k} = (k_{\rm x}, 0, 0)$ in Figure

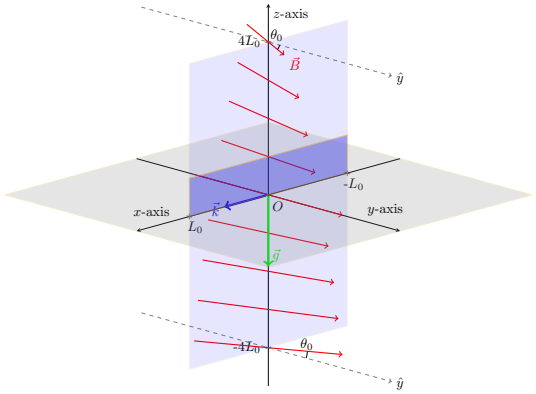

Figure 6.4: Sketch of the initial configuration. The domain of our setup (filled with blue color) is contained in the XOZ plane, where x varies between $-L_0$ and L_0 and z varies between $-4L_0$ and $4L_0$. The magnetic field, **B** (red lines) is contained in the XOY plane (filled with gray color). At the height $z = 0$ the magnetic field has only the component, B_y and it is slowly rotated above and below $z = 0$ by an angle which depends on height, keeping its modulus constant. The value of the angle is antisymmetric with respect to $z = 0$. The maximum angle obtained at the top and the bottom of the atmosphere is indicated by θ_0. When the field is perpendicular, the direction of **B** is along the y-axis for all the heights, $\theta_0 = 0°$. For the sheared magnetic field configurations $\theta_0 = 1°$. The gravity, **g** points in the negative z direction and is indicated by a green line. The direction of the perturbation, **k** is shown by a blue line.

6.4. In order to remove small scale noise, we use the filtering method described by Eq. 3.25 in Chapter 3. We used periodic boundary conditions in the x direction, and reflecting boundary conditions for the vertical velocities of neutrals and charges (velocities are zero at the boundaries) and open for the rest of the variables (space derivatives in the vertical direction are zero at the boundaries) in the z direction. Similarly to Terradas et al. (2015), the reflecting boundary condition for the velocities at the bottom of the atmosphere has an important role in supporting the prominence against gravity.

Table 6.1 shows a list of all the 2D simulations performed. There are three input parameters that are changed throughout of the simulations. They are related to the name of the perturbations shown in the table which is composed by three parts separated by "-".

1. Magnetic field inclination The background magnetic field is contained in the XOY plane. We use two types of configuration, the magnetic field perpendicular to the plane defined by the direction of the perturbation and the gravity XOZ, and a slightly sheared magnetic field.

   - perpendicular magnetic field

   $$B_{y0} = B_0\,, \qquad B_{x0} = 0\,. \tag{6.22}$$

   These simulations are referred in the table with the keyword "P".

   - sheared magnetic field

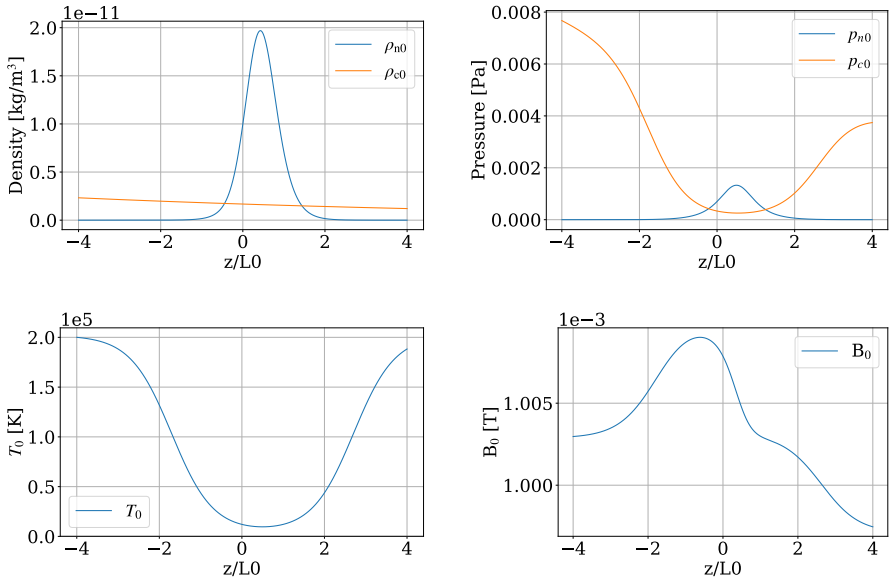

Figure 6.5: Initial configuration used in the model of RTI. Top left: density of neutrals (blue) and charges (orange). Top right: pressure of neutrals (blue) and charges (orange). Bottom left: temperature of both charges and neutrals. Bottom right: modulus of the magnetic field.

$$
\begin{aligned}
&B_{\mathrm{x0}} = B_0 \sin(\theta) \ , B_{\mathrm{y0}} = B_0 \cos(\theta) \\
&\theta(z) = \begin{cases} -\theta_0 \pi/180 & , \text{for } z < 0 \\ \theta_0 \pi/180 & , \text{for } z \geq 0, \end{cases} \quad \text{if } L_{\mathrm{s}} = 0, \\
&\theta(z) = \tanh\left(\frac{z}{L_{\mathrm{s}}}\right) \theta_0 \times \pi/180, \quad \text{otherwise.}
\end{aligned}
\tag{6.23}
$$

We use a fixed value of $\theta_0 = 1°$ and $L_{\mathrm{s}} = L_0$ in Eq. 6.23 throughout the simulations. These simulations are marked in the table by "L1".

2. Physical viscosities and neutral thermal conductivity. We turn off physical viscosities and neutral

thermal conductivity indicated by "V0" in the table. The simulations with physical viscosities and neutral thermal conductivity are marked by "V1" in the table.

3. The dependence of the perturbation on the x direction

   - In most of the simulations the term $r_{\rm x}$ which appears in Eq. 6.21 that describes the perturbation, is generated as multimode perturbation. The functional dependence is similar to that described by Jun et al. (1995a); Khomenko et al. (2014c),

   $$r_{\rm x} = \sum_{n=1}^{m_{\rm x}} \sin\left(\frac{2\pi n x}{L_{\rm x}} + \phi_{\rm n}\right) \tag{6.24}$$

   where $m_{\rm x}$ is the number of points in the x direction, $L_{\rm x}$ is the length of the domain in the x direction, and $\phi_{\rm n}$ is a random phase for each mode inside the interval [-$\frac{\pi}{2}$, $\frac{\pi}{2}$]. The simulations which use this type of perturbation appear marked as "MM".
   - The white noise perturbation, marked with "WN", where $r_{\rm x}$ is a random number in the interval [-1,1] for all the points.

4. The amplitude of the perturbation. The amplitude of the perturbation is varied through the parameter δ in Eq. 6.21 above. We used the value $\delta = 10^{-2}$ in most of the simulations. But for the study of the linear growth rate, we have used a smaller amplitude by a factor of 100, i.e. $\delta = 10^{-4}$, in order to avoid the nonlinear effects. The names of these simulations in the table have an additional suffix "-S".

   Even if the initial perturbation should not have any influence on the linear growth rate, the evolution in the nonlinear phase may depend on it.

In our case, the transition between the prominence and the corona is smooth, and the minimum of the density gradient scale length, $L_{\rm d} = \rho_0 / \frac{\partial \rho_0}{\partial z}$ is larger than zero, contrary to the assumptions made in order to obtain the above Eq. (6.4). Keeping that in mind, we nevertheless computed the cutoff wavelengths λ_c, defined in Eq. 6.4, calculated using the value of $\rho_2 = \rho_0\Big|_{z=L_0/2} \approx 1.83 \times 10^{-11}$ kg/m^3, and $\rho_1 = \rho_0\Big|_{z=-L_0/2} \approx 2.93 \times 10^{-12}$ kg/m^3 above and below the interface, as a function of height in Figure 6.6. We repeated the calculation for the following four values of the shear length $L_{\rm s}$: 0, $L_0/10$, $L_0/2$, and L_0 with black solid lines with increasing width for increasing shear length $L_{\rm s}$. The density gradient scale length, plotted with red dotted lines, attains its minimum of $L_{\rm d} \approx 409$ km at z ≈ 0, and corresponds to the mode number $n_{\rm d} = L_{\rm x}/(2\pi L_{\rm d}) \approx 1$. The density gradient becomes negative in the region $z > L_0/2$, this being the reason for the upper limit of the height on the x-axis in the plot. The shaded region is bounded by the minimum (2 Δz), and maximum (2 L_0) possible wavelengths that can exist in the domain, indicated by blue lines. Alternatively, using the same values mentioned before, for ρ_2 and ρ_1, we tried to match an exponential density profile $\propto \exp(\beta z)$, for z between -$L_0/2$

Table 6.1: List of the simulations

Name	Parameters
P-V1-MM	Perpendicular magnetic field described by Eq. 6.22. Viscosities and neutral thermal conductivity turned on. Multimode perturbation with $\delta = 10^{-2}$ in Eq. 6.21.
P-V0-MM	Perpendicular magnetic field described by Eq. 6.22. Viscosities and neutral thermal conductivity turned off. Multimode perturbation with $\delta = 10^{-2}$ in Eq. 6.21.
L1-V1-MM	Sheared magnetic field described by Eq. 6.23 where the shear length $L_s = L_0$. Viscosities and neutral thermal conductivity turned on. Multimode perturbation with $\delta = 10^{-2}$ in Eq. 6.21.
L1-V1-MM-S	Sheared magnetic field described by Eq. 6.23 with $L_s = L_0$. Viscosities and neutral thermal conductivity turned on. Multimode perturbation with $\delta = 10^{-4}$ in Eq. 6.21.
L1-V1-WN-S	Sheared magnetic field described by Eq. 6.23 with $L_s = L_0$. Viscosities and neutral thermal conductivity turned on. White noise perturbation with $\delta = 10^{-4}$ in Eq. 6.21.
P-V1-MM-S	Perpendicular magnetic field described by Eq. 6.22. Viscosities and neutral thermal conductivity turned on. Multimode perturbation with $\delta = 10^{-4}$ in Eq. 6.21.
P-V1-WN-S	Perpendicular magnetic field described by Eq. 6.22. Viscosities and neutral thermal conductivity turned on. White noise perturbation with $\delta = 10^{-4}$ in Eq. 6.21.

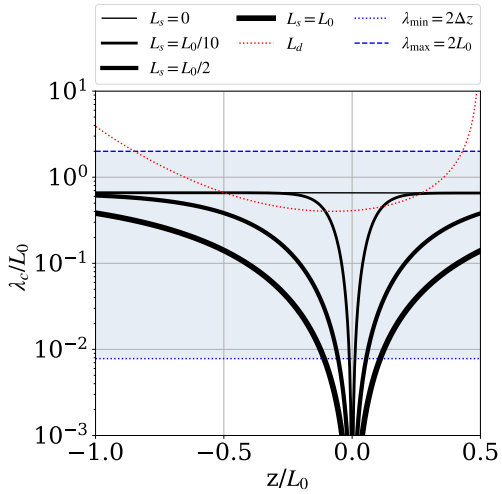

Figure 6.6: Cutoff wavelengths as a function of height computed from Eq. 6.4. Black solid lines correspond to cutoff wavelengths due to the x component of the magnetic field, calculated for the four shear lengths L_s used in the simulations: 0, $L_0/10$, $L_0/2$, and L_0 and shown with increasing width of the line for increasing L_s. The red dotted lines correspond to the density gradient scale length. The blue lines correspond to the minimum (dotted line) and to the maximum (dashed line) wavelengths that can exist in the domain.

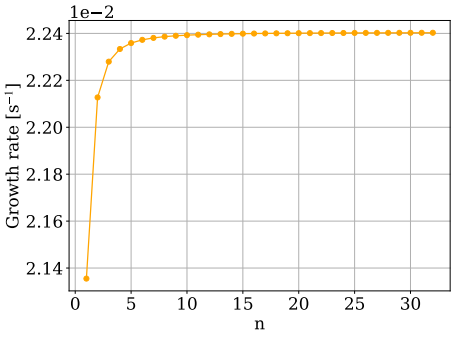

Figure 6.7: Growth rate obtained form the exact solution for the exponential density profile, Eq. 6.11 with uniform $\beta = 1.832 \times 10^{-6}$ m $^{-1}$. The value of β has been matched to our density profile.

and $L_0/2$, with uniform β. We obtained $\beta \approx 1.832 \times 10^{-6}$ m^{-1}. Figure 6.7 shows the growth rate obtained using this value of β and Eq. 6.11. The positive non-zero value of the gradient scale length makes the vertical profile to be seen as a discontinuity for the large scales ($n \leq n_{\rm d}$) and as an uniform profile for smaller scales ($n \gg n_{\rm d}$). Therefore, in this particular case, for the large scales the growth

rate grows with the wave number, while for the smaller scales it is uniform.

We next compute the coefficients of the charge and neutral viscosity, $\nu_{\rm n}^{\rm v}$, $\nu_{\rm c}^{\rm v}$ and the neutral thermal conductivity, $\nu_{\rm n}^{\rm T}$, in units of $\rm m^2/s$, and the ion-neutral and neutral-ion collision frequencies, $\nu_{\rm in}$ and $\nu_{\rm ni}$, all these quantities being calculated for the equilibrium atmosphere:

$$\nu_{\rm n}^{\rm v} = \xi_{\rm n}/\rho_{\rm n}\,; \quad \nu_{\rm c}^{\rm v} = \xi_{\rm c}/\rho_c\,; \quad \nu_{\rm n}^{\rm T} = K_{\rm n} m_{\rm H}/(1.5\rho_{\rm n} k_{\rm B}\gamma)\,; \quad \nu_{\rm in} = \alpha\rho_{\rm n}\,; \quad \nu_{\rm ni} = \alpha\rho_{\rm c}\,, \tag{6.25}$$

where γ is the adiabatic index, and $\xi_{\{\rm n,c\}}$, K_n, and the collisional parameter α have been defined in Eqs. 2.58, and 2.88, respectively.

The density of the neutrals is very low in the corona, and the temperature is high, therefore the coefficients of the neutral viscosity and thermal conductivity when only neutral-neutral collisions are taken into account, as from Eqs. 2.58, are very high. This problem has been described in section 2.1.4 in Chapter 2. At first, in order to overcome the very small time-step imposed by such large coefficients of neutral viscosity and thermal conductivity, we have considered an implicit implementation of the corresponding terms in the momentum and energy equations, but we finally decided to limit the value of these coefficients to 10^9 $\rm m^2/s$ in order to speed up the computation.

Left hand-side panel of Figure 6.8 shows the values of the neutral viscosity and thermal conductivity coefficients, limited as described above, and the viscosity coefficient of the charges. We can observe that the neutral viscosity and thermal conductivity coefficients have almost the same profile, and that the charge viscosity coefficient is one order of magnitude smaller than the neutral viscosity coefficient.

However, if the collisions with charges are also taken into account, the neutral viscosity and thermal conductivity coefficients will have smaller values. The middle panel of Figure 6.8 compares the neutral viscosity coefficient, calculated by considering only neutral-neutral collisions, as from Eq. 2.58, without any upper limit (orange line, labeled "n-n coll.") and the neutral viscosity coefficient, calculated by considering neutral-neutral, as well as neutral-charge collisions, as from Eq. 2.95 (blue line, labeled "n-n, n-c coll."). We can observe that the vertical profile of the neutral viscosity coefficient is more flat, and the values of the coefficient are indeed smaller by five orders of magnitude towards the vertical boundaries, when charges are to be considered. The maximum value of the neutral viscosity coefficient is two orders of magnitude smaller than our artificially imposed limit, when we include the charges. This implementation has to be taken into account in future work.

Right hand-side panel of Figure 6.8 shows the collision frequency between ions and neutrals (blue line) and between neutrals and ions (orange line). The collisional frequency between ions and neutrals decreases towards the vertical boundaries, where the large values of the collisional timescale of more than 1000 s, compared to the hydrodynamical time scale $t_{\rm hydro} = L_0/c_0 \approx 85$ s (the sound speed c_0 used in the calculation was the minimum sound speed for all the heights, attained at the location of minimum temperature) suggest important effects of the interaction between ions and neutrals. The collision timescale between neutrals and ions has the maximum of $\approx 1/20$ s at the point $z = L_0/2$, where the temperature minimum is attained, being much larger than the hydrodynamic timescale, meaning that the collision frequency between neutrals and ions is not relevant for out problem.

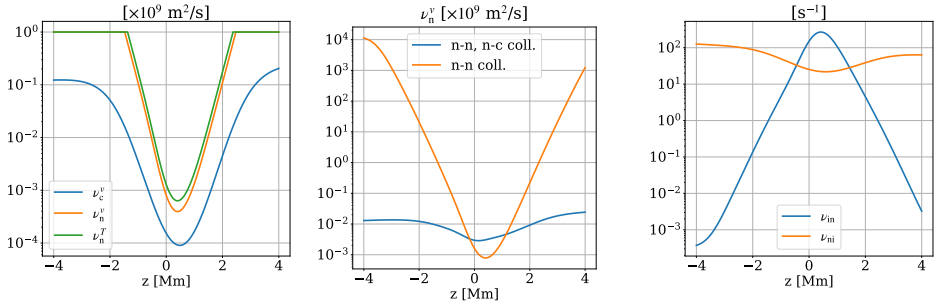

Figure 6.8: **Left:** The coefficients of the viscosity of charges (ν_c^v, blue line) and neutrals (ν_n^v, orange line), the thermal conductivity of neutrals (ν_n^T, green line), in units of m^2/s. The viscosities and thermal conductivity coefficients have been calculated when only collisions between particles of the same species are taken into account, as from Eq. 2.58. The neutral viscosity and thermal conductivity coefficients are limited to 10^9 m^2/s. **Middle:** Comparison between the neutral viscosity coefficient calculated when only neutral-neutral collisions are taken into account, as from Eq. 2.58, without any upper limit (orange line, labeled "n-n coll.") and the neutral viscosity coefficient calculated from Eq. 2.95, when neutral-neutral and neutral-charge collisions are taken into account (blue line, labeled "n-n, n-c coll."), as a function of height. **Right:** Ion-neutral, ν_{in}, (blue) and neutral-ion ν_{ni} (orange) collision frequencies as a function of height. All the quantities plotted are calculated with equilibrium variables.

6.4 Results

Figure 6.9 shows snapshots of the simulations: P-V1-MM (top, left panel), P-V0-MM (top, right panel), L1-V1-MM (bottom, left panel), and L1-V0-MM (bottom, right panel). The velocity of neutrals and charges are indicated by orange arrows in the panels showing the density of neutrals and charges, respectively. The velocities of neutrals and charges are similar in magnitude for P-V1-MM and L1-V1-MM to their corresponding P-V0-MM and L1-V0-MM simulations. For the simulations L1-V1-MM and L1-V0-MM, the in-plane magnetic field lines are shown with red lines, only in the panels of the charges density. We can clearly see more smaller scales and larger gradients for the simulations P-V0-MM and L1-V0-MM, compared to P-V1-MM and L1-V1-MM. The field lines also are less twisted at later times, as can be observed for the simulation L1-V0-MM, compared to L1-V1-MM. Even if initially the phases of the perturbation harmonics (or modes) are random, at later stages, we can observe coherence between the modes, that gives rise to a large structure which develops at the middle of the horizontal domain. In the nonlinear stage, the tangential flow gives rise to Kelvin-Helmholtz secondary instabilities. As a consequence, structures with shapes resembling a mushroom develop. This can be observed in Figure 6.9 for all four simulations. The two layers of increased density of charges, located around $z = -L_0$ and $z = L_0$, which appear for all four simulations, are due to the slow evolution of the background atmosphere through ionization, as it will be shown in the next chapter. If we compare the snapshots at different times, we can observe that the structures are more

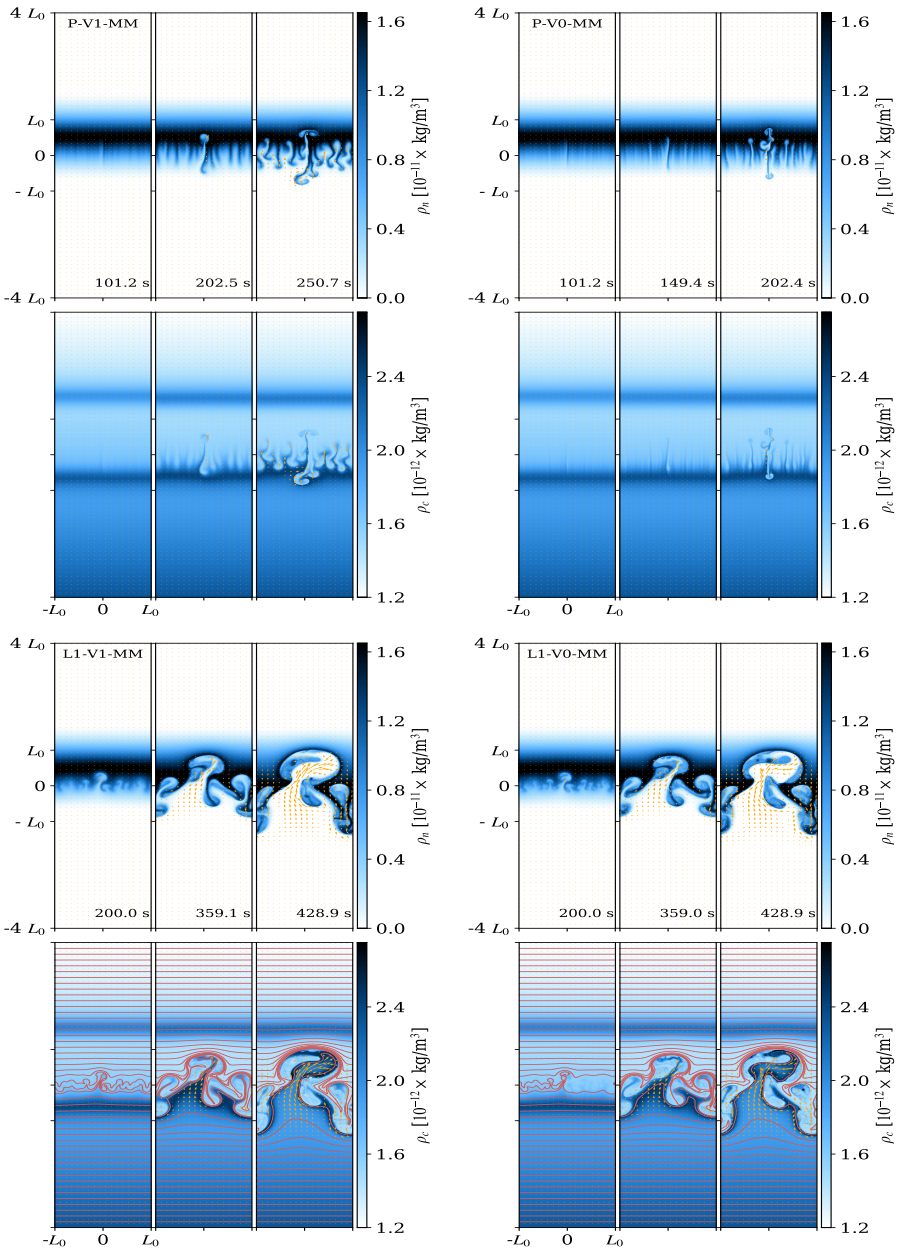

Figure 6.9: Group of panels with snapshots of the densities of neutrals and charges taken at three different times for the following simulations: Top left: P-V1-MM. Top right: P-V0-MM. Bottom left: L1-V1-MM. Bottom right: L1-V0-MM. The in plane (x and z components) velocities of neutrals and charges are represented by orange arrows in the plots which show the densities of neutrals and charges, respectively. For the simulations with sheared magnetic field, L1-V1-MM and L1-V0-MM, the in-plane magnetic field lines are shown with red lines, only in the panels of the charges density.

elongated in the vertical direction for the simulations P-V1-MM and P-V0-MM than for L1-V1-MM and L1-V0-MM, respectively. The structures have larger vertical extent in the negative z-direction than in the positive z-direction.

6.4.1 Growth rate

We calculate the average growth rate for all the simulations using the velocity v as a reference variable,

$$g.r. = \frac{\ln\Big(v(t_2)\Big) - \ln\Big(v(t_1)\Big)}{\Big(t_2 - t_1\Big)}, \tag{6.26}$$

where v is the horizontally averaged vertical velocity of neutrals at the height $z = 0$. The value of the growth rate changes in time. For the calculation in the case of P1-V1-MM, we selected $t_1 = 50$ s and $t_2 = 160$ s. In this interval the growth was observed to be linear, as we can observe in Figure 6.10. The reason for choosing the start time of the linear phase $t_1 > 0$ is that the initial perturbation used as an initial condition is random and does not represent an eigenfunction for the excited modes. Because of the compressibility, the sound speed has a finite value and the formation of the eigenfunctions is not instantaneous (Hillier 2016). The simulation which uses white noise as a perturbation needs more time to setup the eigenfunctions, because periodicity in the x direction is not fulfilled either, initially. For the case of P1-V1-MM, the value of g.r. $\approx 2.2 \times 10^{-2}$ s^{-1} was obtained. This value is similar to the Brunt-Väisälä imaginary frequency, which describes the unstable evolution, Eq. 6.5, calculated in the incompressible assumption as,

$$\sqrt{-N^2} = \sqrt{\frac{g}{L_d}}, \tag{6.27}$$

where g is the gravity. Using the value of $L_d \approx 409$ km, corresponding to the height $z = 0$, we obtain the value of $\sqrt{-N^2} \approx 2.5 \times 10^{-2}$ s^{-1}. This value is also consistent with the value of ≈ 0.02 s^{-1} obtained by Leake et al. (2014) for the same setup.

In order to distinguish between the modes, and to take into account the vertical profile and not only the height $z = 0$, we have repeated the calculation as in Eq. 6.26, but this time separately for each of the modes. For that, we have computed the amplitudes of the modes as the amplitudes of the Fourier coefficients, obtained by doing a FFT of a given quantity (for example vertical velocity of neutrals or charges), in the x direction, at each time moment. We then averaged the amplitudes in the vertical direction between $z = -L_0$ and $z = L_0$, and over four consecutive modes. We have chosen to average over four modes in order to observe the evolution of many modes with better visualization, than seeing the evolution of each mode separately. Figure 6.11 shows the amplitudes of different modes from $n = 1$ to $n = 64$ for P-V1-MM (top left panel), P-V0-MM (top right panel), L1-V1-MM (bottom left panel), and L1-V0-MM (bottom right panel) as a function of time. At a quick glance, we can observe that the modes grow less in the cases with physical viscosities and neutral thermal conductivity, starting with mode $n = 9$, and smaller scales are more affected.

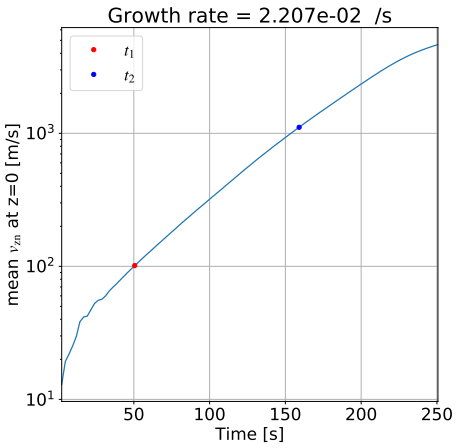

Figure 6.10: Linear growth rate calculated for the simulation P1-V1-MM, as from Eq. 6.26. The linear phase has been chosen between $t_1 = 50$ s, and $t_2 = 160$ s, marked in the panel by a red and blue points, respectively.

For each horizontal scale, the nonlinear phase starts when the horizontal wavelength of the corresponding harmonics is similar to the vertical extent reached by the perturbation. This means that smaller horizontal scales start the nonlinear phase earlier. The three growing regimes, as described by Ristorcelli & Clark (2004), when the amplitudes of velocity grow in the nonlinear phase as $\propto$ t, $t^{-1/2}$, and $t^{-5/4}$ [3], do not have a clear delimitation in our case. The vertical profiles of the physical properties of the equilibrium atmosphere are smooth, and the transition between the three regimes is also smooth. The larger scales (corresponding to $n = 1 - 36$ for P-V1-MM, $n = 1 - 44$ for P-V0-MM, $n = 1 - 28$ for L1-V1-MM, and $n = 1 - 40$ for L1-V0-MM) have initially a linear growth stage when the velocity amplitude grows exponentially. The amplitudes of the modes are larger for the simulations without viscosities and neutral thermal conductivity, especially for the smallest scales.

The modes that do not grow in the linear phase are completely suppressed by neutral viscosity and thermal conductivity, and the interaction between ions and neutrals. The analytical calculations showed that neither the viscosity (Chandrasekhar 1961), nor the interaction between charges and neutrals (Díaz et al. 2012), impose a cutoff frequency, in practice very small growth rates cannot be captured numerically. Therefore, we observe that there exist for all the four cases a critical mode number, that we denote as $n_{\rm cd}$, so that modes with mode number $n > n_{\rm cd}$ do not have an initial linear growth phase. The value of $n_{\rm cd}$ =36, 44, 28, 40 for P-V1-MM, P-V0-MM, L-V1-MM, and L-V0-MM, respectively, as it can be observed in Figure 6.11. We observe that the value of $n_{\rm cd}$ is smaller for

[3]The power laws of evolution of the vertical extent of the perturbations, $\propto t^2$, $t^{1/2}$, and $t^{1/4}$ have been divided by time in order to obtain the power laws for the amplitude of the velocity.

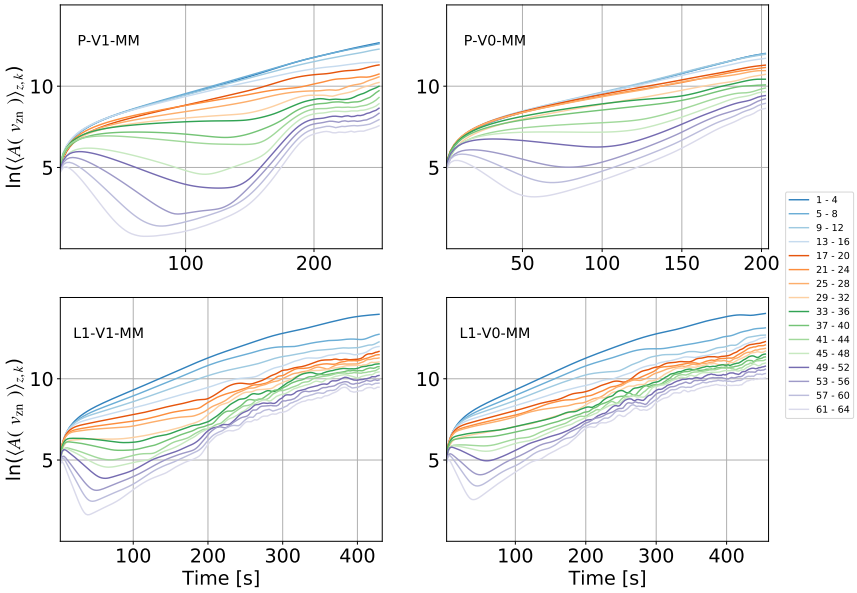

Figure 6.11: Growth rate of individual harmonics, computed from the vertical velocity of neutrals, as a function of time. Different color lines show the Fourier amplitudes of the harmonics, grouped in sets of four, from $n = 1$ to $n = 64$. The amplitudes are averaged between heights -L_0 and L_0. The results for four simulations are shown: P-V1-MM (top left); P-V0-MM (top right); L1-V1-MM (bottom left); L1-V0-MM (bottom right).

the cases with physical viscosities and neutral thermal conductivity. It is also lower for the sheared magnetic field than for the perpendicular field geometry.

The velocity amplitudes corresponding to the large scales ($n \leq n_{\rm cd}$) decrease at the beginning of the nonlinear phase, when they start to transfer energy to smaller scales. Among these large scales, smaller scales start to decrease earlier as they start the nonlinear phase earlier. This can be directly seen in Figure 6.11, e.g. by comparing modes $33 - 36$ to $13 - 16$ for the simulation P-V1-MM. The physical viscosities and thermal conductivity delay the growth of small scales at the the beginning of the nonlinear phase for the simulations P-V1-MM and L-V1-MM, compared to P-V0-MM and L-

V0-MM, where these terms were not included. The high frequency modes only start to grow later, powered by larger scales. The smallest scales (largest n) start earlier the nonlinear phase, and their growth rate is larger than that of the larger scales. The small scales start to grow earlier in the nonlinear phase for the sheared field compared to the perpendicular field geometry.

The dissipative effects of the viscosity are also present for larger scales ($n \leq n_{\rm cd}$), when the growth is decreased, even if not totally suppressed. It has been shown that the mode with the fastest growth ($n_{\rm max}$) is set by the dissipative effect of the viscosity (Chandrasekhar 1961; Livescu 2004). We observe in Figure 6.11 that the largest scales, grouped for the mode numbers $n = 1-4$ have higher amplitudes for the simulations without viscosities and neutral thermal conductivity, therefore the conclusion is that $n_{\rm max} \leq 4$.

In order to understand the differences produced by the action of neutral viscosity, thermal conductivity and the interaction between ions and neutrals, we computed the scales associated to these effects. We did the calculation for the parameters of the background atmosphere. Figure 6.12 shows the mode numbers n corresponding to the ion-neutral decoupling scale and to the neutral viscosity scale. The length scales of the neutral viscosity and the ion-neutral decoupling are defined as:

$$L_{\rm visc_n} = \nu_{\rm n}^{v}/c_{\rm n0}\,, \qquad L_{\nu_{\rm in}} = c_{\rm c0}/\nu_{\rm in}\,, \tag{6.28}$$

where $\nu_{\rm n}^{v}$ and $\nu_{\rm in}$ have been defined in Eq. 6.25, and $c_{\rm n0}$ and $c_{\rm c0}$ are the sound speed of the neutrals and charges, respectively. The mode corresponding to the scale L is obtained as $n = L_{\rm x}/(2\pi L)$. The scales corresponding to the charges viscosity and to neutral-ion decoupling are below the grid cell size and are not shown in the plot. The coefficients for neutral viscosity and thermal conductivity calculated in m^2/s units have very similar height dependence, as shown at the left hand-side panel of Figure 6.8, so the corresponding modes also have similar height dependence and, for this reason, only the modes corresponding to the neutral viscosity are shown in the plot. We limit the horizontal axis between $z = -1.5$ Mm and $z = 1.5$ Mm, these values are considered to be the maximum extent of the structures that form during the instability development. The horizontal dashed and dotted lines are $n = 64$ and $n = 256$, which represent the maximum mode number which appear in Figure 6.11 , and the maximum mode number that can exist in the domain (sampled by two points), respectively.

We observe that the functional dependence on the height is very similar for the modes corresponding to the neutral viscosity and for the modes corresponding the interaction between ions and neutrals, the latter being slightly smaller. For heights below $z = -0.5$ Mm, the neutral viscosity and the interaction between ions and neutrals affect modes that can exist in our domain, i.e. the modes below the horizontal dotted line. The dissipation effects of the neutral viscosity and the interaction between ions and neutrals are more pronounced towards the boundaries, where the mode affected by these effects have numbers $n \approx 10$.

6.5 Analytical growth rate

In this subsection, we try to obtain an analytical linear growth rate in the ideal MHD approximation (when the interaction between neutrals and charges is neglected), neglecting the compressibility, the

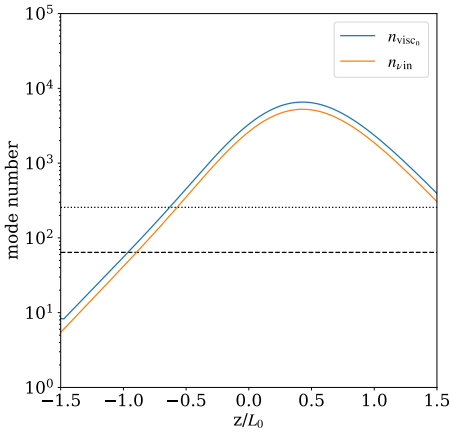

Figure 6.12: Modes corresponding to the neutrals viscosity and ion-neutral decoupling scale as a function of height. The scales are calculated from Eq. 6.28. The horizontal dashed line marks the maximum mode number shown in Figure 6.11, $n = 64$, and the dotted line represents the largest mode number that can be resolved in the domain, using two points, $n = 256$.

viscosities, and neutral thermal conductivity.

In our model, the charges and neutrals are very well coupled by collisions. The equilibrium itself depends on the strong collisional coupling because the magnetic field has been calculated from the magneto-hydrostatic equation for the charges and neutrals together. For this reason, we expect that the single-fluid model might give a good approximate solutions for the linear growth rate. The equations are much easier to solve in the single-fluid than in the two-fluid assumption. For the moment we neglect the compressibility, which simplifies the equations, but the effect of the compressibility is taken into account later, in section 6.6, for the situation without magnetic field. As the incompressible MHD equations are solved in a more general context, this will be our reference analytic MHD solution. In the incompressible approximation, the energy equation is not needed, and the zero-divergence condition of the velocity must be used in order to close the equations. With all these assumptions the equations become:

$$\begin{aligned} \frac{\partial \rho}{\partial t} + \nabla \cdot (\rho \mathbf{u}) &= 0, \\ \nabla \cdot \mathbf{u} &= 0, \\ \frac{\partial (\rho \mathbf{u})}{\partial t} + \nabla \cdot (\rho \mathbf{u}\mathbf{u} + p) &= \mathbf{J} \times \mathbf{B} + \rho \mathbf{g}, \\ \frac{\partial \mathbf{B}}{\partial t} - \nabla \times (\mathbf{u} \times \mathbf{B}) &= 0, \end{aligned} \tag{6.29}$$

We consider the 3D case, when the equilibrium atmosphere is replicated in the y direction, thus the

atmosphere is homogeneous in both x and y directions, but it is not uniform in the z direction, all the equilibrium quantities only depend on height. We use the ansatz of separable solutions and we Fourier transform the Eqs. 6.29, in time and in the x and y spatial directions, after linearizing them, looking for solutions of the form:

$$\{\tilde{\rho}_1, \tilde{p}_1, \tilde{v}_\mathrm{x}, \tilde{v}_\mathrm{y}, \tilde{v}_\mathrm{z}, \tilde{B}_\mathrm{x1}, \tilde{B}_\mathrm{y1}, \tilde{B}_\mathrm{z1}\} = \{\rho_1(z), p_1(z), v_\mathrm{x}(z), v_\mathrm{y}(z), v_\mathrm{z}(z), B_\mathrm{x1}(z), B_\mathrm{y1}(z), B_\mathrm{z1}(z)\} \times \exp\left(i\omega t - ik_\mathrm{x}x - ik_\mathrm{y}y\right). \quad (6.30)$$

As the equations have been linearized, the general solution is a superposition of the solutions defined in Eq. 6.30 above. After linearization and Fourier transformation, the system 6.29 becomes,

$$\begin{aligned}
\rho_1 &= -\frac{1}{i\omega}\frac{\mathrm{d}\rho_0}{\mathrm{d}z}v_\mathrm{z},\\
-ik_\mathrm{x}v_\mathrm{x} - ik_\mathrm{y}v_\mathrm{y} + \frac{\mathrm{d}v_\mathrm{z}}{\mathrm{d}z} &= 0,\\
i\omega\rho_0 v_\mathrm{x} &= ik_\mathrm{x}p_1 + \frac{1}{\mu_0}\left(ik_\mathrm{x}B_\mathrm{y1}B_\mathrm{y0} - ik_\mathrm{y}B_\mathrm{x1}B_\mathrm{y0} + \frac{\mathrm{d}B_\mathrm{x0}}{\mathrm{d}z}B_\mathrm{z1}\right),\\
i\omega\rho_0 v_\mathrm{y} &= ik_\mathrm{y}p_1 + \frac{1}{\mu_0}\left(ik_\mathrm{y}B_\mathrm{x1}B_\mathrm{x0} - ik_\mathrm{x}B_\mathrm{y1}B_\mathrm{x0} + \frac{\mathrm{d}B_\mathrm{y0}}{\mathrm{d}z}B_\mathrm{z1}\right),\\
i\omega\rho_0 v_\mathrm{z} &= -\rho_1 g - \frac{\mathrm{d}p_1}{\mathrm{d}z} - \frac{1}{\mu_0}\left[B_\mathrm{y0}\left(\frac{\mathrm{d}B_\mathrm{y1}}{\mathrm{d}z} + ik_\mathrm{y}B_\mathrm{z1}\right) + B_\mathrm{x0}\left(\frac{\mathrm{d}B_\mathrm{x1}}{\mathrm{d}z} + ik_\mathrm{x}B_\mathrm{z1}\right) + B_\mathrm{x1}\frac{\mathrm{d}B_\mathrm{x0}}{\mathrm{d}z} + B_\mathrm{y1}\frac{\mathrm{d}B_\mathrm{y0}}{\mathrm{d}z}\right],\\
B_\mathrm{x1} &= \frac{1}{i\omega}\left[-ik_\mathrm{y}B_\mathrm{y0}v_\mathrm{x} - v_\mathrm{z}\frac{\mathrm{d}B_\mathrm{x0}}{\mathrm{d}z} + B_\mathrm{x0}\left(ik_\mathrm{y}v_\mathrm{y} - \frac{\mathrm{d}v_\mathrm{z}}{\mathrm{d}z}\right)\right],\\
B_\mathrm{y1} &= \frac{1}{i\omega}\left[-ik_\mathrm{x}B_\mathrm{x0}v_\mathrm{y} - v_\mathrm{z}\frac{\mathrm{d}B_\mathrm{y0}}{\mathrm{d}z} + B_\mathrm{y0}\left(ik_\mathrm{x}v_\mathrm{x} - \frac{\mathrm{d}v_\mathrm{z}}{\mathrm{d}z}\right)\right],\\
B_\mathrm{z1} &= -\frac{1}{\omega}\left(k_\mathrm{x}B_\mathrm{x0} + k_\mathrm{y}B_\mathrm{y0}\right)v_\mathrm{z}\,. \quad (6.31)
\end{aligned}$$

After manipulating the above Eqs. 6.31 we obtain a second order differential equation for v_z:

$$a\frac{\mathrm{d}^2 v_\mathrm{z}}{\mathrm{d}z^2} + \frac{\mathrm{d}a}{\mathrm{d}z}\frac{\mathrm{d}v_\mathrm{z}}{\mathrm{d}z} - k^2\left(a - g\frac{\mathrm{d}\rho_0}{\mathrm{d}z}\right)v_\mathrm{z} = 0 \quad (6.32)$$

where a is defined as:

$$a = \frac{1}{\mu_0}\left(k_\mathrm{x}B_\mathrm{x0} + k_\mathrm{y}B_\mathrm{y0}\right)^2 - \omega^2\rho_0 \quad (6.33)$$

When $B_\mathrm{x0} = B_\mathrm{y0} = 0$, we recover Eq. 42 from Chandrasekhar (1961). The equation 6.32 does not have a general known analytical solution.

In order to obtain the approximate solution, we have discretized spatially Eq. 6.32, using second order centered differences:

$$\frac{\mathrm{d}v_\mathrm{z}}{\mathrm{d}z}[k] = \frac{v_\mathrm{z}[k+1] - v_\mathrm{z}[k-1]}{2d_\mathrm{z}}, \qquad \frac{\mathrm{d}^2 v_\mathrm{z}}{\mathrm{d}z^2}[k] = \frac{v_\mathrm{z}[k+1] - 2v_\mathrm{z}[k] + v_\mathrm{z}[k-1]}{d_\mathrm{z}^2}, \quad (6.34)$$

we obtain a generalized eigenvalue problem of the form:

$$\hat{\mathbf{A}}\mathbf{u} = \lambda\hat{\mathbf{B}}\mathbf{u} \tag{6.35}$$

where $\mathbf{u} = (v_z[1], ...v_z[m_z])$, with m_z being the number of the points in the z direction, and $\lambda = -\omega^2$. We solve the eigenvalue problem for all the wave numbers, and we observe that all the eigenvalues are real. The negative values represent propagating solutions, and the positive values correspond to standing solutions either growing or damped in time at the same rate. We are interested in non-propagating growing solutions, so, for each wave number, we choose the growth rate as the square root of the maximum of the positive eigenvalues obtained. The maximum of the positive eigenvalues corresponds to the fastest growing mode for the chosen mode number. We will refer to this method as semi-analytical. Figure 6.13 shows the vertical eigenfunctions v_z obtained semi-analytically for

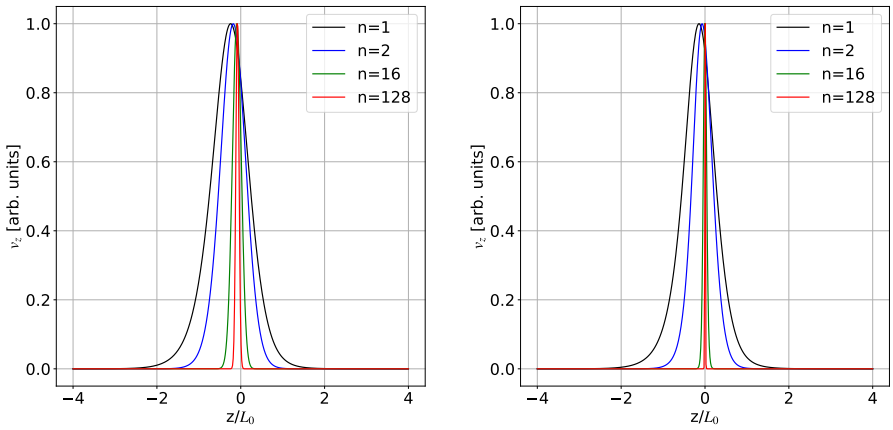

Figure 6.13: Eigenfunctions corresponding to the largest growing rate for the modes specified in the legend, normalized to unity, as a function of height. Left: perp case. Right: $L_s = L_0$ case.

the perpendicular case and the sheared case. The eigenfunctions, normalized to unity, shown in the plots correspond to the fastest growing modes for the wave numbers indicated in the legend. We can observe that the eigenfunctions are more spatially extended for the larger scales (i.e., smaller n). For the same scale considered, they are broader and have the peak slightly shifted towards the negative z direction. The effect is more pronounced for the perpendicular case than for the sheared field case. In order to calculate the growth rate from the simulations we performed the following procedure. First, we re-run the simulations with the smaller amplitudes to ensure the linear phase. Then we Fourier transformed the vertical velocity of neutrals in the x direction for each time moments to obtain the

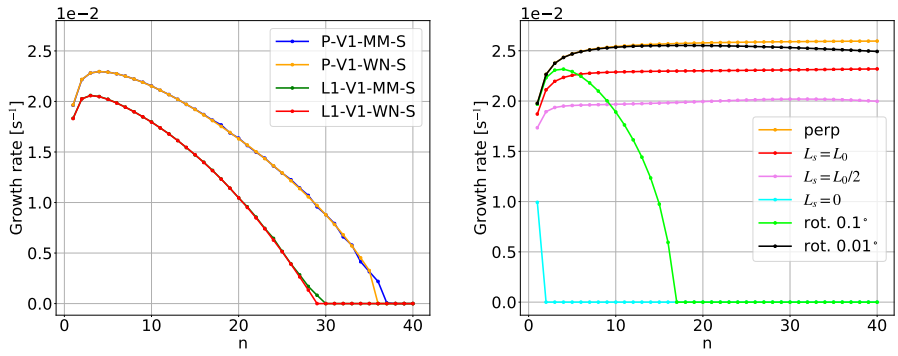

Figure 6.14: Growth rates as a function of the mode number. Left: Growth rate obtained from the simulations P-V1-MM-S (blue), P-V1-WN-S (orange), L1-V1-MM-S (green), L1-V1-WN-S (red). The time interval that we have considered to be the linear phase was [100, 200] s. We can observe that the blue line and the orange line are superposed, as well as the green line and the red line. For the positive growth rates, the error of the fit $\varepsilon = (y_{\rm data} - y_{\rm fit})^2/(N y_{\rm fit}^2) < 10^{-3}$, where $y_{\rm data}$ and $y_{\rm fit}$ are the input and the fitted arrays respectively, both of length N. Right: Growth rate obtained semi-analytically for the following magnetic field configurations: perpendicular (orange); sheared field with shear length L_s equal to: L_0 (red), $L_0/2$ (violet), 0 (cyan); rotated field by an angle of: 0.1° (lime), 0.01° (black).

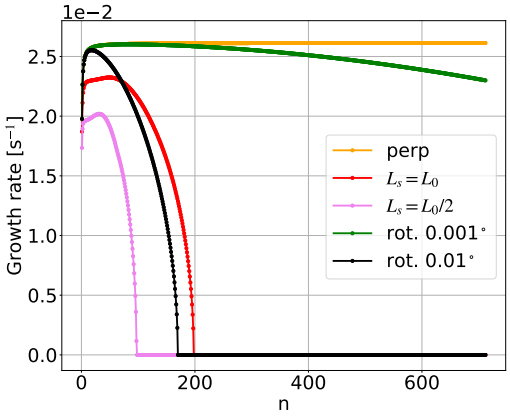

Figure 6.15: Growth rate calculated semi-analytically as a function of the mode number n for a larger range of n (the right plot of Figure 6.14 has been extended to $n = 712$) for the following magnetic field configurations: perpendicular (orange); sheared field with shear length L_s equal to: L_0 (red), $L_0/2$ (violet); rotated field by an angle of: 0.01° (black), 0.001° (green).

Fourier amplitudes of the harmonics. We then averaged these amplitudes over the vertical distance from -L_0 to L_0. The natural logarithm of these amplitudes was plotted as a function of time and a linear fit was performed for a time interval that we identified as a linear phase. The resulting growth rates are plotted at the left panel of Figure 6.14for the following simulations: P-V1-MM-S, L1-V1-MM-S,P-V1-WN-S and L1-V1-WN-S. The time interval considered to be the linear phase was between $t_1 = 100$ s and $t_2 = 200$ s. The error of the fit, $\varepsilon = (y_{\rm data} - y_{\rm fit})^2/(N y_{\rm fit}^2)$, where $y_{\rm data}$ and $y_{\rm fit}$ are the input and the fitted arrays respectively, both of length N, was below 10^{-3} for all the modes, otherwise the growth was set to zero.

We can see that the multimode and white noise perturbations give growth rates that match almost perfectly. This is true for both magnetic field configurations. This match can be considered as a proof for the correctness of the simulations. The right-hand side panel shows the semi-analytical growth rates for the perpendicular magnetic field (perp) and the sheared field with $L_{\rm s} = L_0$. These rates can be compared to the values obtained from the simulations shown at the left hand-side panel. Additionally, we plot the growth rates obtained semi-analytically for various cases of the uniform magnetic field rotated by 0.1°, 0.01°, as well as several cases of sheared field configuration, where the shear length varies between the values: $L_0/2$, and 0.

The decrease with the mode number of the growth rates obtained from the simulations, is not present in the semi-analytical calculation. The decrease is due to the dissipative effects mentioned before. The growth rate becomes zero for all the modes numbers larger than a certain mode number, which therefore appears as a cutoff mode number in the plot of the growth rates obtained from simulations. The value of this cutoff mode number is consistent with the smallest mode number of the modes that do not have an initial linear phase, $n_{\rm cd}$, mentioned above to be equal to 28 and 36 for P-V1-MM and L1-V1-MM, respectively.

The mode with maximum growth rate appears to be $n_{\rm max} = 4$, and $n_{\rm max} = 3$ for the perpendicular case (P-V1-MM and P-V1-WN) and sheared case (L1-V1-MM and L1-V1-WN), respectively. This is consistent with the above deduction that $n_{\rm max} \leq 4$.

The decrease of the growth rate with the mode number is the main difference between the simulations and the analytical calculations. Recall that the analytical calculation does not include dissipation effects. As we will see later, in section 6.6, the compressibility increases the growth rate, so we will conclude that the decrease of the growth rate is due to the viscosities, neutral thermal conductivity and the ion-neutral interactions.

Figure 6.15 shows the semi-analytical growth rate for a larger range of n. The horizontal axis of the right-hand side panel of Figure 6.14 has been extended from mode number $n = 40$ to mode number $n = 712$. The color coding is the same as in Figure 6.14: perpendicular field (orange line labeled "perp"); sheared cases with $L_{\rm s}$ equal to: L_0 (red line labeled "$L_{\rm s} = L_0$"), $L_0/2$ (violet line labeled "$L_{\rm s} = L_0/2$"); and the uniform field rotated by the angle 0.01° (black line labeled "rot. 0.01°"). Additionally, we plot the growth rate for uniform field rotated by 0.001° (green line labeled "rot. 0.01°"). The cutoff that we observe in the semi-analytical calculation appears for the simulations where the magnetic field has a in-plane component. From these plots we can conclude that, for the uniform rotated field configurations the growth rate increases with decreasing angle of rotation. For

the sheared field configurations the growth rate increases with increasing L_s. The cutoff for the sheared case with $L_s = L_0$ is at the mode number $n \approx 200$. This is much larger than the lowest mode number among those suppressed by dissipation effects. The latter, we have seen previously, has a much smaller value of $n \approx 30$.

The largest scales are not affected by the dissipative effects, therefore the overall growth rate remains the same. It has been shown by numerical simulations that RTI flows and their characteristics are identical for the viscous and inviscid models (Doludenko et al. 2019). Mitra et al. (2016) and Gerashchenko & Livescu (2016) found an increased growth rate for all the wave numbers in the inviscid case, compared to the case with viscosity. Depending on the RTI scales considered and the viscosity scales, the viscosity may have an important effect in the development of the RTI.

6.5.1 Analytical approximate expressions for the growth rate

We showed how the growth rate can be obtained semi-analytically by solving a general eigenvalue problem. However, this method does not give an analytical expression for the growth rate. We can estimate the growth rate by making further assumptions.

Exact solution for the exponential density profile

In the absence of the magnetic field, and for an exponential density profile $\propto \exp(\beta z)$ with uniform $\beta > 0$, Eq. 6.32 can be solved exactly. The analytical growth rate, obtained by Chandrasekhar (1961) is given in Eq. 6.11. We obtained the β corresponding to our density profile, and we plotted the analytical growth rate from Eq. 6.11 in Figure 6.7. We can observe that this exact analytical growth rate is very similar to that indicated by the orange line labeled "perp" at the right hand-side panel of Figure 6.14, but the values are smaller.

Flat eigenfunction

In the large k_x limit, and when the equilibrium profile varies only slowly on length scales much larger than the wavelength considered, we can neglect the first two terms in Eq. 6.32. We obtain the dispersion relation of the following form:

$$\frac{1}{\mu_0}\left(k_{\rm x}B_{\rm x0} + k_{\rm y}B_{\rm y0}\right)^2 - \omega^2\rho_0 - g\frac{\partial\rho_0}{\partial z} = 0\,. \tag{6.36}$$

For the 2D case ($k_{\rm y} = 0$), we recover the growth rate for the case of the uniform magnetic field rotated with respect to the direction perpendicular to the direction of perturbation and the gravity, as a function of height. It has the following expression:

$$-\omega^2 = \frac{1}{\rho_0}\left(g\frac{\partial\rho_0}{\partial z} - \frac{1}{\mu_0}k_{\rm x}^2 B_{\rm x0}^2\right)\,. \tag{6.37}$$

For no horizontal magnetic field ($B_{x0} = 0$), Eq. 6.37 recovers the Brunt-Väisälä frequency:

$$-\omega^2 = g\frac{1}{\rho_0}\frac{\partial \rho_0}{\partial z}\,. \tag{6.38}$$

Unfortunately, Eq. 6.37 cannot capture the shear of the magnetic field. This equation is for the case of the uniform rotated field. We can use this equation locally at each height, by changing the field. This will give a growth rate which depends on height, the same as the Brunt-Väisälä frequency from the Eq. 6.38 above. This local approximation should be used only when the frequency obtained as a function of height has very small spatial variations and can be assumed uniform. Unfortunately, this assumption does not hold in our case.

Neglecting the first two terms in Eq. 6.32, i.e. neglecting the vertical derivatives of the eigenfunction v_z comes from the idea that, in the large k_x limit, the vertical profile is smooth enough, so that it looks the same regardless of k_x. With this assumption, for the perpendicular magnetic field, all the modes grow at the same rate with the growth determined by the Brunt-Väisälä frequency (Eq. 6.38). The particular vertical profile does not matter as long as the scales associated with the wave number are below the gradient scale length. This is why, the growth rate corresponding to the exact analytical solution for the non-uniform exponential profile, shown in Figure 6.7 is the same for larger k. The mode number associated to the density gradient scale length calculated at $z = 0$, $L_d = 409$ km is $n \approx 1$. Thus, we expect to have the growth rate independent of the mode number for $n \gg 1$. However, this simplification, when we neglect the vertical derivatives of the eigenfunction, cannot capture the growth for the large scales, comparable to the density gradient scale length ($n \approx 1$), which perceive the vertical profile as a discontinuity, when the growth rate increases with the wave number. We could observe this tendency for smaller k in Figure 6.7 and at the right-hand side panel of Figure 6.14.

6.6 The effect of the compressibility

In the absence of the magnetic field, taking compressibility into account, the equations in the ideal HD assumption, with an adiabatic expression for the energy equation, become:

$$\begin{aligned}
\frac{\partial \rho}{\partial t} + \nabla \cdot (\rho \mathbf{u}) &= 0,\\
\frac{\partial (\rho \mathbf{u})}{\partial t} + \nabla \cdot (\rho \mathbf{u}\mathbf{u} + p) &= \rho \mathbf{g},\\
\frac{\partial p}{\partial t} + \left(\nabla p + c_0^2 \nabla \rho\right) \cdot \mathbf{u} &= 0,
\end{aligned} \tag{6.39}$$

In the 2D case with the atmosphere homogeneous the x direction, where the equilibrium quantities only depend on the height z, we use the ansatz of separable solutions as before and we Fourier transform

the Eqs. 6.39, in time and in the x spatial directions, after linearizing them, looking for solutions of the form:

$$\{\tilde{\rho}_1, \tilde{p}_1, \tilde{v}_\mathrm{x}, \tilde{v}_\mathrm{z}\} = \{\rho_1(z), p_1(z), v_\mathrm{x}(z), v_\mathrm{z}(z)\} \times \exp\big(i\omega t - ik_\mathrm{x}x\big)\,. \tag{6.40}$$

The following system is obtained:

$$\begin{aligned}
\rho_1 &= \frac{1}{i\omega}\left[\rho_0\left(ik_\mathrm{x}v_\mathrm{x} - \frac{\mathrm{d}v_\mathrm{z}}{\mathrm{d}z}\right) - \frac{\mathrm{d}\rho_0}{\mathrm{d}z}v_\mathrm{z}\right],\\
i\omega\rho_0 v_\mathrm{x} &= ik_\mathrm{x}p_1,\\
i\omega\rho_0 v_\mathrm{z} &= -\rho_1 g - \frac{\mathrm{d}p_1}{\mathrm{d}z},\\
p_1 &= \frac{1}{i\omega}\left[c_0^2\left(i\omega\rho_1 + \frac{\mathrm{d}\rho_0}{\mathrm{d}z}v_\mathrm{z}\right) - \frac{\mathrm{d}\rho_0}{\mathrm{d}z}v_\mathrm{z}\right].
\end{aligned} \tag{6.41}$$

With the notation $\lambda = -\omega^2$, after some calculations, a second order ODE for the vertical velocity is obtained:

$$a_1\frac{\mathrm{d}^2 v_\mathrm{z}}{\mathrm{d}z^2} + a_2\frac{\mathrm{d}v_\mathrm{z}}{\mathrm{d}z} + a_3 v_\mathrm{z} = 0\,, \tag{6.42}$$

where:

$$\begin{aligned}
a_1 &= \lambda\rho_0 c_0^2 b_1; \qquad b_1 = \lambda + k_\mathrm{x}^2 c_0^2\,,\\
a_2 &= \frac{\mathrm{d}a_1}{\mathrm{d}z} - k_\mathrm{x}^2\lambda\rho_0\frac{\mathrm{d}\left(c_0^4\right)}{\mathrm{d}z},\\
a_3 &= -\lambda b_1^2\rho_0 + gk_\mathrm{x}^2\lambda\rho_0\frac{\mathrm{d}\left(c_0^2\right)}{\mathrm{d}z} + gk_\mathrm{x}^2 b_1\left(g\rho_0 + c_0^2\frac{\mathrm{d}\rho_0}{\mathrm{d}z}\right).
\end{aligned} \tag{6.43}$$

The incompressible limit is obtained in the limit $c_0 \to \infty$, by retaining the highest order terms in c_0, those proportional to c_0^4, but neglecting the spatial derivative of c_0^4, in the Eq. 6.42 above, and the hydrodynamic case of Eq. 6.32 is obtained.

The equation can be discretized spatially and written as a generalized eigenvalue problem where the order of the polynomial in λ is 3. The generalized eigenvalue problem of arbitrary order n (not to be confused with the mode number),

$$\left(\lambda^n\hat{\mathbf{A}}_\mathbf{n} + ... + \lambda\hat{\mathbf{A}}_\mathbf{1} + \hat{\mathbf{A}}_\mathbf{0}\right)\mathbf{u} = 0 \tag{6.44}$$

can be solved by linearizing it, i.e. solving the corresponding generalized eigenvalue problem:

$$\begin{pmatrix}
-\hat{\mathbf{A}}_\mathbf{n-1} & -\hat{\mathbf{A}}_\mathbf{n-2} & \dots & -\hat{\mathbf{A}}_\mathbf{1} & -\hat{\mathbf{A}}_\mathbf{0}\\
\hat{\mathbb{I}} & \hat{\mathbf{0}} & \dots & \hat{\mathbf{0}} & \hat{\mathbf{0}}\\
\vdots & & & & \\
\hat{0} & \hat{\mathbf{0}} & \dots & \hat{\mathbb{I}} & \hat{\mathbf{0}}
\end{pmatrix}\mathbf{u}' = \lambda\begin{pmatrix}
\hat{\mathbf{A}}_\mathbf{n} & \hat{\mathbf{0}} & \dots & \hat{\mathbf{0}}\\
\hat{\mathbf{0}} & \hat{\mathbb{I}} & \dots & \hat{\mathbf{0}}\\
\vdots & & \ddots & \\
\hat{\mathbf{0}} & \hat{\mathbf{0}} & \dots & \hat{\mathbb{I}}
\end{pmatrix}\mathbf{u}' \tag{6.45}$$

where:

$$\mathbf{u}' = \begin{pmatrix} \mathbf{u} \\ \lambda\mathbf{u} \\ \vdots \\ \lambda^{n-1}\mathbf{u} \end{pmatrix} \tag{6.46}$$

In our case, $\mathbf{u} = (v[1], ...v[m_z])$, with m_z being the number of the points.

Left panel of Figure 6.16 shows the growth rates obtained semi-analytically in the incompressible (solid lines) assumption compared to the compressible case (dotted lines), for the HD case. We can observe that the compressible growth rate is larger than the incompressible growth rate for all the mode numbers. At the right-hand side panel, we plot the vertical eigenfunction profile in the compressible (dotted lines) and incompressible (solid lines) cases for the mode numbers $n = 1$ (black lines) and $n = 16$ (red lines). We can observe that the compressibility shifts the peaks of the eigenfunction towards the positive z direction, this effect being more pronounced for higher mode numbers. We expect that the compressibility effect is smaller in the situation with the magnetic field, because the magnetic field provides additional pressure, making neutrals less compressible, as long as the neutrals are coupled to the field via ions.

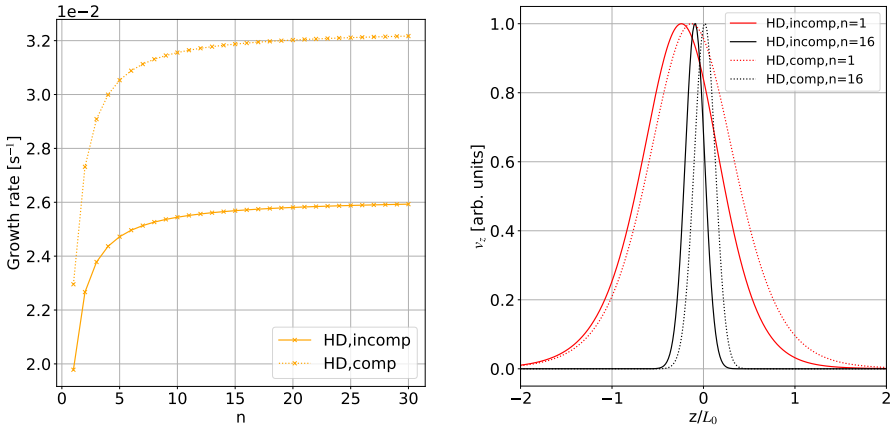

Figure 6.16: Left: Growth rates obtained semi-analytically in the ideal HD approach, in the incompressible (solid lines) case compared to the compressible case (dotted lines). Right: Vertical eigenfunctions profiles obtained semi-analytically for the same cases for mode numbers $n = 1$ (black lines) and $n = 16$ (red lines). For better visualization, the vertical domain has been limited to $-2 \geq z/L_0 \geq 2$.

6.7 Bubbles and spikes

In the neutral fluid the spikes (the structures that fall in the $z < 0$ region) are composed by heavier fluid compared to its surroundings. The bubbles (the structures that rise in the $z > 0$ region) are lighter than the surrounding fluid for the neutrals. The collisional coupling is strong, and the neutrals drag the charges during the development of the instability. However, for the charges, which have a negative gradient of the density in the whole atmosphere, the situation is contrary to the neutrals, the spikes are lighter and the bubbles are heavier. We can observe this reverse in the density contrast between charges and neutrals in the snapshots for all the simulations, e.g. Figure 6.9.

In the linear phase, we can look at the shape of the eigenfunctions shown in Figure 6.13, which is determined by the equilibrium profile. We can observe that the eigenfunctions are symmetric, meaning that the bubbles and spikes grow in the same way in the linear phase, similar to the result of Mikaelian (2014). The peak of the eigenfunctions, which is slightly shifted below $z = 0$, moves the center of the linear instability below $z = 0$. We have defined the center of instability in the following way. First we noticed that the structures (spikes and bubbles) reach different heights with respect to the height of the initial perturbation (that was located at $z = 0$). We therefore measured the average height reached by bubbles, and the average height reached by spikes. The mean value of these two reference heights is defined as the center of RTI. We have measured the structures in the snapshots of density. There is no principal difference in the above definition if, instead of density, other quantity, such as e.g., velocity, is used. The shift of the peak in the negative z direction is more pronounced in the perpendicular field geometry than in the sheared field one. This fact could be observed in Figure 6.9 as the structures were more extended below $z = 0$.

However, in the nonlinear phase, Mikaelian (2014); Carlyle & Hillier (2017) find asymmetry between the growth of bubbles and spikes, compared to the linear phase, the spikes growing faster than the bubbles. Our simulations do not evolve too much in the nonlinear phase so that a proper analysis of the evolution of these structures cannot be performed, and it is subject of future research.

6.8 Decoupling

The decoupling in velocities between charges and neutrals appears when the forces that act on a species become of the same order of magnitude as the coupling term in the momentum equation. In our case, the forces that act differently on the neutrals and charges are the electromagnetic forces that only act on charges and the viscosity which is much larger for the neutral species. Thus, we expect that the decoupling to be affected by the physical viscosity and the change of the magnetic field configuration.

Figure 6.17 shows the decoupling in the horizontal and vertical velocities for the simulations P-V1-MM, P-V0-MM, L1-V1-MM and L1-V0-MM. The quantities plotted are $v_{\rm zn} - v_{\rm zc}$, and $v_{\rm xn} - v_{\rm xc}$, calculated at the same time $t \approx 202$ s for P-V1-MM and P-V0-MM and $t \approx 429$ s for L1-V1-MM and L1-V0-MM for easier comparison. We can observe that the absolute decoupling in velocities, is of same order of magnitude for the two sets of simulations compared. The decoupling is large, of order of few hundreds m/s or even reaching values of km/s. However, as it is highly localized, the average

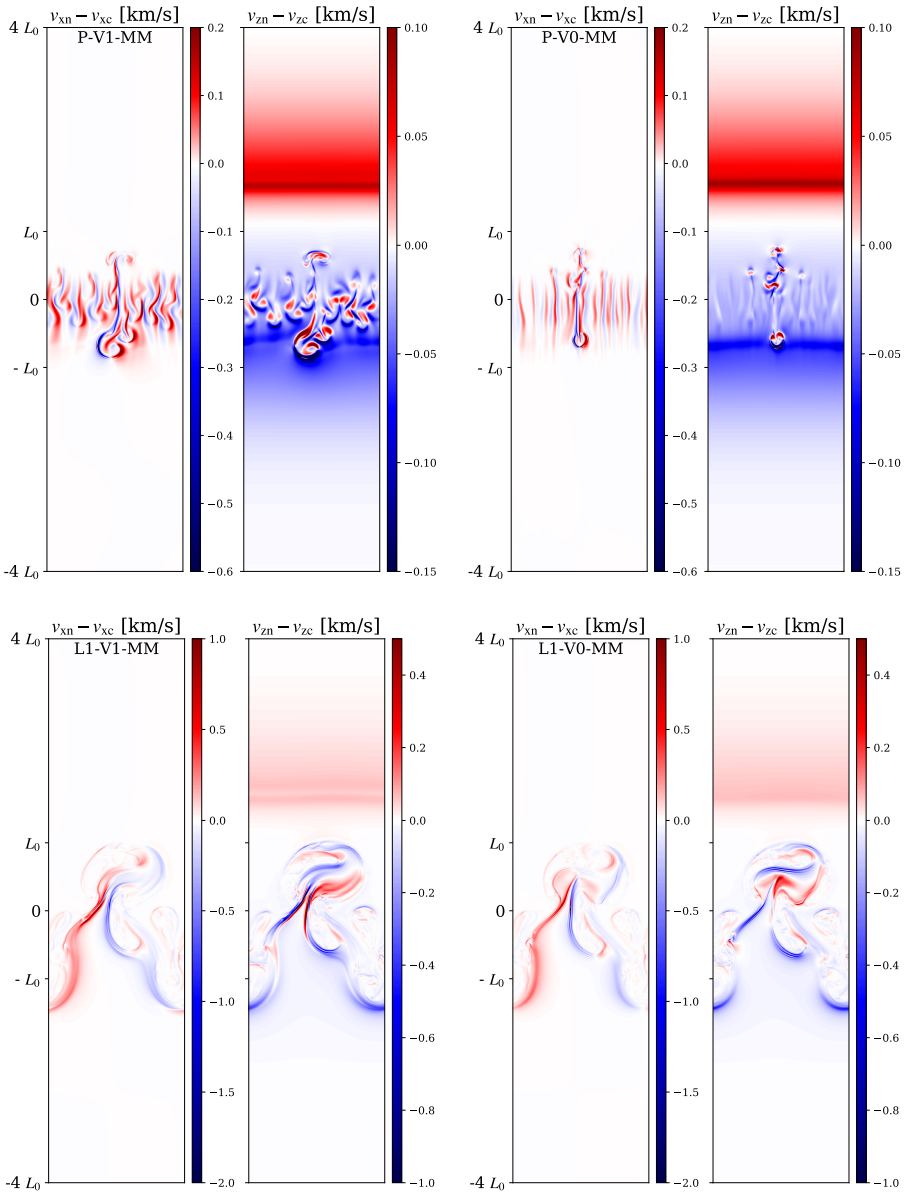

Figure 6.17: Snapshots of the decoupling in horizontal and vertical velocities, grouped for four simulation cases. Top left: P-V1-MM, top right: P-V0-MM, bottom left: L1-V1-MM, bottom right: L1-V0-MM. The snapshots from the first row are taken at time ≈ 202 s, and the snapshots from the bottom row are taken at time ≈ 429 s.

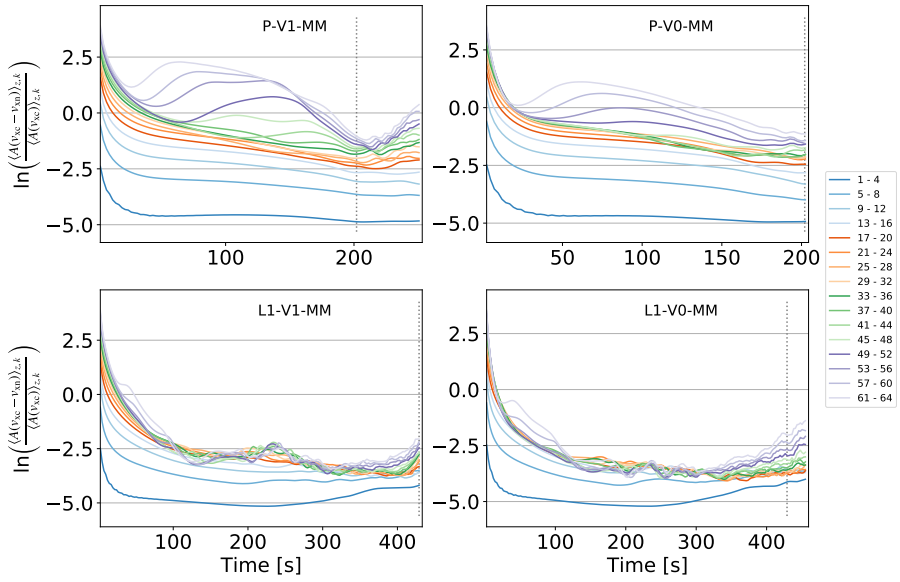

Figure 6.18: Logarithm of the Fourier amplitude of the horizontal decoupling defined by Eq. 6.47. Different curves are for different modes from $n = 1$ to $n = 64$, grouped in sets of 4 modes. Four cases of simulations are shown: Top left: P-V1-MM. Top right: P-V0-MM. Bottom left: L1-V1-MM. Bottom right: L1-V0-MM. The vertical dotted lines indicate the time moments of the snapshots of the decoupling shown in Figure 6.17.

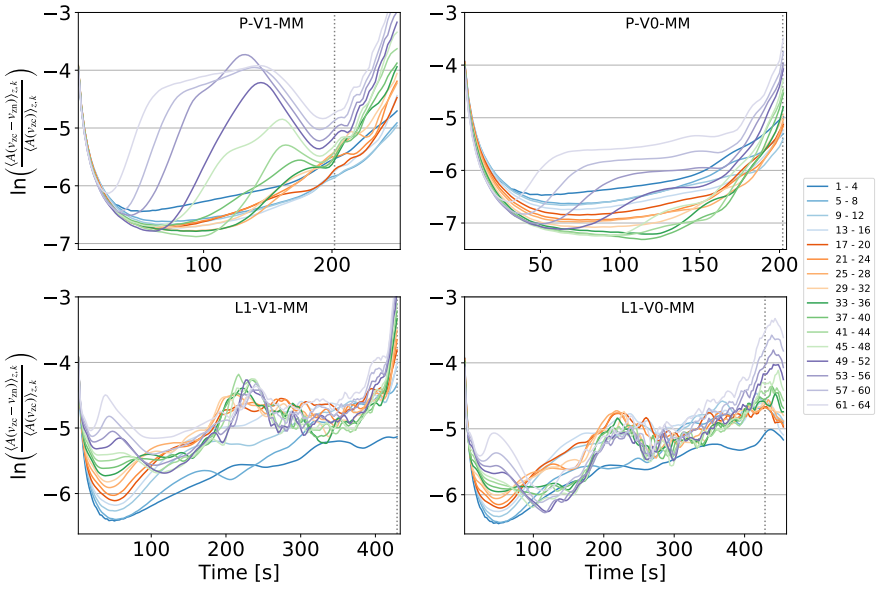

Figure 6.19: Logarithm of the Fourier amplitude of the vertical decoupling defined by Eq. 6.47. Different curves are for different modes from $n = 1$ to $n = 64$, grouped in sets of 4 modes. Four cases of simulations are shown: Top left: P-V1-MM. Top right: P-V0-MM. Bottom left: L1-V1-MM. Bottom right: L1-V0-MM. The vertical dotted lines indicate the time moments of the snapshots shown in Figure 6.17.

value over the domain would be significantly smaller. In order to properly quantify the decoupling, the value of the decoupling in velocity should be compared to the velocity magnitude at each scale.

We plot in Figure 6.19 the horizontal and vertical normalized decoupling,

$$Dec = \ln\left(\frac{\langle A\left(v_{\rm c} - v_{\rm n}\right)\rangle_{z,k}}{\langle A\left(v_{\rm c}\right)\rangle_{z,k}}\right), \tag{6.47}$$

where for the vertical decoupling we use the vertical velocities for charges and neutrals, $v_{\rm zc}$, $v_{\rm zn}$, and for the horizontal decoupling we use the horizontal velocities $v_{\rm xc}$, $v_{\rm xn}$. "A" indicates the Fourier amplitude obtained after applying the FFT in the x direction. The average $\langle\rangle_{z,k}$ means average in the vertical direction between $z = -L_0$ and $z = L_0$, and over 4 consecutive modes. These quantities have been plotted for the four simulations and for the first 64 modes. We can observe that largest decoupling appears at small scales. The differences between the results for the four simulations appears also at these small scales, while the decoupling at large scales seem the same in the four cases. This is true for both vertical and horizontal velocities. The simulation P1-V1-MM has largest normalized decoupling and its positive maximum has a value above 2. In the sheared field case we also observe more decoupling for the simulation L1-V1-MM than for L1-V0-MM. We observe more decoupling for the cases with viscosity during the linear stage, while the small scales are suppressed by the viscosity and do not grow. In the nonlinear stage, the small scales are produced from the direct cascade from larger scales and they start to grow, overcoming the effect of the viscosity. In consequence, the decoupling decreases at the beginning of the nonlinear phase. We observe that, the decoupling is smaller for the simulations L1-V1-MM and L1-V0-MM and that it decreases with time for these simulations compared to P-V1-MM and P-V0-MM for time $t \lessapprox 200$ s. This might be due to the normalization of the difference, because, as we have seen in Figure 6.11 the small scales start the nonlinear phase earlier for the sheared case configuration, and even if the growth rate is smaller than in the perpendicular case, the amplitude will be larger at the same time considered. However, the increase of the amplitudes of the small scales during the nonlinear phase will saturate. This is the reason why we see the increase in the normalized decoupling at later times of the nonlinear stage, for time t$\gtrapprox$220 s for all the simulations, except for P-V0-MM which does not reach this time.

6.9 Power spectra

Figure 6.20 shows the energy power spectra for the simulations: L1-V1-MM and L1-V0-MM at different moments of time. We compute the FFT power of the square root of the energy, and then average the power in the z direction between $z = -L_0$ and $z = L_0$. We obtain the quantity $\langle A(\sqrt{E})^2\rangle_z$, where E is the magnetic energy or the kinetic energy of the neutrals or charges ($E = E_{\rm mag} = B^2/(2\mu_0)$, $E = E_{\rm cc} = \rho_c v_c^2/2$, $E = E_{\rm cn} = \rho_n v_n^2/2$). The Fourier transform is done in the horizontal direction x. The axis of the plot are in logarithmic scale. The mode $k = 0$, (corresponding to the average in the x direction) does not appear in the plot. We omit the 1/2 factor, because of simplicity, and because the plot is in logarithmic scale, the multiplication becomes a translation and it does not affect the shape

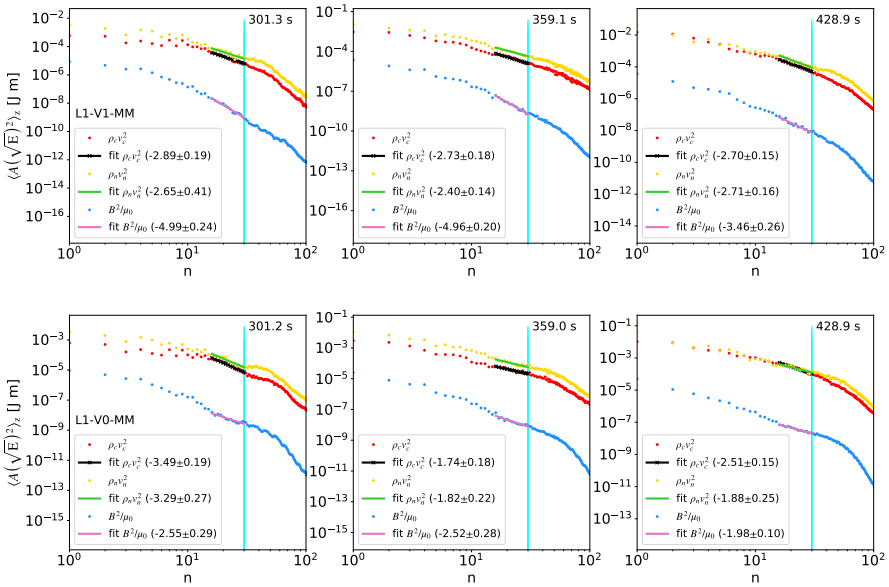

Figure 6.20: Power spectra for different times for the simulations L1-V1-MM (top row), and L1-V0-MM (bottom row) at different time moments. The spectra are shown as a function of the mode number in logarithmic scale. The spectra are computed as FFT in the x direction power of the square root of the kinetic energy of charges, $E_{\rm cc}$ (red points), kinetic energy of neutrals, $E_{\rm cn}$ (yellow points), and magnetic energy, $E_{\rm mag}$ (blue points). A linear fit to each quantity is shown with a solid line: black solid line marked with symbols "x" for $E_{\rm cc}$, green solid line for $E_{\rm cn}$, and violet solid line for $E_{\rm mag}$. The value of the slope and the uncertainty of the fit are indicated at the legend. A solid cyan vertical line located at $n = 30$ delimits the inertial range from the dissipation range.

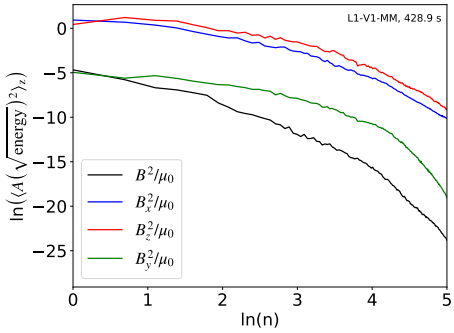

Figure 6.21: Power spectra of magnetic energy for each of the components of the magnetic field calculated at the final time of the simulation L1-V1-MM.

of the curves. We have from Parseval theorem that,

$$\sum_k A_k(\sqrt{E})^2 = \sum_x E\,. \tag{6.48}$$

Like this, because operators $\sum_k$ and $\langle\rangle_z$ commute, $\sum_k\langle A_k(\sqrt{E})^2\rangle_z$ is the total corresponding energy in the x direction, averaged in height between $-L_0$ and L_0.

Turbulence appears in fluids with high Reynolds number, Re=uL/ν^v, where u is the flow velocity, L is typical length scale, and ν^v is the viscosity coefficient, in units of m^2/s, similar to $\nu^v_{\{c,n\}}$ defined for charges and neutrals in Eq. 6.25. The turbulence is created by the excess of the kinetic energy, when the mechanism of dissipation through viscosity is insufficient. It makes the motion unpredictable, but some results based on statistical methods can be obtained.

In our simulations, part of the kinetic energy goes into the work done against the Lorentz force, which twists the field lines and increases the magnetic energy. As this is a 2D simulation, where the field is perpendicular or almost perpendicular to the direction of the perturbation, the increase in the magnetic energy is not very large, much smaller compared to a 3D situation.

In turbulence theory, the inertial range is defined as the range of modes where kinetic energy is transferred from large to small scales without loss. The dissipation range is the range where the kinetic energy is dissipated through viscosity. In our case, the simulations barely enter the nonlinear phase and we can see the onset of the turbulence, but the simulations are far from a stationary regime.

We have done a linear fit to the curves, and we indicate in the legend the slope and the uncertainty of the fit. We have seen in Figure 6.11 that, the scales corresponding to mode numbers up to $n = 28$ for L1-V1-MM and up to $n = 40$ for L1-V0-MM, i.e. modes with $n < n_{cd}$, have a long linear phase. This is the range of modes which contains energy when the simulations enter the nonlinear phase. Based on the these considerations, we considered the delimitation between the inertial and dissipation range to be located at $n = n_{cd} \approx 30$, for all the simulations considered, marked at the panels by a

vertical solid cyan line. The fit is done in the final part of the "inertial range", for n between 15 and 30.

We expect lower dissipation effects at earlier times in our simulations, and larger effects when the structures are extended for the following reasons: (1) the viscosity is larger towards the edges of the domain (2) more smaller scales are created at the beginning of the nonlinear phase by the direct cascade. We can observe indeed in Figure 6.20 smaller values (more negative values) for the kinetic energies.

Because we use the ideal Ohm's law, the magnetic field topology and the total magnetic field should be constant in time. There is still numerical diffusivity due to proper discretization that can slightly influence the behavior of the magnetic field. The magnetic energy should grow because of the twisting of the field lines. It is more difficult to twist the field lines when there are small scales developed. This is the reason for which the magnetic energy is always smaller for L1-V1-MM than for L1-V0-MM.

For L1-V0-MM, in the absence of physical viscosities and neutral thermal conductivity, the small scales develop, compared to L1-V1-MM. For the same reason, all the slopes are larger for L1-V1-MM than for L1-V0-MM. The curves of $E_{\rm cn}$ are more affected than the curves of $E_{\rm cc}$, because the viscosity of neutrals is larger than that of charges. We can observe that the curves of $E_{\rm cn}$ and $E_{\rm cc}$ start to diverge at $n \gtrapprox 30$, which is the beginning of what we have defined as the "dissipation range". This can be is seen in all the panels, especially for L1-V1-MM, at the latest time. The result is similar to the result obtained by Brandenburg (2019).

The slope of the magnetic energy increases (the absolute value of the slope decreases) in time, together with the twisting of the field lines. Figure 6.21 shows the spectra of the magnetic energy for each of the components for the final time of the simulation L1-V1-MM. The B_z magnetic energy dominates. Similar result was obtained by Jun et al. (1995b). This is due to the bending of the field lines in the vertical direction as a consequence of the development of the instability. This bending creates the vertical component of the magnetic field, which was missing in the initial configuration. The most interesting feature observed in Figure 6.21 is that the magnetic energy for each of the components dominates over the total magnetic energy at small scales. This can indicate the formation of a flux rope as the different components of the magnetic field are out of phase.

The simulations were at the beginning of the nonlinear phase and the spectra changed with time. In our simulations we have considered a relatively small physical domain and high resolution, therefore, there are few scales to analyze in our system, and the fit of the inertial range was done over a small number of points. As the above analysis serve as an estimation, in the future some other methods could be considered, which give better results when the inertial range is not well defined in the Fourier spectra (Xie & Bühler 2019).

Conclusions

In this chapter we have studied the Rayleigh-Taylor instability at the interface between a solar prominence and the corona. We have run 2D simulations with different magnetic field configurations: perpendicular magnetic field and sheared magnetic field with respect to the plane defined by the di-

rection of the perturbation and the gravity. We also studied the effect of the compressibility, viscosity on the dependency of the growth rate on the wave number, decoupling between neutrals and charges, and energy power spectra. The findings are summarized below.

- The viscosity, thermal conductivity, and ion-neutral elastic collisions suppress the small scales with wavelengths below the typical scales defined by the above processes. Thanks to that, the small scales do not have an initial linear growth phase. The largest mode number of the modes which grow in the linear regime is $n = 36$ for P-V1-MM, $n = 44$ for P-V0-MM, $n = 28$ for L1-V1-MM, and $n = 40$ for L1-V0-MM, as observed from Figure 6.11.
- The component of the magnetic field parallel to the direction of the perturbation suppresses the growth of the small scales. Both in simulations, and in the analytical calculations using simplified MHD treatment, the growth rate decreases with the decrease of the shear length of the magnetic field (Figures 6.14, 6.15). The smaller scales start to grow earlier for the sheared magnetic field configuration than for the perpendicular configuration.
- We have run simulations for two configurations of the magnetic field, and using two different perturbation for each configuration. For the two configurations, the growth rate obtained from simulations is independent from the properties of the initial perturbation (multi-mode or white noise), which gives us an additional confidence in our results (left panel of Figure 6.14).
- The vertical profile of the atmosphere makes that the peak of the vertical velocity's eigenfunction is shifted toward the negative z direction. This fact causes the development of structures more at the lower part of the simulated prominence thread. The symmetry of the eigenfunction makes the bubbles and the spikes growing at the same rate during the linear phase.
- The compressibility increases the growth rate in the hydrodynamic case. The compressibility also shifts the center of the RTI towards the positive z direction, compared to the incompressible case.
- We observe decoupling in velocities of the order of 10^2 to 10^3 m/s in all the cases considered. The decoupling affects more the smaller scales. The action of the magnetic field and the physical viscosities and neutral thermal conductivity are the main reasons of the decoupling. The scales that decouple during the linear stage, are those which do not grow during this stage, as they are suppressed by viscosity and conductivity, $n \gtrapprox 36$ for P-V1-MM, $n \gtrapprox 44$ for P-V0-MM, $n \gtrapprox 28$ for L1-V1-MM, and $n \gtrapprox 40$ for L1-V0-MM. The absolute decoupling is larger for larger velocities, and, when normalized, the difficulty in comparing the normalized decoupling arises from the fact that the small scales start the nonlinear phase earlier, thus having larger velocities at the same moment of time, compared to the perpendicular magnetic field case.
- The slope of the magnetic energy increases (the absolute value of the slope decreases) in time because of the production of magnetic energy at small scales. The magnetic energy contained

in individual components of the magnetic field is larger than the total magnetic energy, for the small scales. Such behavior can indicate the twisting of the magnetic field and formation of a flux rope. The magnetic energy becomes lower in the case physical viscosity and conductivity are acting.

The role of the neutrals is not fully understood in the development of the RTI. We tried to simulate a solar prominence thread, where, even if the collision frequency between neutral and charged particles is high, we could observe the ion-neutral collision effects. With a component of the magnetic field parallel to the direction of the perturbation, the presence of the neutrals has a destabilizing effect for the scales close to the cutoff imposed by the magnetic field. On the other hand, regardless the equilibrium atmosphere, the collisions between ion and neutrals decrease the growth rate of then instability similarly to the viscosity. This effect should be compared to the single-fluid model with ambipolar diffusion and is subject of future research.

7

Rayleigh-Taylor instability. Application to observations

In this chapter we study how the difference in behavior of ions and neutrals during the development of the Rayleigh-Taylor instability (RTI) can possibly be detected in observations. For this reason, we consider variations of the parameters that one could measure. We use the same setup as in Chapter 6, and study the development of RTI in the models where we change the contrast of density and the background magnetic field strength. We run simulations where we turn off ionization/recombination or increase artificially the elastic collisional coupling. We conclude that the ionization-recombination inbalance results in creation of a layer of increased density of charges. This layer follows the evolution of the eddies. Elastic collisions influence the growth rate similarly to the viscosity: an increase of collisions results in a larger growth rate at small scales. Larger density contrast increases the growth rate, contrary to the effect of increasing the strength of the magnetic field.

7.1 Introduction

The prominences are clouds of chromospheric material, present in the solar corona, being sustained against gravity by the existing magnetic structures. They are colder and denser than the surrounding medium. Prominences seen on-disc are called filaments. The physical properties of the prominences and their observations have been already introduced in Chapter 1, section 1.2.2. A comprehensive review on the magnetic field configuration of the prominences is given in Mackay et al. (2010). Filaments are usually located above Polarity Inversion Lines (PILs), i.e. lines in the photosphere where the vertical component of the magnetic field changes sign. Filaments are located in filament channels, i.e. regions in the chromosphere surrounding PILs where the chromospheric fibrils are aligned with the PIL.

The topology of the magnetic field can be inferred by the alignment between the fibrils and the PIL,

but most direct determination comes from the inversion of spectro-polarimetric data. The data shows the magnetic field has a strong axial component along the PIL, being sheared in the form of an arcade or a flux rope.

Using the magnetic field strength, one can distinguish between Active Region (AR) prominences and quiescent ones. The magnetic field measured in quiescent prominences has a strength of 3-15 G. The field is mostly horizontal and makes an acute angle of about 40° with respect to the long axis of the prominence (Bommier & Leroy 1998). Later observations by Collados et al. (2003) show that the magnetic vector is rotated with respect to the filament axis by an angle in the range 15 to 25 degrees. In quiescent prominences with lower field strength (< 10 G), the magnetic field lines are distorted by the weight of the prominence plasma and present dips. The magnetic tension associated with these dips contributes to the equilibrium force balance as e.g. in the Kippenhahn-Schlüter models (Kippenhahn & Schlüter 1957). Paletou et al. (2001) find values of the magnetic field between 30 and 45 G in an active prominence by inverting Stokes V polarization parameters. Aulanier & Démoulin (2003) estimates limits for the magnetic field magnitude used in 3D prominence models based on magnetic dips and calculated with a linear force free extrapolation method of: 2.5-3 G (quiescent), 13-15 G (intermediate), 35-45 G (active) and for the magnetic field gradient of: 0.01 G/Mm (quiescent), 0.05 G/Mm (intermediate), and 0.15 G/Mm (active), at the prominence height and above.

Figure 7.1, taken from Berger et al. (2017) shows a prominence bubble which rises, collapses and reforms. These bubbles have been observed to rise through the prominence with approximately constant speeds (of ≈ 1.3 km/s in the observations of Berger et al. (2017)). It has been suggested by Low (2007) that the origin of the prominence bubbles is the magnetic flux emergence, which occurs in a region near the prominence, consistent with observations of Berger et al. (2017). Small-scale upflows, also called plumes, have been seen at the top border of the bubbles. The plumes are highly dynamic columns of plasma, that rise from below the prominence and propagate upwards with speeds of ≈ 15 km/s. It is believed that they appear due to the Rayleigh-Taylor instability (RTI) (Berger et al. 2010; Orozco Suárez et al. 2014; Berger et al. 2017). The shear flow on the bubble boundary gives rise to subsequent plumes as a result of the Kelvin-Helmholtz instabilities (KHI) (Berger et al. 2017). A layer of enhanced emission situated at the edges of the bubble can be seen.

As we have seen in the previous chapter, the growth rate of the RTI depends on the density profile and the magnetic field. By comparing the measured growth rate of the instability to analytic expressions, the magnetic field can be inferred. Berger et al. (2017) found a magnetic flux density across the bubble boundary of ≈ 10 G at an angle of $\approx 70°$ to the prominence plane. The review by Hillier (2018) shows more examples of the determination of the field strengths from the growth rates in several contexts and the uncertainties associated with these methods.

The RTI occurs when a heavier fluid is accelerated against a lighter fluid. In the observations of the RTI in the solar atmosphere, the acceleration is due to the gravity. Generally, in astrophysics the acceleration may have other origins, such as the pressure of the confined relativistic plasma which accelerates a "skin" of ejecta at the boundary of the Crab Nebula (Hester et al. 1996). The "skin" is composed of high ionization material and, similarly to inner filaments present inside the nebula, it is brighter, most possibly because of higher (electron) density (Clark et al. 1983; Hester et al. 1996).

The increase of the contrast density is equivalent to increasing the nondimensional Atwood number (A=$(\rho_2 - \rho_1)/(\rho_2 + \rho_1)$, where $\rho_2 > \rho_1$ is the density of the heavier fluid). In the hydrodynamic case it has been shown that the growth rate is larger for larger density contrast (Chandrasekhar 1961). The is also true when taking into account the effects of the viscosity (Chandrasekhar 1961), or when the density profile is not discontinuous, but exponentially stratified with height (Livescu 2004). The magnetic field modifies the growth rate at small scales, depending on the configuration, but the growth rate is still larger for larger A (Dolai et al. 2016). The unstabilizing effect of the compressibility is larger for smaller A (Livescu 2004; Ribeyre et al. 2005).

Increasing the density contrast will result in higher growth rate, thinner fingers and less roll-up at the tip of the fingers, which is due to secondary KHI, developing preferentially at low A (Youngs 1984; Gardner et al. 1988; Jun et al. 1995b). However, the RTI can occur for a wide range of A from A $\approx$ 0 to A $\approx$ 1. The A $\approx$ 0 limit produces the classic symmetric upflow and downflow plumes. The limit A $\rightarrow$ 1, or $\rho_2 \gg \rho_1$ is also called the "bubble limit", when rising bubbles can be observed, with little or no accompanying spikes (Sharp 1984; Berger et al. 2010).

Measurements of Berger et al. (2010) revealed that most of the plumes are not accompanied by symmetric downflows, see Figure 7.2. The Atwood number in plume observations of Berger et al. (2010) has been estimated as A $\approx$ 0.7, being indeed to the "bubble limit" mentioned above. The minor downflows compared to the plume upflows may also explain the observed gradual collapse of the cavities over time.

In this chapter, we study the effect of the collisions between neutrals and charges, the effect of the ionization/recombination processes in section 7.3, and that of the elastic collisions in section 7.4. We modify the background atmosphere, we increase the Atwood number, by increasing the density contrast, and we further increase the magnetic field strength. We the study in section 7.5 the effects of these modifications on the growth rate, the decoupling and energy power spectra.

7.2 Setup

We use the same 2D setup as described in the previous chapter. Table 7.1 shows a list of all the 2D simulations performed. In most of the simulations, we use a white noise perturbation in the density of neutrals (keyword "WN"). Otherwise, the multimode perturbation presented in the previous chapter is used (keyword "MM"). In some simulations, where we have calculated the linear growth rate, the amplitude was decreased by a factor of 100, having $\delta = 10^{-4}$ in Eq. 6.21. These simulations are indicated in Table 7.1 by the suffix "-S" in their names. There are four input parameters that are changed throughout of the simulations:

1. Inelastic collisions. We turn off ionization/recombination. The simulation appears with the keyword "-I0" in the table.

2. Elastic collisions. We increase the elastic collision frequency by multiplying the value of the collisional parameter α, calculated as in Eq. 2.90 by a factor of 10^4 ("-α" keyword).

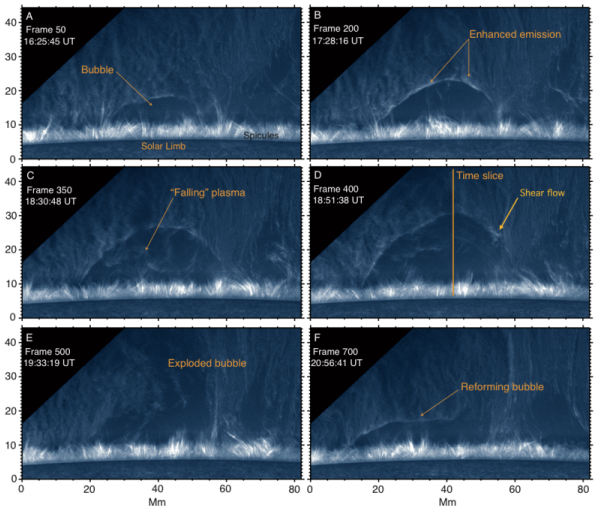

Figure 7.1: Quiescent solar prominence observed on the 16th of August, 2007 in the SOT Ca II H-line 3968 Å channel at 90W, 47N heliographic coordinates. Fig. 1 from Berger et al. (2017).

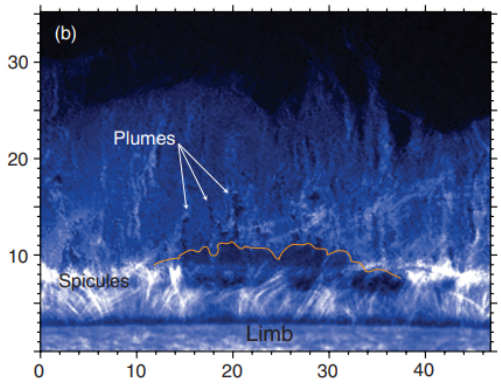

Figure 7.2: Prominence on the west limb seen in Ca II H-line on the 30th of November, 2006. Tick mark labels at the image borders are Mm. Part of Fig. 10 from Berger et al. (2010).

3. Density contrast. The value of the peak density of neutrals is changed in some of the simulations, by increasing the value of n_{n00} in Eq. 6.16) by a factor of 10. These simulations appear marked with the "NN" keyword in their name.

4. Magnetic field magnitude. The value of B_{00} in Eq. 6.18 which describes the magnetic field configuration is increased by a value of 3 (the "B" keyword).

Two simulations from the previous Chapter 6, P-V1-MM and P-V1-WN-S, also appear referenced in this chapter with the same notation conventions (the 5th and 6th entries of Table 7.1). In all the simulations we included the physical viscosities and neutral thermal conductivity. We used the same boundary conditions and the filtering mechanism, as described in the previous Chapter 6.

Because of the smooth profile, the value of the gradient scale length calculated at $z = 0$ does not change considerably when the peak in the density of neutrals is increased by a factor of 10. The gradient scale height decreases from $L_d \approx 409$ km to $L_d \approx 337$ km for larger $n_{\mathrm{n}00}$, and the corresponding Brunt-Väisälä frequency slightly increases from the value of $N \approx 2.5 \times 10^{-2}$ s^{-1} to the value of $N \approx 2.8 \times 10^{-2}$ s^{-1} at $z = 0$.

Figure 7.3 shows the cutoff wavelengths, calculated from Eq. 6.4 for these three cases with sheared magnetic field with shear length $L_s = L_0$: (1) original density contrast $n_{\mathrm{n}00} = 10^{16}$ m^{-3} and magnetic field magnitude $B_{00} = 10^{-3}$ T (solid line, labeled "$L_s = L_0$"), (2) increased density contrast $n_{\mathrm{n}00} = 10^{17}$ m^{-3} and original field magnitude $B_{00} = 10^{-3}$ T (dashed line labeled "$L_s = L_0$,NN"), and (3) both increased density contrast $n_{\mathrm{n}00} = 10^{17}$ m^{-3} and field magnitude $B_{00} = 3 \times 10^{-3}$ T field (dotted line labeled "$L_s = L_0$,NN,B") with black lines. The cutoff wavelength in the latter case ("$L_s = L_0$,NN,B") is similar to the cutoff wavelength in the first case ("$L_s = L_0$"), as we indeed observe in the figure. The density gradient scale heights are plotted with red lines for the original value of $n_{\mathrm{n}00} = 10^{16}$ m^{-3} (dotted line labeled "L_d"), and for the increased density contrast case when $n_{\mathrm{n}00} = 10^{17}$ m^{-3} (dashed line labeled "L_d,NN"). The maximum (dashed line) and the minimum (dotted line) wavelengths that can exist in our horizontal domain, are shown with blue lines.

Table 7.1: List of the simulations

Name	Parameters
P-MM-I0	Perpendicular magnetic field described by Eq. 6.22. Ionization/recombination terms turned off. Original value of the elastic collisions. Original values of $n_{\mathrm{n}00} = 10^{16}$ m^{-3} in Eq. 6.16, $B_{00} = 10^{-3}$ T in Eq. 6.18. Multimode perturbation with $\delta = 10^{-2}$ in Eq. 6.21.
P-MM-I0-S	Perpendicular magnetic field described by Eq. 6.22. Ionization/recombination terms turned off. Original value of the elastic collisions. Original values of $n_{\mathrm{n}00} = 10^{16}$ m^{-3} in Eq. 6.16, $B_{00} = 10^{-3}$ T in Eqs. 6.18. Multimode perturbation with $\delta = 10^{-4}$ in Eq. 6.21.
P-WN-NN	Perpendicular magnetic field described by Eq. 6.22 Original value of the elastic collisions. Ionization/recombination terms turned on. Increased value of $n_{\mathrm{n}00} = 10^{17}$ m^{-3} in Eq. 6.16, and original value of $B_{00} = 10^{-3}$ T in Eqs. 6.18. White noise perturbation with $\delta = 10^{-2}$ in Eq. 6.21.

P-WN-NN-S	Perpendicular magnetic field described by Eq. 6.22 Original value of the elastic collisions. Ionization/recombination terms turned on. Increased value of $n_{\mathrm{n}00} = 10^{17}$ m^{-3} in Eq. 6.16, and original value of $B_{00} = 10^{-3}$ T in Eqs. 6.18. White noise perturbation with $\delta = 10^{-4}$ in Eq. 6.21.
P-V1-MM	Perpendicular magnetic field described by Eq. 6.22. Original values of $n_{\mathrm{n}00} = 10^{16}$ m^{-3} in Eq. 6.16, $B_{00} = 10^{-3}$ T in Eq. 6.18. Multimode perturbation with $\delta = 10^{-2}$ in Eq. 6.21. Also described in Chapter 6.
P-V1-WN-S	Perpendicular magnetic field described by Eq. 6.22. Original values of $n_{\mathrm{n}00} = 10^{16}$ m^{-3} in Eq. 6.16, $B_{00} = 10^{-3}$ T in Eq. 6.18. White noise perturbation with $\delta = 10^{-4}$ in Eq. 6.21. Also described in Chapter 6.
L1-WN	Sheared magnetic field described by Eq. 6.23 with $L_s = L_0$. Original value of the elastic collisions. Ionization/recombination terms turned on. Original values of $n_{\mathrm{n}00} = 10^{16}$ m^{-3} in Eq. 6.16, $B_{00} = 10^{-3}$ T in Eq. 6.18. White noise perturbation with $\delta = 10^{-2}$ in Eq. 6.21.
L1-WN-NN	Sheared magnetic field described by Eq. 6.23 with $L_s = L_0$. Original value of the elastic collisions. Ionization/recombination terms turned on. Increased value of $n_{\mathrm{n}00} = 10^{17}$ m^{-3}, and original value of $B_{00} = 10^{-3}$ T in Eqs. 6.18. White noise perturbation with $\delta = 10^{-2}$ in Eq. 6.21.
L1-WN-S	Sheared magnetic field described by Eq. 6.23 with $L_s = L_0$. Original value of the elastic collisions. Ionization/recombination terms turned on. Original values of $n_{\mathrm{n}00} = 10^{16}$ m^{-3} in Eq. 6.16, $B_{00} = 10^{-3}$ T in Eqs. 6.18. White noise perturbation with $\delta = 10^{-4}$ in Eq. 6.21.
L1-WN-NN-S	Sheared magnetic field described by Eq. 6.23 with $L_s = L_0$. Original value of the elastic collisions. Ionization/recombination terms turned on. Increased value of $n_{\mathrm{n}00} = 10^{17}$ m^{-3} in Eq. 6.16, and original value of $B_{00} = 10^{-3}$ T in Eqs. 6.18. White noise perturbation with $\delta = 10^{-4}$ in Eq. 6.21.
L1-WN-NN-B	Sheared magnetic field described by Eq. 6.23 with $L_s = L_0$. Original value of the elastic collisions. Ionization/recombination terms turned on. Increased value of $n_{\mathrm{n}00} = 10^{17}$ m^{-3} in Eq. 6.16, and of $B_{00} = 3 \times 10^{-3}$ T in Eqs. 6.18. White noise perturbation with $\delta = 10^{-2}$ in Eq. 6.21.
L1-WN-NN-B-S	Sheared magnetic field described by Eq. 6.23 with $L_s = L_0$. Original value of the elastic collisions. Ionization/recombination terms turned on. Increased value of $n_{\mathrm{n}00} = 10^{17}$ m^{-3} in Eq. 6.16, and of $B_{00} = 3 \times 10^{-3}$ T in Eqs. 6.18. White noise perturbation with $\delta = 10^{-4}$ in Eq. 6.21.
L2-MM	Sheared magnetic field described by Eq. 6.23 with $L_s = L_0/2$. Original value of elastic collisions. Ionization/recombination terms turned on. Original values of $n_{\mathrm{n}00} = 10^{16}$ m^{-3} in Eq. 6.16, $B_{00} = 10^{-3}$ T in Eqs. 6.18. Multimode perturbation with $\delta = 10^{-2}$ in Eq. 6.21.

L2-MM-S	Sheared magnetic field described by Eq. 6.23 with $L_s = L_0/2$. Original value of elastic collisions. Ionization/recombination terms turned on. Original values of $n_{\mathrm{n}00} = 10^{16}$ m^{-3} in Eq. 6.16, $B_{00} = 10^{-3}$ T in Eqs. 6.18. Multimode perturbation with $\delta = 10^{-4}$ in Eq. 6.21.
L2-MM-α	Sheared magnetic field described by Eq. 6.23 with $L_s = L_0/2$. Elastic collisions artificially increased by a factor of 10^4. Ionization/recombination terms turned on. Original values of $n_{\mathrm{n}00} = 10^{16}$ m^{-3} in Eq. 6.16, $B_{00} = 10^{-3}$ T in Eq. 6.18. Multimode perturbation with $\delta = 10^{-2}$ in Eq. 6.21.
L2-MM-α-S	Sheared magnetic field described by Eq. 6.23 with $L_s = L_0/2$. Elastic collisions artificially increased by a factor of 10^4. Ionization/recombination terms turned on. Original values of $n_{\mathrm{n}00} = 10^{16}$ m^{-3} in Eq. 6.16, $B_{00} = 10^{-3}$ T in Eqs. 6.18. Multimode perturbation with $\delta = 10^{-4}$ in Eq. 6.21.

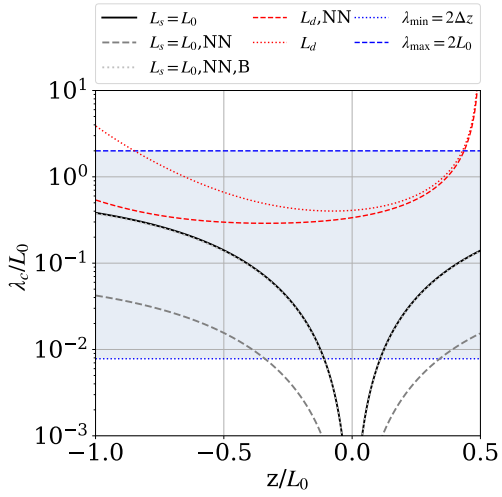

Figure 7.3: Cutoff wavelengths (black lines) and total density gradient scale lengths (red lines) as a function of height. Black lines correspond to cutoff wavelengths due to the in-plane component of the magnetic field, calculated for the shear length $L_s = L_0$ for: original values of $n_{\mathrm{n}00} = 10^{16}$ m^{-3} and $B_{00} = 10^{-3}$ T (solid line); increased value of $n_{\mathrm{n}00} = 10^{17}$ m^{-3} and original value of $B_{00} = 10^{-3}$ T (dashed line); increased value of $n_{\mathrm{n}00} = 10^{17}$ m^{-3}, and of $B_{00} = 3 \times 10^{-3}$ T (dotted line) in Eqs. 6.16 and 6.18, which describe the equilibrium neutral density and magnetic field, respectively. We observe that the black dotted line overlaps the black solid line. The red lines correspond to the density gradient scale length for the original value of $n_{\mathrm{n}00} = 10^{16}$ m^{-3} (dotted line) and to the increased value of $n_{\mathrm{n}00} = 10^{17}$ m^{-3} (dashed line). The blue lines correspond to the minimum (dotted line) and to the maximum (dashed line) wavelengths that can exist in the domain.

7.3 The effect of the inelastic collisions

We want to study the effect of inelastic collisions on the development of the instability. For this purpose, we turn off and on ionization/recombination in the simulation with perpendicular magnetic field. Figure 7.4 compares the simulations P-V1-MM and P-MM-I0. We show the charges density and the difference between temperature of neutrals and charges, $T_{\rm n} - T_{\rm c}$. We can observe an increased contrast in the density of charges. The sharp edge of the structures developed in the charged fluid is due to the ionization of the neutrals in the hot surrounding corona. This could be a reason for the enhanced emission observed at the prominence corona transition region (PCTR), at the edges of the bubble, even if the bubble is not formed as a result of the RTI, shown in Figure 7.1. The excessive brightness of the layer of high-ionization material seen at the boundary of the Crab Nebula (Clark et al. 1983; Hester et al. 1996) can also be explained by a higher (electron) density.

The background atmosphere is not completely in ionization/recombination equilibrium and evolves slowly. This peculiarity has been already mentioned in the previous chapter in section 6.4 in order to explain the layers of increased density which appeared in Figure 6.9. We show in Figure 7.5 the source term in the continuity equation of the neutral species calculated with equilibrium variables,

$$S_{\rm n} = \rho_{\rm c0}\Gamma^{\rm rec} - \rho_{\rm n0}\Gamma^{\rm ion}\,, \tag{7.1}$$

as a function of height. We can observe that this quantity is not zero everywhere, it has two minimum peaks located at $z = -1.27$ Mm and $z = 2.25$ Mm, which correspond to the locations of the increase in the charges density at these heights, that can be observed in the charges density snapshots for all the simulations with ionization/recombination. In particular, it can be seen for the simulation P-V1-MM at the left hand-side panel of Figure 7.4.

The neutrals transfer internal energy to the charges as they are ionized, as deduced from the last terms in the expressions for $M'_{\rm n}$ and $M'_{\rm c}$ given in Eqs. 3.12, in Chapter 3. The temperature of the neutrals drops, and as a consequence, the decoupling between the temperature of neutrals and the temperature of charges has a more negative value for the simulation P-V1-MM at the PCTR and at the heights where the ionization due to the evolution of the equilibrium atmosphere can be observed.

Figure 7.6 show the growth rates obtained from the simulations P-V1-MM-S and P-MM-I0-S. We can see that the curves match almost perfectly, and we can conclude that inelastic processes do not affect the linear growth rate in our case.

In a study of RTI in galactic winds, Ricotti (2014) found that the absorption of ionizing radiation inside the H II region due to hydrogen recombinations suppresses the growth of instabilities. In our case, the ionization/recombination effects appear mostly at the boundary between the prominence and corona, contrary to the above study, where the ionization was an important process in the whole region, and, although the multifluid effects may influence the stability of the interface, the growth rate of the instability is not affected.

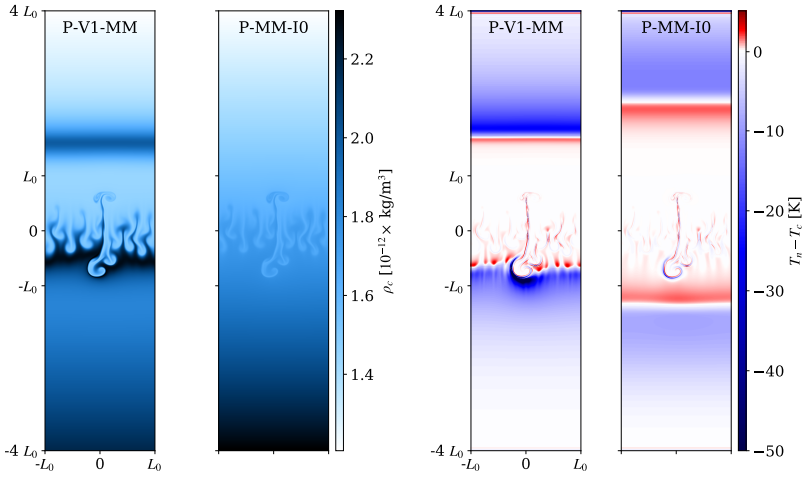

Figure 7.4: Comparison between the density of charges (left panel) and the decoupling in temperature (right panel) for two snapshots taken at the same time for the simulations P-V1-MM and P-MM-I0.

7.4 Elastic collisions

In this section we wish to investigate how the elastic collisional coupling between charges and neutrals affects the growth rate of the RTI and the increase in the temperature. For that we compare the simulations L2-MM and L2-MM-α, run in the same conditions, with the difference that in the latter, the collisional frequency between charges and neutrals was increased artificially by a factor of 10^4. Left panel of Figure 7.7 compares the snapshots of the densities for the simulations L2-MM and L2-MM-α at the same time (≈ 453 s). Both considered cases fall in the strong coupling regime. However, we can observe more smaller scales developed when the collision frequency is increased artificially by a factor of 10^4. This is why, visually, the snapshot for the simulation with the collisions increased artificially has better contrast, similarly to the simulation without physical viscosities and neutral thermal conductivity from the previous chapter. The explanation is that the collisions inside the same species, or between different species, destroy the scales smaller than the collisional mean free path. The modes affected by the ion-neutral decoupling calculated for the background atmosphere have been shown in previous chapter in Figure 6.12. The neutral-ion mean free path is below the grid cell size.

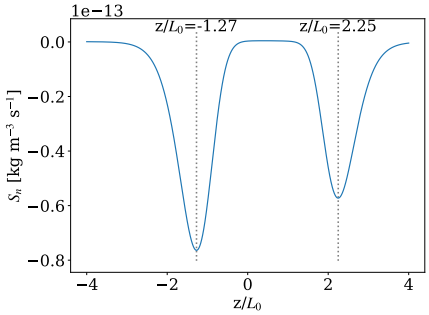

Figure 7.5: The source term which enters the equation of continuity of the neutrals calculated in the equilibrium atmosphere from Eq. 7.1 as a function of height.

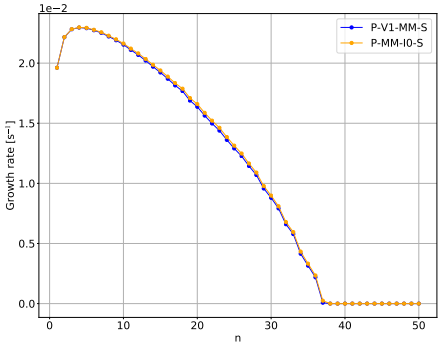

Figure 7.6: Growth rate calculated for the simulations P-V1-MM-S (blue line) and P-MM-I0-S (orange line). The two lines overlap almost perfectly. The time interval where the linear phase has been considered for the fit was [100, 200] s. The error of the fit, as explained for Figure 6.14, was below 10^{-3} for positive growth rates.

Díaz et al. (2012) studied analytically the instability in a two-fluid approach where they consider a 3D setup with two uniform regions separated by an interface, and a uniform magnetic field everywhere. They find a much smaller growth rate in the two-fluid approach compared to the single-fluid approach, the reason of the decrease being the ion-neutral interaction, not taken into account in the MHD approximation.

The study of Arber et al. (2007) of flux emergence in a 3D setup compares the case of the fully ionized plasma to the case of partial ionized plasma, where they include the partial ionized effects through a generalized Ohm's law. In the partial ionized case, they include in the expression for the electric field the Ohmic and the ambipolar terms. Arber et al. (2007) show that in a fully ionized plasma, more chromospheric material is uplifted to the corona, compared to a partial ionized plasma, because of the ambipolar term. In their study, the RTI is suppressed when the neutrals are included.

Nóbrega-Siverio et al. (2020) suggest that, as the nonequilibrium ionization and recombination give different number densities than those calculated in local thermodynamical equilibrium (LTE) assumption, the ambipolar coefficient is overestimated if the latter case. In their simulations of flux emergence Nóbrega-Siverio et al. (2020) find that the ambipolar diffusion does not significantly affect the amount of total unsigned emerged magnetic flux, but it is important in the shocks that cross the emerged region, heating the plasma.

Khomenko et al. (2014c) included partial ionization effects through the ambipolar term in their RTI simulations. They found an increase in the growth rate by 50% in the simulations that included the

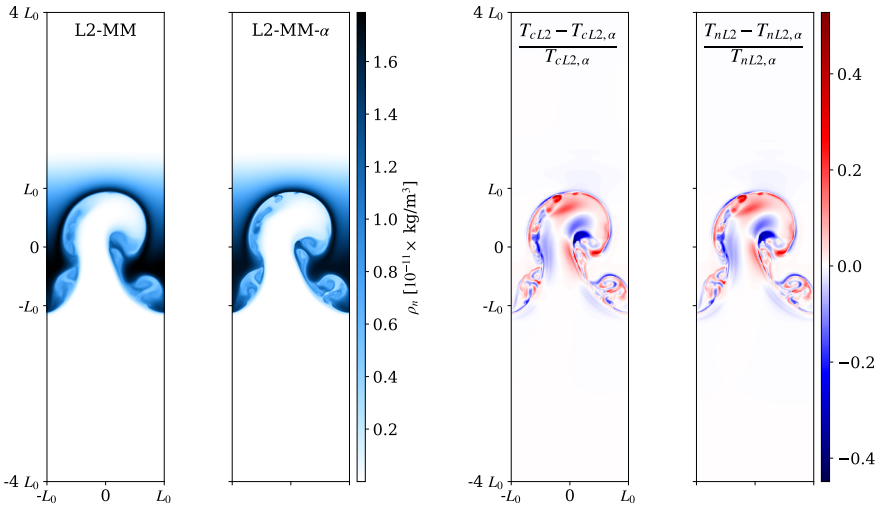

Figure 7.7: **Left:** Comparison of the snapshots of the density of neutrals for the simulations with sheared magnetic field L2-MM and L2-MM-α. **Right:** Difference of temperatures between the simulation L2-MM and L2-MM-α, normalized to the temperature in the simulation L2-MM-α at time ≈ 453 s. It has been calculated for the temperatures of both neutrals and charges as $\left(T_{L2} - T_{L2,\alpha}\right)/T_{L2,\alpha}$. We have used the notations $T_{\mathrm{n}L2}$, $T_{\mathrm{c}L2}$ in order to indicate the temperature for neutral and charged fluid, respectively for the simulation L2-MM; and $T_{\mathrm{n}L2,\alpha}$ and $T_{\mathrm{c}L2,\alpha}$ for the temperatures obtained in the simulation L2-MM-α.

ambipolar term, compared to the pure MHD simulations. The increase of the growth rate happens at smaller scales, where in the single-fluid approximation, the in-plane component of the magnetic field imposes a cutoff wave number. When partial ionization effects are taken into account, allowing for neutrals and charges to partially decouple, the scales in the neutral fluid which did not grow in purely single-fluid assumption, are now able to grow, as the magnetic field suppresses the scales in the charged fluid, in agreement with the analytical study of Díaz et al. (2014).

As explained by Martínez-Sykora et al. (2015), in the case of the flux emergence, the ambipolar diffusion allows the magnetic field to diffuse into the atmosphere. Since neutrals move through the expanding magnetic field in the chromosphere, the magnetic field lines lift less matter. As a result, the ambipolar diffusion may inhibit the RTI in this case. By contrast, a completely different configuration,

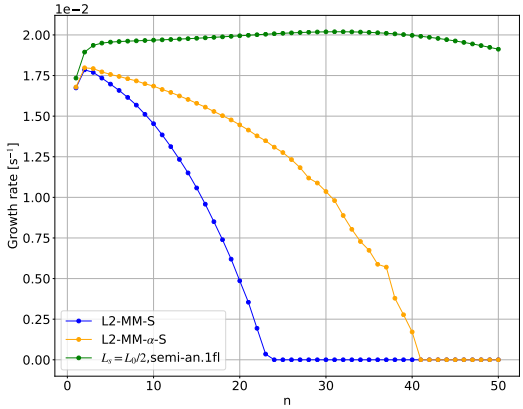

Figure 7.8: Linear growth rate for the simulations L2-MM-S (blue line), L2-MM-α-S (orange line) as a function of the mode number n. The linear phase was considered between $t = 100$ and $t = 200$ s. The error of the fit, as explained for Figure 6.14, was below 10^{-3} for positive growth rates. The green line shows the semi-analytical solution in the incompressible MHD approximation, described in subsection 6.5 in Chapter 6.

as that of Khomenko et al. (2014c) will increase the growth rate of the small scales.

The attempt to solve the two-fluid equations, presented in Appendix .0.1, was unsuccessful for the moment, and we proceed analytically with the solution obtained in the single-fluid approximation, as in Chapter 6, for the case of continuous interface (unlike the previous analytical works by other authors mentioned above).

7.4.1 Growth rate

Figure 7.8 shows the growth rate obtained from the two simulations L2-MM-S (blue line) and L2-MM-α-S (orange line) as a function of the mode number n. The linear phase was considered to be between $t = 100$ and $t = 200$ s. The semi-analytical growth rate obtained in the single-fluid, incompressible approximation is plotted for comparison with a green line. As the elastic collisions have been artificially increased by a factor of 10^4 in the simulation L2-MM-α-S, this simulation can be considered the MHD limit. The difference between the growth rate in this case, and the analytical one, can be due to the viscosity which was not taken into account in the semi-analytical solution. Recall that the effect of the compressibility is to enhance the growth rate. The difference between the numerical solution of the simulation L2-MM-S and the simulation L2-MM-α-S can be due to the weaker interaction between the neutrals and the charges. We can see that in our case the effect of the elastic collisions is similar to the effect of the viscosity, both producing the decrease of the growth rate, the effect being larger for smaller scales.

Our result is similar to Díaz et al. (2012) in the fact that the collisional interaction between neutrals and charges decreases the growth rate. The difference from the results of Khomenko et al. (2014c), where the growth rate of the small scales is increased, comes from the fact that, in our case, the scales

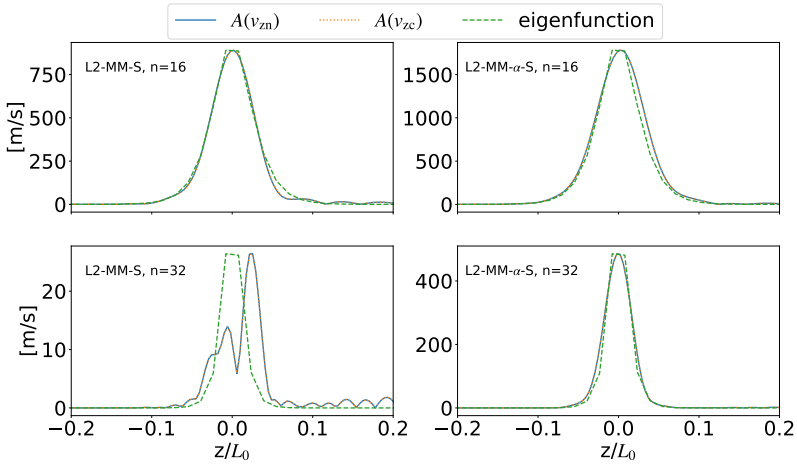

Figure 7.9: Fourier amplitudes of the vertical velocities of neutrals (blue solid line) and charges (orange dotted line) and the vertical eigenfunction of the velocity obtained in the single-fluid approach (green dashed line), as a function of height between -0.2 Mm and 0.2 Mm. **Top left panel:** L2-MM-S, n=16; **Top right panel:** L2-MM-S-α, n=16; **Bottom left panel:** L2-MM-S, n=32; **Bottom right panel:** L2-MM-S-α, n=32; The eigenfunction is normalized to the maximum of the velocities amplitudes. The snapshots of the simulations are taken at the end of the linear phase at time ≈ 190.4 s. The blue solid line and the orange dotted line superpose. Notice that the profile of the eigenfunction is not so smooth as it has been obtained on a grid with 512 points, compared to the profiles of the velocities obtained from the simulations which used 2048 points in the vertical direction.

at which the the collisions between neutrals and charges act as the viscosity are much larger than the scales at which the component of the magnetic field parallel to the perturbation direction becomes important. The cutoff mode number calculated semi-analytically and shown in the the previous chapter in Figure 6.15 is $n \approx 100$ and the smallest mode number affected by neutral-charge interaction, as from Figure 7.8, is $n = 3$.

7.4.2 Vertical profile of the Fourier amplitudes of v_{zn} and v_{zc} compared to the single-fluid eigenfunction profile

Another way to compare the numerical solution to the analytical solution is to compare the vertical profile of the Fourier (FFT in x direction) amplitudes of the velocities of neutrals and charges obtained from the simulation to to the profile of the vertical eigenfunction obtained in the single-fluid incompressible assumption, for a chosen mode. Recall that the eigenfunctions are obtained in a MHD

semi-analytical approach, where the equilibrium is constructed from the two-fluid equilibrium atmosphere, i.e. the same magnetic field and the density and the pressure are the sum of the neutral and charge's densities and pressures, respectively. By comparing the analytical and numerical calculations, one can, potentially, attribute the differences between them to either ion-neutral decoupling, viscosity, or to compressibility, not taken into account in the analytical approach. Since it takes some time for the simulation to establish the eigenfunction, the exact time of the comparison to the analytical solution is a free parameter, and it is not well defined. All these parameters, except for the ion-neutral interaction would affect the two simulations L2-MM-S and L2-MM-α-S in the same way.

Figure 7.9 shows the Fourier amplitudes of the vertical velocities of neutrals and charges, obtained after a FFT in the x direction, and the vertical eigenfunction of the velocity obtained in the single-fluid approach, as a function of height between $z = -0.2$ Mm and $z = 0.2$ Mm. The eigenfunction is normalized so that the maximum of velocity amplitude from simulations and from analytical calculations coincide. These quantities are plotted for two modes: $n = 16$ (top row) and $n = 32$ (bottom row), and for the two simulations: L2-MM-S (left column) and L2-MM-S-α (right column). The Fourier amplitudes are computed from velocities obtained from snapshots taken at the end of the linear phase at time ≈ 190 s. The effects of the compressibility, seen in the previous Chapter as a shift of the maximum of the eigenfunction to the positive z values, cannot be appreciated in this case of the sheared field. We observe that the profile of the velocities Fourier amplitudes and the eigenfunction match each other well for $n = 16$, for both simulations. However, this is not the case for the $n = 32$ mode. The profile of the velocities Fourier amplitudes is different from the profile of the eigenfunction (even if the vertical profiles of the Fourier amplitudes of the velocities of charges and neutrals coincide) for the simulations L2-MM-S, i.e. the case with less coupling (bottom left panel of Fig. 7.9). This suggests that the mode $n = 32$ is affected by the decoupling in the L2-MM-S.

7.4.3 Increase in temperature

When the two fluids are not completely coupled by collisions, the friction between the two generates heat, which can be observed as an increase in the temperature. The difference between the temperatures in the two simulations, L2-MM and L2-MM-alpha, normalized to the temperature in the simulation L2-MM-α has been shown above at the left panel of Figure 7.7. Similarly to Khomenko et al. (2014c), we can observe in this figure that there are both regions where L2-MM simulation shows hotter or cooler temperatures than L2-MM-alpha, and we can observe that the difference between L2-MM and L2-MM-α is up to $\approx 50\%$.

The average in the whole domain of the normalized temperature difference is positive, but has a small value:

$$\langle \Big(T_{cL2} - T_{cL2,\alpha} \Big) / T_{cL2,\alpha} \rangle_{\text{domain}} = 3.7 \times 10^{-4}$$
$$\langle \Big(T_{nL2} - T_{nL2,\alpha} \Big) / T_{nL2,\alpha} \rangle_{\text{domain}} = 2 \times 10^{-4} \tag{7.2}$$

The neutrals have less density in the simulation L2-MM compared to the simulation L2-MM-α because

of ionization,

$$\langle \rho_{nL2} - \rho_{nL2,\alpha} \rangle_{\text{domain}} = -3.7 \times 10^{-15} \text{kg/m}^3 \,, \tag{7.3}$$

Higher ionization rate in the simulation L2-MM compared to the simulation L2-MM-α might also be due to the higher temperatures in this simulation.

7.5 Modifications to the background atmosphere

In order to see how the density contrast and the magnitude of the magnetic field affect the growth rate of the RTI, we performed simulations where we increased the density contrast, by increasing the peak in the neutral density by a factor of 10. We increase the density contrast for the simulation with sheared field with $L_s = L_0$, and for the simulation with perpendicular field. The importance of the Lorentz force decreases compared to the gravitational force, and the cutoff wave number due to the in-plane component of the magnetic field should be shifted to a larger value when the density contrast is increased. Contrary to this, when the magnitude of the field is increased, the cutoff wave number should be smaller. We compare here three simulations, L1-WN, L1-WN-NN and L1-WN-NN-B. The three simulations with sheared field have been initialized with exactly the same perturbation, so that it is easy to compare them. We also use here for comparison the simulation with the perpendicular field, P-WN-NN. Notice that this simulation has a different initial perturbation that the one discussed in the section above (P-V1-MM).

Figure 7.10 shows snapshots of the four simulations: L1-WN, L1-WN-NN, L1-WN-NN-B and P-WN-NN taken at different times. We can observe that the structures are more extended in the vertical direction for the simulation L1-WN-NN at time $t \approx 322.1$ s, than for the simulation L1-WN and L1-WN-NN-B at time $t \approx 359.1$ s, a similar time. This means that the growth rate is larger when the density contrast is increased. Increasing the magnitude of the magnetic field has an opposite effect. The growth rate for L1-WN-NN-B appears to be larger than for L1-WN if we compare the vertical extent of the structures at time $t \approx 359.1$ s. We will see later, that this impression is consistent with the growth rate obtained semi-analytically.

The P-WN-NN simulation should be compared to the P-V1-MM simulation, presented in the previous chapter, in Figure 6.9. We can observe structures that are more extended in the vertical direction for P-WN-NN at time $t \approx 200$ s than for P-V1-MM at time $t \approx 202$ s, a similar time, but the difference is not so pronounced as for the case with the sheared field.

We also observe that more smaller scales develop when the density contrast is increased. The latter can be seen when we compare the snapshots of L1-WN to the snapshots of L1-WN-NN, but also also when we compare P-WN-NN to P-V1-MM.

In the simulations with increased density contrast, the density gradient scale length is smaller than in the simulations with original density contrast in the lower part of the domain. This shifts the center of the RTI in the negative z direction. The center of the instability was defined in the previous chapter as the average of the heights of the upper and lower boundaries of the structures. The shift in the center of the RTI can be observed in Figure 7.10 if we compare L1-WN-NN to L1-WN, or P-WN-NN

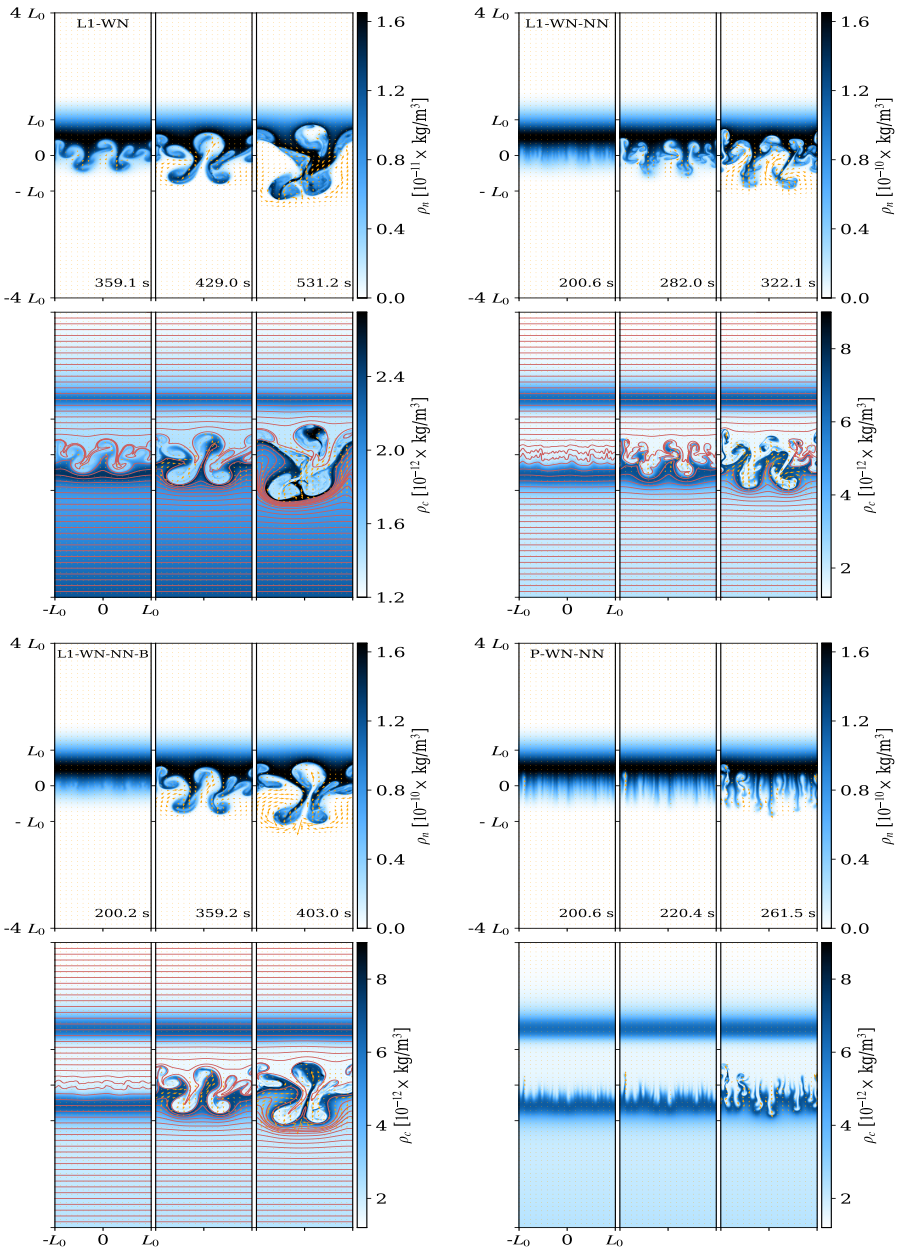

Figure 7.10: Time series of the snapshots of neutral and charged densities, for the simulations L1-WN (top, left group of panels), L1-WN-NN (top, right group of panels), L1-WN-NN-B (bottom, left group of panels), P-WN-NN (bottom, right group of panels). The in plane (x and z components) velocities of neutrals and charges are represented by orange arrows in the plots which show the densities of neutrals and charges, respectively. For the simulations with sheared magnetic field (bottom row), the in plane magnetic field lines are shown with red lines in each group of panels.

to P-V1-MM.

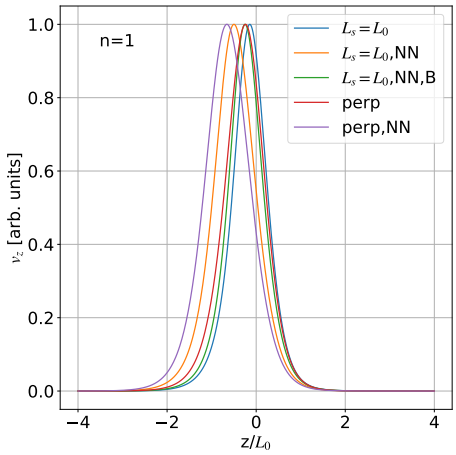

Figure 7.11: Eigenfunctions calculated semi-analytically in the incompressible MHD approximation for the mode number n = 1, for the configuration with sheared magnetic field with $L_s = L_0$. Different lines show cases with different parameters of the calculation: for the original values of density contrast and magnetic field (blue line, labeled "$L_s = L_0$"), increased density contrast and original value of the magnetic field (orange line, labeled "$L_s = L_0$,NN"), and for both increased density contrast and magnetic field (green line, labeled "$L_s = L_0$,NN,B"); and for the configuration with perpendicular magnetic field: for the original values of density contrast (red line, labeled "perp"), and for the increased density contrast (violet line, labeled "perp,NN")

Figure 7.11 compares the eigenfunctions calculated semi-analytically in the incompressible MHD approximation for the mode number $n = 1$, and sheared magnetic field with $L_s = L_0$ for several cases: (1) original values of density contrast and magnetic field (blue line, labeled "$L_s = L_0$"; (2) increased density contrast and original value of the magnetic field (orange line, labeled "$L_s = L_0$,NN"); (3) increased density contrast and magnetic field (green line, labeled "$L_s = L_0$,NN,B"). Additionally, it shows the case of the perpendicular magnetic field: (1) original values of the density contrast (red line, labeled "perp"); (2) increased density contrast (violet line, labeled "perp,NN"). We can observe how increasing the density contrast, shifts the peak of the eigenfunction towards the negative z direction for both configurations of the magnetic field. Therefore, the center of the RTI is shifted in the negative z direction when the density contrast is increased. The eigenfunctions profiles are symmetric, so the bubbles and the spikes grow in the same way in the linear phase.

The asymmetry between the growth of the bubbles and spikes develops in the nonlinear phase. As already said in the previous chapter, our simulations did not evolve so much in the nonlinear phase, to allow us to study the asymmetry between the bubbles and the spikes. However, the "bubble limit" observed by Berger et al. (2017), where at high Atwood number mostly bubbles are observed and no corresponding spikes, apparently contradicts the fact that the growth of the spikes measured from numerical simulations was larger than the growth of the bubbles for increasing Atwood number (Mikaelian 2014; Carlyle & Hillier 2017). The disconcordance might be related to different background atmospheres, or the vertical asymmetry of the initial perturbation, and it should be investigated in

the future.

7.5.1 Growth rate

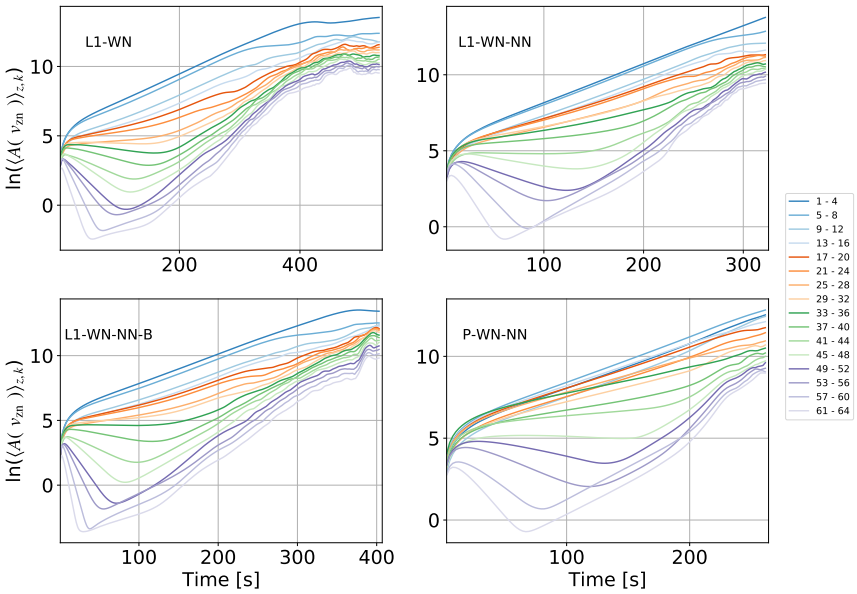

Figure 7.12: Growth rate of individual harmonics, computed from the vertical velocity of neutrals, as a function of time. Different color lines show the Fourier amplitudes of the harmonics, grouped in sets of four, from $n = 1$ to $n = 64$. The amplitudes are averaged between heights -L_0 and L_0. Different panels are for different simulations: L1-WN (top left); L1-WN-NN (top right); L1-WM-NN-B (bottom left); P-WN-NN (bottom right).

Next, we study how the density contrast and the magnitude of the magnetic field affects the growth rate of the Fourier modes. For that, we repeat the calculation from the previous Chapter 6. The Fourier amplitudes of $v_{\rm zn}$ are averaged in height between $z = -L_0$ and $z = L_0$ and over four consecutive modes. Figure 7.12 shows the natural logarithm of the Fourier amplitudes for the first 64 modes. One can observe in this figure, by comparing the top-left panel (L1-WN) and the top-right panel (L1-WN-

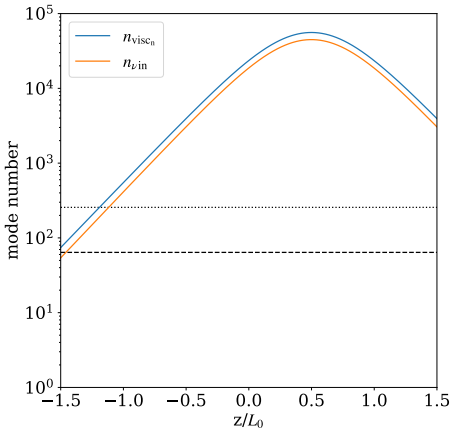

Figure 7.13: Mode numbers corresponding to the neutrals viscosity (blue solid line) and neutral-ion decoupling scale (orange solid line) for the increased density contrast profile. The horizontal black lines represent $n = 64$ (dashed line) and $n = 256$ (dotted line).

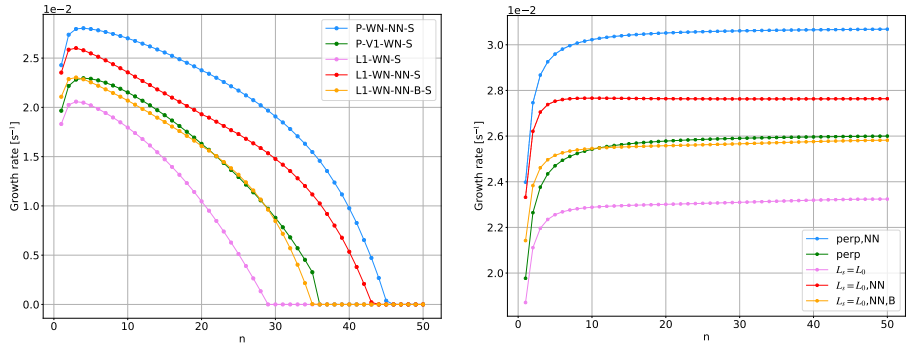

Figure 7.14: Comparison between the growth rates obtained from simulations (left) and semi-analytically in the incompressible MHD approximation (right) as functions of the mode number n, for n between 1 and 50. The time interval for which the linear growth has been considered was [100, 200] s for P-V1-WN-S (green lines), P-WN-NN-S (blue lines), L1-WN-S (violet lines) and [100, 150] s for L1-WN-NN-S (red lines) and L1-WN-NN-B-S (yellow lines). The error of the fit, as explained for Figure 6.14, was below 10^{-3} for positive growth rates.

NN) that the increase in the magnetic field decreases the growth rate of all the modes. This effect

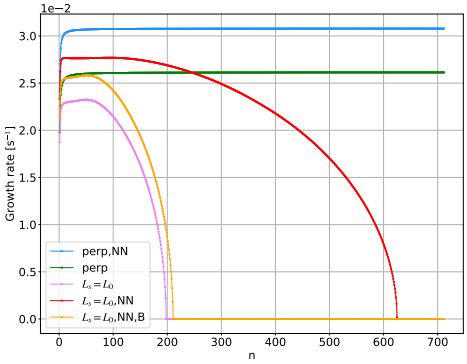

Figure 7.15: Semi-analytical growth rate as a function of the mode number n. The format of the figure and the color coding are the same as the right-hand side panel of 7.14, but extended from $n = 50$ to $n = 712$.

can be seen as a lower amplitude of the Fourier harmonics in the top-left panel, compared to the panel top-right. Notice that the time extent of the horizontal axis in all the panels of this Figure is different, and that the amplitudes have to be compared at the same moments of time. By comparing the top-left and the top-right panels of Figure 7.12, corresponding to the simulations L1-WN and L1-WN-NN, at time $t = 200$ s, for example, we see that the smaller scales grow more when the density contrast is increased. The largest mode number of the modes that grow in the linear phase is larger for L1-WN-NN (33) than for L1-WN (25). Analytically it has been shown by Chandrasekhar (1961) that the growth rate increases with increasing the Atwood number. Chandrasekhar (1961) shows that the result holds when the viscosity is taken into account. By considering a constant and uniform viscosity coefficient, Chandrasekhar (1961) shows that the increase of the density contrast shifts the minimum mode number affected by viscosity to a larger value. This result is valid for both uniform and non-uniform density and pressure profiles (Livescu 2004).

The viscosity coefficient is smaller in the model with enhanced density contrast, following its direct calculation from the model parameters. The viscosity and the neutral thermal conductivity coefficients in units of m^2/s, defined in Eq. 6.25 are inversely proportional to the neutral density. When the peak of the neutral density is increased, these coefficients have smaller values. The ion-neutral collision frequency, which is proportional to the neutral density, increases when the density contrast is increased. The mode numbers corresponding to all of these scales, as defined in Eq. 6.28 are all larger in the model with enhanced density contrast compared to the model with original values of the density. Figure 7.13 shows the modes corresponding to the neutral viscosity, and to ion-neutral collision frequency. We observe that the mode numbers are indeed larger than those corresponding to the model with original values of neutral density, shown in Figure 6.12.

At the beginning of the nonlinear phase, at time $t \approx 200$ s, the energy is transferred from larger to smaller scales (direct cascade). This fact can be seen in Figure 7.12 for the four simulations from

the sudden increase of the amplitude of small scales, while the amplitude of the large scales decreases (notice how violet lines and orange lines converge around this time). The direct cascade occurs at the beginning of the nonlinear phase because the small scales have been suppressed during the linear phase. At later times, the saturated small scales join to form larger scales (inverse cascade). This can be seen more clearly for the simulation L1-WN at time $t \approx 500$ s and for L1-WN-NN-B at time $t \approx 400$ s. In the simulations performed by Porth et al. (2014), initially, the dominant mode is small-scale, and the inverse cascade is obtained first in the nonlinear phase when larger scales overtake the saturated small scales, but this trend is reversed at later times when a sudden creation of new small scale features occurs. The ordering of the energy cascades depends on many factors. A multimode perturbation may favor the appearance of the inverse cascade first, as the case of Porth et al. (2014). Another effect may come from the fact that the small scales are suppressed at the beginning, while the large scales grow exponentially, thus favoring the direct cascade to appear first at the beginning of the nonlinear phase. It appears that the latter effect was more important in our case.

If we look again at the snapshots of the simulations L1-WN, L1-WN-NN and L1-WW-NN-B in Figure 7.10, it seems that the increase in the density contrast favors the direct cascade, while the increase of the magnetic field strength favors the inverse cascade. This can be seen in the evolution of the structures over time. The latter can also be seen by noticing the divergence of green and violet lines at time $t \approx 350$ s in the bottom left panel of Figure 7.12. In the nonlinear regime, mode interactions should erase memory of initial conditions, and the simulations should be comparable at later times, (see, e.g. Stone & Gardiner 2007). As we have discussed before, our simulations do not reach this stage. The simulations with multimode perturbation are more prone to the direct cascade than the white noise because of the large structure that forms in the middle caused by the coherence of the modes superposed in the initial perturbation.

Figure 7.14 compares the growth rates as a function of the mode number n for the first 50 modes for the simulations and semi-analytical calculations. We show cases of P-WN-NN-S (blue lines), P-V1-WN-S (green lines), L1-WN-S (pink lines), L1-WN-NN-S (red lines), L1-WN-NN-B-S (yellow lines) at the left-hand side panel. The analytical growth rates are shown at the right-hand side of the figure. We can observe that the linear growth rate obtained from simulations starts to decrease for relatively small wave numbers in all the cases. The explanation for this decrease is, as in the previous chapter, the neutral viscosity and thermal conductivity, and the ion-neutral interaction. In the previous chapter we found that the compressibility increases the growth rate. Theoretically, the viscosity does not impose a cutoff, the growth rate starts to decrease with increasing mode number for the mode numbers larger than the mode number of the fastest growing mode and, in the infinitely large wave number limit, the growth rate is zero (Chandrasekhar 1961). When we obtain the growth rates from simulations, numerically, very small growth rates cannot be captured and in practice, the growth rate is zero for mode numbers larger than a certain value, indicated in the previous chapter by $n_{\rm cd}$. We can observe that $n_{\rm cd} < 50$ for all the four cases. When the density contrast is increased, the growth rate is larger and $n_{\rm cd}$ is also larger. Increasing the magnetic field has an opposite effect, the values of the growth rates and $n_{\rm cd}$ are smaller. Even if the growth rates obtained semi-analytically do not decrease with n for the modes considered in Figure 7.14, the ordering between the growth rates for different simulations

is maintained.

Figure 7.15 shows the growth rate as a function of wave number obtained semi-analytically for a larger domain in the horizontal direction. We have extended the horizontal axis of the right panel of Figure 7.14 from mode number $n = 50$ to mode number $n = 712$ in order to see the cutoff frequencies in the cases with a in-plane component of the magnetic field. We can see that for both perpendicular and sheared magnetic field configurations, the growth rates and magnetic cutoff wave numbers are larger for larger density contrast. When the magnetic field is increased, the growth rate and the magnetic cutoff wave number are smaller.

7.5.2 The effect of the compressibility

In order to understand how the compressibility effect depends on the density contrast, we solve semi-analytically the compressible HD equations for the profile with increased density contrast, as described in section 6.6 from the previous chapter. Left panel of Figure 7.16 shows the growth rates obtained semi-analytically in the incompressible (solid lines) assumption compared to the compressible case (dotted lines), for the HD case, in the two cases: the original (orange lines) and the increased (blue lines) density contrast. We can observe that the compressible growth rate is larger than the incompressible growth rate when the density contrast is increased, similarly to the original situation. We can observe however, that the growth rate is less affected by the compressibility when the density contrast is smaller. This is similar to the conclusion of Livescu (2004); Ribeyre et al. (2005).

At the right-hand side panel of Figure 7.16 we plot the vertical eigenfunction profile for the increased density contrast in the compressible (dotted lines) and incompressible (solid lines) cases for the mode numbers $n = 1$ (black lines), and $n = 16$ (red lines). We can compare this plot to the plot shown at the right-hand side panel of Figure 6.16. We can observe that the shift of the peak of the eigenfunction towards the positive z direction in the compressible case compared to the incompressible case is more pronounced for the increased density contrast than for the original density contrast. We can also observe that the shift is more pronounced for higher mode numbers and the high modes are more affected when the density contrast is increased.

7.5.3 Decoupling

Figure 7.17 compares the normalized charges-neutral decoupling in v_z, as calculated from Eq. 6.47, for the simulations: L1-WN (top left), L1-WN-NN (top, right), L1-WN-NN-B (bottom left), and P-WN-NN (bottom right). Comparing the decoupling for the simulations L1-WN and L1-WN-NN, we can see that there is less decoupling for L1-WN-NN, when the density contrast is increased, confirming our intuition that the increase in the density contrast decreases the importance of the magnetic field. Neutral viscosity is one of the important agents as well, affecting the behavior of the decoupling. The large viscosity for the neutral species allow the neutrals to decouple from the charges. The viscosity is smaller for increased density contrast case, therefore neutrals are less affected, and the decoupling is less pronounced. Because of the smaller viscosity, the simulation with perpendicular field, P-WN-NN also

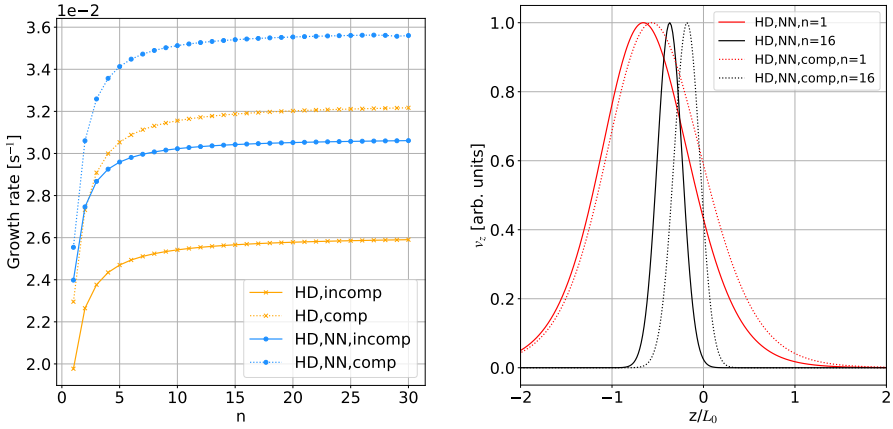

Figure 7.16: Left: Growth rates obtained semi-analytically in the MHD approach, for the perpendicular field, for the original density contrast (orange lines) and the increased density contrast (blue lines) in the incompressible (solid lines) case compared to the compressible case (dotted lines). Right: Vertical eigenfunctions profiles obtained semi-analytically with the same assumptions for mode numbers $n = 1$ (black lines) and $n = 16$ (red lines). For better visualization, the vertical domain has been limited to $-2 < z/L_0 < 2$.

has less decoupling when the density contrast is increased, compared to the simulation P-V1-M from Figure 6.19 in the previous chapter. However, now the simulation L1-WN-NN has more decoupling compared to the simulation P-WN-NN, while with smaller density contrast the situation was reversed: the decoupling calculated for the simulation L-V1-M was smaller than for P-V1-M. Contrarily, when the magnetic field is increased, the decoupling increases. The simulation L1-WN-NN-B has the largest decoupling from all the simulations presented in Figure 7.17.

7.5.4 Power spectra

Figure 7.18 compares the power spectra for L1-WN, L1-WN-NN, and L1-WN-NN-B simulations taken at different times. We have considered the kinetic energy of neutrals (yellow markers) and charges (red markers) and the magnetic energy (blue markers). The slopes obtained by a linear fit are indicated in the legend, together with the uncertainty of the fit.

The simulations with increased density contrast (second and third rows) have smaller slopes (if we look at the closest moments of time, i.e. the last plots of the second and third rows compared to the first plot of the first row) because they are less affected by the viscosity. The increase of the slope in time can be explained by the direct energy cascade, and the decrease of the slope (to a more

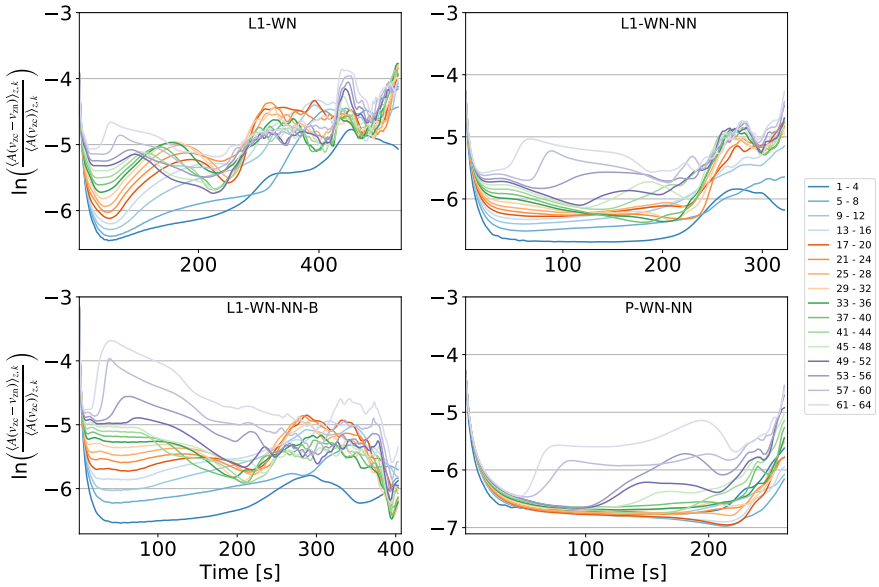

Figure 7.17: Normalized decoupling in vertical velocity, computed according to Eq. 6.47, in Chapter 6 as a function of time. Different panels are for different simulations: Top left: L1-WN; Top, right: L1-WN-NN; Bottom left: L1-WN-NN-B; Bottom right: P-WN-NN.

negative value) can be explained by the inverse cascade or by the fact that the small scales begin to be suppressed. The suppression of the small scales is by the neutral viscosity and thermal conductivity, ion-neutral interaction or the magnetic field. The magnetic field is responsible for the decrease of the slopes for the simulation L1-WN-NN-B. The content of magnetic energy is larger for all the modes in the simulation L1-WN-NN-B compared to L1-WN and for the simulation L1-WN-NN compared to L1-WN-NN-B. The explanation is that the growth rates are ordered in the same way: the growth rate for the simulation L1-WN-NN is larger than the growth rate for L1-WN-NN-B, which in turn is larger than the growth rate calculated for L1-WN, see Figure 7.14. The larger growth rate implies more twisting of the field lines, therefore larger magnetic energy. The field lines are more difficult to bend when the magnetic field is large, but the bending will create more magnetic energy. For this reason, the slope of the magnetic energy increases faster for L1-WN-NN-B at the beginning but stagnates at later times, while for the L1-WN-NN simulation it grows faster at later times.

The drawback of the power spectra analysis is, as mentioned in the previous chapter, the small number of scales and the fact that the simulations did not evolve enough in the nonlinear phase and the spectra still had large variations in time.

7.6 Energy

Figure 7.19 shows the energies averaged in the whole domain: magnetic energy (solid line), kinetic energies of neutrals (dotted line) and charges (dashed-dotted line) as a function of time. The value of the magnetic energy at time $t = 0$ has been subtracted from the magnetic energy. The right panel shows the principal terms that contribute to the increase of temperature, averaged in the whole domain: frictional heating (solid line), neutral viscous heating (dotted line) as a function of time. The two panels use the same color coding, different for the three simulations shown: blue for L1-WN, orange for L1-WN-NN, and green for L1-WN-NN-B.

The magnetic energy decreases for the simulation L1-WN-NN at the beginning of the nonlinear phase, but it increases later. For the other two simulations, the magnetic energy always increases with time. The situation is more difficult to understand if we take into account that we observed more magnetic energy for all the modes in the simulation L1-WN-NN, compared to the other two, see Figure 7.18. We believe that the reason of the decrease of the magnetic energy at the beginning of the nonlinear phase for L1-WN-NN, with highest growth rate over the three simulations, is that the field lines are pushed away from the domain. The decrease with time of the magnetic energy at the beginning of the nonlinear phase also occurs for the simulation P-WN-NN (this is not shown in Figure 7.19). The fact that the field lines are pushed away as the structures develop is also the reason why we plot averages in the whole vertical domain, even if the structures develop mainly between $z = -L_0$ and $z = L_0$. We checked that the magnetic energy averaged only between $z = -L_0$ and $z = L_0$ decreases with time for the three simulations.

The bubbles are lighter for neutrals, but heavier for charges, and the spikes are the opposite. Therefore, the work done by the gravitational force of neutrals is always positive and that of charges always negative. The release of the gravitational energy through the (positive) work done by neutrals increases

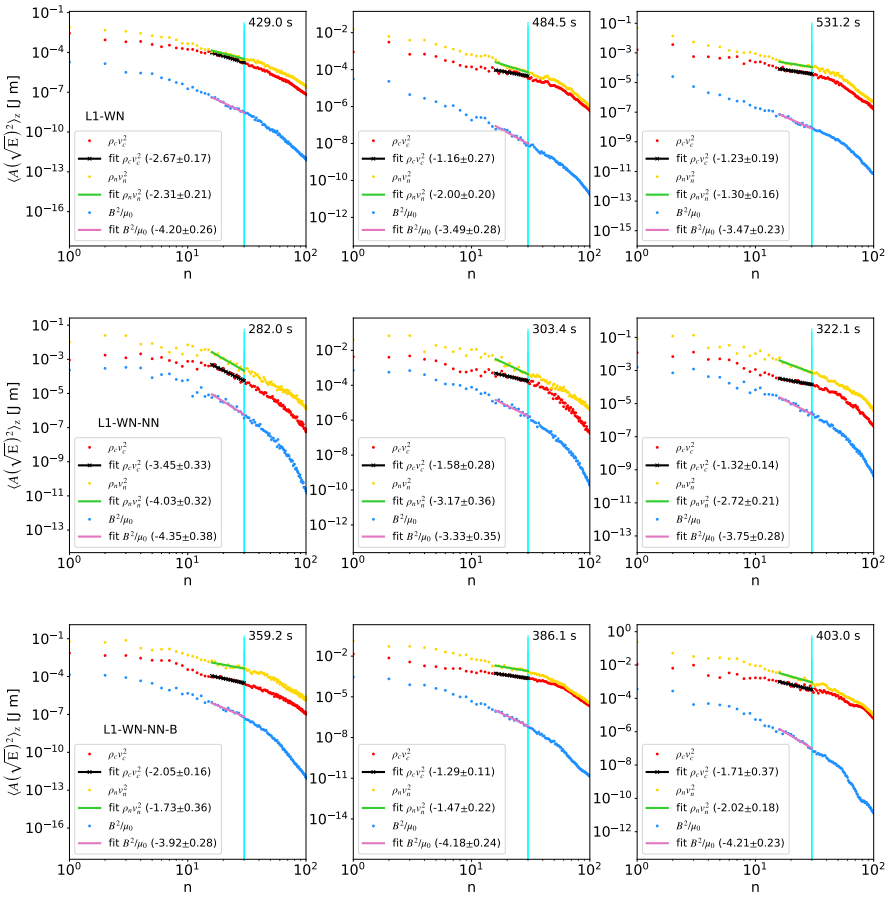

Figure 7.18: Power spectra of energies for different times for the simulations L1-WN, L1-WN-NN, and L1-WN-NN-B. Kinetic energies of charges and neutrals and the magnetic energy are marked with red, yellow and blue points, respectively. A linear fit to each quantity is shown with a solid line, and the value of the slope and the uncertainty of the fit are indicated in the legend.

the neutrals kinetic energy. Because of the strong collisional coupling, the charges are dragged, and their kinetic energy increases. The internal energy of charges increases, and that of the neutrals decreases, mainly due to the ionization/recombination processes, as discussed above in Section 7.3.

The frictional heating has a positive value from the beginning and is constant for a large interval of time, after which it starts to increase abruptly. Similarly to what we have seen in Chapter 5, the frictional heating, which depends on densities and temperatures, is constant, and has the value approximately equal to that for equilibrium variables, since the variation in time in the background can be considered negligible. The frictional heating is larger and also increases faster for the enhanced density case. The viscous heating is initially negligible, but starts to increase at later times, together with the frictional heating.

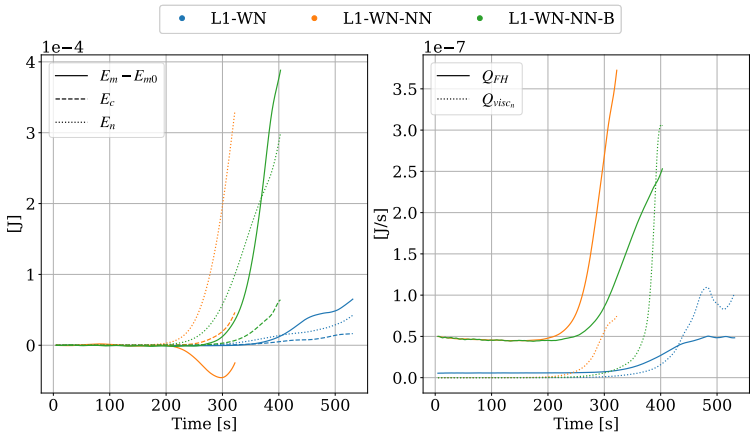

Figure 7.19: **Left:** Evolution of energies in time: magnetic energy (solid line), kinetic energy of neutrals (dotted line) and charges (dotted-dashed line). The value of the magnetic the value at time t = 0 has been subtracted from the values of the magnetic energy. **Right:** Evolution of the terms in the energy equation: frictional heating (solid line), and viscous heating (dotted line). The color coding is the same for both panels: blue for L1-WN, orange for L1-WN-NN, and green for L1-WN-NN-B.

7.7 Conclusions

In this chapter we have studied the changes in the development of the Rayleigh-Taylor instability with the inclusion of the elastic and inelastic collisions, the modification of the background atmosphere, such as the density contrast and the magnetic field strength. Some of aspects considered, such as

the decoupling, the growth rate and the asymmetry between bubbles and spikes can be deduced from observations. The conclusions of this chapter are summarized below:

- The action of inelastic processes of ionization/recombination makes the structures in the charges fluid to develop a sharp edge, following the evolution of the eddies. The sharp edge is due to the ionization of the neutrals which enter in the much hotter corona. The ionization/recombination also causes the temperature of charges and neutrals to decouple stronger, when we observe decoupling in temperature of several hundreds of K.
- The elastic collisions between ions and neutrals suppress the small scales, which can be viewed as a loss of contrast in the density snapshots. Elastic collisions cause the decrease of the growth rate at small scales. The action of elastic collisions at small scales is equivalent to the action of viscosity. The typical scale imposed by elastic collisions in our model is smaller than the cutoff imposed by the in-plane component of the magnetic field.
- When the density contrast is increased, smaller scales develop, the growth rate is larger and the decoupling is smaller. The peak of the vertical velocity's eigenfunction is more shifted toward the negative z direction for the increased density contrast than for the original case. Therefore, we can see more structures developed in the lower part of the domain.
- In the hydrodynamic case, the unstabilizing effect of the compressibility is smaller for higher density contrast. The compressibility shifts the center of the RTI towards the positive z direction, compared to the incompressible case, the effect being more pronounced for higher density contrast.
- The increase of the magnetic field magnitude decreases the growth rate. The decoupling is larger.
- The magnetic energy is larger for the enhanced density contrast at all scales.
- The work done by neutral gravitational force is the main responsible for the increase of the kinetic energies of both neutrals and charges.
- The frictional heating has a positive value from the beginning. It is constant for a large interval of time, after which it starts to increase suddenly. The increase is faster when the density contrast is enhanced.

In the last two chapters we studied the evolution of the RTI in a thread of a solar prominence. Because the size of the system was small relative to the neutral viscosity and thermal conductivity, and ion-neutral collisional scales, our simulations did not have enough scales. These dissipation mechanisms were insufficient during the nonlinear phase, and the simulations did not evolve enough during the nonlinear phase so that we can compare the results to observations or to other results obtained from turbulence models. In the future we intend to simulate larger systems, with the possibility to dynamically resolve smaller scales as they form, as for example through the use of an adaptive mesh

refinement (AMR). In order to compare to observations a more realistic model should have a 3D geometry. In this model we have used neutral viscosity and thermal conductivity defined by neutral-neutral collisions only, which led to high neutral viscosity and thermal conductivity coefficients, that we have artificially limited in the upper part. The scales of the ion-neutral decoupling and the scales of the neutral viscosity and thermal conductivity were very similar and the two effects on the growth could not be properly separated. In the future we plan to perform simulations where we include collisions with particles of other species in the calculation of the coefficients of viscosity and thermal conductivity, and this makes their values two orders of magnitude smaller in the corona. More work has to be done in the future in order to relate the simulations to the observations.

8

Conclusions and future prospects

In this work we show how, starting from the existing MANCHA3D code, we implement the two-fluid equations in a new code, MANCHA3D 2F. In order to verify the newly developed code, we present some tests of wave propagation in a uniform atmosphere. We perform more realistic simulations of simulations of wave propagation in non-uniform atmosphere and the Rayleigh-Taylor instability. Below, we summarize the main conclusions.

8.1 The numerical implementation. Wave propagation in uniform atmosphere

The collisional terms that appear in the equations of continuity, momentum, and energy are proportional to the variables that evolve in time (density, momentum, energy), with the collision frequency being the proportionality constant. This means that the time step should be at most the inverse of the collision frequency in order to ensure the stability of these terms in an explicit scheme. The deep layers of the solar atmosphere are coupled by collisions, and here the timescale associated with the collisional terms is very small, much smaller than the hydrodynamic time scale, meaning for stability this imposes a very small CFL time step. In order to overcome this restriction the collisional terms are implemented implicitly in a semi implicit scheme, making it possible to use the time step determined by the ideal CFL condition.

We have performed some tests in order to verify the code. The propagation of acoustic and Alfvén waves in a uniform atmosphere have exact analytic solution. We can compare our numerical solutions with the analytical solutions in order to establish the accuracy of the scheme for the two regimes, uncoupled and coupled. At the end of Chapter 4 we performed a test in a stratified, isothermal atmosphere which has an almost exact analytical solution.

- For the choice of the scheme parameter $\beta = 1/2$, it can be proved theoretically that the scheme is second order accurate.

- The comparison between analytical and numerical results shows very good match and proves the second order accuracy of the scheme when $\beta = 1/2$. However, in some of the cases, it can be observed that the error is smaller when $\beta = 1$.
- The semi-implicit implementation speeds up the code considerably as compared to a fully explicit implementation. In the case of the wave propagation in the stratified atmosphere the semi-implicit scheme is 75 times faster.
- The simulation in the stratified atmosphere deal with the situation where the waves pass from a collisionally coupled regime to a decoupled regime, and the numerical results are satisfactory
- The analytical study shows that the waves are damped because of the collisions between ions and neutrals, and damping of the waves is maximum when the collisional frequency is equal to the wave temporal frequency. This result is in concordance with other results from the literature.

8.2 Wave propagation in stratified atmosphere

We perform simulations of fast magneto-acoustic waves in a stratified atmosphere permeated by a horizontal magnetic field and we observe damping of the waves, partly due to shock formation, but mostly because of the incomplete collisional coupling reflected in the relationship between the wave frequency and the collision frequency. We perform a simulation in the single fluid approach, including the ambipolar term which models the interactions between charges and neutrals and the solutions is similar to the two fluid numerical solution.

- Waves in neutrals and charges, initially coupled in the photosphere, become decoupled at some height in the chromosphere, meaning that velocities of co-located fluid elements for neutrals and charges become different. In our simulations, the decoupling happens above 0.7 - 1 Mm height. The difference in the charges-neutral velocity can reach up to 30-50% of the initial wave amplitude at the bottom of the domain (about 0.5 Mm in our model).
- The temperatures of neutrals and charges are effectively coupled by the thermal exchange and oscillate with the same amplitude and phase.
- The decoupling in the wave velocity is a function of the wave period, its amplitude and the background magnetic field strength. In general, waves with smaller periods show greater decoupling at the same height. Decoupling happens at lower heights for stronger magnetic fields.
- Charge-neutral collisions cause significant wave damping. We observe significant damping of the shorter period waves, 1 and 5 seconds in our simulations. In such cases, the absolute value of the decoupling is smaller compared to the less damped case, because the velocity amplitude strongly decreases after some height in the chromosphere and, in some cases, the perturbation associated with the waves completely disappears. Waves are damped at lower heights when the magnetic field is larger, but the damping length is shorter in the case of the smaller magnetic field.

- The damping obtained in the simulations in the linear regime can be rather precisely described by the analytic theory solving linear two-fluid equations using the WKB approach. This level of agreement suggests that the damping observed in such simulations is determined by the linear effects due to decoupling.
- Non-linear wave propagation effects and steepening of wave fronts largely enhance the effects of the linear collisional damping. Non-linear effects for the damping are more pronounced for the shorter period waves, because the shock formation happens at lower heights.
- Collisional damping produces an effective frictional heating and local background temperature increase. The rate of the temperature increase is constant in time and is proportional to the square of the velocity amplitude.
- The simulations done with a corresponding setup in the single-fluid assumption, where the interaction between neutrals and charges is introduced through the ambipolar term, showed that, the solutions obtained with the two models are in very good agreement at the bottom of the atmosphere. In the upper part, the damping in the two-fluid model is smaller than the damping obtained in the single-fluid model, in agreement with the analytical study of (Zaqarashvili et al. 2011b). The increase in the temperature was several times larger in the two-fluid model compared to the single-fluid model.

8.3 The Rayleigh-Taylor instability

We perform simulations for the Rayleigh-Taylor instability (RTI), following the setup of Leake et al. (2014). We study how the instability is influenced by different physical agents, such as the presence or absence of physical viscosity and conductivity, the strength of elastic ion-neutral collisions, the ionization/recombination. We also study the influence of the density contrast and magnetic field strength. We study the growth rate of the instability, the development and evolution of different scales in the linear and non-linear regime, the power spectra of perturbations, and the energy balance. We are also interested in the decoupling between velocities and temperatures of the charged and neutral components.

- The growth rate is most affected by the magnetic field strength, shear, and also by the density contrast of the structure. The component of the magnetic field parallel to the direction of the perturbation suppresses the growth of the small scales. Both in simulations, and in the analytical calculations using simplified MHD treatment, the growth rate decreases with the decrease of the shear length of the magnetic field. The growth rate also decreases with the increase of the magnetic field modulus. The increase of the density contrast cause faster growth rates, especially at small scales.
- The growth rate obtained from simulations is independent from the properties of the initial perturbation (multi-mode or white noise), which gives us an additional confidence in our results.

- The viscosity, thermal conductivity, and ion-neutral elastic collisions suppress the small scales with wavelengths below the typical scales defined by the above processes. Thanks to that, the small scales do not have an initial linear growth phase.
- In the hydrodynamic case, the compressibility has a destabilizing effect, increasing the growth rate. The effect of compressibility is smaller for higher density contrast. The compressibility also shifts the center of the RTI towards the positive z direction, compared to the incompressible case. This shift is more pronounced for higher density contrast.
- The elastic collisions between ions and neutrals suppress the small scales, which can be viewed as a loss of contrast in the density snapshots. Elastic collisions cause the decrease of the growth rate at small scales. The action of elastic collisions at small scales is equivalent to the action of viscosity. The typical scale imposed by elastic collisions in our model is smaller than the cutoff imposed by the in-plane component of the magnetic field.
- The action of inelastic processes of ionization/recombination makes the structures in the charges fluid to develop a sharp edge, following the evolution of the eddies. The sharp edge is due to the ionization of the neutrals which enter in the much hotter corona. The ionization/recombination also causes the temperature of charges and neutrals to decouple stronger.
- The vertical profile of the atmosphere makes that the peak of the vertical velocity's eigenfunction is shifted toward the negative z direction. This fact causes the development of structures more at the lower part of the simulated prominence thread. The shift is larger for higher density contrast. The symmetry of the eigenfunction makes the bubbles and the spikes growing at the same rate during the linear phase.
- In the nonlinear phase we observe both direct and inverse cascades of energy.
- We observe decoupling in velocities of the order of 10^2 to 10^3 m/s in all the cases considered. The decoupling affects more the smaller scales. The action of the magnetic field and the physical viscosities and neutral thermal conductivity are the main reasons of the decoupling. The scales that decouple during the linear stage, are those which do not grow during this stage, as they are suppressed by viscosity and conductivity. The decoupling becomes larger when the strength of the magnetic field in the modeled prominence thread is increased. The increase of the density contrast produces the opposite effect.
- The slope of the magnetic energy power spectrum increases in time because of the production of magnetic energy at small scales. The magnetic energy contained in individual components of the magnetic field is larger than the total magnetic energy, for the small scales. Such behavior can indicate the twisting of the magnetic field and formation of a flux rope. The magnetic energy becomes lower in the case physical viscosity and conductivity are acting. The increase of the density contrast causes the increase of the magnetic energy.

- The work done by neutral gravitational force is the main responsible for the increase of the kinetic energies of both neutrals and charges.

- The frictional heating has a positive value from the beginning of the evolution of the RTI. It keeps constant for a large interval of time, after which it starts to increase abruptly. The increase is faster when the density contrast is enhanced.

8.4 Future prospects

There are some open questions which are subject of future investigations. These are described below.

- The implementation of a mechanism that ensures that the divergence of the magnetic field is zero has to be considered.

- We should investigate the problem of the viscosity when the density is low, described in section 2.1.4 in Chapter 2. When only collisions inside same species are considered in the calculation of the coefficients of viscosity and thermal conductivity, these terms become very large in the cases with low density. In the simulations we have limited the values of the coefficients to 10^9 m^2/s. We have seen that this problem could possibly be solved by taking into account the collisions with charges, besides neutral-neutral collisions for the calculation of these coefficients.

- The accuracy of the scheme could be improved. It should also take into account more operators, such as an implicit operator for diffusivity, which for the moment makes the scheme first order accurate, regardless the value of the parameter β. This is somehow related to the previous problem. There has been an attempt to implement the neutral viscosity and thermal conductivity implicitly. In this case, because the terms contain spatial derivatives, they cannot be implemented in a point implicit scheme, as in the case of the collisional terms. However, we can see that, if we want to implement them implicitly, and we write explicitly the discretization for the spatial fourth order scheme, we obtain a big tridiagonal linear system of equations, which can be solved efficiently using the algorithm BiCGStab. We have observed that the scheme is stable if this implicit update is done after the implicit update of the collisional terms. It is not clear yet how we can keep the second order accuracy, and have a stable scheme at the same time.

- The design of the scheme should be reconsidered if more fluids are to be added, because in this case, the inversion required by the implicit implementation is done analytically and uses the fact that there are only two species.

- The collisional terms related to current density **J** have been neglected for the moment. They are proportional to the electron density and have been assumed small, but no calculation has been done.

- The model is a very simple one, where we have only hydrogen. We should improve its realism by including more species, realistic equations of state instead the ideal gas law (also include the ionization energy in the internal energy of charges), and radiation. Having a separate equation for the energy of electrons should also be taken into account.
- In order to see how the elastic collisions affect the growth rate for larger wave number closer to the cutoff frequency due to the magnetic field we should solve semi-analytically the equations of RTI in the two-fluid approximation with elastic collisional coupling.
- We should study the effect of the compressibility with magnetic field.
- More work is needed in order to relate the RTI simulations to the observations. The large decoupling observed at the prominence-corona interface in the RTI simulations could be possibly observed with the forthcoming solar telescopes EST and DKIST.

9

Conclusiones y perspectivas futuras

En este trabajo mostramos cómo, partiendo del código existente MANCHA3D, implementamos las ecuaciones de dos fluidos en un nuevo código, MANCHA3D 2F. Con el propósito de verificar dicho código, presentamos algunas pruebas relizadas de simulaciones de propagación de ondas en una atmósfera uniforme. A continuación, realizamos simulaciones mas realistas de propagación de ondas en una atmósfera estratificada e inestabilidad de Rayleigh-Taylor. Abajo, resumimos las principales conclusiones.

9.1 La implementación numérica. Propagación de ondas en atmósfera uniforme

Los términos de colisión que aparecen en las ecuaciones de continuidad, momento y energía son proporcionales a las variables que evolucionan en el tiempo (densidad, momento, energía), y la constante de proporcionalidad es la frecuencia de colisión. Esto significa que el paso de tiempo máximo debería ser el inverso de la frecuencia de colisión para garantizar la estabilidad de estos términos en un esquema explícito. Las capas profundas de la atmósfera solar están acopladas por colisiones, y aquí los términos de colisión tienen escalas de tiempo mucho más pequeñas que las escalas de tiempo hidrodinámico, y la condición de estabilidad impondría pasos de tiempo CFL muy pequeños. Para superar esta restricción, los términos de colisión se implementan implícitamente en un esquema semi implícito, haciendo posible usar el paso de tiempo determinado por la condición CFL. Hemos realizado algunos tests para verificar el código, resolviendo problemas de propagación de las ondas acústicas y de Alfv én en una atmósfera uniforme, que tienen solución analítica exacta, para los dos regímenes diferentes, desacoplado y acoplado. Comparando las soluciones numéricas con las soluciones analíticas podemos determinar la precisión del esquema. Al final del Capítulo 4 realizamos un test en una atmósfera isotérmica estratificada que tiene una solución analítica casi exacta.

- Para la elección del parámetro del esquema $\beta = 1/2$, se puede demostrar teóricamente que el esquema tiene precisión de segundo orden.

- La comparación entre las soluciones numéricas y analíticas muestra muy buena correspondencia entre las dos y demuestra que el esquema tiene precisión de segundo orden cuando $\beta = 1/2$. Sin embargo, en algunos de los casos, se puede observar que el error es menor cuando $\beta = 1$.
- La implementación semiimplícita acelera considerablemente el código en comparación con una implementatción completamente explícita. En el caso de la propagación de ondas en la atmósfera estratificada, el esquema semiimpícito es 75 veces más rápido.
- Los resultados de la simulación en la atmósfera estratificada muestran que el código maneja bien la situación donde las ondas pasan de un régimen acoplado por colisiones a un régimen desacoplado.
- El estudio analítico muestra que las ondas están amortiguadas debido a las colisiones entre iones y neutros, y el amortiguamiento de las ondas es máximo cuando la frecuencia de colisión es igual a la frecuencia temporal de la onda. Este resultado está en concordancia con otros resultados de la literatura.

9.2 Propagación de ondas en atmósfera estratificada

Realizamos simulaciones de ondas magneto-acústicas rápidas en una atmósfera estratificada con un campo magnético horizontal. Observamos el amortiguamiento de las ondas, en parte debido a la formación de choques, pero principalmente debido a la interacción de los neutros y cargas que no están completamente acoplados por colisiones. Realizamos una simulación en la approximación de un fluido único, incluyendo el término ambipondar, que modela las interacciones entre cargas y neutros. Observamos pequeñas diferencias en la tasa de amortiguamiento, siendo un poco más baja en el modelo de dos fluidos en la parte superior de la atmósfera. Sin embargo, la diferencia entre el incremento en tempertura es varias veces más grande en el modelo de dos fluidos comparado con el modelo de un fluido.

- Las ondas en neutros y cargas, inicialmente acopladas en la fotosfera, se desacoplan a cierta altura en la cromosfera. En nuestras simulaciones, el desacoplamiento ocurre por encima de 0.7 - 1 Mm de altura. La diferencia entre las velocidades de cargas y neutros puede alcanzar hasta el 30-50 % de la amplitud de onda inicial en la parte inferior del dominio (aproximadamente 0.5 Mm en nuestro modelo).
- Las temperaturas de los neutros y las cargas están efectivamente acopladas por el término de intercambio térmico y oscilan con la misma amplitud y fase.
- El desacoplamiento en la velocidad de la onda es una función del período de la onda, su amplitud y la intensidad del campo magnético de la atmósfera de equilibrio. En general, las ondas con períodos más pequeños muestran un mayor desacoplamiento a la misma altura. El desacoplamiento ocurre a alturas más bajas para campos magnéticos más fuertes.

- Las colisiones entre neutros y cargas causan un amortiguamiento significativo de las ondas. Observamos un amortiguamiento significativo de las ondas con período más corto (1 y 5 segundos en nuestras simulaciones). En estos casos, el valor absoluto del desacoplamiento es menor en comparación con el caso menos amortiguado, porque la amplitud de la velocidad disminuye rápidamente por encima de cierta altura en la cromosfera, y, en algunos casos, la perturbación asociada con las ondas desaparece por completo. Las ondas se amortiguan a alturas más bajas cuando el campo magnético es más grande, pero la longitud característica de amortiguamiento es más corta en el caso del campo magnético más pequeño.

- El amortiguamiento obtenido en las simulaciones en el régimen lineal puede describirse con bastante precisión mediante la teoría analítica que resuelve ecuaciones lineales de dos fluidos utilizando la aproximación WKB. Esto sugiere que el amortiguamiento observado en las simulaciones está determinado por los efectos lineales debidos al desacoplamiento.

- Los efectos de propagación de ondas no lineales contribuyen a los efectos del amortiguamiento lineal por colisiones. Los efectos no lineales del amortiguamiento son más pronunciados para las ondas de período más corto, porque la formación de choque ocurre a alturas más bajas.

- El amortiguamiento por las colisiones produce calentamiento por fricción y aumento local de la temperatura del background. La tasa de aumento de temperatura es constante en el tiempo y es proporcional al cuadrado de la amplitud de la velocidad.

- Las simulaciones realizadas con una configuración correspondiente en la aproximación de un fluido único, donde la interacción entre neutros y cargas se introduce a través del término ambipolar, mostraron que las soluciones obtenidas con los dos modelos están muy de acuerdo en la base de la atmósfera. En la parte superior, el amortiguamiento en el modelo de dos fluidos es menor que el amortiguamiento obtenido en el modelo de un fluido, de acuerdo con el estudio analítico de (Zaqarashvili et al. 2011b). El aumento de la temperatura fue varias veces mayor en el modelo de dos fluidos en comparación con el modelo de un solo fluido.

9.3 La inestabilidad de Rayleigh-Taylor

Realizamos simulaciones de la inestabilidad de Rayleigh-Taylor (RTI), siguiendo la configuración de Leake et al. (2014). Estudiamos cómo la inestabilidad está influenciada por diferentes factores físicos, como la presencia o ausencia de viscosidad física y conductividad térmica, las colisiones elásticas entre iones y neutros, los procesos de ionización/recombinación. También estudiamos la influencia del contraste de densidad y la magnitud del campo magnético. Estudiamos la tasa de crecimiento lineal de la inestabilidad, el desarrollo y la evolución de diferentes escalas en el régimen lineal y no lineal, los espectros de potencia de las perturbaciones y el balance de energía. También calculamos el desacoplamiento en las velocidades y temperaturas entre cargas y neutros.

- La tasa de crecimiento se ve más afectada por la magnitud y la cizalladura del campo magnético, y también por el contraste de densidad de la estructura. La componente del campo magnético paralela a la dirección de la perturbación suprime el crecimiento de las escalas pequeñas. Tanto en simulaciones, como en cálculos analíticos en la aproximación MHD ideal, la tasa de crecimiento disminuye con la disminución de la longitud característica de cizalladura del campo magnético. La tasa de crecimiento también disminuye con el aumento del módulo del campo magnético. El aumento del contraste de densidad causa tasas de crecimiento más grandes, especialmente a escalas pequeñas.

- La tasa de crecimiento obtenida de las simulaciones es independiente de las propiedades de la perturbación inicial (multimodo o ruido blanco), lo que nos da una confianza adicional en nuestros resultados.

- La viscosidad, conductividad térmica y las colisiones elásticas entre iones y neutros suprimen las escalas pequeñas con longitudes de onda por debajo de las escalas típicas definidas por los procesos anteriores. Debido a eso, las escalas pequeñas no tienen una fase inicial de crecimiento lineal.

- En el caso hidrodinámico, la compresibilidad aumenta la tasa de crecimiento. El efecto de la compresibilidad es más pequeño para mayor contraste de densidad. La compresibilidad también desplaza el centro de la inestabilidad hacía la dirección positiva de z, en comparación con el caso incompresible. Este desplazamiento es más pronunciado para un mayor contraste de densidad.

- Las colisiones elásticas entre iones y neutros suprimen las escalas pequeñas. Este hecho se puede ver como una pérdida de contraste en los snapshots de densidad. Las colisiones elásticas causan la disminución de la tasa de crecimiento a escalas pequeñas. La acción de las colisiones elásticas a escalas pequeñas es equivalente a la acción de la viscosidad. La escala típica impuesta por las colisiones elásticas en nuestro modelo es más pequeña que la longitud de onda de corte impuesta por la componente del campo magnético paralela a la dirección de perturbación.

- La acción de los procesos inelásticos de ionización/recombinación hace que las estructuras en las cargas desarrollen un borde con densidad incrementada. Este borde se debe a la ionización de los neutros que entran en la corona mucho más caliente. Los procesos de ionización/recombinación también causan el desacoplamiento más fuerte en la temperatura entre las cargas y los neutros.

- El perfil vertical de la atmósfera hace que el pico de la función propia (eigenfunction) de la velocidad vertical esté desplazado hacia la dirección negativa z. Este hecho provoca el desarrollo de estructuras más en la parte inferior del hilo de prominencia simulada. La simetría de la función propia hace que las burbujas y las espigas crezcan a la misma velocidad durante la fase lineal.

- En la fase no lineal observamos cascadas directas e inversas de energía.

- Observamos desacoplamiento en velocidades del orden de 10^2 a 10^3 m/s en todos los casos considerados. El desacoplamiento afecta más a las escalas más pequeñas. La acción del campo magnético, la viscosidad física y la conductividad térmica de los neutros son las principales razones del desacoplamiento. Las escalas que se desacoplan durante la etapa lineal, son aquellas que no crecen durante esta etapa, ya que están suprimidas por la viscosidad y la conductividad. El desacoplamiento es mayor cuando se aumenta la magnitud del campo magnético en la prominencia modelada. El aumento del contraste de densidad produce el efecto contrario.
- La pendiente del espectro de energía de la energía magnética aumenta con el tiempo debido a la producción de energía magnética a pequeñas escalas. La energía contenida en los componentes individuales del campo magnético es mayor que la energía magnética total, para las escalas pequeñas. Tal comportamiento puede indicar la torsión del campo magnético y la formación de una cuerda de flujo. La energía magnética disminuye en el caso con viscosidad física y conductividad térmica. El aumento del contraste de densidad causa el aumento de la energía magnética.
- El trabajo realizado por la fuerza gravitacional de los neutros es el principal responsable para el aumento de las energías cinéticas tanto de neutros como de cargas.
- El calentamiento por fricción tiene un valor positivo desde el comienzo de la evolución de la RTI. Se mantiene constante durante un gran intervalo de tiempo, después de que comienza a aumentar abruptamente. El aumento es más rápido cuando el contraste de densidad está incrementado.

9.4 Perspectivas futuras

Hay algunas preguntas abiertas que son objeto de futuras investigaciones. Estos se describen a continuación.

- Se debe considerar la implementación de un mecanismo que garantice que la divergencia del campo magnético sea cero.
- Deberíamos investigar el problema de la viscosidad cuando la densidad es baja, descrita en la sección 2.1.4 en el Capítulo 2. Porque los coeficientes de viscosidad y conducción térmica no dependen del número de densidad (la dependencia del número de densidad se cancela cuando solo se consideran colisiones dentro de la misma especie en el cálculo), los términos de viscosidad y conductividad se vuelven muy grandes en comparación con los otros términos en la ecuación de momento y energía, respectivamente. Este fue el caso de las simulaciones RTI presentadas en la última parte de la tesis. Los coeficientes de la viscosidad y la conductividad térmica de los neutros se hicieron muy grandes, debido al alto grado de ionización de la corona. En las simulaciones hemos limitado los valores de los coeficientes a 10^9 m^2/s. Hemos visto que este problema podría resolverse teniendo en cuenta las colisiones con cargas, además de colisiones neutro-neutro para el cálculo de estos coeficientes.

- La precisión del esquema podría mejorarse. También debe tener en cuenta más operadores, como un operador implícito para la difusividad, que por el momento hace que el esquema sea de primer orden, independientemente del valor del parámetro β. Esto de alguna manera está relacionado con el problema anterior. Se ha intentado implementar la viscosidad y la conductividad térmica de los neutros de forma implícita. En este caso, debido a que los términos contienen derivadas espaciales, no se pueden implementar de forma parecida a los términos de colisión. Sin embargo, podemos ver que, si queremos implementarlos de forma implícita, y escribimos explícitamente la discretización para el esquema espacial de cuarto orden, obtenemos un gran sistema lineal de ecuaciones tridiagonal, que se puede resolver de manera eficiente utilizando el algoritmo BiCGStab. Hemos observado que el esquema es estable si esta actualización implícita se realiza después de la actualización implícita de los términos de colisión. Todavía no está claro cómo podemos mantener la precisión del segundo orden y tener un esquema estable al mismo tiempo.
- El diseño del esquema debe reconsiderarse si se van a agregar más fluidos. Esto es así, porque en este caso, la inversión requerida en la implementación implícita se realiza de forma analítica y utiliza el hecho de que solo hay dos especies.
- Los términos de colisión relacionados con la densidad de corriente **J** se han despreciado por el momento. Son proporcionales a la densidad de electrones y se supone que son pequeños, pero no se ha realizado ningún cálculo.
- El modelo es muy simple, donde solo tenemos hidrógeno. Deberíamos mejorar su realismo al incluir más especies, ecuaciones de estado realistas en lugar de la ley de los gases ideales (también incluir la energía de ionización en la energía interna de las cargas), y radiación. También deberíamos tener en cuenta una ecuación para la energía de los electrones.
- Para ver cómo las colisiones elásticas afectan la tasa de crecimiento para un número de onda mayor más cerca de la frecuencia de corte debido al campo magnético, deberíamos resolver semi-analíticamente las ecuaciones de RTI en la aproximación de dos fluidos, con acoplamiento por colisiones elásticas.
- Se necesita más trabajo para relacionar las simulaciones RTI con las observaciones. Es posible que el gran desacoplamiento en velocidad observado en la interfaz entre la prominencia y la corona en las simulaciones de RTI se pueda observar con la siguiente generación de telescopios solares, como el EST o DKIST

Bibliography

Abarzhi, S. I. 2010, Philosophical Transactions of the Royal Society A: Mathematical, Physical and Engineering Sciences, 368, 1809

Alvarez Laguna, A., Lani, A., Mansour, N. N., Deconinck, H., & Poedts, S. 2017, The Astrophysical Journal, 842, 117

Alvarez Laguna, A., Lani, A., Poedts, S., Mansour, N. N., & Kosovichev, A. G. 2014, AGU Fall Meeting Abstracts

Anan, T., Ichimoto, K., & Hillier, A. 2017, A&A, 601, A103

Anderson, L. S., & Athay, R. G. 1989, ApJ, 336, 1089

Anuchina, N., Volkov, V., Gordeychuk, V., et al. 2004, Journal of Computational and Applied Mathematics, 168, 11 , selected Papers from the Second International Conference on Advanced Computational Methods in Engineering (ACOMEN 2002)

Arber, T. D., Brady, C. S., & Shelyag, S. 2016, ApJ, 817, 94

Arber, T. D., Haynes, M., & Leake, J. E. 2007, The Astrophysical Journal, 666, 541

Athay, R. G., & House, L. L. 1962, ApJ, 135, 500

Aulanier, G., & Demoulin, P. 1998, A&A, 329, 1125

Aulanier, G., & Démoulin, P. 2003, A&A, 402, 769

Babcock, H. W., & Babcock, H. D. 1955, ApJ, 121, 349

Ballester, J. L., Alexeev, I., Collados, M., et al. 2018, Space Sci. Rev., 214, 58

Bello González, N., Flores Soriano, M., Kneer, F., & Okunev, O. 2009, A&A, 508, 941

Bello González, N., Flores Soriano, M., Kneer, F., Okunev, O., & Shchukina, N. 2010a, A&A, 522, A31

Bello González, N., Franz, M., Martínez Pillet, V., et al. 2010b, ApJ, 723, L134

Bellot Rubio, L., & Orozco Suárez, D. 2019, Living Reviews in Solar Physics, 16, 1

Berenger, J.-P. 1994, Journal of Computational Physics, 114, 185

Berger, T., Hillier, A., & Liu, W. 2017, The Astrophysical Journal, 850, 60

Berger, T. E., Shine, R. A., Slater, G. L., et al. 2008, ApJ, 676, L89

Berger, T. E., Slater, G., Hurlburt, N., et al. 2010, ApJ, 716, 1288

Bhatia, P. K. 1974, Ap&SS, 26, 319

Bittencourt, J. A. 2004, Fundamentals of Plasma Physics, 3rd edn. (Fundamentals of Plasma Physics, Third Edition by J.A. Bittencourt. Published by Springer-Verlag, New York, Inc.; 2004. ISBN 0-387-20975-1.)

Blake, G. M. 1972, MNRAS, 156, 67

Bogdan, T. J., Carlsson, M., Hansteen, V. H., et al. 2003, ApJ, 599, 626

Bommier, V., & Leroy, J. L. 1998, in Astronomical Society of the Pacific Conference Series, Vol. 150, IAU Colloq. 167: New Perspectives on Solar Prominences, ed. D. F. Webb, B. Schmieder, & D. M. Rust, 434

Borrero, J. M., & Ichimoto, K. 2011, Living Reviews in Solar Physics, 8, 4

Brady, C. S., & Arber, T. D. 2016, ApJ, 829, 80

Braginskii, S. I. 1965, Reviews of Plasma Physics, 1, 205

Brandenburg, A. 2019, Monthly Notices of the Royal Astronomical Society, 487, 2673–2684

Brunt, D. 1927, Quarterly Journal of the Royal Meteorological Society, 53, 30

Cally, P. S. 2006, Philosophical Transactions of the Royal Society of London Series A, 364, 333

Cally, P. S., & Goossens, M. 2008, Sol. Phys., 251, 251

Carlsson, M., & Stein, R. F. 2002, in ESA Special Publication, Vol. 505, SOLMAG 2002. Proceedings of the Magnetic Coupling of the Solar Atmosphere Euroconference, ed. H. Sawaya-Lacoste, 293–300

Carlyle, J., & Hillier, A. 2017, A&A, 605, A101

Centeno, R., Collados, M., & Trujillo Bueno, J. 2009, ApJ, 692, 1211

Chandrasekhar, S. 1961, Hydrodynamic and Hydromagnetic Stability, International series of monographs on physics (Clarendon Press)

Cherniavski, M. V., & Shtemler, Y. 2013, Washington DC American Geophysical Union Geophysical Monograph Series, doi:10.1029/GM083p0097

Cheung, M. C. M., & Cameron, R. H. 2012, ApJ, 750, 6

Cho, J., & Lazarian, A. 2003, Monthly Notices of the Royal Astronomical Society, 345, 325

Clark, D. H., Murdin, P., Wood, R., et al. 1983, MNRAS, 204, 415

Collados, M., Trujillo Bueno, J., & Asensio Ramos, A. 2003, in Astronomical Society of the Pacific Conference Series, Vol. 307, Solar Polarization, ed. J. Trujillo-Bueno & J. Sanchez Almeida, 468

Cook, A. W., & Dimotakis, P. E. 2001, Journal of Fluid Mechanics, 443, 69–99

Courant, R., Friedrichs, K., & Lewy, H. 1967, IBM Journal of Research and Development, 11, 215

Cowling, T. 1953, Solar Electrodynamics. Chapter 8 in the book "The Sun" Ed. by GP Kuiper

de la Cruz Rodríguez, J., & Socas-Navarro, H. 2011, A&A, 527, L8

Díaz, A. J., Khomenko, E., & Collados, M. 2014, A&A, 564, A97

Díaz, A. J., Soler, R., & Ballester, J. L. 2012, The Astrophysical Journal, 754, 41

Dolai, B., Prajapati, R. P., & Chhajlani, R. 2016, Physics of Plasmas, 23, 113704

Doludenko, A. N., Fortova, S. V., Shepelev, V. V., & Son, E. E. 2019, Phys. Scr, 94, 094003

Dorf, M. 2014, arXiv e-prints, arXiv:1408.3677

Draine, B. T. 1980, ApJ, 241, 1021

Draine, B. T., & McKee, C. F. 1993, ARA&A, 31, 373

Draine, B. T., Roberge, W. G., & Dalgarno, A. 1983, ApJ, 264, 485

Felipe, T., Khomenko, E., & Collados, M. 2010, ApJ, 719, 357

Fermi, E., & Von Neumann, J. 1955, Taylor Instability of Incompressible Liquids, AECU (United States Atomic Energy Commission, Technical Information Service)

Fossum, A., & Carlsson, M. 2006, ApJ, 646, 579

Gardner, C. L., Glimm, J., McBryan, O., et al. 1988, The Physics of Fluids, 31, 447

Gerashchenko, S., & Livescu, D. 2016, Physics of Plasmas, 23, 072121

Gilbert, H., Kilper, G., & Alexander, D. 2007, ApJ, 671, 978

Gilbert, H. R., Hansteen, V. H., & Holzer, T. E. 2002, ApJ, 577, 464

Goedbloed, H., Keppens, R., & Poedts, S. 2019, Magnetohydrodynamics of Laboratory and Astrophysical Plasmas (Cambridge University Press), doi:10.1017/9781316403679

González-Morales, P. A., Khomenko, E., Downes, T., & de Vicente, A. 2018, A&A, submitted

Gupta, G. R. 2014, A&A, 568, A96

Hester, J. J., Stone, J. M., Scowen, P. A., et al. 1996, ApJ, 456, 225

Hillier, A. 2016, Monthly Notices of the Royal Astronomical Society, 462, stw1805

—. 2018, Reviews of Modern Plasma Physics, 2, doi:10.1007/s41614-017-0013-2

—. 2019, Physics of Plasmas, 26, 082902

—. 2020, in prep.

Hillier, A., Shibata, K., & Isobe, H. 2010, Publications of the Astronomical Society of Japan, 62, 1231

Hillier, A., Takasao, S., & Nakamura, N. 2016, A&A, 591, A112

Hillier, A., & van Ballegooijen, A. 2013, ApJ, 766, 126

Howard, R. 1959, ApJ, 130, 193

Hu, F. Q. 1996, J. Comput. Phys., 129, 201

Hunana, P., Tenerani, A., Zank, G. P., et al. 2019, arXiv e-prints, arXiv:1901.09354

Isobe, H., & Tripathi, D. 2006, A&A, 449, L17

Jess, D. B., Mathioudakis, M., Erdélyi, R., et al. 2008, ApJ, 680, 1523

Jess, D. B., Morton, R. J., Verth, G., et al. 2015, Space Sci. Rev., 190, 103

Jun, B.-I., Norman, M. L., & Stone, J. M. 1995a, ApJ, 453, 332

—. 1995b, ApJ, 453, 332

Keppens, R., Nool, M., Tóth, G., & Goedbloed, J. P. 2003, Computer Physics Communications, 153, 317

Khomenko, E. 2017, Plasma Physics and Controlled Fusion, 59, 014038

Khomenko, E., & Collados, M. 2006a, ApJ, 653, 739

—. 2006b, ApJ, 653, 739

—. 2009, A&A, 506, L5

—. 2012, ApJ, 747, 87

—. 2015, Living Reviews in Solar Physics, 12, 6

Khomenko, E., Collados, M., Díaz, A., & Vitas, N. 2014a, Physics of Plasmas, 21, 092901

—. 2014b, Physics of Plasmas, 21, 092901

Khomenko, E., Collados, M., & Díaz, A. J. 2016, ApJ, 823, 132

Khomenko, E., Collados, M., Shchukina, N., & Díaz, A. 2015, A&A, 584, A66

Khomenko, E., Díaz, A., de Vicente, A., Collados, M., & Luna, M. 2014c, A&A, 565, A45

Khomenko, E., & Santamaria, I. C. 2013, in Journal of Physics Conference Series, Vol. 440, Journal of Physics Conference Series, 012048

Khomenko, E., Vitas, N., Collados, M., & de Vicente, A. 2017, A&A, 604, A66

—. 2018, ArXiv e-prints, arXiv:1807.01061

Kippenhahn, R., & Schlüter, A. 1957, ZAp, 43, 36

Klimchuk, J. A., Tanner, S. E. M., & De Moortel, I. 2004, ApJ, 616, 1232

Kudoh, T., & Shibata, K. 1999, ApJ, 514, 493

Kuperus, M., & Raadu, M. A. 1974, A&A, 31, 189

Labrosse, N., Heinzel, P., Vial, J. C., et al. 2010, Space Sci. Rev., 151, 243

Landau, L. D., & Lifshitz, E. M. 1987, Fluid Mechanics, Second Edition: Volume 6 (Course of Theoretical Physics), 2nd edn., Course of theoretical physics / by L. D. Landau and E. M. Lifshitz, Vol. 6 (Butterworth-Heinemann)

Lani, A., Yalim, M. S., & Poedts, S. 2014, Computer Physics Communications, 185, 2538

Leake, J. E., & Arber, T. D. 2006, A&A, 450, 805

Leake, J. E., Lukin, V. S., & Linton, M. G. 2013, Physics of Plasmas, 20, 061202

Leake, J. E., Lukin, V. S., Linton, M. G., & Meier, E. T. 2012, ApJ, 760, 109

Leake, J. E., DeVore, C. R., Thayer, J. P., et al. 2014, Space Sci. Rev., 184, 107

Lee, E., Lukin, V. S., & Linton, M. G. 2014, A&A, 569, A94

Leenaarts, J. 2010, Mem. Soc. Astron. Italiana, 81, 576

Leighton, R. B. 1959, ApJ, 130, 366

Leighton, R. B., Noyes, R. W., & Simon, G. W. 1962, ApJ, 135, 474

Li, T., & Zhang, J. 2012, ApJ, 760, L10

Li, X. L. 1993, Physics of Fluids A, 5, 1904

Livescu, D. 2004, Physics of Fluids, 16, 118

Loughhead, R., & Bray, R. 1961, Australian Journal of Physics, 14, 347

Lukin, V. S., Glasser, A. H., Lowrie, W., & Meier, E. T. 2016, ArXiv e-prints, arXiv:1608.06030

Luna, M., Terradas, J., Oliver, R., & Ballester, J. L. 2008, ApJ, 676, 717

Mackay, D. H., Karpen, J. T., Ballester, J. L., Schmieder, B., & Aulanier, G. 2010, Space Sci. Rev., 151, 333

Maneva, Y. G., Alvarez Laguna, A., Lani, A., & Poedts, S. 2017, ApJ, 836, 197

Martínez-Gómez, D., Soler, R., & Terradas, J. 2017, ApJ, 837, 80

Martínez González, M. J., Collados, M., Ruiz Cobo, B., & Beck, C. 2008, A&A, 477, 953

Martínez González, M. J., Pastor Yabar, A., Lagg, A., et al. 2016, A&A, 596, A5

Martínez-Sykora, J., Bart, D., Viggo, H., & Mat, C. 2015, Philosophical Transactions of the Royal Society A: Mathematical, Physical and Engineering Sciences, 373, doi:10.1098/rsta.2014.0268

Martínez-Sykora, J., De Pontieu, B., Carlsson, M., & Hansteen, V. 2016, ApJ, 831, L1

Martínez-Sykora, J., De Pontieu, B., & Hansteen, V. 2012, ApJ, 753, 161

Mathew, S. K., Lagg, A., Solanki, S. K., et al. 2003, A&A, 410, 695

McLaughlin, J. A., De Moortel, I., Hood, A. W., & Brady, C. S. 2009, A&A, 493, 227

Meier, E., Lukin, V., & Shumlak, U. 2010, Computer Physics Communications, 181, 837

Meier, E. T. 2011, PhD thesis, University of Washington

Meier, E. T., & Shumlak, U. 2012, Physics of Plasmas, 19, 072508

Mikaelian, K. 2014, Physical review. E, Statistical, nonlinear, and soft matter physics, 89, 053009

Mitra, A., Roychoudhury, R., & Khan, M. 2016, Physics of Plasmas, 23, 024503

Mullan, D. J. 1971, MNRAS, 153, 145

Musielak, Z. E., Rosner, R., Stein, R. F., & Ulmschneider, P. 1994, ApJ, 423, 474

Naveh, A., T. Matthews, M., & I. Abarzhi, S. 2019

Newcomb, W. A. 1983, Physics of Fluids, 26, 3246

Ni, L., Lukin, V. S., Murphy, N. A., & Lin, J. 2018, ApJ, 852, 95

Nishikawa, K. I., & Sakai, J. 1982, Physics of Fluids, 25, 1384

Nye, A. H., & Thomas, J. H. 1976, ApJ, 204, 573

Nóbrega-Siverio, D., Moreno-Insertis, F., Martínez-Sykora, J., Carlsson, M., & Szydlarski, M. 2020, Astronomy & Astrophysics, 633, A66

Ofman, L., Nakariakov, V., & N. Sehgal, a. 2008, ApJ, 533, 1071

Orozco Suárez, D., Díaz, A. J., Asensio Ramos, A., & Trujillo Bueno, J. 2014, ApJ, 785, L10

Osterbrock, D. E. 1961, ApJ, 134, 347

Østerby, O. 2003, BIT Numerical Mathematics, 43, 811

Paletou, F., López Ariste, A., Bommier, V., & Semel, M. 2001, A&A, 375, L39

Parchevsky, K. V., & Kosovichev, A. G. 2007, ApJ, 666, L53

Pikelner, S. B. 1963, Soviet Ast., 6, 757

Pneuman, G. W., Solanki, S. K., & Stenflo, J. O. 1986, A&A, 154, 231

Popescu Braileanu, B., Lukin, V. S., Khomenko, E., & de Vicente, Á. 2019a, A&A, 627, A25

—. 2019b, A&A, 630, A79

Porth, O., Komissarov, S. S., & Keppens, R. 2014, MNRAS, 443, 547

Provornikova, E., Laming, J. M., & Lukin, V. S. 2018, ArXiv e-prints, arXiv:1803.11212

Quintero Noda, C., Borrero, J. M., Orozco Suárez, D., & Ruiz Cobo, B. 2014, A&A, 569, A73

Rempel, M., Schüssler, M., & Knölker, M. 2009, ApJ, 691, 640

Ribeyre, X., Tikhonchuk, V. T., & Bouquet, S. 2005, Ap&SS, 298, 75

Ricotti, M. 2014, Monthly Notices of the Royal Astronomical Society, 437, 371

Rijs, C., Rajaguru, S. P., Przybylski, D., et al. 2016, ApJ, 817, 45

Ristorcelli, J. R., & Clark, T. T. 2004, Journal of Fluid Mechanics, 507, 213–253

Sakai, J., & Nishikawa, K. I. 1983, Sol. Phys., 88, 241

Santamaria, I. C., Khomenko, E., Collados, M., & de Vicente, A. 2017, A&A, 602, A43

Schutgens, N. 1997, Astronomy and Astrophysics, 325, 352

Sharp, D. 1984, Physica D: Nonlinear Phenomena, 12, 3

Shelyag, S., Khomenko, E., de Vicente, A., & Przybylski, D. 2016, ApJ, 819, L11

Smirnov, B. M. 2003, Physics of Atoms and Ions (Springer-Verlag New York), XIII, 443, doi:10.1007/b97560

Smith, P. D., & Sakai, J. I. 2008, A&A, 486, 569

Snow, B., & Hillier, A. 2019, arXiv e-prints, arXiv:1904.12518

Soler, R., Carbonell, M., Ballester, J. L., & Terradas, J. 2013a, ApJ, 767, 171

Soler, R., Diaz, A. J., Ballester, J. L., & Goossens, M. 2013b, A&A, 551, A86

Soler, R., & Terradas, J. 2015, ApJ, 803, 43

Song, P., & Vasyliūnas, V. M. 2011, Journal of Geophysical Research (Space Physics), 116, A09104

Stanier, A., Daughton, W., Le, A., Li, X., & Bird, R. 2019, Physics of Plasmas, 26, 072121

Sterling, A. C. 2000, Sol. Phys., 196, 79

Stone, J. M., & Gardiner, T. 2007, Physics of Fluids, 19, 094104

Stone, J. M., & Gardiner, T. 2007, ApJ, 671, 1726

Terradas, J., Soler, R., Luna, M., Oliver, R., & Ballester, J. L. 2015, ApJ, 799, 94

Tóth, G., van der Holst, B., Sokolov, I. V., et al. 2012, Journal of Computational Physics, 231, 870 , special Issue: Computational Plasma PhysicsSpecial Issue: Computational Plasma Physics

Vaisala, V. 1925, Soc. Sci. Fennica, Commentationes Phys.-Math. II, 19, 37

van de Hulst, H. C. 1953, The Chromosphere and the Corona, ed. G. P. Kuiper, 207

van den Oord, G. H. J., Schutgens, N. A. J., & Kuperus, M. 1998, A&A, 339, 225

van der Holst, B., Tóth, G., Sokolov, I. V., et al. 2011, ApJS, 194, 23

Vandervoort, P. O. 1961, ApJ, 134, 699

Vasquez, B. J. 2005, Journal of Geophysical Research (Space Physics), 110, A10S02

Vernazza, J. E., Avrett, E. H., & Loeser, R. 1981, ApJS, 45, 635

Verwichte, E., Nakariakov, V. M., Ofman, L., & Deluca, E. E. 2004, Sol. Phys., 223, 77

Vitas, N., & Khomenko, E. 2015, Annales Geophysicae, 33, 703

Vögler, A., Shelyag, S., Schüssler, M., et al. 2005, A&A, 429, 335

Voronov, G. 1997, Atomic Data and Nuclear Data Tables, 65, 1

Vranjes, J., & Krstic, P. S. 2013, A&A, 554, A22

Wiehr, E., Stellmacher, G., & Bianda, M. 2019, The Astrophysical Journal, 873, 125

Withbroe, G. L., & Noyes, R. W. 1977, Annual Review of Astronomy and Astrophysics, 15, 363

Xie, J.-H., & Bühler, O. 2019, Journal of Fluid Mechanics, 877, R3

Xue, C., & Ye, W. 2010, Physics of Plasmas, 17, 042705

Youngs, D. L. 1984, Physica D: Nonlinear Phenomena, 12, 32

Zaqarashvili, T. V., Khodachenko, M. L., & Rucker, H. O. 2011a, A&A, 534, A93

—. 2011b, A&A, 529, A82

Zaqarashvili, T. V., Khodachenko, M. L., & Soler, R. 2013, A&A, 549, A113

Zhou, y. 2017a, Physics Reports, 720-722, doi:10.1016/j.physrep.2017.07.005

Zhou, Y. 2017b, Physics Reports, 723-725, 1 , rayleigh–Taylor and Richtmyer–Meshkov instability induced flow, turbulence, and mixing. II

.0.1 Analytical approach for the calculation of the linear growth rate in the two-fluid approximation

We consider a more general 3D setup, when the atmosphere is homogeneous in both x and y directions, but it is not uniform in the z direction, and all the equilibrium quantities only depend on height. We use the ansatz of separable solutions and we Fourier transform the linearized equations in time and in the x and y spatial directions, looking for solutions of the form:

$$\begin{aligned}\left\{\tilde{\rho}_{\rm n1},\tilde{p}_{\rm n1},\tilde{v}_{\rm xn},\tilde{v}_{\rm yn},\tilde{v}_{\rm zn},\tilde{\rho}_{\rm c1},\tilde{p}_{\rm c1},\tilde{v}_{\rm xc},\tilde{v}_{\rm yc},\tilde{v}_{\rm zc},\tilde{B}_{\rm x1},\tilde{B}_{\rm y1},\tilde{B}_{\rm z1}\right\} = \left\{\rho_{\rm n1}(z),p_{\rm n1}(z),v_{\rm xn}(z),v_{\rm yn}(z),v_{\rm zn}(z),\right.\\ \left.\rho_{\rm c1}(z),p_{\rm c1}(z),v_{\rm xc}(z),v_{\rm yc}(z),v_{\rm zc}(z),B_{\rm x1}(z),B_{\rm y1}(z),B_{\rm z1}(z)\right\}\times\exp\left(i\omega t-ik_{\rm x}x-ik_{\rm y}y\right). \quad (1)\end{aligned}$$

We write the linearized equations for both neutrals and charges, with the collisional coupling in the momentum equations, and introducing the ansatz of Eq. 1, we obtain a set of equations similar to that obtained in the single-fluid model, Eqs. 6.31 described in Chapter 6. We separate these equations in three groups, presented below:

Neutrals continuity, momentum and velocity divergence-free condition:

$$\begin{aligned}\rho_{\rm n1} &= -\frac{1}{i\omega}\frac{{\rm d}\rho_{\rm n0}}{{\rm d}z}v_{\rm zn},\\ -ik_{\rm x}v_{\rm xn}-ik_{\rm y}v_{\rm yn}+\frac{{\rm d}v_{\rm zn}}{{\rm d}z} &= 0,\\ i\omega\rho_{\rm n0}v_{\rm xn} &= ik_{\rm x}p_{\rm n1}+\alpha\rho_{\rm n0}\rho_{\rm c0}\left(v_{\rm xc}-v_{\rm xn}\right),\\ i\omega\rho_{\rm n0}v_{\rm yn} &= ik_{\rm y}p_{\rm n1}+\alpha\rho_{\rm n0}\rho_{\rm c0}\left(v_{\rm yc}-v_{\rm yn}\right),\\ i\omega\rho_{\rm n0}v_{\rm zn} &= -\rho_{\rm n1}g-\frac{{\rm d}p_{\rm n1}}{{\rm d}z}+\alpha\rho_{\rm n0}\rho_{\rm c0}\left(v_{\rm zc}-v_{\rm zn}\right), \quad (2)\end{aligned}$$

Charges continuity, momentum and velocity divergence-free condition:

$$\begin{aligned}\rho_{\rm c1} &= -\frac{1}{i\omega}\frac{{\rm d}\rho_{\rm c0}}{{\rm d}z}v_{\rm zc},\\ -ik_{\rm x}v_{\rm xc}-ik_{\rm y}v_{\rm yc}+\frac{{\rm d}v_{\rm zc}}{{\rm d}z} &= 0,\\ i\omega\rho_{\rm c0}v_{\rm xc} &= ik_{\rm x}p_{\rm c1}+\frac{1}{\mu_0}\left(ik_{\rm x}B_{\rm y1}B_{\rm y0}-ik_{\rm y}B_{\rm x1}B_{\rm y0}+\frac{{\rm d}B_{\rm x0}}{{\rm d}z}B_{\rm z1}\right)+\alpha\rho_{\rm n0}\rho_{\rm c0}\left(v_{\rm xn}-v_{\rm xc}\right),\\ i\omega\rho_{\rm c0}v_{\rm yc} &= ik_{\rm y}p_{\rm c1}+\frac{1}{\mu_0}\left(ik_{\rm y}B_{\rm x1}B_{\rm x0}-ik_{\rm x}B_{\rm y1}B_{\rm x0}+\frac{{\rm d}B_{\rm y0}}{{\rm d}z}B_{\rm z1}\right)+\alpha\rho_{\rm n0}\rho_{\rm c0}\left(v_{\rm yn}-v_{\rm yc}\right),\\ i\omega\rho_{\rm c0}v_{\rm zc} &= -\rho_{\rm c1}g-\frac{{\rm d}p_{\rm c1}}{{\rm d}z}-\frac{1}{\mu_0}\left[B_{\rm y0}\left(\frac{{\rm d}B_{\rm y1}}{{\rm d}z}+ik_{\rm y}B_{\rm z1}\right)+B_{\rm x0}\left(\frac{{\rm d}B_{\rm x1}}{{\rm d}z}+ik_{\rm x}B_{\rm z1}\right)+B_{\rm x1}\frac{{\rm d}B_{\rm x0}}{{\rm d}z}+B_{\rm y1}\frac{{\rm d}B_{\rm y0}}{{\rm d}z}\right]\\ &\quad+\alpha\rho_{\rm n0}\rho_{\rm c0}\left(v_{\rm zn}-v_{\rm zc}\right), \quad (3)\end{aligned}$$

Induction equations:

$$
\begin{aligned}
B_{\mathrm{x1}} &= \frac{1}{i\omega}\left[-ik_{\mathrm{y}}B_{\mathrm{y0}}v_{\mathrm{xc}} - v_{\mathrm{zc}}\frac{\mathrm{d}B_{\mathrm{x0}}}{\mathrm{d}z} + B_{\mathrm{x0}}\left(ik_{\mathrm{y}}v_{\mathrm{yc}} - \frac{\mathrm{d}v_{\mathrm{zc}}}{\mathrm{d}z}\right)\right],\\
B_{\mathrm{y1}} &= \frac{1}{i\omega}\left[-ik_{\mathrm{x}}B_{\mathrm{x0}}v_{\mathrm{yc}} - v_{\mathrm{zc}}\frac{\mathrm{d}B_{\mathrm{y0}}}{\mathrm{d}z} + B_{\mathrm{y0}}\left(ik_{\mathrm{x}}v_{\mathrm{xc}} - \frac{\mathrm{d}v_{\mathrm{zc}}}{\mathrm{d}z}\right)\right],\\
B_{\mathrm{z1}} &= -\frac{1}{\omega}\left(k_{\mathrm{x}}B_{\mathrm{x0}} + k_{\mathrm{y}}B_{\mathrm{y0}}\right)v_{\mathrm{zc}}\,.
\end{aligned}
\tag{4}
$$

The above Eqs. 2, 3, 4 simplify to a system of two coupled ODEs, and with the notation $\lambda = i\omega$, we obtain:

$$
\begin{aligned}
&\lambda\alpha\rho_{\mathrm{n0}}\rho_{\mathrm{c0}}\left(\frac{\mathrm{d}^2v_{\mathrm{zc}}}{\mathrm{d}z^2} - \frac{\mathrm{d}^2v_{\mathrm{zn}}}{\mathrm{d}z^2}\right) + \lambda\alpha\rho_{\mathrm{n0}}\rho_{\mathrm{c0}}\left(k_{\mathrm{x}}^2 + k_{\mathrm{y}}^2\right)\left(v_{\mathrm{zn}} - v_{\mathrm{zc}}\right) - \frac{\mathrm{d}^2v_{\mathrm{zc}}}{\mathrm{d}z^2}\left(\lambda^2\rho_{\mathrm{c0}} + b\right)\\
&\qquad -\frac{\mathrm{d}v_{\mathrm{zc}}}{\mathrm{d}z}\left(\lambda^2\frac{\mathrm{d}\rho_{\mathrm{c0}}}{\mathrm{d}z} + \frac{\mathrm{d}b}{\mathrm{d}z}\right) + v_{\mathrm{zc}}\left(k_{\mathrm{x}}^2 + k_{\mathrm{y}}^2\right)\left(\lambda^2\rho_{\mathrm{c0}} + b - g\frac{\mathrm{d}\rho_{\mathrm{c0}}}{\mathrm{d}z}\right) = 0\,,\\
&\lambda\alpha\rho_{\mathrm{n0}}\rho_{\mathrm{c0}}\left(\frac{\mathrm{d}^2v_{\mathrm{zn}}}{\mathrm{d}z^2} - \frac{\mathrm{d}^2v_{\mathrm{zc}}}{\mathrm{d}z^2}\right) + \lambda\alpha\rho_{\mathrm{n0}}\rho_{\mathrm{c0}}\left(k_{\mathrm{x}}^2 + k_{\mathrm{y}}^2\right)\left(v_{\mathrm{zc}} - v_{\mathrm{zn}}\right) - \frac{\mathrm{d}^2v_{\mathrm{zn}}}{\mathrm{d}z^2}\lambda^2\rho_{\mathrm{n0}}\\
&\qquad -\frac{\mathrm{d}v_{\mathrm{zn}}}{\mathrm{d}z}\lambda^2\frac{\mathrm{d}\rho_{\mathrm{n0}}}{\mathrm{d}z} + v_{\mathrm{zn}}\left(k_{\mathrm{x}}^2 + k_{\mathrm{y}}^2\right)\left(\lambda^2\rho_{\mathrm{n0}} - g\frac{\mathrm{d}\rho_{\mathrm{n0}}}{\mathrm{d}z}\right) = 0\,,
\end{aligned}
\tag{5}
$$

where we have used the notation:

$$
b = \frac{1}{\mu_0}\left(k_xB_{\mathrm{x0}} + k_yB_{\mathrm{y0}}\right)^2 \tag{6}
$$

In principle, one can attempt to discretize simultaneously the two ODEs, Eqs.5, and solve the quadratic eigenvalue problem (QEP) by the linearization method described in section 6.6 in Chapter 6, where the order of the polynomial in λ is 2 and $\mathbf{u} = (v_{\mathrm{zn}}[1], ...v_{\mathrm{zn}}[m_{\mathrm{z}}], v_{\mathrm{zc}}[1], ...v_{\mathrm{zc}}[m_{\mathrm{z}}])$, with m_{z} being the number of the points. We can observe that in the first equation, none of the free terms (which do not contain λ) or coefficients of λ^2 contains terms related to neutral velocity. Similarly, none of the free terms or coefficients of λ^2 contains terms related to charge's velocity in the second equation. Therefore, the matrices $\hat{\mathbf{A}}_{\mathbf{2}}$ and $\hat{\mathbf{A}}_{\mathbf{0}}$ are singular, and the above method does not work in this case. Yet another idea is to define the variables:

$$
u_1 = v_{\mathrm{zn}}\,, \quad u_2 = \frac{\mathrm{d}v_{\mathrm{zn}}}{\mathrm{d}z}\,, \quad u_3 = v_{\mathrm{zc}}\,, \quad u_4 = \frac{\mathrm{d}v_{\mathrm{zc}}}{\mathrm{d}z}\,, \tag{7}
$$

and the vector:

$$
\mathbf{u} = \begin{pmatrix} u_1 \\ u_2 \\ u_3 \\ u_4 \end{pmatrix} \tag{8}
$$

and to write Eqs. 5 in the form,

$$\frac{\mathrm{d}\mathbf{u}}{\mathrm{d}z} = \hat{\mathbf{A}}(\mathbf{z})\mathbf{u}\,. \tag{9}$$

From the definition of the variables in Eq. 7, the second and the fourth rows of A are $(0, 1, 0, 0)$, and $(0, 0, 0, 1)$, respectively, and the first and the third rows are obtained from the two second order ODEs, Eqs. 5. We have twice the number of variables now (four instead of two), but the simplification comes from the fact that the homogeneous system of linear second order ODEs has transformed into a homogeneous system of linear first order ODEs. We can look for a suitable method to solve this system, however, the linearization of the QEP is equivalent to the transformation of the system of second order ODEs to a system of first order ODEs. There exist other methods to solve the QEP, such as the Arnoldi algorithms, the Second Order Arnoldi method (SOAR) being extensively described in the literature. However, this is not done here and requires future research.